Universidad Autónoma de Madrid

Instituto de Física Teórica UAM-CSIC

Gauge theories with dynamical adjoint fermions at large-N_c

Autor:
Pietro Butti

Dirigida por:
Antonio González-Arroyo

Co-dirigida por:
Margarita García Pérez

Memoria de Tesis Doctoral
presentada para optar al Título de Doctor ante del

Departamento de Física Teórica
de la Universidad Autónoma de Madrid

June 2023

ABSTRACT

This thesis explores the study of Yang-Mills theories with matter in the adjoint representation, focusing on the limit of large number of colors (large-N_c). The research leverages the property of Eguchi-Kawai reduction, where the theory becomes independent of the torus size in the large-N_c limit, facilitating simulation as a matrix model on a lattice with a single spacetime point. Key to this approach is the application of twisted boundary conditions (TEK reduction), providing a solid and efficient way to formulate and simulate Yang-Mills theory, including its extension with matter in the adjoint representation. The thesis provides a comprehensive overview of the lattice formulation of volume-reduced theories, presenting a review of pertinent concepts. It then presents a collection of results that encompass various research areas, offering insights into multiple topics of investigation. The primary field of application is the pure Yang-Mills theory in the large-N_c limit, of which we present a tree-level improved methodology to perform the scale setting. Furthermore, we present a preliminary calculation of the Λ-parameter in the $\overline{\text{MS}}$ scheme and the chiral condensate of the theory. Moving on to the case of $\mathcal{N} = 1$ SUSY Yang-Mills theory, we conducted simulations featuring a single Majorana adjoint fermion. Consistent results were obtained by determining lattice spacing through various observables. We then studied the supersymmetric limit and extrapolated the lattice scale in the massless gluino limit, revealing the expected dependence on bare couplings in the supersymmetric theory.

RESUMEN

Esta tesis explora el estudio de las teorías de Yang-Mills con materia en la representación adjunta, centrándose en el límite en el que el número de colores es N_c es grande. La investigación aprovecha la propiedad de la reducción de Eguchi-Kawai, donde la teoría se vuelve independiente del tamaño del espaciotiempo en el límite de N_c grande, facilitando la simulación como un modelo matricial en una red con un único punto del espaciotiempo. La clave de este enfoque es la aplicación de condiciones de contorno "twisted" (reducción TEK), que proporciona una forma sólida y eficiente de formular y simular la teoría de Yang-Mills, incluyendo su extensión con materia en la representación adjunta. La tesis proporciona una visión global de la formulación reticular de las teorías de volumen reducido, presentando una revisión de los conceptos pertinentes. A continuación, presenta una colección de resultados que abarcan diversas áreas de investigación, ofreciendo una visión de múltiples temas de investigación. El principal campo de aplicación es la teoría pura de Yang-Mills en el límite de N_c grande, de la que presentamos una metodología mejorada a nivel de árbol para realizar el ajuste de escala. Además, presentamos un cálculo preliminar del parámetro Λ en el esquema $\overline{\text{MS}}$ y el condensado quiral de la teoría. Pasando al caso de la teoría $\mathcal{N} = 1$ SUSY Yang-Mills, realizamos simulaciones con un único fermión adjunto Majorana. Se obtuvieron resultados consistentes determinando el espaciado de la red a través de varios observables. A continuación, estudiamos el límite supersimétrico y extrapolamos la escala de reticulo en el límite del gluino sin masa, recuperando la dependencia esperada de los acoplamientos desnudos en la teoría supersimétrica.

PUBLICATIONS

This Thesis is partly based on the following publications.

[1] Ed Bennett, Andreas Athenodorou, Georg Bergner, Pietro Butti, and Biagio Lucini. "Update on SU(2) with one adjoint Dirac flavor." In: *PoS* LATTICE2022 (2023), p. 204. DOI: 10.22323/1.430.0204. arXiv: 2212.09173 [hep-lat].

[2] Pietro Butti, Margarita García Pérez, Antonio González-Arroyo, Ken-Ichi Ishikawa, and Masanori Okawa. "Adjoint fermions at large-N_c on the lattice." In: *PoS* LATTICE2022 (2023), p. 365. DOI: 10.22323/1.430.0365. arXiv: 2212.02138 [hep-lat].

[3] Pietro Butti, Margarita García Pérez, Antonio González-Arroyo, Ken-Ichi Ishikawa, and Masanori Okawa. "Scale setting for large-N_c SUSY Yang-Mills on the lattice." In: *JHEP* 07 (2022), p. 074. DOI: 10.1007/JHEP07(2022)074. arXiv: 2205.03166 [hep-lat].

[4] Pietro Butti, Margarita García Pérez, Antonio González-Arroyo, K. I. Ishikawa, and M. Okawa. "Scale setting for $\mathcal{N} = 1$ SUSY Yang-Mills at large-N_c through volume-reduced twisted matrix model." In: *PoS* LATTICE2021 (2022), p. 474. DOI: 10.22323/1.396.0474. arXiv: 2111.03607 [hep-lat].

[5] Ken-Ichi Ishikawa, Pietro Butti, Antonio González-Arroyo, Masanori Okawa, and Margarita García Pérez. "Large N_c simulation of the twisted reduced matrix model with an adjoint Majorana fermion." In: *PoS* LATTICE2021 (2021), p. 334. DOI: 10.22323/1.396.0334. arXiv: 2111.00386 [hep-lat].

[6] Pietro Butti and Antonio González-Arroyo. "Asymptotic scaling in Yang-Mills theory at large-N_c." In: *in preparation* (2023).

[7] Claudio Bonanno, Pietro Butti, Margarita García Pérez, Antonio González-Arroyo, Ken-Ichi Ishikawa, and Masanori Okawa. "The QCD chiral condensate at large-N_c on the lattice." In: *in preparation* (2023).

ACKNOWLEDGMENTS

I am deeply in debt to my two supervisors, Marga and Tony, who conceived and directed this project. Their supervision marked intensely my experience and gave me knowledge that goes beyond Theoretical Physics. The work presented here has been made possible by all the interactions, discussions and exchange of enthusiasm with the members of the lattice group at the IFT and of the EuroPLEx project. Among the first, I am particularly grateful to Claudio Bonanno and Jorge Dasilva, with whom professional interaction has mixed with the pleasure of spending time together at IFT and in Madrid. Among the people related to the EuroPLEx project, I am thankful to Leonardo Chimirri, with which I am happy to have shared part of the last ten years, starting from the first days of undergrad school in Torino. Lastly, my most heartfelt thanks go to my dear friend Alessandro Conigli, whose presence has been crucial in this journey and with whom, apart of countless discussions and ping-pong and padel matches, I shared the feeling of growing together.

I acknowledge support from the project H2020-MSCAITN-2018-813942 (EuroPLEx) and the EU Horizon 2020 research and innovation programme, This work used computational resources of SX-ACE (Osaka U.) and Oakbridge-CX (U. of Tokyo) through the HPCI System Research Project (Project ID: hp220011, hp210027, hp200027, hp190004) and Subsystem B of ITO system (Kyushu U.). We acknowledge the use of the Hydra, Analysis and Ciclope clusters at IFT and HPC resources at CESGA (Supercomputing Centre of Galicia).

CONTENTS

I INTRODUCTION 1

1 QUANTUM FIELDS FOR STRONG INTERACTIONS 3
- 1.1 Strongly interacting theories in the continuum 3
  - 1.1.1 The large-N_c limit 7
  - 1.1.2 Chiral symmetry 9
  - 1.1.3 Supersymmetry 12
- 1.2 Yang-Mills theories on the lattice 15
  - 1.2.1 $SU(N_c)$ Yang-Mills theories on the lattice 15
  - 1.2.2 The fate of (fermionic) symmetries on the lattice 21
  - 1.2.3 Lattice field theory simulations 24

2 QUANTUM FIELDS ON THE TORUS AND REDUCTION 31
- 2.1 Yang-Mills field on the torus 31
- 2.2 Implementing twisted boundary conditions on the lattice 34
- 2.3 Large-N_c limit and volume reduction 36
  - 2.3.1 A historical perspective 37
  - 2.3.2 Finite-N_c corrections 40
- 2.4 Fermion fields on the twisted lattice 41
  - 2.4.1 Reducing fermion action 42
  - 2.4.2 Meson correlators and spectroscopy in the reduced model 47

II LARGE-N_c SIMULATIONS ON A SINGLE-SITE LATTICE 49

3 TECHNICAL ASPECTS OF SINGLE SITE SIMULATIONS 51
- 3.1 $N_f = 0$: simulating the TEK model 51
  - 3.1.1 The Fabricius-Haan algorithm 52
- 3.2 $N_f > 0$: a theory with dynamical adjoint fermions 56
  - 3.2.1 $N_f = \frac{1}{2}$: One adjoint Majorana fermion 58
  - 3.2.2 $N_f = 1, 2$ adjoint Dirac fermions 62
- 3.3 Dealing with autocorrelation 62
- 3.4 Scale setting 66
  - 3.4.1 Scale setting with the Wilson flow scale 66
- 3.5 Spectroscopy on a single-site lattice 73

4 RESULTS FOR YANG-MILLS THEORY AT LARGE-N_c 77
- 4.1 $N_f = 0$: The scale of Yang-Mills theory at large-N_c 77
  - 4.1.1 Outside the window 83
- 4.2 Testing (asymptotic) scaling at large-N_c 88
  - 4.2.1 The Λ-parameter 89
- 4.3 The chiral condensate of Yang-Mills theory at large-N_c 95

4.3.1 The condensate from the GMOR relation 96
4.3.2 The chiral condensate from the Banks-Casher relation 97
5 RESULTS FOR YANG-MILLS THEORY COUPLED WITH $N_f = \frac{1}{2}$ ADJOINT FERMIONS 105
5.1 The Wilson flow scale 105
5.2 Other determinations of the scale $N_f = \frac{1}{2}$ 109
5.2.1 The scale from Wilson loops 109
5.2.2 The scale from fundamental meson spectrum 112
5.2.3 Scales comparison 117
5.3 The supersymmetric limit 119
5.3.1 Determination from the PCAC mass 120
5.3.2 Determination from the eigenvalues of Q_w 123
5.4 The lattice spacing and the β-function in the SUSY limit 125
5.5 The case of $N_f = 1, 2$ 128
5.5.1 The dependence on the scale on the fermion mass 129
BIBLIOGRAPHY 141

INTRODUCTION

The Standard Model (SM) of particle physics has been a highly successful theory since its inception in the Sixties, with countless experimental verifications confirming its validity. One of the most significant experimental confirmations of the SM came in 2012 with the discovery of the Higgs boson by the ATLAS and CMS groups at the Large Hadron Collider (LHC) at CERN [1, 2]. This discovery was a significant milestone in particle physics, providing strong evidence in support of the SM's description of known particle interactions. Ten years after the discovery of the Higgs boson, the "last missing piece of the puzzle", the field of particle physics has shifted towards new frontiers in research. One of these frontiers is precision physics, which aims to measure quantities related to particle interactions with unprecedented experimental accuracy. This approach requires theoretical predictions for these quantities to be of the same precision as experimental measurements, in the hope that small significant deviations from experimental results could unveil the presence of new physics. Among the different quantities, a noticeable mention goes to the magnetic moment of the muon, referred to as $(g_\mu - 2)$, whose most precise experimental value was revealed by Fermilab in April 2021 [3]. On the theoretical side, a consensus prediction is still to be achieved: a data-driven dispersive approach leads to a value that shows a 4.2σ discrepancy with the experimental result [4], while ab-initio SM calculations reduce this tension to 1.5σ [5]. This thrilling divergence on the theoretical side can be considered one of the major problems in modern theoretical physics.

Another frontier in particle physics is the search for new theoretical frameworks that can address more fundamental problems. This is the case of the so-called *hierarchy problem*, which refers to the challenge of explaining the significant difference between the electroweak scale and the Planck scale in particle physics that requires an "unnatural" amount of fine-tuning. Another intriguing issue is the one called the *strong* CP *problem* which, specifically, explores the absence of significant violation of the combined symmetry of charge conjugation (C) and parity (P) in strong interactions. These problems, among others, led to the necessity to look at extensions of the SM theories that could provide a solution to these problems, waiting for new experimental results to give bounds. Among the most popular candidates, we cite *supersymmetry* and *technicolor* models. The first class of theories involves enlarging the spectrum by adding a "super"-partner with opposite spin and statistics to each of the SM fields, while technicolor theories add to the SM gauge group a new interaction $SU(N_c)$, and

N_{tf} massless flavors of technifermions. As we continue to explore and gain a better understanding of the fundamental problems posed by the Standard Model, it is possible that any potential solutions could offer valuable insights into other significant issues in modern particle physics, including those whose input motivation comes from cosmology, such as dark matter.

As the expert reader may have noticed, the overview provided here covers several of the unresolved issues in the SM, which are tied together by a common theme. The key underlying factor among these challenges is that they all require an understanding of quantum field theories featuring a strong interaction. Looking back in history, one of the first notable examples of a strongly interacting theory was QCD, the sector of the SM responsible for the strong nuclear force emerging from the interaction between quarks and gluons. The exploration of QCD and its properties has been a major endeavor in physics over the past century and has greatly influenced our comprehension of QFTs. Since the discovery of asymptotic freedom in the early Seventies [6, 7], QCD has led to several predictions that have been experimentally validated in hadronic physics. Nonetheless, due to its fundamentally non-perturbative nature, strong interaction is challenging to study theoretically. The intriguing phenomena of hadronic physics, such as confinement, occur in the low-energy regime where the theory is entirely non-perturbative, and conventional analytical methods are limited in their effectiveness. Although nowadays we are still far from a complete understanding of the mechanism underlying these phenomena, in the last 50 years a lot of progress has been done. When determining a significant year to mark the beginning of this journey, as suggested in [8], it is impossible not to acknowledge 1974. This was the year when Gerard 't Hooft's "*A Planar Diagram Theory for Strong Interactions*" was published in Nuclear Physics B [9], and Kenneth Geddes Wilson's "*Confinement of Quarks*" was published in Physical Review D a few months later [10]. These papers had a significant impact on the study and comprehension of high-energy physics in the ensuing decades, and they led to the development of two distinct yet occasionally intersecting lines of research. In the first quoted paper, striking properties of non-Abelian gauge theories were demonstrated to emerge from the limit in which the number of color charges N_c is taken to be very large and vanishing gauge coupling. First of all, Feynman diagrams can be organized in an expansion in $1/N_c$, and in the aforementioned limit, the only surviving terms have well-defined topological properties. On the other hand, the second paper formulated a quantum field theory on a discretized space-time and showed how the confinement of quarks emerged in the (unphysical) limit in which the coupling grows to infinity. Apart from the result on confinement, the paper led the foundations of the field of Lattice Gauge Theories, a natural way of regularizing a QFT providing a rigorous

formulation of the path integral and a natural link to statistical field theory. In particular, this analogy opens the possibility to study QFTs through methods and techniques belonging to other fields in theoretical physics, like Monte-Carlo computations. Due to the complexity of the matter, simulating a Quantum Field Theory (QFT) on a lattice to generate quantitative predictions is still considered nowadays one of the most challenging and expensive tasks in Computer Science. This is the reason why LGTs were not employed as a quantitative tool for prediction until the last two decades. However, the recent advancements in computing power and algorithmic development have significantly increased the use of the lattice approach to explore strongly interacting QFTs and nowadays is considered among the leading theoretical tools in theoretical physics.[1]

This Thesis frames itself somehow in between these two important topics in the context of the study of strongly interacting gauge theories aimed at a better understanding of QCD and QCD-like theories that can be used as possible extensions for the SM. Our main goal will be based on the study of the lattice of the large-N_c limit of $SU(N_c)$ Yang-Mills theories coupled with fermionic matter on the lattice. In recent years, the investigation of the large-N_c limit on the lattice has been an important area of study.[2] However, one significant challenge encountered in this line of inquiry is the computational complexity, which escalates as the number of colors increases. While large-N_c results do not necessarily require the precision achieved by lattice simulations generating results that can be compared with real-world phenomena, obtaining accurate quantitative predictions still poses challenges. One of these challenges is the substantial computational cost associated with simulating gauge theories that include dynamical fermions and a sufficiently large number of colors. In the large-N_c limit, it is well-established that fundamental fermions become "quenched," meaning their dynamical effects can be neglected, drastically reducing the computational effort required by the simulation. However, when large-N_c results are obtained with extrapolation from relatively small N_c, it becomes crucial to ensure that the dynamical effects of fermions do not significantly affect the accuracy of the extrapolation. Moreover, if one aims to simulate theories with adjoint fermions (or fermions in a representation larger than the fundamental), the natural quenching no longer applies, and one is limited to simulating these theories with a small number of colors, far from the large-N_c limit. This thesis will utilize an alternative paradigm,

1 In the aforementioned muon $(g_\mu - 2)$ puzzle, the ab-initio SM result comes indeed from state-of-art lattice simulation. The reference quoted refers to the first result of the BMW collaboration. The interested reader can refer to [11] for the most recent (up-to-date) review on the topic.

2 For a general review of the recent effort in this field up to 2013, the reader can refer to [8]. More specifically on the large-N_c limit of QCD, the reader may look also at [12].

known as *twisted volume reduction* [13], to overcome the aforementioned issues. As it is well known in the literature, $SU(N_c)$ gauge theories possessing center-symmetry exhibit volume independence in the large-N_c limit when compactified on a torus. By using twisted boundary conditions, one can exploit this feature safely and use it to formulate and simulate the theory on a single-site lattice. Up to now, twisted models are the only methods that allow simulating gauge theories at values of N_c of the order of $10^2 - 10^3$. Over the past 15 years, this method has been applied successfully to various physical applications on the lattice. More recently, it has also been applied to Yang-Mills theory coupled with N_f dynamical flavors of fermions in the adjoint representation, which is the focus of this thesis. This work poses itself as a natural continuation in this line of research, extending some of the present topics and opening new ones.

The first part of the results we are interested in is the pure Yang-Mills theory in the large-N_c limit, which, as motivated in the first part of this introduction, is at the base of QCD and the strong sector in the SM. The other main part is related to the usage of adjoint fermions. As it is well known, QCD is a $SU(3)$ gauge theory where quark fields are fermions in the fundamental representation and therefore the usage of adjoint fermions may sound artificial. The reason why we are interested in theories with such nonconventional matter content is manifold. First of all, gauge theories with adjoint fermions are among the possible candidates of relevance in the context of BSM technicolor model. Another interesing point of view, is the one suggested by the *orientifold equivalence* [14, 15], which provides a natural parallelism between QCD with adjoint fermions to QCD with Dirac fermions in a two-index symmetric or anti-symmetric representation. In the large-N_c limit, the latter is equivalent to the fundamental representation and thus the model can be seen as the natural generalization of QCD in the large-N_c limit.

Another reason can be found in the remarkable plethora of different physical scenarios that can be achieved by studying such theories. A single adjoint Majorana fermion can be seen as the super-partner of the gluon, and therefore the respective gauge theory is the simplest realization of a supersymmetric theory. On the other hand, a gauge theory featuring two adjoint Dirac fermions has been considered a valid potential BSM candidate. However, recent lattice investigations calculated an anomalous dimension that exceeded the limit set by phenomenology, thus ruling out the theory as a viable option. It should be noted, though, that this theory is known to be conformal, making it interesting from a theoretical point of view since it exhibits a completely different behavior than confining theories. The case of a single adjoint Dirac fermion is also extremely relevant in a variety of different contexts, from the other potential candidate for a BSM theory to condensed matter physics. In the former context, the confining

or conformal nature is actively still debated in the literature, and precious insights could come from the study of the large-N_c limit.

After establishing the context for the framework to which this Thesis belongs, we will now delve into a more detailed explanation of the topics and objectives at hand.

In Chapter 1, we deal with the formulation of strongly interacting gauge theories and their relevant features. We will go through some of the details of the formulation of a Yang-Mills theory on Euclidean space-time, dedicating some space to introduce the large-N_c limit and the properties emerging from coupling this gauge theory to fermions, such as chiral symmetry and supersymmetry. In the second part of the Chapter, we will go through the formulation of these theories on the lattice, exploring the consequences of the space-time discretization. In the last part, we will give an overview of how Monte-Carlo methods can be applied to extract relevant physical quantities.

In Chapter 2, we will introduce the concept of twisted boundary conditions and how their usage provides a way to mix the color and volume degrees of freedom. On the base of that, we will also see how volume reduction emerges as a feature when the large-N_c limit is taken. We will apply the reduction to formulate the Twisted Eguchi-Kawaii (TEK) model, which is going to be our main tool to simulate $SU(N_c)$ Yang-Mills theories on a single-site lattice. In the last part of the Chapter, we will overview how fermions can be coupled and simulated in the single-site framework.

After this general introduction, in Chapter 3 we overview the main algorithmic ideas and issues to implement actual simulations of the different theories we introduced in the previous Chapters. We will present lists of the different statistical ensembles of configurations we generated for the case of the pure Yang-Mills theory and Yang-Mills theory coupled with N_f flavors of adjoint fermions in the adjoint representation. We will also provide details on how the problem of autocorrelation is dealt with in our error analysis.

Chapter 4 is dedicated to the results of the pure Yang-Mills theory, denoted as $N_f = 0$. We first present our methodology to set the scale of the lattice theory, which is based on standard gradient flow techniques adapted to our case and improved with perturbation theory at the tree level to deal with systematic effects coming from the lattice discretization and finite N_c corrections. After testing and performing scale setting, we dedicate a section to discuss scaling and asymptotic scaling in our simulation, giving an estimate of the Λ-parameter for Yang-Mills theory in the large-N_c limit. The last part of the Chapter is dedicated to the calculation of the chiral quark condensate.

In Chapter 5 we deal with the case of dynamical adjoint fermions. We first perform the scale setting with the Wilson flow in the case of one adjoint Majorana fermion ($N_f = \frac{1}{2}$), which in the continuum corresponds to $\mathcal{N} = 1$ SUSY Yang-Mills. We then proceed to study

the limit in which the lattice theory recovers supersymmetry by employing two different methodologies, obtaining compatible results. Combining the values of the scale we extracted with the results concerning the supersymmetric limit, we study the dependence of the lattice spacing on the bare coupling for the supersymmetric theory confronting the results with theoretical predictions of the β-function. The rest of the Chapter is dedicated to performing the scale setting on the theory following other two methodologies and comparing the results. In the last part, we apply the Wilson flow scale setting procedure to the ensembles for 1 and 2 adjoint Dirac fermions ($N_f = 1, 2$), which allows us to study the dependence of the scale on the adjoint fermion mass highlighting the behavior of the theories in the massless and the heavy mass limit.

The last Chapter will be dedicated to the conclusions, where we collect and summarize the main results we obtained in this Thesis.

INTRODUCCIÓN

El Modelo Estándar (SM) de la física de partículas ha sido una teoría de gran éxito desde su creación en los años sesenta, con innumerables verificaciones experimentales que confirman su validez. Una de las confirmaciones experimentales más significativas del Modelo Estandard (SM) se produjo en 2012 con el descubrimiento del bosón de Higgs por los grupos ATLAS y CMS en el Gran Colisionador de Hadrones (LHC) del CERN [1, 2]. Este descubrimiento fue un hito significativo en la física de partículas, proporcionando una fuerte evidencia en apoyo de la descripción del SM de las interacciones de partículas conocidas. Diez años después del descubrimiento del bosón de Higgs, la "última pieza que faltaba en el rompecabezas", el campo de la física de partículas se ha desplazado hacia nuevas fronteras en la investigación. Una de estas fronteras es la física de precisión, cuyo objetivo es medir las cantidades relacionadas con las interacciones de las partículas con una precisión experimental sin precedentes. Este enfoque exige que las predicciones teóricas de estas cantidades tengan la misma precisión que las mediciones experimentales, con la esperanza de que pequeñas desviaciones significativas de los resultados experimentales puedan desvelar la presencia de nueva física. Entre las distintas cantidades, destaca el momento magnético del muón, denominado $(g_\mu - 2)$, cuyo valor experimental más preciso fue revelado por el Fermilab en abril de 2021 [3]. En el lado teórico, aún no se ha alcanzado una predicción de consenso: un enfoque dispersivo basado en datos conduce a un valor que muestra una discrepancia de 4,2 σ con el resultado experimental [4], mientras que los cálculos SM ab-initio reducen esta tensión a 1.5σ [5]. Esta emocionante divergencia en el lado teórico puede considerarse uno de los principales problemas de la física teórica moderna.

Otra frontera en la física de partículas es la búsqueda de nuevos marcos teóricos que puedan abordar problemas más fundamentales. Este es el caso del llamado *problema de jerarquía*, que se refiere al reto de explicar la diferencia significativa entre la escala electrodébil y la escala de Planck en la física de partículas que requiere una cantidad "no natural" de ajuste fino. Otra cuestión intrigante es el denominado *problema* CP *fuerte* que, en concreto, explora la ausencia de violación significativa de la simetría combinada de conjugación de carga (C) y paridad (P) en las interacciones fuertes. Estos problemas, entre otros, llevaron a la necesidad de buscar extensiones de las teorías del SM que pudieran proporcionar una solución a estos problemas, a la espera de que nuevos resultados experimentales dieran límites. Entre los candidatos más populares, citamos los modelos *supersimetría* y

tecnicolor. La primera clase de teorías implica ampliar el espectro añadiendo un "super" compañero con spin y estadística opuestos a cada uno de los campos SM, mientras que las teorías technicolor añaden al grupo gauge SM una nueva interacción $SU(N_c)$, y N_{tf} sabores sin masa de technifermiones. A medida que continuamos explorando y adquiriendo una mejor comprensión de los problemas fundamentales que plantea el Modelo Estándar, es posible que cualquier solución potencial pueda ofrecer valiosos conocimientos sobre otras cuestiones significativas para la física de partículas moderna, incluidas aquellas cuya motivación procede de la cosmología, como la materia oscura.

Como habrá observado el lector experto, la visión general que aquí se ofrece abarca varias de las cuestiones sin resolver del SM, unidas por un tema común. El factor clave subyacente entre estos retos es que todos ellos requieren una comprensión de las teorías cuánticas de campos fuertemente acopladas. Historicamente, uno de los primeros ejemplos notables de una teoría con interacción fuerte fue la QCD, el sector del SM responsable de la fuerza nuclear fuerte que surge de la interacción entre quarks y gluones. La exploración de la QCD y sus propiedades ha sido una de las principales tareas de la física durante el siglo pasado y ha influido enormemente en nuestra comprensión de las QFT. Desde el descubrimiento de la libertad asintótica a principios de los setenta [6, 7], la QCD ha conducido a varias predicciones que han sido validadas experimentalmente en la física hadrónica. Sin embargo, debido a su naturaleza fundamentalmente no-perturbativa la interacción fuerte es difícil de estudiar teóricamente. Los fenómenos intrigantes de la física hadrónica, como el confinamiento, ocurren en el régimen de baja energía, donde la teoría es totalmente no-perturbativa, y los métodos analíticos convencionales tienen una eficacia limitada. Aunque hoy en día todavía estamos lejos de comprender completamente el mecanismo que subyace a estos fenómenos, en los últimos 50 años han habido muchos avances. Si queremos señalar un año especialmente significativo que marcase el inicio de este viaje, como se sugiere en [8], es imposible no mencionar 1974. Este fue el año en que se publicó "*A Planar Diagram Theory for Strong Interactions*" de Gerard 't Hooft en Nuclear Physics B [9], y "*Confinement of Quarks*" de Kenneth Geddes Wilson en Physical Review D unos meses después [10]. Estos artículos tuvieron un impacto significativo en el estudio y la comprensión de la física de altas energías en las décadas siguientes, y condujeron al desarrollo de dos líneas de investigación distintas que cruzarian caminos más de una vez. En el primer artículo citado, se demostró que surgen propiedades sorprendentes de las teorías gauge no abelianas a partir del límite en el que el número de cargas de color N_c se considera muy grande y el acoplamiento gauge se desvanece. En primer lugar, los diagramas de Feynman pueden organizarse en una expansión en $1/N_c$ y en el límite mencionado, los únicos términos restantes tienen propiedades

topológicas bien definidas. Por otro lado, el segundo artículo formulaba una teoría cuántica de campos en un espacio-tiempo discretizado y mostraba cómo surgía el confinamiento de quarks en el límite (no físico) en el que el acoplamiento crece hasta el infinito. Aparte del resultado sobre el confinamiento, el artículo sentó las bases del campo de las teorías gauge en el reticulo, una forma natural de regularizar una QFT que proporciona una formulación rigurosa de la integral de camino, además de un vínculo natural con la teoría estadística de campos. En particular, esta analogía abre la posibilidad de estudiar las QFT mediante métodos y técnicas pertenecientes a otros campos de la física teórica, como los cálculos de Monte-Carlo. Debido a la complejidad del asunto, la simulación de una Teoría Cuántica de Campos (QFT) en una red para generar predicciones cuantitativas sigue siendo considerada hoy en día una de las tareas más desafiantes y costosas en Ciencias de la Computación. Esta es la razón por la que las QFT no se emplearon como herramienta cuantitativa de predicción hasta las dos últimas décadas. Sin embargo, los recientes avances en potencia computacional y desarrollo algorítmico han incrementado significativamente el uso de la aproximación reticular para explorar QFTs de fuerte interacción y sigue siendo considerada hoy en día como una de las herramientas teóricas líderes en física teórica.[3]

Esta Tesis se enmarca de alguna manera entre estos dos importantes tópicos en el contexto del estudio de teorías gauge fuertemente interactuantes orientadas a una mejor comprensión de la QCD y de las teorías QCD-like que pueden ser utilizadas como posibles extensiones para el SM. Nuestro objetivo principal se basará en el estudio en la red del límite grande N_c de las teorías de $SU(N_c)$ Yang-Mills acopladas con materia fermiónica. En los últimos años, la investigación del límite de grande N_c en la red ha sido un área de estudio importante.[4] Sin embargo, un reto importante que se encuentra en esta línea de investigación es la complejidad computacional, que crece a medida que aumenta el número de colores. Aunque los resultados a N_c grande no requieren necesariamente la precisión alcanzada por las simulaciones reticulares que generan resultados que pueden compararse con fenómenos del mundo real, la obtención de predicciones cuantitativas precisas sigue planteando retos. Uno de estos retos es el considerable coste computacional asociado a la simulación de teorías gauge que incluyen fermiones dinámicos y un número suficientemente grande de colores. En el límite de N_c grande, está bien establecido que los fermiones fundamentales se "apagan", lo que

3 En el enigma del muón $(g_\mu - 2)$ antes mencionado, el resultado ab-initio SM procede de una simulación de reticulo de última generación. La referencia citada se refiere al primer y (hasta la fecha) más preciso resultado de la colaboración BMW.

4 Para una revisión general de los esfuerzos recientes en este campo hasta 2013, el lector puede consultar [8]. Más específicamente sobre el límite de N_c grande de QCD, el lector puede consultar también [12].

significa que sus efectos dinámicos pueden despreciarse, reduciendo drásticamente el esfuerzo computacional que requiere la simulación. Sin embargo, cuando se obtienen resultados de N_c grandes mediante extrapolación a partir de N_c relativamente pequeños, resulta crucial garantizar que los efectos dinámicos de los fermiones no afecten significativamente la precisión de la extrapolación. Además, si se pretende simular teorías con fermiones adjuntos (o fermiones en una representación mayor que la fundamental), el temple natural ya no es aplicable, lo que limita las simulaciones a teorías con un número pequeño de colores, lejos del límite de gran N_c.

Esta tesis utilizará un paradigma alternativo, conocido como *reducción de volumen twisted* [13], para superar los problemas mencionados. Como es bien conocido en la literatura, las teorías gauge $SU(N_c)$ que poseen simetría de centro exhiben independencia de volumen en el límite grande-N_c cuando se compactan en un toro. Mediante el uso de condiciones de contorno "twisted", se puede explotar esta característica de forma segura y utilizarla para formular y simular la teoría en una red de un solo sitio. Hasta ahora, los modelos twisted son los únicos métodos que permiten simular teorías gauge en valores de N_c del orden de $10^2 - 10^3$. Durante los últimos 15 años, este método se ha aplicado con éxito a diversas aplicaciones físicas en la red. Más recientemente, también se ha aplicado a la teoría de Yang-Mills acoplada con N_f sabores dinámicos de fermiones en la representación adjunta, que es el foco de esta tesis. Este trabajo se plantea como una continuación natural en esta línea de investigación, ampliando algunos de los temas actuales y iniciando otros nuevos.

La primera parte de los resultados en los que estamos interesados es la teoría pura de Yang-Mills en el límite N_c grande, que, como se ha motivado en la primera parte de esta introducción, está en la base de la QCD y del sector fuerte en el SM. La otra parte principal está relacionada con el uso de fermiones adjuntos. Como es bien sabido, la QCD es una teoría gauge $SU(3)$ en la que los campos de quarks son fermiones en la representación fundamental y, por tanto, el uso de fermiones adjuntos puede sonar artificial. Las razones por la que estamos interesados en teorías con tal contenido de materia no convencional son múltiples. En primer lugar, las teorías gauge con fermiones adjuntos se encuentran entre los posibles candidatos relevantes en el contexto del modelo tecnicolor BSM. Otro punto de vista interesante, es el sugerido por la *orientifold equivalence* [14, 15], que proporciona un paralelismo natural entre la QCD con fermiones adjuntos a la QCD con fermiones de Dirac en una representación simétrica o anti-simétrica de dos índices. En el límite de N_c grande, esta última es equivalente a la representación fundamental y, por tanto, el modelo puede verse como la generalización natural de la QCD en el límite de N_c grande. Otra razón puede encontrarse en la notable plétora de escenarios físicos diferentes que pueden alcanzarse estudiando tales

teorías. Un único fermión de Majorana adjunto puede considerarse como el supercompañero del gluón y, por tanto, la teoría gauge correspondiente es la realización más sencilla de una teoría supersimétrica. Por otro lado, una teoría gauge con dos fermiones de Dirac adyacentes se ha considerado un candidato potencial BSM. Sin embargo, recientes investigaciones en reticulo calcularon una dimensión anómala que superaba el límite establecido por la fenomenología, descartando así la teoría como opción viable. Cabe señalar, no obstante, que se sabe que esta teoría es conforme, lo que la hace interesante desde un punto de vista teórico, ya que exhibe un comportamiento completamente distinto al de las teorías con confinamiento. El caso de un único fermión de Dirac adjunto también es extremadamente relevante en una variedad de contextos diferentes, desde ser otro potencial candidato BSM hasta la física de la materia condensada. En el primer contexto, la naturaleza confinante o conforme sigue debatiéndose activamente en la literatura, y el estudio del límite de N_c grande podría aportar valiosos conocimientos. Tras establecer el contexto del marco al que pertenece esta Tesis, nos adentraremos en una explicación más detallada de los temas y objetivos que nos ocupan.

En el Capítulo 1, tratamos la formulación de teorías gauge de interacción fuerte y sus características relevantes. Repasaremos algunos de los detalles de la formulación de una teoría de Yang-Mills en el espacio-tiempo euclídeo, dedicando algo de espacio a introducir el límite de N_c grande y las propiedades que surgen del acoplamiento de esta teoría gauge a fermiones, como la simetría quiral y la supersimetría. En la segunda parte del capítulo, repasaremos la formulación de estas teorías en la red, explorando las consecuencias de la discretización del espacio-tiempo. En la última parte, daremos una visión general de cómo se pueden aplicar los métodos de Monte-Carlo para extraer cantidades físicas relevantes.

En el Capítulo 2, introduciremos el concepto de condiciones de contorno twisted y cómo su uso proporciona una forma de mezclar los grados de libertad de color y de volumen. Basándonos en ello, veremos también cómo la reducción de volumen cuando se toma el límite N_c grande. Aplicaremos la reducción para formular el modelo Twisted Eguchi-Kawaii (TEK), que va a ser nuestra principal herramienta para simular teorías de Yang-Mills $SU(N_c)$ en una red de un solo punto. En la última parte del capítulo, veremos cómo pueden acoplarse y simularse fermiones en el marco de esta teoría con unico punto.

Después de esta introducción general, en el Capítulo 3 se describen las principales ideas y problemas algorítmicos para implementar simulaciones reales de las diferentes teorías que hemos introducido en los capítulos anteriores. Presentaremos listas de los diferentes conjuntos estadísticos de configuraciones que generamos para el caso de la teoría de Yang-Mills pura y la teoría de Yang-Mills acoplada con N_f

sabores de fermiones en la representación adjunta. También proporcionaremos detalles sobre cómo se trata el problema de la autocorrelación en nuestro análisis de errores.

El Capítulo 4 está dedicado a los resultados de la teoría Yang-Mills pura, denotada como $N_f = 0$. Primero presentamos nuestra metodología para establecer la escala de la teoría en el reticulo, que se basa en técnicas estándar de flujo de gradiente adaptadas a nuestro caso y mejoradas con teoría de perturbaciones a nivel de árbol para tratar con efectos sistemáticos procedentes de la discretización de reticulo y correcciones finitas N_c. Después de probar y realizar el ajuste de escalas, dedicamos una sección a discutir el escalado y el escalado asintótico en nuestra simulación, dando una estimación del parámetro Λ para la teoría de Yang-Mills en el límite de N_c grande. La última parte del capítulo está dedicada al cálculo del condensado quark quiral.

En el Capítulo 5 tratamos el caso de fermiones dinámicos adjuntos. Primero realizamos el ajuste de escala con el flujo de Wilson en el caso de un fermión de Majorana adjunto ($N_f = \frac{1}{2}$), que en el continuo corresponde a $\mathcal{N} = 1$ SUSY Yang-Mills. A continuación procedemos a estudiar el límite en el que la teoría de reticulo recupera la supersimetría empleando dos metodologías diferentes, obteniendo resultados compatibles. Combinando los valores de la escala que extrajimos con los resultados relativos al límite supersimétrico, estudiamos la dependencia del espaciado de la red con el acoplamiento desnudo para la teoría supersimétrica confrontando los resultados con las predicciones teóricas de la función β. El resto del capítulo se dedica a realizar el ajuste de escala en la teoría siguiendo las otras dos metodologías y comparando los resultados. En la última parte, aplicamos el procedimiento de ajuste de escala del flujo de Wilson a los conjuntos para 1 y 2 fermiones de Dirac adjuntos ($N_f = 1, 2$), lo que nos permite estudiar la dependencia de la escala con la masa del fermión adjunto destacando el comportamiento de las teorías en el límite sin masa y con masa pesada.

El último Capítulo estará dedicado a las conclusiones, donde recogemos y resumimos los principales resultados que hemos obtenido en esta Tesis.

Part I

INTRODUCTION

1

QUANTUM FIELDS FOR STRONG INTERACTIONS

1.1 STRONGLY INTERACTING THEORIES IN THE CONTINUUM

The most generic description of QCD and QCD-like theories is formulated in terms of a non-abelian Yang-Mills theory, coupled with several flavors of fermions. These theories possess a local invariance under a gauge group $SU(N_c)$, where N_c is the number of color charges. The gauge fields are hermitian traceless matrices whose elements are $A_\mu^{(R)}(x) = A_\mu^a(x)T_{(R)}^a$, where the index a runs in $1,\dots,N_c^2-1$ and labels the generator $T_{(R)}^a$ of the algebra of $SU(N_c)$ in a generic representation R. The generators are defined to satisfy $\mathrm{tr}\left(T_{(R)}^a T_{(R)}^b\right) = \delta^{ab}T(R)$, being $T(R)$ a numerical factor proper of the representation R. For simplicity, for the fundamental representation, we will omit the index R. As standard in Yang-Mills theories, the gauge fields are a connection in the gauge space and define a natural covariant derivative defined as

$$D_\mu^{(R)}(x) \equiv \partial_\mu - igA_\mu^{(R)}(x)\,, \tag{1.1.1}$$

where g is the bare coupling constant. The associated field-strength tensor is given by

$$F_{\mu\nu} \equiv \partial_\mu A_\nu - \partial_\nu A_\mu - ig[A_\mu, A_\nu]\,, \tag{1.1.2}$$

where we omitted the space-time point x. A *gauge transformation* is implemented with a generic special unitary local rotation $\Omega(x) \in SU(N_c)$ through

$$A_\mu(x) \to A'_\mu(x) = \Omega(x)A_\mu(x)\Omega(x)^\dagger - \frac{i}{g}(\partial_\mu\Omega(x))\Omega^\dagger(x)\,. \tag{1.1.3}$$

Matter fields are included in the description via N_f fermionic fields $\psi(x)$ and $\bar\psi(x)$, which are Grassmann-valued variables carrying a spinor index and a color index. Fermions are coupled to gluons through the covariant Dirac operator

$$\not{D}^{(R)}\psi \equiv \gamma^\mu D_\mu^{(R)}(x)\psi(x) = \gamma^\mu\left(\partial_\mu\psi(x) - igA_\mu^{(R)}(x)\psi(x)\right), \tag{1.1.4}$$

where the product between the fermion and the gauge field has to be understood within the representation R

$$\left(A_\mu^{(R)}(x)\psi(x)\right)_i \equiv A_\mu^a(x)\sum_{j=1}^{\dim R}(T_{(R)}^a)_{ij}\psi_j(x)\,, \tag{1.1.5}$$

where the sum over a is implicit. A local gauge transformation $\Omega_{(R)}(x) \in SU(N_c)$ acts as

$$\psi(x) \to \psi'(x) = \Omega_{(R)}(x)\psi(x), \quad \bar{\psi}(x) \to \bar{\psi}'(x) = \bar{\psi}(x)\Omega^{\dagger}_{(R)}(x) . \tag{1.1.6}$$

The Lagrangian of the theory is defined as

$$\mathscr{L} = -\frac{1}{2}\,\mathrm{tr}\, F_{\mu\nu}F^{\mu\nu} + \sum_{f=1}^{N_f} \bar{\psi}_f (i\not{D}^{(R)} - m_f)\psi_f \,, \tag{1.1.7}$$

where we omitted the dependence of the fields on the space-time point x. On the other hand, the *action*, is a functional of the fields defined as

$$S[A, \psi, \bar{\psi}] = \int d^4x\, \mathscr{L}(x) \,, \tag{1.1.8}$$

which is symmetric under the transformations (1.1.3) and (1.1.6), namely

$$S[A, \psi, \bar{\psi}] = S[A', \psi', \bar{\psi}'] \,. \tag{1.1.9}$$

The quantum description of the theory is formulated with the path integral approach, whose central object is the *generating functional*, defined as

$$Z = \int [DA_\mu][D\bar{\psi}][D\psi] e^{iS[A_\mu, \bar{\psi}, \psi]} \,, \tag{1.1.10}$$

where the functional integral extends over all the possible configurations of the field A_μ, $\bar{\psi}$ and ψ. As known from standard QFT, quantum fields are operators acting over the Hilbert space of physical states, and observables are the vacuum expectation values of generic operators $\hat{\mathcal{O}}$, combinations of quantum fields generating some state from the vacuum with some definite quantum numbers. In the language of path integrals, observables can be calculated as

$$\left\langle \hat{\mathcal{O}} \right\rangle = \frac{1}{Z} \int [DA_\mu][D\bar{\psi}][D\psi] e^{iS[A_\mu, \bar{\psi}, \psi]} \hat{\mathcal{O}}[A_\mu, \bar{\psi}, \psi] \,. \tag{1.1.11}$$

A connected correlation function of operators $\hat{\mathcal{O}}_a$ build from gauge fields and fermion bilinear can be studied by adding in the path integral a corresponding source term of the form $\mathcal{J}_a \hat{\mathcal{O}}_a$

$$Z_{\mathcal{J}} = \int [DA_\mu][D\bar{\psi}][D\psi] e^{i\int d^4x \left(\mathscr{L}(x) + \mathcal{J}_a(x)\hat{\mathcal{O}}_a(x)\right)} \,, \tag{1.1.12}$$

and taking functional derivatives with respect to them

$$\left\langle \hat{\mathcal{O}}_1(x_1) \cdots \hat{\mathcal{O}}_n(x_n) \right\rangle_c = i^{-n} \frac{\delta}{\delta \mathcal{J}_1(x_1)} \cdots \frac{\delta}{\delta \mathcal{J}_n(x_n)} \log Z_{\mathcal{J}} \Big|_{\mathcal{J}=0} \tag{1.1.13}$$

Several interesting properties of this quantum field theory can be studied in detail after the so-called *Wick's rotation*, i. e.an analytic continuation of the partition function to imaginary time. The complete prescription reads

$$(x^0, x^i) \to (x_4 \equiv ix^0, x_i) \tag{1.1.14a}$$
$$(\partial_0, \partial_i) \to (\partial_4 \equiv -i\partial_0, \partial_i) \tag{1.1.14b}$$
$$(\gamma^0, \gamma^i) \to (\gamma_4 \equiv \gamma^0, \gamma_i = -i\gamma^i) \tag{1.1.14c}$$
$$(A_0, A_i) \to (A_4 \equiv -iA_0, A_i) \tag{1.1.14d}$$
$$(\bar{\psi}, \psi) \to (\bar{\psi}, \psi)\,. \tag{1.1.14e}$$

Wick-rotated world is also referred to as *Euclidean*, as the Minkowski metric $\eta^{\mu\nu}$ becomes $\delta^{\mu\nu}$ (modulo a global sign depending on the definition of η). In the Euclidean, the generating functional in Eq. (1.1.10) becomes

$$Z_E = \int [DA_\mu][D\bar{\psi}][D\psi] e^{-S_E[A_\mu, \bar{\psi}, \psi]}\,, \tag{1.1.15}$$

where

$$S_E = \int d^4x \left[\frac{1}{2} \operatorname{tr} F_{\mu\nu} F_{\mu\nu} + \sum_{f=1}^{N_f} \bar{\psi}_f (\not{D} + m_f) \psi_f \right], \tag{1.1.16}$$

where we omitted the superscript R in the covariant derivative. From now on, we will work always in Euclidean space and therefore we will drop the subscript E everywhere.

Eq. (1.1.15) has a well-known immediate interpretation in terms of statistical mechanics. If we imagine the functional integral as a "sum" over every possible configuration that the fields can assume, the generating functional in Eq. (1.1.10) can be interpreted as the *partition function* of a statistical system in the canonical ensemble

$$Z = \sum_{\{\phi\}} e^{-\beta \hat{\mathcal{H}}(\phi)}\,, \tag{1.1.17}$$

where we denoted with ϕ the generic field configuration. In this analogy, the action plays the role of the Hamiltonian $\hat{\mathcal{H}}$ of the system and each microstate (field configuration) is weighted with a real Boltzmann factor $e^{-\beta E}$. This statistical average can be expressed as

$$\left\langle \hat{\mathcal{O}} \right\rangle = \frac{1}{Z} \int [DA_\mu][D\bar{\psi}][D\psi] e^{-S[A_\mu, \bar{\psi}, \psi]} \hat{\mathcal{O}}[A_\mu, \bar{\psi}, \psi]\,, \tag{1.1.18}$$

which can be interpreted as a mean value over an ensemble of field configurations distributed according to the following probability distribution

$$P[\bar{\psi}, \psi, A_\mu] = \frac{e^{-S[\bar{\psi}, \psi, A_\mu]}}{Z}\,. \tag{1.1.19}$$

Rep.	$\dim(R)$	$T(R)$	$\mathscr{C}_2(R)$
F	N_c	$\frac{1}{2}$	$\frac{N_c^2-1}{2N_c}$
adj	N_c^2-1	N_c	N_c

Table 1: Dimension and Casimir invariants of the fundamental (F), and adjoint adj representation of $SU(N_c)$.

A crucial observation is that since the gauge coupling constant g is dimensionless, in the limit in which fermions are massless the theory has no other mass scale, i.e. there is a scale invariance. However, upon quantization, the coupling acquires a dependence on an energy scale μ, namely the scale at which the UV divergences are subtracted. This process is commonly referred to as *dimensional transmutation*. The common approach is to transfer the analytic dependence on the energy scale on the coupling constant g (or $\alpha \equiv g^2/4\pi$). This "running" of the coupling g, i.e. the dependence of the coupling on the energy scale μ is dictated by the renormalization group equations

$$\frac{dg^2}{d\log\mu^2} = \beta(g)\,, \tag{1.1.20}$$

where the β-function is a function that depends on the theory under consideration and that can be expanded around $g = 0$:

$$\beta(g) = -\beta_0 g^4 - \beta_1 g^6 + \mathcal{O}(g^8)\,. \tag{1.1.21}$$

Although a generic coefficient $\beta_{i>1}$ is dependent on the renormalization scheme, the first two coefficients β_0 and β_1, are universal and are given by

$$(4\pi)^2\beta_0 = \frac{11}{3}\mathscr{C}_2 - \frac{4}{3}T(R)N_f \tag{1.1.22a}$$

$$(4\pi)^4\beta_1 = \frac{34}{3}{\mathscr{C}_2}^2 - \left(\frac{20}{3}\mathscr{C}_2 + 4\mathscr{C}_2(R)\right)T(R)N_f\,, \tag{1.1.22b}$$

where the numerical coefficients $T(R)$, $\mathscr{C}_2$ and $\mathscr{C}_2(R)$ are, respectively, the trace normalization, the quadratic Casimir of the adjoint and the quadratic Casimir of the representation R, summarized in Tab. 1 for some of the representations of $SU(N_c)$. Although the perturbative version of the β-function can predict the running in the weak-coupling regime and not in the full energy spectrum, some important overall information of the theory can be extracted from the first coefficients in the expansion. Further information about the running of the coupling will be given in Sec. 1.2.3.3.

At this point, one has to tackle two problems. The first one is that we do not have a formal definition of the integration measure appearing in Eq. (1.1.15) and in the definition of the observables. The second one is more practical: once the path integral has been defined, we

have to give an operational implementation of the calculation of the observables. Both of these problems will be solved by the lattice formulations of gauge theories which we are going to review in Sec. 1.2. Before doing so, in the next subsections, we will go through some of the relevant aspects that will be targeted in the result chapters of this thesis. Although some of the concepts will be discussed in some detail, this should not be taken as a complete treatment of the matter for which we refer to standard textbooks in QCD and quantum field theories such as [16, 17].

1.1.1 *The large-N_c limit*

The standard way to study analytically a strongly interacting theory is to expand the path integrals in power series of the bare coupling constant g. Another approach is to treat the rank of the gauge group N_c as a parameter, and perform an expansion in powers of $1/N_c$, justified when N_c is large. This scenario was first explored by 't Hooft in the '70s [9], which observed first that for this limit to make sense, the gauge coupling g must be taken to zero, in such a way that the 't Hooft coupling $\lambda \equiv g^2 N_c$ remains constant. The observation about how to take the limit becomes clear if one looks at Eq. (1.1.21): although a naive $N_c \to \infty$ limit is ill-defined, when rescaling the coupling, the RG equation for the 't Hooft coupling λ becomes

$$\frac{d\lambda}{d\log\mu} = -\left(11 - \frac{4N_f T_R}{N_c}\right)\frac{\lambda^2}{24\pi^2} + \mathcal{O}(\lambda^3)\,, \tag{1.1.23}$$

and the $N_c \to \infty$ limit is perfectly defined, once the representation R is specified. In the case where no fermions are considered, i.e. $N_f = 0$, Eq. (1.1.23) shows that pure $SU(N_c)$ Yang-Mills theories are asymptotically free in the large-N_c limit, being the leading order coefficient smaller than zero.

TWO DIFFERENT LARGE-N_c LIMITS The case in which we consider fermions deserves special attention. In Eq. (1.1.23), the coefficient in front of the $\mathcal{O}(\lambda^2)$ term depends on the number of flavors we couple to gauge fields and their representation. In the case of QCD, quarks are in the fundamental representation, for which $T_{\text{fund}} = 1/2$. In this case, their contribution to the β-function vanishes when N_c is taken to be large, provided the number of flavors N_f remains constant. This is typically referred to as the *'t Hooft limit*, in which $N_f/N_c \to 0$ while λ remains constant.

Another possible scenario is when the number of flavors N_f is also sent to infinity, holding the N_f/N_c ratio fixed. In this case, also known as the *Veneziano limit* [18]: the number of fermionic degrees of freedom grows with the same power as the number of gluonic ones, and their contribution does not disappear in the large-N_c limit. A similar

scenario relevant to this work is the case in which fermions are in a higher dimensional representation such as the adjoint, for which $T_{adj} = N_c$. In this case, even though the number of flavors is left constant, the number of fermionic degrees of freedom is by definition the number of gauge ones, being gluon fields in the adjoint representation of $SU(N_c)$.

LARGE-N_c COUNTING RULES An advantage of having a structural parameter of the theory such as the rank of the gauge group going to be sent to infinity is that dynamical quantities can be ordered based on the different powers of N_c they carry. For this reason, it is very instructive to be able to keep explicit track of the N_c dependence of relevant quantities such as vertices and propagators in perturbation theory. First of all, we have to rescale gauge and fermion fields in the following way

$$A_\mu(x) \to \frac{1}{g} A_\mu(x)\,, \quad \psi(x) \to \sqrt{N_c}\psi(x)\,. \tag{1.1.24}$$

A useful tool is the so-called "ribbon" or "double-line" notation for Feynman diagrams, which consists in replacing each line in the diagram with as many lines as fundamental color indices the corresponding propagator carries. For example, the propagator of a fundamental quark $\langle \psi^i(x)\bar{\psi}(y)_j \rangle \propto \delta^i_j$ is diagonal in color space, therefore it will be drawn as a single oriented color line. On the other hand, the propagator of an object in the adjoint representation such as a gluon or an adjoint fermion will be represented by a couple of (oppositely oriented) color lines, being $\langle A_\mu(x)^i{}_j A_\mu(x)^k{}_l \rangle \propto \delta^i_l\delta^k_j - \delta^i_j\delta^k_l/N_c$. In the final diagram, the overall power of N_c can be deduced using the following rules: each closed color line contributes with a single N_c factor, while each vertex brings a g into the product, which can be substituted with $\sqrt{\lambda/N_c}$. We can summarize the main result in the following rules

- Non-planar diagrams are subleading in N_c and then suppressed in the large-N_c limit.
- Diagrams with internal fundamental fermion loops are suppressed as $\frac{N_f}{N_c}$.

These conclusions are summarized in Fig. 1. The first bullet can be formulated from a topological consideration. In the 't Hooft limit, the perturbative expansion of any observable $\mathcal{O}$ can be organized in a double expansion, both in powers of the coupling and also in powers of $1/N_c$:[1]

$$\mathcal{O} = \sum_{h,b=0}^{\infty} N_c^{2-2h-b} \sum_{n=0}^{\infty} \lambda^n c_{h,b,n} \tag{1.1.25}$$

1 See e. g.[8] and references therein for a complete treatment.

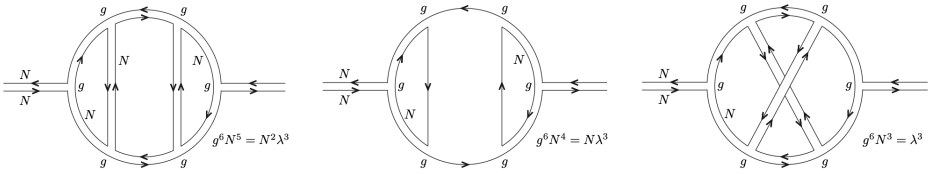

Figure 1: Three different Feynmann diagrams with three loops contributing to the gluon propagator. Only the one in the left panel survives the large-N_c limit. The picture is taken from [8].

where h is the number of *handles* and b is the number of *boundaries* of the simplest Riemann surface the diagram can be written on without crossing lines and with quark lines along the boundary. One could also verify that the number of boundaries b corresponds to the number of quark loops. Along the line of what we mentioned before, the leading contribution $\mathcal{O}(N_c^2)$ comes from $h = b = 0$, i.e. a planar diagram with no boundaries. For this reason, the 't Hooft limit is also referred to as the *planar limit* of gauge theories. Note that the simplification in the large-N_c limit involving fermions corresponds to the so-called *quenched approximation* in lattice QCD. Observables involving fundamental fermions can be therefore described by neglecting the effect of sea quarks induced by the determinant of the Dirac operator and hadronic states can be described well by properties of valence quarks.

1.1.2 *Chiral symmetry*

The matter content of the class of theories we are studying has crucial dynamical consequences and influences heavily the phenomenology. It is worthwhile to review in some detail some of the relevant concepts regarding symmetries that interest fermionic degrees of freedom.

We recall that, in addition to color degrees of freedom, fermion fields carry information about spin, i.e. they belong to a representation of the Lorentz group. From standard group theory arguments, we know that in $3+1$ dimension, Dirac fermions are a reducible representation of the Lorentz group, consisting of a right-handed (RH) and a left-handed (LH) Weyl fermion. The same concept can be expressed in terms of the projection operators

$$\mathbb{P}_\pm = \frac{\mathbb{1} \pm \gamma_5}{2}\,, \tag{1.1.26}$$

which "isolate" one Weyl component of the fermion, i.e. project a generic fermion onto an eigenstate $\psi_\pm$ of the *chiral operator* γ_5:

$$\mathbb{P}_\pm \psi = \psi_\pm, \qquad \gamma_5 \psi_\pm = \pm \psi_\pm\,. \tag{1.1.27}$$

SINGLE FLAVOR CASE For simplicity let us start by considering the case of a single Dirac fermion $N_f = 1$. It is easy to show that the kinetic part in the fermionic action can be written as

$$\bar{\psi} i \not{D} \psi = \bar{\psi}_+ i \not{D} \psi_+ + \bar{\psi}_- i \not{D} \psi_- , \tag{1.1.28}$$

while the mass term is

$$m \bar{\psi} \psi = m(\bar{\psi}_+ \psi_- + \bar{\psi}_- \psi_+) \tag{1.1.29}$$

It is straightforward to notice that the kinetic term does not mix the Weyl components of the fermion, while an explicit mass term does.

At this point, we can make some observations about the symmetries of the kinetic part of the fermionic action in Eq.(1.1.28). First, it has an exact symmetry under the following $U(1)_V$ transformation

$$\psi \to e^{i\alpha} \psi, \qquad \bar{\psi} \to e^{-i\alpha} \bar{\psi} . \tag{1.1.30}$$

(α being a real number), associated with the conservation of fermion number. This transformation is a phase shift that acts in the same way on LH and RH components, this is why it is usually referred to as *vector* symmetry, which explains the subscript of the unitary group. On the other hand, when considering an *axial* rotation, namely

$$\psi \to e^{i\gamma_5 \alpha} \psi, \qquad \bar{\psi} \to \bar{\psi} e^{i\gamma_5 \alpha} , \tag{1.1.31}$$

the transformation distinguishes between LH and RH components of the spinor and only the kinetic term is symmetric, being the only one that does not mix chiralities. However, we can say that the massless theory possesses axial symmetry whose explicit breaking is proportional to the fermion mass.

MULTIPLE FLAVOR CASE If we consider the case of N_f several flavors, the theory is invariant under independent chiral transformations if $m = 0$ that also mixes flavor

$$\psi_+^a \to U_{ab} \psi_+^b, \qquad \psi_-^a \to V_{ab} \psi_-^b , \tag{1.1.32}$$

with $U^\dagger U = V^\dagger V = \mathbb{1}$. The total symmetry group is $U(N_f)_L \otimes U(N_f)_R$, where the subscript denotes the components of the spinor over which the transformation acts. Using the fact that a unitary transformation is a product of a special unitary transformation and a complex phase, we can write the flavor symmetry group for the massless theory as

$$U(N_f)_L \otimes U(N_f)_R \simeq SU(N_f)_L \otimes SU(N_f)_R \otimes U(1) \otimes U(1)_A \tag{1.1.33}$$

where the two $U(1)$ groups are the ones we commented on the single flavor case.

1.1.2.1 *Chiral symmetry breaking*

In the previous section, we commented on how a mass term breaks axial symmetry explicitly. The massless theory, however, seems protected against chiral symmetry breaking, at least at a classical level.

Although the massless Lagrangian manifests symmetry under chiral transformation, two phenomena can occur. The first is the well-known spontaneous breaking of the symmetry, namely when the vacuum is not symmetric under chiral rotations. This is analogous to what happens to ferromagnetic spin systems, where the ground state microstate is with all spins aligned in one direction. This spin configuration is not invariant under a global flip (change of sign), thus leading to a macroscopic magnetization of the system. Analogously, QCD-like systems whose ground state is not invariant under chiral rotations develop a non-vanishing *chiral condensate*, defined as

$$\left\langle \bar{\psi}(x)\psi(x)\right\rangle . \tag{1.1.34}$$

Note that the chiral condensate transforms as a mass term, therefore it is a suitable order parameter for the breaking of the symmetry, analogous to the magnetization in spin systems. This phenomenon is known as *spontaneous* breaking of the chiral symmetry. A dynamic insight into how this mechanism occurs was provided by Banks and Casher in [19], who proposed that low-modes of the Dirac operator undergo a condensation with a consequent formation of the typical scale. The average *spectral density* of the Dirac matrix is defined as

$$\rho(\lambda, m) = \frac{1}{V}\sum_{k=1}^{\infty}\left\langle \delta(\lambda-\lambda_k)\right\rangle , \tag{1.1.35}$$

where $i\lambda_k$ are the eigenvalues of the euclidean massive Dirac operator in a volume V. The remark of Banks and Casher establishes

$$\lim_{\lambda\to 0}\lim_{m\to 0}\lim_{V\to\infty}\rho(\lambda, m) = \frac{\Sigma}{\pi}, \tag{1.1.36}$$

where Σ represents the chiral condensate

$$\Sigma = -\lim_{m\to 0}\lim_{V\to\infty}\left\langle \bar{\psi}\psi\right\rangle . \tag{1.1.37}$$

In the infinite volume limit, a non-zero density of quark modes implies that chiral symmetry is broken and vice-versa.

Another crucial consequence of the spontaneous breaking of chiral symmetry is the formation of massless excitation in the spectrum of the theory, called Nambu-Goldstone bosons. The most illustrative case is QCD, where pions can be seen as "pseudo" Nambu-Goldstone bosons, whose small masses, around 140 MeV, are a consequence of the explicit breaking of the symmetry by the light quarks mass. This concept is well summarized in $N_f = 2$ QCD with degenerate quarks

$m_u = m_d = m_q$, where the so-called *pion mass formula*, or *Gell-Mann-Oakes-Renner (GMOR) relation* [20] reads

$$m_\pi^2 = \frac{2 m_q \Sigma}{f_\pi^2} \tag{1.1.38}$$

which relates the mass of the lightest meson in the spectrum, the pion, to the chiral condensate (and the pion decay constant f_π).

The other phenomenon that might occur is an *anomalous* breaking of the symmetry: the usage of a regulator for the quantum version of the theory introduces symmetry-breaking terms that do not vanish once the regulator is removed. There are several different ways in which this problem can be described, we are going to review the basic concepts here, for a more technical treatment, the interested reader can refer to e. g. [21]. One can see that the measure of the path integral is not invariant under chiral rotations by studying the Jacobian of the transformation à-la Fujikawa [22]. Another way is to calculate explicitly the 4-divergence of the axial current $J^\mu_A \equiv \bar{\psi}\gamma^\mu\gamma^5\psi$, which should vanish at a classical level in the massless theory thanks to Noether's theorem. After an explicit calculation, in the $m \to 0$ limit the divergence of the axial current $\partial_\mu J^\mu_A$ result to be proportional to the *topological charge density* Q, whose volume integral is an integer number that labels the different topological sectors in the space of configurations. The topological charge is a complex object and can be seen from a lot of perspectives. An intriguing way is to use the famous Atiyah-Singer theorem [23] that states

$$Q = n_R - n_L \,, \tag{1.1.39}$$

where with $n_{R/L}$ we indicate the right/left-handed zero modes of the Dirac operator. This theorem has a crucial interpretation for the axial anomaly: *instanton*-like ($Q \neq 0$) configurations in the vacuum of the theory interact with fermion flipping the chirality of some of their zero-modes. This decompensation is what causes the anomalous breaking of the $U(1)_A$ subgroup of the full axial group $U(N_f)_A$. The remaining $SU(N_f)$ subgroup is broken spontaneously in the vacuum as mentioned before.

1.1.3 *Supersymmetry*

Another interesting property that these theories could manifest is *supersymmetry* (SUSY), namely the invariance under a transformation that exactly maps bosonic degrees of freedom into fermionic ones and conversely. Although QCD is not invariant under such transformations, the action formulated as in Eq. (1.1.8) manifests a supersymmetric behavior for some type of fermion fields. In this subsection, we will give some general details about SUSY, referring to [24–26] for details.

In a nutshell, supersymmetry can be viewed as an extension of Poincaré algebra, describing the symmetries of the spacetime under translation, boosts and rotations. If we call P_μ and $L_{\mu\nu}$ the infinitesimal generator of translations and Lorentz transformations, respectively, we can qualitatively write the Poincaré algebra as

$$[P, P] = 0, \quad [P, L] \sim P, \quad [L, L] \sim L\,. \tag{1.1.40}$$

At this point we can extend the Poincaré algebra with $\mathcal{N}$ set of complex Grassmann generators Q called *supercharges* which satisfy the following (qualitative) relations

$$[P, Q] = 0, \quad [Q, L] \sim Q, \quad \{Q, \bar{Q}\} \sim P\,. \tag{1.1.41}$$

When considering Majorana fermions, defined by the condition $\psi = \hat{\mathcal{C}}\psi$, a supercharge Q can be viewed as an operator that changes boson into fermions and vice versa

$$Q\,|\text{boson}\rangle = |\text{fermion}\rangle\,, \qquad Q\,|\text{fermion}\rangle = |\text{boson}\rangle\ . \tag{1.1.42}$$

Supersymmetry naturally induces several interesting properties that make the corresponding theory extremely appealing from a theoretical perspective. We just list some of these features in the following:

- The spectrum of the theory is composed of bound states called *supermultiplets*, which contain the same number of bosonic and fermionic states with the same mass. An example of such a multiplet is a spin-$1/2$ Majorana fermion, a scalar and a pseudoscalar boson.
- Unbroken supersymmetric theories have an exactly zero vacuum energy, without the need for renormalization and arbitrariness of an additive constant. Consequently, vacuum energy is an order parameter for SUSY breaking.
- The trace of the Witten index predicts whether SUSY is broken: a non-zero value forbids its spontaneous breaking [27].
- The "non-renormalization" theorem [28]: bosonic loops in quantum corrections are canceled by those of their fermionic superpartners. When supersymmetry is manifest at tree-level in perturbation theory it cannot be broken by higher-order corrections, thus SUSY holds at all orders.

1.1.3.1 $\mathcal{N} = 1$ *SUSY Yang-Mills model*

This model is the simplest supersymmetric realization of the gluonic sector of QCD, namely Yang-Mills theory. Although the matter content of this theory is fairly simple, i.e. only one *gluino* (an adjoint Majorana fermion), it manifests several non-trivial properties. The theory

is confining at low energy and zero temperature, and the spectrum is composed of a supermultiplet degenerate in mass [18, 29, 30].

As mentioned before, gluino fields are Majorana fermions in the adjoint representation, namely they have $N_c^2 - 1$ color degrees of freedom (as gluons). We will indicate the corresponding quantum field as $\lambda(x)$, not to be confused with the 't Hooft coupling, always denoted with the same Greek letter. The Majorana condition reads

$$\bar{\lambda} = {}^t\lambda\hat{\mathcal{C}}\,, \tag{1.1.43}$$

being $\hat{\mathcal{C}}$ the charge conjugation matrix defined as

$$\hat{\mathcal{C}}\gamma_\mu\hat{\mathcal{C}}^{-1} = -{}^t\gamma_\mu\,. \tag{1.1.44}$$

The Majorana condition (1.1.43), states that they are self charge-conjugated particles, i.e. $\lambda^c = \lambda$ and impose a constraint on the spin component of the fermion. In fact, a Majorana fermion carries half of the degrees of freedom of a Dirac fermion, which is the reason why it is denoted as $N_f = 1/2$. The Euclidean action of the theory is

$$S_{\mathcal{N}=1} = \int d^4x \left[\frac{1}{2}\,\mathrm{tr}\,F_{\mu\nu}F^{\mu\nu} + \frac{1}{2}{}^t\lambda(i\hat{\mathcal{C}}\not{D})\lambda\right] \tag{1.1.45}$$

which, on top of the standard gauge invariance, it is also invariant under infinitesimal supersymmetric transformations.

At the classical level, the theory possesses a global $U(1)_A$ symmetry, corresponding to axial rotations of the gluino

$$\lambda(x) \to e^{i\theta\gamma_5}\lambda(x)\,. \tag{1.1.46}$$

This "chiral" symmetry is called R-symmetry for historical reasons and does not commute with supersymmetry as there is no analogous rotation for the gluons. At the quantum level, this symmetry is broken by the anomaly to the $\mathbb{Z}_{2N_c}$ subgroup of the transformations

$$\lambda(x) \to e^{\frac{2\pi i}{2N_c}n\gamma_5}\lambda(x)\,, \tag{1.1.47}$$

labeled by the integers n modulo $2N_c$. At this point, the vacuum states can develop a non-zero gluino condensate $\langle\bar{\lambda}\lambda\rangle$ which breaks spontaneously the remaining symmetry down to $\mathbb{Z}_2$, i.e. a change of sign

$$\lambda \to -\lambda\,. \tag{1.1.48}$$

To summarize, the overall pattern of symmetry breaking is

$$U(1)_A \xrightarrow[\text{anomaly}]{} \mathbb{Z}_{2N_c} \xrightarrow[\langle\bar{\lambda}\lambda\rangle]{} \mathbb{Z}_2\,. \tag{1.1.49}$$

In this case, the spontaneous breaking happens for a discrete group and thus the Goldstone theorem does not apply.

This model will be the subject of one of our simulations whose results will be analyzed in detail in Chapter 5. The formulation of supersymmetry theory on the lattice though is not straightforward and one has to face several problems. We are going to summarize these issues in Sec. add ref to lattice SUSY.

1.2.1 $SU(N_c)$ *Yang-Mills theories on the lattice*

1.2.1.1 *Discretizing gauge fields*

We consider a *lattice*, i.e. a spacetime grid of spacing a of volume $V = L_1 L_2 L_3 L_4$. The generic spacetime point x will be given by a vector of integers n_μ as

$$x = (an_1, an_2, an_3, an_4) \quad \text{with } n_\mu \in [0, \dots, L_\mu - 1]\,, \tag{1.2.1}$$

and will be also denoted as n. The gauge degrees of freedom are given in terms of $U_\mu(n) \in SU(N_c)$ matrices living on the links of the lattice. They are defined such that

$$U_{-\mu}(n + \hat{\mu}) \equiv U_\mu^\dagger(n)\,. \tag{1.2.2}$$

A general gauge transformation mediated by $\Omega(n) \in SU(N_c)$, as expressed in Eq.(1.1.3), translates into

$$U_\mu(x) \to \Omega(x) U_\mu(x) \Omega(x + \hat{\mu})^\dagger\,, \tag{1.2.3}$$

Using this formalism, the trace of every product of link fields $U_\mu(n)$ following a closed path is gauge-invariant. Defining a closed path γ, the trace of the path-ordered product of the link variables $U(\gamma)$ is called a *Wilson loop*. The simplest loop one can build is called *plaquette* and is given by

$$P_{\mu\nu}(n) = U_\mu(n) U_\nu(n + \hat{\mu}) U_\mu^\dagger(n + \hat{\nu}) U_\nu^\dagger(n)\,. \tag{1.2.4}$$

One of the possible actions for these link variables is the *Wilson action*

$$S_w[U] = b N_c \sum_n \sum_{\mu \neq \nu} \mathrm{Re}\,\mathrm{tr}\Big(\mathbb{1} - U_\mu(n) U_\nu(n + \hat{\mu}) U_\mu^\dagger(n + \hat{\mu}) U_\nu^\dagger(n)\Big) \tag{1.2.5}$$

where b is an overall coefficient to be determined.

The Wilson action is far from being unique, every gauge-invariant action that reproduces the continuum Yang-Mills action in the $a \to 0$ limit works. We can easily see that, by expanding the gauge fields as

$$U_\mu(n) = e^{-iagA_\mu(n)} = 1 - iagA_\mu(n) + \mathcal{O}\big(a^2\big)\,, \tag{1.2.6}$$

Eq. (1.2.5) becomes

$$\begin{aligned} S_w &= -b N_c \sum_n \sum_{\mu \neq \nu} \mathrm{Re}\,\mathrm{tr}\left(-ia^2 g \hat{F}_{\mu\nu}(n) - \frac{a^4 g^2}{2} \hat{F}_{\mu\nu}(n)^2 + \mathcal{O}\big(a^6\big)\right) \\ &= b N_c \frac{g^2}{2} a^4 \sum_n \sum_{\mu \neq \nu} \mathrm{tr}\big(\hat{F}_{\mu\nu}(n)^2\big) + \mathcal{O}\big(a^6\big)\,, \end{aligned} \tag{1.2.7}$$

where $\hat{F}_{\mu\nu}$ is defined through

$$\operatorname{tr} e^{iga^2\hat{F}_{\mu\nu}(n)} \equiv \operatorname{tr} e^{-iagA_\mu(n)} e^{-iagA_\nu(n+\hat{\mu})} e^{iagA_\mu(n+\hat{\nu})} e^{iagA_\nu(n)} \tag{1.2.8}$$

By setting

$$a^4 \sum_n \to \int d^4x\,, \qquad b = \frac{1}{g^2 N_c} = \frac{1}{\lambda}\,, \tag{1.2.9}$$

the Wilson action reproduces the standard (euclidean) Yang-Mills action.[2]

It is worth mentioning that Wilson's action (1.2.5) is real and positively defined

$$S_w[U] \geqslant 0\,, \tag{1.2.10}$$

the inequality being saturated only when the link variables are unit matrices modulo gauge transformations. Given its positivity, $e^{-S_w[U]}$ is a well-defined weight for the link configuration in the Euclidean path integral for Yang-Mills fields. To define the path integral, we still have to define the measure of integration $[dU]$ in a gauge-invariant way. First we will denote as $[dU]$ the product over the measures for all gauge fields

$$[dU] = \prod_{\mu,n} dU_\mu(n)\ . \tag{1.2.11}$$

Taken a generic element $U \in SU(N_c)$, which is a compact group, the group invariant integration measure is given by the Haar measure, which can be proven to be unique and satisfies the properties

$$dU = dVU = dUV \tag{1.2.12a}$$

$$\int_{SU(N_c)} dU = 1 \tag{1.2.12b}$$

where $V \in SU(N_c)$. Since the parameterization of a generic $SU(N_c)$ element is a complicated expression, the construction of the Haar measure is lengthy and we will not go through the details. However, since we adopt a numerical approach the general expression for dU is not needed.

Any gluonic gauge-invariant observables can be obtained from the expectation value of (the trace of) a product of gauge fields along a close path $\hat{\gamma}$ on the lattice. By setting $\hat{\gamma} = [n, n+\mu_1, \ldots, n-\mu_n]$, we can defined a *Wilson loop* the following quantity

$$W(\hat{\gamma}) \equiv \frac{1}{N_c} \langle \operatorname{tr} U[\hat{\gamma}] \rangle\,, \quad U[\hat{\gamma}] = U_{\mu_1}(n) U_{\mu_2}(n+\hat{\mu}_1) \cdots U^\dagger_{\mu_n}(n)\,.$$

2 Usually, in standard literature $\beta = \frac{2N_c}{g^2} = \frac{2N_c^2}{\lambda}$ is used instead of b.

(1.2.13)

The expectation value will be evaluated by means of Eq. (1.1.15) using the Wilson action as

$$W(\hat{\gamma}) = \frac{1}{Z}\int [dU] e^{-S_w[U]} \frac{\operatorname{tr} U[\hat{\gamma}]}{N_c} \tag{1.2.14}$$

1.2.1.2 *Discretizing fermions*

The Euclidean fermion action for $N_f = 1$ in the continuum reads

$$\int d^4x\, \bar{\psi}(x)(\gamma_\mu(\partial_\mu - iA_\mu(x)) + m)\psi(x)\,. \tag{1.2.15}$$

The lattice fermionic action can be given in terms of the discretized version of the (massive) Dirac operator, which can be written as a matrix when the fermionic degrees of freedom are countable, as on a discretized spacetime. It can be written as

$$S_F[U, \bar{\psi}, \psi] = a^4 \sum_{n,m} \bar{\psi}(n) D(n, m) \psi(m)\,, \tag{1.2.16}$$

and must reduce to Eq. (1.2.15) when expanding the analytical expression around $a \to 0$. The product between the Dirac matrix D and the fermion field ψ has to be intended as an actual matrix-vector product in the vector space in which the representation R lives.

$$D(n, m) = m + \sum_{\mu=1}^{4} \gamma_\mu \frac{U_\mu(n)\delta(n + \hat{\mu}, m) - U_\mu^\dagger(n - \mu)\delta(n - \hat{\mu}, m)}{2a}\,, \tag{1.2.17}$$

which is known to suffer from the presence of unphysical states, called *doublers*. To quantify this statement, we must analyze the free spectrum of the theory, study i.e. Eq. (1.2.17) in momentum space after setting $U_\mu(n) = \mathbb{1}$. We can write

$$\begin{aligned}
\tilde{D}(p, q) &= \frac{1}{\sqrt{V}} \sum_{n,m} e^{-iap\cdot n} D(n, m) e^{iaq\cdot m} \\
&= \frac{1}{\sqrt{V}} \sum_{n} e^{-i(p-q)\cdot n} \left(\sum_\mu \gamma_\mu \frac{e^{iaq_\mu} - e^{-iaq_\mu}}{2a} + m \right) \\
&= \delta(p, q)\tilde{D}(p)
\end{aligned}$$

where

$$\tilde{D}(p) = m + \frac{i}{a} \sum_\mu \gamma_\mu \sin(ap_\mu)\,, \tag{1.2.18}$$

where the momentum is given by a four-vector whose components p_μ are integer multiple of $\frac{2\pi}{l}$, where $l = aL$ and $V = l^4$. Since the Dirac

matrix is diagonal in momentum space, its inverse, i.e. the *propagator* can be simply calculated as

$$\tilde{D}^{-1}(p) = \frac{m - \frac{i}{a}\sum_\mu \gamma_\mu \sin(ap_\mu)}{m^2 + \frac{1}{a^2}\sum_\mu \sin(ap_\mu)^2}\,. \tag{1.2.19}$$

One can prove that, for the massless case $m = 0$, in the limit $a \to 0$, the propagator becomes $-i\not{p}/p^2$ whose only pole is at $p = (0,0,0,0)$, as expected. Nevertheless, the lattice version of the propagator in Eq. (1.2.19) has a pole every time a component of the momentum is either 0 or π/a, thus leading to 15 unwanted poles. The solution is to employ the so-called *Wilson* discretization, which reads

$$D_w(n,m) = \left(m + \frac{4}{a}\right) - \frac{1}{2a}\sum_\mu [(\mathbb{1} - \gamma_\mu)U_\mu(n)\delta(n+\hat{\mu},m) + (\mathbb{1} + \gamma_\mu)U^\dagger_\mu(n-\hat{\mu})\delta(n-\hat{\mu},m)]\,. \tag{1.2.20}$$

By following the same procedure we did for naive fermions, one can see that the Dirac operator in momentum space reads

$$\tilde{D}_w(p) = m + \frac{i}{a}\sum_\mu \gamma_\mu \sin(ap_\mu) + \frac{1}{a}\sum_\mu (1 - \cos(ap_\mu))\,. \tag{1.2.21}$$

For the physical pole at $p = 0$ the Wilson term vanishes, while for the mass term of the doublers is modified as

$$m + \frac{2l}{a}\,, \tag{1.2.22}$$

l being the number of components $p_\mu = \pi/a$. It is clear that in the $a \to 0$ limit, doublers become infinitely massive and they decouple. The Dirac-Wilson matrix D_w is the discretized version of a continuum operator that amounts to add to the fermion largrangian in Eq. (1.2.15) an operator $\mathcal{O}_w$ proportional to the laplacian operator, i. e.

$$\mathcal{O}_w \sim -\frac{a}{2}\bar{\psi}(x)\,\triangle\psi(x)\,, \tag{1.2.23}$$

which takes the name of *Wilson's term*. As a first observation, the Wilson operator $\bar{\psi}\,\triangle\psi$ has mass dimension 5 and therefore a factor a is necessary to make the Wilson term dimensionless in the action. As a consequence the Wilson term naively disappears when taking the $a \to 0$ limit, for this reason, it is said to be *irrelevant* in the IR. The second important observation that we can make is that the Wilson term breaks chiral symmetry in the same way as a mass term. These considerations have deep consequences we are going to comment on more in detail in Sec. 1.2.2.

In our lattice simulations, the Dirac matrix is implemented by rescaling Eq. (1.2.20) with a factor $1/(am+4)$. In this way the first term is

just 1 and in front of the sum over directions we obtain the inverse of

$$\kappa \equiv \frac{1}{2(am+4)}\,, \tag{1.2.24}$$

called *hopping* parameter. This small modification can be done by paying no price: any overall numerical constant can be absorbed in the definitions of the fermion fields. The hopping parameter contains the same physical information as the (bare) mass parameter in the action. For $\kappa = 0$ ($m = \infty$), the Dirac matrix becomes the unit matrix, namely infinitely heavy quarks. On the other side, the limit of free quarks $m = 0$, corresponds to $\kappa = 1/8$.

GLUINOS ON THE LATTICE Eq. (1.2.20) is valid for any Dirac fermions on the lattice in an arbitrary representation. Since it is going to be the object of one of our simulations, it is worthwhile to comment on how the general picture gets modified when Majorana fermions are considered. Given a Dirac fermion field ψ, we can build two separate Majorana fermions as

$$\begin{cases} \lambda^{(1)} = \frac{1}{\sqrt{2}}(\psi + \hat{\mathcal{C}}\,{}^t\bar{\psi}) \\ \lambda^{(2)} = \frac{i}{\sqrt{2}}(-\psi + \hat{\mathcal{C}}\,{}^t\bar{\psi})\,. \end{cases} \tag{1.2.25}$$

With this definition, the fields $\lambda^{(i)}$ satisfies the Majorana condition $\bar{\lambda}^{(i)} = {}^t\lambda^{(i)}\mathcal{C}$ expressed in Eq. (1.1.43). The Wilson-Dirac action for a single Dirac fermion thus breaks into the sum of the action for two Majorana fermions

$$S_f = \bar{\psi} D \psi = \frac{1}{2} \sum_{i=1,2} {}^t\lambda^{(i)} \mathcal{C} D_w \lambda^{(i)}\,. \tag{1.2.26}$$

The fact one Dirac fermion corresponds to two independent Majorana ones reflects the intuition that a Majorana fermion corresponds to $N_f = \frac{1}{2}$.

1.2.1.3 *Fermion determinant and quenched approximation*

In the path integral, the exponential of the fermionic Wilson-Dirac action is added to the Wilson action (1.2.5) in the Boltzmann weight factor. To lighten the notation, we could rescale the fermion fields

$$\psi \to a^{-\frac{3}{2}}\psi\,, \tag{1.2.27}$$

in such a way the fermion action in Eq. (1.2.16) would be also rescaled as $a^4\bar{\psi}D_w\psi \to \bar{\psi}(aD_w)\psi$. The extra overall factor a can be included in the definition of the Dirac matrix by eliminating every factor a in Eq. (1.2.20) (and every derived expression). When writing the fermion

action as a quadratic form in the fields ψ and $\bar{\psi}$ by means of Eq. (1.2.16), one could write

$$Z_F[U] \equiv \int [d\bar{\psi}][d\psi] e^{-\bar{\psi} D_w \psi} = \prod_f \det\left(D_w[U, m_f]\right), \tag{1.2.28}$$

where we allowed for different flavors f and $D_w[U, m_f]$ indicates the Wilson-Dirac matrix (1.2.20) calculated in the background gauge fields U. To summarize, we can write the complete euclidean path integral (1.1.15) on the lattice as

$$Z = \int [dU] \left(\prod_f \det(D_w[U, m_f]) \right) e^{-S_w[U]}, \tag{1.2.29}$$

from which one can evince that the determinant is the only term that includes information about the quantum dynamics of fermions. The determinant has the same role as diagrams with fermion loops in perturbation theory. A full computation of the determinant of the Wilson-Dirac operator is typically extremely expensive in terms of computational costs, given that the Dirac matrix usually has $\mathcal{O}(10^{12})$ complex (sparse) entries in standard lattice simulations. One possible approach is to just neglect this term in the path integral, i.e. setting $\det(D_w) = 1$ in expectation values. This assumption is called *quenched approximation* and corresponds to neglecting the effect of fermion loops in perturbation theory, i.e. to assume that valence fermions have an infinite mass and do not contribute to the dynamics. Although the quenched calculation cannot be used for a precision determination of observables on the lattice, it can be used as an approximation. On top of that, we recall that in the large-N_c limit loops of fundamental fermions are automatically suppressed and the quenched approximation is exact. However, the large-N_c limit of the quenched theory corresponds with the one of the dynamical theory only for those cases in which fermionic degrees of freedom are subleading to gluonic ones. For example, in theories with adjoint matter, the quenched approximation is not justified.

As a last comment, we note that the expression (1.2.28) gets modified when considering gluinos. In fact, the path integral of a theory with a single Majorana fermion gives

$$\int [d\lambda] e^{-\frac{1}{2} {}^t\lambda \mathcal{C} D_w \lambda} = \mathrm{Pf}(\mathcal{C} D_w), \tag{1.2.30}$$

where Pf stands for *Pfaffian*. Since the Pfaffian satisfy $\mathrm{Pf}(M)^2 = \det\{M\}$, we can write

$$\mathrm{Pf}(\mathcal{C} D_W) = |\det(\mathcal{C} D_W)|^{\frac{1}{2}} \mathrm{sign}(\mathcal{C} D_W). \tag{1.2.31}$$

The fact that the sign of the Pfaffian can be negative makes the probability distribution problematic to be sampled. We will deal with the issue of generating configurations with such a sign problem in Chapter 3.

1.2.2 *The fate of (fermionic) symmetries on the lattice*

In Sec. 1.1.2 and Sec. 1.1.3 we analyzed chiral symmetry and supersymmetry in the continuum formulation of strongly interacting Yang-Mills theories. Both of them are deeply affected by lattice regularization and it is worthwhile to comment on how such symmetries should be seen when approached in a lattice simulation.

First, we note that the operators appearing in a theory play a different role when following a RG trajectory depending on their dimensionality. While *irrelevant* operators like Wilson's in Eq. (1.2.23) vanish in the continuum limit and thus they do not contribute to IR physics, *relevant* operators like a fermion mass term survive the removal of the regulator and influences the long-distance modes. As a general consideration, following the argument of [26], if the bare theory possesses a certain global symmetry, renormalization cannot generate radiatively a symmetry-breaking term in perturbation theory. On the other hand, when the symmetry is broken explicitly by a term in the lagrangian, other symmetry-breaking operators could appear in the renormalized theory. In the absence of a symmetry "protecting" the mass operator, it is not natural to expect the corresponding mass to be "light" (i. e. $m \ll 1/a$). Radiative corrections can result in large additive renormalization factors, and "miraculous" cancellations have to take place.

This is the case of a mass-operator for a fermion $m\bar{\psi}\psi$: although it explicitly violates chiral symmetry, in the process of renormalization only mixes with itself and receives correction proportional to the mass itself, i. e. it gets *multiplicatively renormalized*. In this case, we talk about "approximate chiral symmetry", and the mass term is "protected" against large additive renormalization that would have otherwise to be unnaturally fine-tuned to leave behind a light fermion. On the other hand, the case of Wilson fermions is substantially different. A Wilson operator $a\bar{\psi}\triangle\psi$ is an irrelevant operator of dimension 5 which breaks chiral symmetry, and in the renormalization process gets mixed with lower dimensional operators, such as the simple mass term. This mixing thus generates an additive renormalization factor that shifts the mass term proportionally to $1/a$. This additive renormalization needs fine-tuning to describe a world with arbitrarily light fermions:

$$am_q = am - am_c\,, \tag{1.2.32}$$

where m represents the bare parameter in the action and m_c is the additive correction we just described. The quantity in am_q is typically referred to as the *subtracted mass*. In Sec. 1.2.2.1 we are going to make this statement more quantitatively, giving also a practical description of how this additive renormalization can be calculated on the lattice. From an equivalent perspective, the observations we

just made are the manifestation of a well-known property of a large class of Dirac operators, formulated in a "no-go" theorem known as *Nielsen-Ninomiya theorem* [31–33]. At its core, it states that local Dirac operators of the form (1.2.16) cannot be simultaneously free from doublers and conserve a complete chiral symmetry.

Supersymmetry, on the other hand, is also problematic on the lattice. The breaking of continuous spacetime transformations to discrete subgroups implies that on the lattice infinitesimal translations cannot exist. Consequently, on the lattice, there cannot be any definition of SUSY charges Q, whose anti-commutation is related to infinitesimal translations. However, even though Poincaré symmetry is broken in the lattice (UV) theory, gauge invariance forbids any relevant operator to break the symmetry in the continuum limit. In this case, where the symmetry-breaking operators are only of irrelevant types, we talk about *accidental symmetries*. Although SUSY is broken on the lattice, can it emerge as an accidental symmetry in the IR? As argued by Kaplan in [26, 34] the answer for $\mathcal{N} = 1$ SUSY is yes: the only relevant operator that breaks SUSY and can be added to the Lagrangian is a mass term, which also breaks the $\mathbf{Z}_{2N_c}$ chiral symmetry (R-symmetry) as argued in Sec. 1.1.3.1. So imposing the R-symmetry in the target theory, the gluino mass is forbidden and the IR theory is accidentally supersymmetric. A practical prescription for this accidentally-supersymmetric scenario in lattice simulations was proposed by Curci and Veneziano in [35] which, by analyzing the axial and supersymmetric Ward identities, were able to demonstrate that the same tuning of the gluino mass restores chiral symmetry and supersymmetry at the same time in the continuum limit. Following this line, several results on the lattice have been obtained in the literature,[3] confirming that in the limit in which the gluino is massless and in the continuum limit one recovers evidence for a supersymmetric theory. We also are going to follow this approach and analyze in detail this supersymmetric limit in Chapter 5.

Now, the question we aim to answer is more practical: how can define suitable quantities to tune the theory to the "chiral" limit? We are going to answer in the following subsection.

1.2.2.1 *Axial ward identities and PCAC mass*

A non-singlet axial infinitesimal transformation of the fermion fields can be written as $\psi \to \psi + \delta\psi$ where the variation takes the following form

$$\delta\psi(x) = i\epsilon_a T^a \gamma_5 \psi(x) \tag{1.2.33a}$$

$$\delta\bar{\psi}(x) = i\epsilon_a \bar{\psi}(x) T^a \gamma_5 \,, \tag{1.2.33b}$$

3 See, e. g. [36–40] and references therein.

being T^a the generator of the $SU(N_f)$ flavor group. The invariance of the partition function of the theory reflects the expectation value of a generic observable $\mathcal{O}$ through the following condition

$$0 = \langle \delta \mathcal{O} \rangle - \langle (\delta S) \mathcal{O} \rangle \, , \tag{1.2.34}$$

where δ denotes the linear change under the transformations (1.2.33). In the particular case $\mathcal{O} = \mathbb{1}$, the variation equation reduces to the simple form $\langle \delta S \rangle = 0$ which leads to relations analogous to Noether's conservation laws, called *nonsinglet axial Ward identity* (AWI). When writing them for renormalized quantities, in the case of non-singlet axial currents in the case of $N_f = 2$ with degenerate fermion mass $m_u = m_d = m$, they take the following form

$$\partial_\mu A_\mu^{(r)\,a} = 2 m^{(r)} P^{(r)\,a} \tag{1.2.35}$$

where we define

$$m^{(r)} \equiv \frac{m_q}{Z_S}, \quad P^{(r)\,a} \equiv Z_P P^a, \quad A^{(r)\,a}_\mu \equiv Z_A A^a \, , \tag{1.2.36}$$

where Z_S, Z_P and Z_A are the renormalization factors, and $A^a_\mu \equiv \bar{\psi} \gamma_\mu \gamma_5 T^a \psi$ and $P^a \equiv \frac{1}{2} \bar{\psi} \gamma_5 T^a \psi$. If considering an operator $\mathcal{O}$ which produces a state out of the vacuum with the quantum numbers of the pion, the resulting version of the AWI is

$$\langle 0 | \partial_\mu A_\mu^{(r)\,a} | \pi \rangle = 2 m^{(r)} \langle 0 | P^{(r)\,a} | \pi \rangle \, , \tag{1.2.37}$$

from which one can extract the renormalized quark mass $m^{(r)}$. On the lattice, one would have to use a discretized version of Eq. (1.2.37), although is not completely straightforward how to relate the current in the continuum to lattice quantities. Moreover one also would need the renormalization factors Z_A and Z_P, which are typically cumbersome to calculate on the lattice. [4] What is usually done is to consider an ultralocal version of the axial vector current and an interpolating operator for the pion with optimized projection onto the pseudoscalar channel ground state. Further details on how such an observable can be implemented on the lattice will be given in Sec. 3.5 of Chapter 3. The result is a 2-point correlation function $\mathcal{C}_{AB}(t)$ of the operators corresponding to channels A and B. For the left-hand side of Eq. (1.2.37) we use the discretized time derivative of the correlator with channel $\gamma_0 \gamma_5$ and γ_5, while for the right-hand side the one of channel γ_5 and γ_5. By neglecting the renormalization constants one defines the asymptotic ratio of the unnormalized correlators

$$\frac{\mathcal{C}_{\gamma_0\gamma_5,\gamma_5}(t+a) - \mathcal{C}_{\gamma_0\gamma_5,\gamma_5}(t-a)}{4\mathcal{C}_{\gamma_5,\gamma_5}(t)} \sim a m_{\mathrm{PCAC}} \, , \tag{1.2.38}$$

4 For a textbook overview, the interested reader can consult Chapter 11 of [41] and references therein.

which takes the name of partially conserved axial current (PCAC) mass. This quantity relates to the renormalized quark mass as

$$a m^{(r)} = \frac{Z_A}{Z_P} a m_{\mathrm{PCAC}} \,. \tag{1.2.39}$$

Being directly proportional to the renormalized quark mass, $a m_{\mathrm{PCAC}}$ already includes the additive renormalization caused by the chiral symmetry-breaking effect of the Wilson operator and thus it can be tuned to zero to extract the critical value of the bare mass m_c (or the hopping parameter κ_c) without the need for an explicit calculation of the renormalization factor Z_S. Alternatively, in theories in which the chiral symmetry is spontaneously broken, one can tune directly the mass of the pseudo-Goldstone boson to obtain κ_c.

To conclude this section we also recall that the tuning of $a m_{\mathrm{PCAC}}$ to zero, should also restore supersymmetry in $\mathcal{N} = 1$ SUSY Yang-Mills in the continuum limit, although in this case the R-symmetry plays a slightly different role of chiral symmetry in QCD, as the Goldstone theorem is not applicable. We are going to give further details and analyze the massless gluino limit in Chapter 5.

1.2.3 *Lattice field theory simulations*

In the last sections we outlined (some of) the main features possessed by Yang-Mills theories with the fermionic matter when discretized on a discrete space-time. We gave an explicit construction for the Euclidean path integral defined in Eq.(1.1.15) for bosonic and fermionic quantities, and we argued about interesting properties emerging from the lattice formulation of the corresponding quantum theory. However, to give quantitative predictions we still have to give an operative implementation of the path integral that can allow one to perform the explicit computation of the observables. On top of that, we have to define operatively how the calculation of physical observables can be implemented and how physical quantities have to be extracted. Lastly, we have to understand how the output of the simulations relates to the continuum physics. These matters are the topic of this section.

1.2.3.1 *Numerical approach for computing the path integral*

From a practical perspective, a direct "naive" numerical computation of the path integral is doomed to fail catastrophically due to the unfeasible number of integrals to perform with a standard method such as Simpson's: only for a pure-gauge $SU(N_c)$ theory discretized on a lattice made of L^4 points, the number of multiple integrals in Eq.(1.1.15) is $d(N_c^2 - 1)L^4$, which rapidly approaches a huge number. On the other hand, a more favorable way is given by a Monte-Carlo approach which consists in replacing the integral with an average

over the lattice observables evaluated over a sample of N configurations distributed with probability $\propto e^{-S[U]}$

$$\langle \mathcal{O} \rangle \approx \frac{1}{N} \sum_{U \sim e^{-S}} \mathcal{O}[U] \,, \tag{1.2.40}$$

where the symbol $\sim$ in the sum indicates that the link variables U have been sampled from a given probability distribution proportional to the Boltzmann factor e^{-S}. The $\approx$ sign in Eq. (1.2.40) refers to the fact that the approximation becomes exact in the limit of infinite samples $N \to \infty$ and the error scales as $N^{-\frac{1}{2}}$ as dictated by probability theory. The problem has now shifted to how to generate (efficiently) a sample of N configuration generated from a given probability distribution

$$P[U] = \frac{e^{-S[U]}}{Z} \,, \tag{1.2.41}$$

where the action S can also include fermionic degrees of freedom through the determinant of the Dirac matrix as in Eq. (1.2.29). The way this problem is tackled is through the employment of a Markov process known as Markov Chain Monte Carlo (MCMC). The idea is to initiate the system to a starting configuration U_0 and evolve it in discrete steps following a stochastic process

$$U^{(0)} \to U^{(1)} \to U^{(2)} \to \cdots \tag{1.2.42}$$

In this case, the superscript is just an index that labels the "stages" of this process that evolves the initial configuration. The change of the configuration from one stage to another in Eq. (1.2.42) is called an *update* and the subscript is typically referred to as the *Monte-Carlo* or *Markov time*, not to be mistaken with the physical Euclidean time. A stochastic process like (1.2.42) is called a *Markov Chain* if the configuration at some Markov time U_t only depends on the "earlier" configuration U_{t-1}. The evolution from one state U_t to another one U_s is characterized by a transition probability $P(t \to s)$ for any given Markov times s and t. If this transition probability satisfies the *detailed balance* condition

$$P(t \to s) e^{-S[U_t]} = P(s \to t) e^{-S[U_s]} \,, \tag{1.2.43}$$

the process evolves towards a stable asymptotic distribution called *equilibrium distribution* given by Eq. (1.2.41). For a review on common algorithms used to simulate gauge theories the reader can refer to [41, 42]. In Chapter 3 we are going to review the main algorithm used in our simulations.

A crucial point in the decision of which algorithm to adopt is efficiency, i. e. how fast the Markov process explores the configuration space and therefore how fast will produce enough configurations to have a good determination of observables through (1.2.40). A good

estimate of the efficiency of an algorithm is the *correlation time*. Given an observable $\mathcal{O}$ calculated at two different Markov times t and $t+\tau$, their correlator is expected to behave as

$$\langle \mathcal{O}(t)\mathcal{O}(t+\tau)\rangle \propto e^{-\frac{\tau}{\tau_{\mathcal{O}}}}, \tag{1.2.44}$$

where the correlation time $\tau_{\mathcal{O}}$ depends both on the observable and on the Markov process. Another issue encountered when dealing with correlated data is that the final average of the observable $\bar{\mathcal{O}}$ might be biased and differ from $\langle\mathcal{O}\rangle$. Popular techniques to take into account autocorrelation and bias are jack-knife and bootstrap, which we do not enter in the details. Modern lattice calculations have developed several techniques that allow a precise and fair estimation of the statistical errors coming from the stochastic process at the base of the production of the configurations. See e. g. [41, 43] for a complete review of a numerical method for treating these problems. At the end of Chapter 3, we will give more details on how autocorrelation and error analysis is implemented in our case.

1.2.3.2 *Computation of observables*

Once an ensemble of configurations at equilibrium is sampled from the desired distribution, we want to be able to compute the expectation value of gauge-invariant observables. Following the standard quantum mechanics formulation, any observable $\mathcal{O}$ corresponds to an operator $\hat{\mathcal{O}}$ acting on physical states which are vectors in a Hilbert space. When acting on the ground state $|0\rangle$ of the theory, the operator creates a state with some quantum numbers, specified by the operator itself. When we specify a direction on the lattice and we call it (Euclidean) time t, the correlator of two observables $\mathcal{O}_1$ and $\mathcal{O}_2$ can be written as

$$\langle \mathcal{O}_1(t)\mathcal{O}_2(0)\rangle = \sum_n \langle 0|\hat{\mathcal{O}}_1|n\rangle \langle n|\hat{\mathcal{O}}_2|0\rangle e^{-tE_n}, \tag{1.2.45}$$

where the sum is taken over a discrete, orthonormal and complete base of eigenstates of the Hamiltonian

$$\hat{H}|n\rangle = E_n|n\rangle . \tag{1.2.46}$$

Assuming that the states are ordered $E_n > E_{n'}$ for $n > n'$, we expect that for asymptotically big Euclidean time $t \to \infty$, the sum in Eq.(1.2.45) is dominated by the state with the lowest energy, i. e.the *fundamental state*

$$\langle \mathcal{O}_1(t)\mathcal{O}_2(0)\rangle \propto e^{-tE_0}(1+\mathcal{O}(e^{-t\Delta E})), \tag{1.2.47}$$

where $\Delta E = E_1 - E_0$ is the difference in energy between the fundamental and the first excited state. Since we want our states to have a

definite spatial momentum $\mathbf{p}$, a Fourier transform over spatial components is performed

$$\tilde{\mathcal{O}}(\mathbf{p}, t) = \frac{1}{\sqrt{V_3}} \sum_{\mathbf{n}} \mathcal{O}(\mathbf{n}, t) e^{-i\mathbf{n}\cdot\mathbf{p}}, \tag{1.2.48}$$

where V_3 is the number of points in the spatial volume. The advantage of such a procedure is that in momentum space, the energies of the states are defined by the relativistic dispersion relation

$$E(\mathbf{p}) \approx \sqrt{m^2 + \mathbf{p}^2}, \tag{1.2.49}$$

and therefore $E(\mathbf{0}) = m$. In Eq. (1.2.49), the $\approx$ sign refers to the fact that the formula is only valid in the continuum and receives $\mathcal{O}(a)$ corrections on the lattice.

The operator $\mathcal{O}$ can be purely gluonic observable (Wilson or Polyakov loops) or describe a hadronic state. An example of purely gluonic operators can be a rectangular Wilson loop of sides R and L, $W(R, T)$. Its expectation value can be seen as the correlator of an operator that creates a static quark-antiquark pair at a distance R and annihilates them after a time T. We thus expect that for large T,

$$\langle W(R, T) \rangle = e^{-TV(R)} (1 + \mathcal{O}(e^{-T\Delta E})). \tag{1.2.50}$$

where we used the notation $V(R) = E_0$ to indicate a generic number which is a function of the separation R. If the theory shows confinement, Wilson loops are expected to follow the so-called *area-law*, where this "potential" is expected to grow linearly for large R, i. e. $V(R) = \sigma R$, and thus

$$\langle W[R, T] \rangle \propto e^{-\sigma RT}, \tag{1.2.51}$$

where σ is known as *string tension*.

An example of fermionic quantities is the so-called *meson interpolator*, defined as

$$\mathcal{O} = \bar{\psi} \Gamma \psi', \tag{1.2.52}$$

where ψ and ψ' are fermionic fields of different flavors and Γ is a general combination of γ_μ matrices with definite quantum numbers. As an example, we consider the case of $N_f = 2$ fermions, whose non-singlet interpolator is $\mathcal{O}_\Gamma = \bar{d}\Gamma u$. A generic correlator is given by

$$\left\langle \mathcal{O}_\Gamma(x) \mathcal{O}_\Gamma^\dagger(y) \right\rangle = \langle \bar{d}(x) \Gamma u(x) \bar{u}(y) \Gamma d(y) \rangle \tag{1.2.53a}$$

$$= -\operatorname{tr} \left[\Gamma D_w^{-1}(x, y) \Gamma D_w^{-1}(y, x) \right] \tag{1.2.53b}$$

which involves two inversions of the Dirac matrix. Such inversion falls into the category of those numerical problems involving the numerical computation of quantities from large sparse matrices, typically to be performed with the paradigm of distributed or parallel calculus. More details on the computation of the correlators in our setup will be given in the last Section of the next Chapter.

1.2.3.3 *The continuum limit*

After being calculated on the lattice, any observable has to be extrapolated to the continuum limit $a \to 0$, which is practically approached by sending the lattice coupling to infinity $b \to \infty$, by virtue of asymptotic freedom. Since the lattice theory only contains dimensionless parameters (the gauge coupling b, and the fermion masses in lattice units m_f), simulations can only output pure numbers, namely dimensionless physical quantities, while the lattice scale has to be fixed with external physical inputs. This is typically done by choosing a reference observable $\bar{\mathcal{O}}$ that is accessible on the lattice with rather good precision and using it as a reference scale. Supposing that this observable has the dimension of a mass, the lattice spacing will thus be extracted as

$$a(b) = \frac{\langle \bar{\mathcal{O}} \rangle_b}{\bar{\mathcal{O}}_{\text{exp}}}\,, \tag{1.2.54}$$

where $\langle \cdot \rangle_b$ indicates that the lattice estimate is done at some fixed value of the bare coupling b and $\bar{\mathcal{O}}_{\text{exp}}$ is the experimental value of $\bar{\mathcal{O}}$, when accessible, or a more general reference value, otherwise. Equivalently, the prediction for any other physical quantity $\mathcal{O}_i$ of mass dimension is obtained by [5]

$$\mathcal{O}_i = R_i \bar{\mathcal{O}}_{\text{exp}}, \quad \text{where } R_i = \lim_{a(b)\to 0} \frac{\langle \mathcal{O}_i \rangle_b}{\langle \bar{\mathcal{O}} \rangle_b}\,. \tag{1.2.55}$$

The assumption that all observables on the lattice depend on the lattice spacing only through a "dimensionality factor" which thus cancels in dimensionless ratios giving a constant value in the continuum limit is called *scaling*. More formally, the statistical field theory described by the quantum fields undergoes a phase transition as the 't Hooft coupling λ is tuned to its critical value $\lambda_c = 0$ ($b_c = \infty$): at the critical point, all the correlation lengths of irrelevant operators diverge with a well-determined rate that renders all dimensionless ratios tend to a constant value.

A meaningful continuum limit requires a precise functional dependence of the lattice spacing on the lattice coupling. There are some cases in which there is a known analytical relation between a and the bare lattice coupling λ (or b). E. g., in the vicinity of the trivial critical point $\lambda_c = 0$, perturbation theory fixes the relation between the coupling λ_s given in some scheme s and the regulator a through the RG equations (1.1.20), written here for the 't Hooft coupling

$$\frac{d\lambda_s}{d \log a^2} = -\beta_s(\lambda_s) \tag{1.2.56}$$

5 In this example we consider only observables having dimensions of a mass. Clearly, the considerations we made are valid for any other observables, providing that the lattice spacing a is properly defined with the right power in Eq. (1.2.54).

whose solution is typically expressed as

$$a(\lambda_s) = \frac{1}{\Lambda_s} f(\lambda_s) \tag{1.2.57}$$

with

$$f(\lambda_s) \equiv (b_0\lambda_s)^{-\frac{b_1}{2b_0^2}} e^{-\frac{1}{2b_0\lambda_s}} \times \\ \times e^{-\int^{\lambda_s} dx \left(\frac{1}{2\beta_s(x)} + \frac{1}{2b_0x^2} - \frac{b_1}{2b_0^2 x}\right)}, \tag{1.2.58}$$

where Λ_s is the integration constant and is dependent on the scheme chosen. The β-function admits a perturbative expansion as[6]

$$\beta_s(\lambda_s) \to -b_0\lambda_s^2 - b_1\lambda_s^3 - b_2^{(s)}\lambda_s^4 + \mathcal{O}(\lambda_s^5), \tag{1.2.59}$$

where, although the first two coefficients b_0 and b_1 are universal, higher-order corrections to Eq. (1.2.58) are not and thus the Λ-parameter is dependent on the renormalization scheme. Using these results, we expect that any generical observable of mass dimension $\mathcal{O}$ close to the continuum limit has a dependence on the bare coupling dictated by

$$\langle \mathcal{O} \rangle_b \simeq \frac{\mathcal{O}_\infty}{\Lambda} f(1/b) \tag{1.2.60}$$

where $\mathcal{O}_\infty$ represents the value of $\mathcal{O}$ extrapolated at $b = \infty$. However, although Eq. (1.2.60) combined with the perturbative β-function in Eq. (1.2.58) (*asymptotic scaling*) is valid in the vicinity of the continuum limit, scaling is known to take place well beyond the region of couplings where the solution in Eq. (1.2.58) provides a good approximation. For a generic value of the bare coupling, Eq. (1.2.60) is not expected to be valid and the continuum limit can be taken as in Eq. (1.2.55) after the scale has been fixed with a reference observable as in Eq. (1.2.54). Nevertheless, the region of predictivity of Eq. (1.2.58) can be extended by making some considerations we are briefly going to list here.

First of all, one can consider the effect of $\mathcal{O}(\lambda^4)$ corrections. In this scenario, the higher-order coefficients of the β-function depend on the renormalization scheme. Although the lattice renormalization scheme with the Wilson action $\lambda_w = \frac{1}{b}$ is known to have higher-order perturbative corrections, other choices of the coupling $\lambda_I(\lambda_w)$, called *improved* schemes are known to mitigate the problem. We will take care of the scale setting of our lattice simulations for Yang-Mills theory in Chapter 4 and in Sec. 4.2 we will study the applicability of asymptotic scaling by means of some of these improved coupling. Another observation we can make is allowing for small deviations of scaling, by modifying Eq. (1.2.58) allowing for a generic quadratic term in a^2 in units of some reference observable, whose constant coefficient has to be determined from a fit together with the Λ parameter.

6 The coefficients of Eq. (1.1.20) and Eq. (4.2.3) are simply related through $\beta_n = N_c^{n+1} b_n$.

2

QUANTUM FIELDS ON THE TORUS AND REDUCTION

The requirement of quantitative predictions for physical observables follows along with a deep understanding of the beautifully non-trivial nature of gauge theories. An intriguing aspect of Yang-Mills theories emerges when they are formulated on a torus endowed with some boundary conditions for the quantum fields. One crucial aspect of such a framework is that the physical size of the torus provides a natural low-energy scale for the theory which can be related to the characteristic energy scale emerging in Yang-Mills theory. In this way, one can assign a dynamical role to the volume of spacetime, and control it to study the theory over a large range of energy scales. Over the last forty years, a flourishing number of works regarding the study of this topic both on the lattice and in the continuum have been populating the literature, and complete treatment goes beyond the scope of this work. Nevertheless, since we will heavily rely on some of these results, is necessary to go through some selected topics, to have a complete understanding of the framework we work in. We will try to review these concepts in a modern and concise way, highlighting in some detail those aspects which are relevant to our work, but citing and referring to the original works for additional details.

2.1 YANG-MILLS FIELD ON THE TORUS

The first attempt at formulating Yang-Mills theory on a torus was put forward by 't Hooft at the turn of the '70s and the '80s [44, 45] in his early efforts to characterize the different possible phases of Yang-Mills theories. Given a pure-gauge $SU(N_c)$ Yang-Mills theory defined on a 4-dimensional torus of size l_μ in each μ direction, the requirement is that gauge-invariant quantities need to be periodic. This boundary condition (BC) translates into the following requirement for the gauge potential

$$A_\mu(x + l_\nu \hat{\nu}) = \Omega_\nu(x) A_\mu(x) \Omega_\nu^\dagger(x) + i\Omega_\nu \partial_\mu \Omega_\nu^\dagger(x)\,, \tag{2.1.1}$$

where the matrices $\Omega_\nu(x)$ belong to $SU(N_c)$. However, these matrices are not completely arbitrary, as the gauge transformations have to be consistent in the corner of the hypercube: when relating the field $A_\mu(x)$ with $A_\mu(x + l_\nu\hat{\nu} + l_\rho\hat{\rho})$, the order of the directions $\hat{\nu}$ and $\hat{\rho}$ has to be irrelevant. After some algebra, one easily finds the following consistency condition

$$\Omega_\mu(x + l_\nu\hat{\nu})\Omega_\nu(x) = z^*_{\mu\nu}\Omega_\nu(x + l_\mu\hat{\mu})\Omega_\mu(x) \tag{2.1.2}$$

that reduces the number of possible gauge transformations admitted by this choice of boundary conditions. In Eq. (2.1.2), the $z_{\mu\nu}$ denotes an element of the center $\mathbf{Z}_{N_c}$ of $SU(N_c)$, hence it can be written as

$$z_{\mu\nu} = e^{\frac{2\pi i}{N_c} n_{\mu\nu}} \tag{2.1.3}$$

where $n_{\mu\nu}$ is an antisymmetric tensor of integers modulo N_c which is usually referred to as the *twist tensor*. The trivial "no-twist" choice, i.e. $n_{\mu\nu} = 0 \mod N_c$ leads to the well-known case of *periodic* boundary conditions, while the general case of a non-zero twist tensor is usually referred to as *twisted* boundary conditions. As it was clear since the first studies that followed 't Hooft original work [46–50], although the choice of periodic boundary conditions is the simplest, it comes with serious complications related to the existence of infinitely many gauge-inequivalent zero-action configurations, the *torons*. The problem can be formulated in terms of gauge zero-momentum modes, which dominate the low energy dynamics and are cumbersome to treat perturbatively. The first clear advantage of using twisted BC comes clear in this context: as we will see, zero modes are incompatible with this choice at the boundary, and one can perform calculations also in perturbation theory without the complications of dealing with zero modes.

A significant class of solutions for Eq. (2.1.2) is when the $\Omega_\mu(x)$ are constant matrices, conventionally called Γ_μ and referred to as *twist-eaters*. Using the twist-eaters, Eq. (2.1.1) and Eq. (2.1.2) become, respectively,

$$A_\mu(x + l_\nu \hat{\nu}) = \Gamma_\nu A_\mu(x) \Gamma_\nu^\dagger \,, \tag{2.1.4}$$

and

$$\Gamma_\mu \Gamma_\nu = z_{\nu\mu} \Gamma_\nu \Gamma_\mu \,. \tag{2.1.5}$$

The solution of this equation is not unique since any transformation of the gauge field under a symmetry of the action gives an equivalent configuration. In particular, given a gauge transformation $\Omega \in SU(N_c)$ and an element of the center $z_\mu \in \mathbb{Z}_{N_c}$ we can build other zero-action solution through the

$$\Gamma_\mu \to \Omega \Gamma_\mu \Omega^\dagger \tag{2.1.6a}$$

$$\Gamma_\mu \to z_\mu \Gamma_\mu \tag{2.1.6b}$$

The existence of solutions for the twist equation (2.1.5) for a generic twist tensor $n_{\mu\nu}$ is only guaranteed in $d \leqslant 3$, while for $d = 4$ an additional assumption is required

$$\epsilon_{\mu\nu\rho\lambda} n_{\mu\nu} n_{\rho\lambda} = 0 \bmod N_c \tag{2.1.7}$$

which is usually referred to as *orthogonal twist*.[1] Another important condition we will require for the twist tensor is *irreducibility*. Irreducible twists are defined as the ones for which solutions to the twist equations (2.1.5) are unique modulo global gauge transformations and multiplication by elements of the center. In four dimensions, only N_c^2 inequivalent twist-eating solutions can be constructed, which are all roots of the identity, i. e. they satisfy $\Gamma_\mu^{N_c} = \mathbb{1}$. For more details regarding the choice of the twist tensor and the construction of twist-eating irreducible and orthogonal solutions, we refer the reader to [51]. In the following, we are going to analyze in some detail one possible choice of orthogonal and irreducible twist tensor that we are going to use in the rest of this Thesis, called *symmetric twist*, defined by

$$n_{\mu\nu} = k\hat{L} \quad \text{for } \mu > \nu \tag{2.1.8}$$

where k and $\hat{L}$ are integers. Irreducibility of the twist is ensured by the requirement that $\hat{L}$ and k are coprime. In our practical implementations, we constrain N_c to be a square number and set $\hat{L} = \sqrt{N_c}$. In this way, the twist factor appearing in the commutation relations results by

$$z_{\mu\nu} = e^{\frac{2\pi i k}{\sqrt{N_c}}} \quad \text{for } \mu > \nu\,. \tag{2.1.9}$$

As analyzed in detail in [52], we can define a Fourier decomposition consistent with the choice of the boundary condition by using

$$A_\mu(x) = \frac{1}{\sqrt{V}} \sum_q{}' e^{iqx} \tilde{A}_\mu(q) \hat{\Gamma}(q)\,. \tag{2.1.10}$$

The $\hat{\Gamma}$ are the following set of matrices,[2] labeled by a 4-vector q

$$\hat{\Gamma}(q) \equiv \frac{e^{i\alpha(q)}}{\sqrt{2N_c}} \Gamma_1^{s_1(q)} \Gamma_2^{s_2(q)} \Gamma_3^{s_3(q)} \Gamma_4^{s_4(q)}\,, \tag{2.1.11}$$

where $\alpha(q)$ denotes an arbitrary complex phase and

$$s_\mu(q) = -\bar{k}\,\tilde{\epsilon}_{\mu\nu} m_\nu \text{ where } q_\nu = \frac{2\pi m_\nu}{\sqrt{N_c} l_\nu}\,, \tag{2.1.12}$$

where m_μ is an integer and in which we introduced

$$\bar{k}k = 1 (\mathrm{mod}\, \hat{L}), \quad \sum_\rho \tilde{\epsilon}_{\mu\rho} \epsilon_{\rho\nu} = \delta_{\mu\nu}\,, \tag{2.1.13}$$

1 The name "orthogonal" refers to the fact that the twist tensor $n_{\mu\nu}$ can be written using two different 3-vectors $\vec{k}$ and $\vec{m}$ such that $n_{ij} = \epsilon_{ijk} m_k$ and $n_{0i} = k_i$. Using this notation, the orthogonality of the twist expressed in Eq. (2.1.7) reduces to standard euclidean orthogonality $\vec{k} \cdot \vec{m} = 0 (\mathrm{mod}\, N_c)$.

2 The $\hat{\Gamma}$ matrices were introduced for the first time in this context in [13].

and $\epsilon_{\mu\nu} = -\epsilon_{\nu\mu} = 1$ for $\mu > \nu$. One can demonstrate that the matrices $\hat{\Gamma}(q)$ are linearly independent and traceless, except the corresponding to $s_\mu = 0 (\mathrm{mod}\sqrt{N_c})$, which is proportional to the identity. By excluding it, this set of $N_c^2 - 1$ matrices can be used as a basis for the Lie algebra of $SU(N_c)$. The primed sum in Eq. (2.1.10) is to indicate that in the sum we remove those $\hat{\Gamma}$ whose $q_\mu = 0(\ \mathrm{mod}\sqrt{N_c})$ in all directions. The corresponding eigenstates are the so-called "zero modes", that in the context of twisted BC get automatically removed. Eq. (2.1.10) generalizes the standard Fourier expansion: by summing over q we are simultaneously taking into account the expansion in "plane waves" and the sum over the generators of the group. It is interesting to notice how momenta are quantized as multiples of $2\pi/l_\mu\sqrt{N_c}$, as momenta on a periodic "effective" torus whose size is $\sqrt{N_c}l_\mu$. We will explore more in detail this conclusion in Sec. 2.3.

It is interesting therefore to write explicitly the commutation relation from which one can derive the structure constant. In this basis, the structure constants become momentum dependent and read

$$\left[\hat{\Gamma}(p), \hat{\Gamma}(q)\right] = iF(p, q, -(p+q))\hat{\Gamma}(p+q)\,, \tag{2.1.14}$$

where

$$F(p, q, -(p+q)) = \sqrt{\frac{2}{N_c}} \sin\left(\frac{\theta_{\mu\nu} p_\mu q_\nu}{2}\right) \tag{2.1.15}$$

and

$$\theta_{\mu\nu} = \frac{\tilde{l}_\mu \tilde{l}_\nu}{2\pi} \tilde{\epsilon}_{\mu\nu}\hat{\theta}, \quad \text{where } \hat{\theta} = \frac{\bar{k}}{\sqrt{N_c}}\,, \tag{2.1.16}$$

being $\tilde{l}_\mu \equiv l_\mu\sqrt{N_c}$. As it is well-known, the structure constant appears in perturbation theory in the Feynman rules in the vertices, which become dependent on the effective momentum degrees of freedom. As was first observed in [13], surprisingly cancel exactly in planar diagrams which are the only ones surviving the large-N_c limit, while contributing to cancel the non-planar ones. Surprisingly these Feynman rules correspond to those appearing in a non-commutative field theory and [46, 53] was the first time in which they appear in the literature.

2.2 Implementing twisted boundary conditions on the lattice

Twisted BC are a powerful tool to study gauge theories at finite volume, both on the lattice and in the continuum. In this section, we will review basic concepts and discuss in some detail the implementation of twisted BC in Yang-Mills theories.

We will consider a 4-dimensional symmetric lattice of sizes $L_\mu = L$ ($l_\mu = aL_\mu$) on which gauge fields $V_\mu(n)$ are periodic up to a gauge transformation $\Omega_\mu(n) \in SU(N_c)$

$$V_\mu(n + L\hat{\nu}) = \Omega_\nu(n) V_\mu(n) \Omega_\nu^\dagger(n + \hat{\mu}) \,. \tag{2.2.1}$$

In this and in the following expression we will set $a = 1$. The dynamics is governed by the usual Wilson action defined in Eq. (1.2.5) (substituting U_μ with V_μ). We stress the fact that Eq. (2.2.1) corresponds to Eq. (2.1.1) formulated on a lattice and consequently, the transformation matrices obey the consistency conditions expressed in Eq. (2.1.2) given by

$$\Omega_{\mu\nu} \equiv \Omega_\nu^\dagger(0)\Omega_\mu^\dagger(L\hat{\nu})\Omega_\nu(L\hat{\mu})\Omega_\mu(0) = z_{\mu\nu}\mathbb{1} \,, \tag{2.2.2}$$

where the last equality remarks that $\Omega_{\mu\nu}$ is an element of the center, as stated by Eq. (2.1.2). This guarantees that the boundary conditions are independent of the ordering of the directions taken. Since in the Wilson action, (1.2.5) gauge fields only appear in terms of plaquettes, we have to explicit the gauge transformation only in those plaquettes having at least one link lying on the edge of the lattice. There are two cases: the plaquette with only one link lying on the edge of the lattice ("edge" plaquettes) and the one with two links ("corner" plaquettes). When using Eq. (2.2.1) to transform the link lying on the boundary, we can absorb the Ω matrices in the definition of those links in the plaquette "pointing to the edge". We can summarize the main change of variable as

$$U_\mu(x) \equiv \begin{cases} V_\mu(x)\Omega_\mu(x) & \text{if} \quad x_\mu = (L-1)\hat{\mu} \\ V_\mu(x) & \text{otherwise} \end{cases} \tag{2.2.3}$$

With this change of variable, the twist matrices get completely reabsorbed in the edge plaquettes, while in the corner plaquette appears the product $\Omega_{\mu\nu}$ from Eq. (2.2.2). By iterating this procedure for every edge and corner plaquette lying at the boundary, the twist matrices Ω should disappear from the action, only leaving a twist factor in every corner plaquettes. To write explicitly the twisted BC Wilson action in a compact form, we can assign a point-dependent twist factor $Z_{\mu\nu}(n)$ to each plaquette which is always 1 except for the plaquette at each corner in which they are $z_{\mu\nu}$:

$$S_w^{tBC} = bN_c \sum_n \sum_{\mu\neq\nu} \mathrm{Re}\,\mathrm{tr}\left[\mathbb{1} - Z_{\mu\nu}(n) U_\mu(n) U_\nu(n+\hat{\mu}) U_\mu^\dagger(n+\hat{\nu}) U_\nu^\dagger(n)\right] , \tag{2.2.4}$$

where $U_\mu(n) \in SU(N_c)$ are now periodic. These point-dependent twist factors can also be choosen in a more general way: the can also be different from 1 in each plaquette but, to respect consistency, the

product of all the twist factors in a plane has to give the aforementioned $z_{\mu\nu}$

$$\prod_{n\in(\mu,\nu)} Z_{\mu\nu}(n) = z_{\mu\nu}\,, \tag{2.2.5}$$

and the product of each twist factor associated with plaquettes on the faces of a cube (with orientation) has to be 1. All the factors can be absorbed into the gauge fields by a change of variables, except the one in the corners.

The same change of variables that led to Eq. (2.2.4) influences also a generic Wilson loop $W(\hat{\gamma})$. Following the same rationale, the final expression is

$$W(\hat{\gamma}) = \frac{z(\hat{\gamma})}{N_c} \langle \mathrm{tr}\, U(\hat{\gamma})\rangle \tag{2.2.6}$$

where $U(\hat{\gamma})$ is the product of gauge variables along a closed path $\hat{\gamma}$ and $z(\hat{\gamma})$ is the product of twist factors in all the plaquettes belonging to a surface whose boundary is the $\hat{\gamma}$.

2.3 LARGE-N_c LIMIT AND VOLUME REDUCTION

In trying to apply lattice methods to the study of large-N_c gauge theories one faces the difficulty of dealing with the infinite number of internal degrees of freedom. However, in the Eighties an idea emerged that can be used to ameliorate the situation: Volume reduction. This concept states that in the large-N_c limit, the expectation value of certain physical observables becomes independent of the lattice size. Let us be more precise and explain the implications for lattice gauge theory formulated on a box of size L^4 and twisted boundary conditions. For simplicity we restrict ourselves to Wilson action with parameter b and a symmetric twist with flux k, including the periodic BC case of $k = 0$. With the standard methodology in order to obtain the expectation value of the observable at infinite volume and infinite N_c , one should first take the thermodynamic limit

$$\lim_{L\to\infty} \mathcal{O}(b, N_c, L, k) = \mathcal{O}(b, N_c)\,, \tag{2.3.1}$$

then the large-N_c limit

$$\lim_{N_c\to\infty} \mathcal{O}(b, N_c) = \mathcal{O}(b)\,, \tag{2.3.2}$$

The statement of volume independence is a conjecture about the order of these two limits and predicts

$$\lim_{N_c\to\infty} \mathcal{O}(b, N_c, L, k(N_c)) = \mathcal{O}(b)\,. \tag{2.3.3}$$

This idea allows us to omit taking the thermodynamic limit reducing the spatial degrees of freedom. If this principle holds for all values of L it can allow obtaining the same infinite volume result $\mathcal{O}(b)$ from a one-point lattice $L = 1$.

2.3.1 *A historical perspective*

In the early Eighties volume reduction appeared first in a paper [54] by Eguchi and Kawai, where they studied the large-N_c limit of gauge theories using the loop equations formulated on the lattice, already introduced by Makeenko and Migdal a couple of years before [55]. Their striking observation was that the physics of the large-N_c limit would be independent of the spatial volume: the equations showed no dependence on the lattice size, provided the following two conditions hold: factorization of observables in the large-N_c limit and invariance of the 4-dimensional theory under the center of the gauge group $\mathbf{Z}_{N_c}^4$. The implications of this idea are incredibly appealing: a d-matrix model (EK model) with action

$$S_{EK}[U_\mu] = bN_c \sum_{\mu \neq \nu} \mathrm{tr}\left(\mathbb{1} - U_\mu U_\nu U_\mu^\dagger U_\nu^\dagger\right) \tag{2.3.4}$$

describing gauge field on a single-site periodic lattice could encompass the large-N_c physics of gauge theories at infinite volume, b being the inverse of the 't Hooft coupling.

As mentioned, the EK reduction validity relies heavily on symmetry under center transformations.[3] "Center symmetry" is a symmetry of the finite size theory that amount to the multiplication of the "transition matrices" by an element of the center. This affects loops with non-trivial windings (non-trivial elements of the fundamental group). In the infinite volume theory, there are no Polyakov loops and thus the equivalent terms are open loops whose expectation value is zero because of gauge invariance. On the other hand, finite volume Polyakov lines are gauge invariant and the vanishing of the expectation values is assured only if the global center-symmetry is unbroken. However, the assumption that center symmetry remains intact is not always verified, there could be values of the coupling at which $\mathbf{Z}_{N_c}$ gets spontaneously broken in the vacuum. The assumption is safe in the *strong-coupling* limit ($b \to 0$): the $SU(N_c)$ Haar measure dominates the path integral and the expectation value of any Polyakov loop is automatically zero. This is not true anymore when considering the opposite regime, i. e.the *weak-coupling* limit, in which center symmetry could break spontaneously in the vacuum. This was clear from the beginning, as reads a note added by Eguchi and Kawai themselves at the end of their original paper. Evidence for this spontaneous symmetry breaking was indeed found in the same year [46, 56–58] using both analytical considerations and lattice sim-

3 In Eguchi and Kawai's argument when formulating loop equations in the reduced setup, traces of Polyakov loops appear in the form of disconnected diagrams. They are not relatable to any term in the large-volume version, therefore their expectation value has to vanish to have an exact correspondence between the two setups.

ulations at small values of N_c. [4] A possible workaround is known as Quenched Eguchi-Kawai (QEK): after "freezing" the eigenvalues to a suitable center-symmetry preserving distribution, one could calculate the path integral over such values [56, 58, 59]. Several years later, simulations suggested that Polyakov loops winding in various directions might still break center symmetry [60]. This conclusion has been questioned recently [61], reviving the validity of the model.

Another way of solving the issue was made by González-Arroyo and Okawa [13, 62] who proposed reformulating the model using twisted boundary conditions, showing that the initial arguments of Eguchi-Kawai also hold in this case and showing that at weak coupling a sufficiently large subgroup of center-symmetry is preserved. This is going to be the topic of the next subsection.

2.3.1.1 *Volume reduction on the twisted torus and the single site model*

The paradigm of volume reduction can be exploited in practical applications, including the extreme case where the entire volume of the torus collapses to a single point ($L = 1$), in the spirit of the original work by Eguchi and Kawaii in the 80's. This case, called *Twisted Eguci-Kawai* (TEK) model [13, 62], is going to be our main model to simulate the large-N_c limit of gauge theories. Now, we will review the TEK model as it will be used in this Thesis. After the formulation, we will briefly discuss how the TEK model solves the problem of center symmetry breaking described in the previous section.

The starting point is to write the Wilson action on a single-site twisted lattice. There are two prescriptions we can adopt. One is starting directly with the Wilson action (1.2.5) (where we use the letter $V_\mu(n)$ for the gauge fields)

$$V_\mu(n) \to V_\mu \tag{2.3.5a}$$

$$V_\mu(n+\hat{\nu}) \to \Gamma_\nu V_\mu \Gamma_\nu^\dagger\,, \tag{2.3.5b}$$

and to the following change of variables

$$U_\mu \equiv V_\mu \Gamma_\mu\,. \tag{2.3.6}$$

4 An instructive way of illustrating the problem is by looking at the partition function of the lattice theory of the EK model and writing it in terms of the eigenvalues of the gauge fields on the lattice. In the strong coupling limit, the only term that survives is a function of the difference of the eigenvalues, which is symmetric under $\mathbf{Z}_{N_c}$ transformations, whose only effect is to shift the eigenvalues. In the opposite limit, configurations with the eigenvalues uniformly distributed along the $U(1)$ circle (i. e. center-symmetric) are exponentially suppressed in $d > 2$. The favored configurations are hence those in which eigenvalues attract in the complex plane inducing spontaneous symmetry breaking. For a review of the discussion, the reader can refer to [8] and references therein.

Equivalently, the same prescription corresponds just to remove the dependence on the space-time point n in (2.2.4). The resulting action is

$$S_{\text{TEK}} = bN_c \sum_{\mu\neq\nu} \text{tr}\Big(\mathbb{1} - z_{\mu\nu} U_\mu U_\nu U_\mu^\dagger U_\nu^\dagger\Big)\,. \tag{2.3.7}$$

We adopt the choice of an orthogonal (2.1.7) and symmetric (2.1.8) twist, for which the twist factor becomes the one defined in Eq. (2.1.9), which we rewrite for completeness

$$n_{\mu\nu} = k\sqrt{N_c}, \quad z_{\mu\nu} = e^{\frac{2\pi i k}{\sqrt{N_c}}} \quad \text{for } \mu < \nu\,.$$

On top of that, we will choose $\sqrt{N_c}$ to be a prime number to avoid the center-symmetry group having improper subgroups. We recall that the flux k has an important role in the picture, as it has to be tuned to preserve center symmetry. One thus has to choose it to be coprime with $\sqrt{N_c}$. In this framework, paths in the extended lattice map to a collection of directions in the reduced lattice

$$[n, n+\hat{\mu}_1, n+\hat{\mu}_1+\hat{\mu}_2, \ldots] \to [\mu_1, \mu_2, \ldots]\,. \tag{2.3.8}$$

The corresponding observable is defined consistently as the product of the four matrices following this collection of indices.

$$W_{\text{TEK}}(\gamma) = \frac{z(\gamma)}{N_c} \langle \text{tr}\, U(\gamma)\rangle_{\text{TEK}}\,, \quad U(\gamma) = U_{\mu_1} U_{\mu_2} \cdots \tag{2.3.9}$$

where $z(\gamma)$ is the product of all the twist factors in every plaquette enclosed by the path γ.

A complete discussion on the reason why this choice of parameters is enough to rescue center symmetry can be found in [63–65], we present here a short discussion that aims to review some of the relevant concepts behind it. The crucial difference with the periodic BC case ($k = 0$) is that the vacuum configurations of the twisted model are given by the twist eaters $U_\mu^{(0)} = \Gamma_\mu$ and thus a generic Wilson line is given by the matrices $\hat{\Gamma}(q)$ in Eq. (2.1.11). By construction, all Wilson lines are thus traceless except for those whose length in each direction is a multiple of $\sqrt{N_c}$, i.e. those having $q_\mu = 0 \bmod \sqrt{N_c}$ in all directions, which can be seen as lines that wind around one direction of the effective torus having $L = \sqrt{N_c}$. This ensures that center symmetry breaks down at most to $\mathbf{Z}^4_{\sqrt{N_c}}$, which ensures the reduction to hold in the large-N_c limit.

Based on these observations, the original version of the twisted model ($k = 1$) survived untouched for almost three decades until was put to the test when the results of further lattice investigations [66–68] joined the debate around 2008. The central observation was that at some intermediate values of the lattice coupling b, for big values of $N_c > 100$, TEK model showed a pattern of center symmetry breaking

resembling a transition. Although the continuum limit is achieved in the weak-coupling limit where reduction works untouched, the transition point seemed to move to higher and higher values in b as N_c is increased, leaving no way out for the reduction. The possible explanation for this symmetry breaking could be the existence in the vacuum of configurations having non-vanishing traces despite being extrema of the TEK action. For certain values of b, fluctuations could overcome the potential barrier and the system could tunnel toward configurations that might induce center symmetry breaking. In [63], the authors of the original TEK model proposed that the problem can be avoided by tuning the choice of the flux k as the large-N_c limit is taken. In particular, for the symmetric twist, the value of k should not be kept constant when increasing N_c. The prescription is to keep both $k/\sqrt{N_c}$ and $\bar{k}/\sqrt{N}$ larger than a certain value as N_c is increased.

2.3.2 *Finite-N_c corrections*

Our previous study of the twisted torus allows us to understand how volume reduction emerges in perturbation theory as shown in [13, 63, 69]. Furthermore, it also allows us to understand the nature and size of the finite N_c corrections to observables. We had a hint in this direction when we wrote the Fourier expansion in Eq. (2.1.10) and the consequent momenta in Eq. (2.1.12). On the lattice, the momenta q_μ can be written in a more illustrative way as

$$q_\mu = \frac{2\pi}{\sqrt{N_c}L_\mu} m_\mu + \frac{2\pi}{L_\mu} r_\mu \equiv q_\mu^{(c)} + q_\mu^{(s)} \tag{2.3.10}$$

where m_μ are integer numbers modulo $\sqrt{N_c}$. This momenta structure is very peculiar: the second term in Eq.(2.3.10) assumes the standard form of the momentum in a periodic lattice: we will refer to it as the *spatial* momentum, while the first term will be called *color* momentum. The crucial observation is that, unlike the case of a periodic lattice in which momenta are quantized in units of $2\pi/L$, on a twisted lattice, additional factors of $\sqrt{N_c}$ appear in the denominator. Momenta are now quantized like multiples of $2\pi/\tilde{L}$ where $\tilde{L} = L\sqrt{N_c}$ represent the "effective" size of our lattice. This gives an insight into the concept of volume independence arising in the large-N_c limit: the dynamics of gauge modes is governed not by the number of color N_c and the physical torus size $l = aL$ separately, but rather by the effective length $\tilde{l} = a\tilde{L}$, which in the case we analyzed is given by the product $\sqrt{N_c}l$. When the number of colors is large compared to the volume of the torus, the latter becomes irrelevant in the dynamics of the theory. In fact, following this line of thought, Eq. (2.3.3) can be seen as a "thermodynamic limit" in $\tilde{l}$.

Given that the complete reduction is true in the large-N_c limit, it is straightforward to ask what happens to the volume reduction when

the value of $\tilde{L}$ is not infinite, in particular when we are dealing with actual lattice simulation and we have a finite value of N_c also when $L = 1$. The problem of interpreting these finite-N_c corrections is also very practical: although the number of colors in the simulations can be pushed to rather big values, having a solid understanding of the nature of finite-N_c corrections allows one to have control over systematic effects arising. Some information on the nature of finite-N_c effects comes from perturbation theory. As was already observed in the original works, the gluon propagators in the TEK model are identical to those of a lattice of finite size $\sqrt{N_c}$. On top of that, as we saw in the first section, the Feynman rules for the vertices acquire extra phases which depend on the effective momentum degrees of freedom which disappear in planar diagrams and help to suppress the non-planar ones in the large-N_c limit. Analytical studies of perturbation theory for the plaquette and Wilson loops [13, 52, 64, 70] confirm this scenario about finite-N_c corrections. The idea that the "true" scale that governs the physics of finite volume effects is the effective volume is also exploited in more recent investigations [71, 72], in which the quantity $\tilde{l}$ rather than the actual physical size of the torus, is used as the energy scale to define the running coupling of the gauge theory.

2.4 FERMION FIELDS ON THE TWISTED LATTICE

The inclusion of matter fields on the torus with twisted BC presents more complications than gauge fields. The main reason is that the representation in which fermions live is not always compatible with the boundary conditions that we impose on the gauge fields. Considering a generic representation R, the condition that fermion fields have to respect at the boundary reads

$$\psi^R(x + l_\mu \hat{\mu}) = \Omega^R_\mu(x)\psi^R(x)\,, \tag{2.4.1}$$

where the matrices Ω^R_μ are the same ones we used for gauge fields in Eq. (2.2.1) which thus have to satisfy the twist equation (2.1.2) in the representation R

$$\Omega^R_\mu(x + l_\nu \hat{\nu})\Omega^R_\nu(x) = z^R_{\mu\nu}\Omega^R_\nu(x + l_\mu \hat{\mu})\Omega^R_\mu(x)\,, \tag{2.4.2}$$

where the twist factor $z^R_{\mu\nu}$ has to be the image representation of the $SU(N_c)$ matrix $z_{\mu\nu}\mathbb{1}$. In general, we can write that

$$z^R_{\mu\nu} = (z_{\mu\nu})^{\mathcal{K}_R} \tag{2.4.3}$$

where $\mathcal{K}_R$ is the $\mathcal{K}$-ality of the representation R: for the *fundamental* representation $\mathcal{K}_{\text{fund}} = 1$, while for the *adjoint* $\mathcal{K}_{\text{adj}} = 0$. This has some important implications we must address.

First of all, in the fundamental representation, the presence of the twist factor spoils the whole formulation: when imposing the condition of consistency for the fermion field at the corner of the torus

$\psi^{(\mathrm{fund})}(x + L\hat{\mu} + L\hat{\nu})$, the non-commutativity of the twist matrices leads to an inconsistency. One can try to find an ad-hoc solution for this problem by considering additional flavors of fundamental fermions which get also twisted by the boundary conditions in the same way as colors. The other possibility, as advocated in [73] is to allow fermions to propagate in a lattice of any size on which the gauge fields work as a background field. This is going to be the main idea we will follow for practical application. On the other hand, the *adjoint* representation can host several flavors of matter fields without any complication arising from compatibility with boundary conditions. Of course, the requirements of consistency would be indeed the same as the one for gauge fields and therefore one does not have to make any extra assumptions.

2.4.1 *Reducing fermion action*

The Wilson discretization for the Dirac operators on the lattice was given in Eq. (1.2.16). Just for clarity, we rewrite the Wilson-Dirac operator as

$$S_f = \sum_n \Bigg[\bar{\psi}(n)\psi(n) - \kappa \sum_{\mu=1}^{4} \Big[(\mathbb{1} - \gamma_\mu)\bar{\psi}(n) V_\mu^{(R)}(n)\psi(n+\hat{\mu}) + (\mathbb{1} + \gamma_\mu)\bar{\psi}(n) V_\mu^{(R)}(n-\hat{\mu})^\dagger \psi(n-\hat{\mu}) \Big] \Bigg], \quad (2.4.4)$$

where we used $V_\mu^{(R)}$ instead of $U_\mu^{(R)}$, where superscript R identifying the representation of fermion. As anticipated in the last section, we allow fermions to propagate on a generic lattice of volume $V = l_0 L \times L^3$ with integer l_0.[5] We will see that this lattice can be combined with the boundary conditions in such a way as to perform a full or partial reduction, depending on the representation. The goal of this section is to derive relevant expressions for the observables we are going to need in the following. We will follow in some detail the derivation that the interested reader can also find in [73, 74].

2.4.1.1 *Reducing the adjoint fermion action*

The case of the adjoint representation is the simplest, as adjoint fermions are of the same nature as gauge fields and therefore they do not suffer the problem of incompatibility with twisted BC. In fact, if choosing constant twist matrices $\Omega_\mu(n) = \Gamma_\mu$, we can write

$$\psi(n + \hat{\mu}) = \Gamma_\mu \psi(n) \Gamma_\mu^\dagger . \quad (2.4.5)$$

5 The reason why the "temporal" extent is enlarged by a factor l_0 is a standard choice in lattice spectroscopy to increase time resolution in observables such as correlators.

using the so-called *bi-fundamental* representation.[6] The reduction process will then be completely analogous to the gauge actions: we will just consider fermions to live on a single-site lattice $\psi(n) \to \psi$. At this point, we change variables as $U_\mu = V_\mu \Gamma_\mu$ and the final form of the Wilson-Dirac matrix will then be

$$D_w^{\text{adj}} = \mathbb{1} - \kappa \sum_\mu \left[(\mathbb{1} - \gamma_\mu) U_\mu^{\text{adj}} + (\mathbb{1} + \gamma_\mu)(U_\mu^{\text{adj}})^\dagger \right] \tag{2.4.8}$$

where $U_\mu^{\text{adj}} \psi = U_\mu \psi U_\mu^\dagger$ using gauge field in the fundamental representation. The dimension of the matrix will then be $(4(N_c^2 - 1))^2$. Being adjoint fermion objects of the same kind of gauge fields, in practical implementation, we have to impose a traceless-ness condition to the resulting vector $D_w^{\text{adj}} \psi$.

2.4.1.2 *Reducing the fundamental fermion action*

For fundamental fermions, the reduction is more involved. First of all, we apply the reduction prescription to gauge fields, namely

$$V_\mu(n) = \Gamma(n) V_\mu \Gamma(n)^\dagger \,, \tag{2.4.9}$$

where we used $V_\mu \equiv V_\mu(0)$ and we choose a "rectangular" straight path for the twist eaters as

$$\Gamma(n) \equiv \Gamma_1^{n_1} \Gamma_2^{n_2} \Gamma_3^{n_3} \Gamma_4^{n_4} \,, \tag{2.4.10}$$

and we also apply the usual change of variables $V_\mu = U_\mu \Gamma_\mu$. It is also useful to make an additional change of variables to the fermion fields $\psi(n) = \Gamma(n) \Psi(n)$, we can write the Dirac operator as

$$\begin{aligned} D_w^{\text{fund}}(n, m) = \mathbb{1} - \kappa \sum_\mu [(\mathbb{1} - \gamma_\mu) U_\mu \Gamma_\mu^\dagger \Gamma^\dagger(n) \Gamma(n + \hat{\mu}) \delta(n + \hat{\mu}, m) + \\ (\mathbb{1} + \gamma_\mu) \Gamma^\dagger(n) \Gamma(n - \hat{\mu}) \Gamma_\mu U_\mu^\dagger \delta(n - \hat{\mu})] \,. \end{aligned} \tag{2.4.11}$$

---

6 Fermion fields on the lattice carry three indices, a spinor one α, a color one a and a "volume" one n: $\psi_a^\alpha(n)$. In components, the displacement reads

$$\psi_a^\alpha(n + \hat{\mu}) = \sum_{b=1}^{N_c^2 - 1} \left[\Gamma_\mu^{(\text{adj})} \right]_{ab} \psi_b^\alpha(n) \,. \tag{2.4.6}$$

In the adjoint representation, the color index runs over $N_c^2 - 1$ possible values and therefore the fermion field can be seen as a traceless $N_c \times N_c$ matrix. Using this representation notation, the $\Gamma_\mu^{(\text{adj})}$ in the left-hand side of the previous equation acts as

$$\psi_{ij}^\alpha(n + \hat{\mu}) = \sum_{k,l=1}^{N_c} [\Gamma_\mu]_{ik} \psi_{kl}^\alpha(n) \left[\Gamma_\mu^\dagger \right]_{lj} \,, \tag{2.4.7}$$

where Γ_μ are the $N_c \times N_c$ twist eaters in the fundamental representation.

We can simplify further this expression by noting that, using standard identities for the twist eaters we end up with

$$\Gamma_\mu^\dagger \Gamma^\dagger(n)\Gamma(n+\hat{\mu}) = e^{i\omega_\mu(n)}\mathbb{1} \tag{2.4.12}$$

The complex phase $\omega_\mu(n)$ assumes the following form

$$\omega_\mu(n) = \frac{2\pi k}{\sqrt{N_c}} \sum_{\nu>\mu} n_\nu \,. \tag{2.4.13}$$

We are thus left with the following expression:

$$D_w^{\text{fund}}(n,m) = \mathbb{1} - \kappa \sum_\mu [(\mathbb{1}-\gamma_\mu)U_\mu e^{i\omega_\mu(n)}\delta(n+\hat{\mu},m) + (\mathbb{1}+\gamma_\mu)U_\mu^\dagger e^{-i\omega_\mu(n-\hat{\mu})}\delta(n-\hat{\mu},m)] \,. \tag{2.4.14}$$

In order to follow with the derivation, it comes useful to define the matrices $\tilde{\Gamma}_\mu$, whose components are

$$\tilde{\Gamma}_\mu(n,m) = e^{i\omega_\mu(n)}\delta(n+\hat{\mu},m) \,. \tag{2.4.15}$$

We can observe that the matrices $\tilde{\Gamma}_\mu$ satisfy the following version of the twist-equation

$$\tilde{\Gamma}_\mu \tilde{\Gamma}_\nu = z^*_{\mu\nu}\tilde{\Gamma}_\nu\tilde{\Gamma}_\mu \,, \tag{2.4.16}$$

and thus they are a *reducible* representation of the twist group in $V \times V$ matrices, providing V is an integer multiple of N_c. In principle, we could say that there is a transformation Ω such that

$$\tilde{\Gamma}_\mu = \Omega\big(\Gamma_\mu^* \otimes D_\mu\big)\Omega^{-1} \,. \tag{2.4.17}$$

being D_μ a diagonal matrix. Let us make some observations about the dimension of these matrices. The $\tilde{\Gamma}_\mu$ matrices are $(V \times V)$-dimensional, while the twist-eaters are $N_c \times N_c$, being them an irreducible representation of the twist group. This means that the dimension of matrices D_μ has to be $V/N_c \times V/N_c$. This is an additional confirmation that (an arbitrary number of) fundamental fermions cannot be fully reduced on the lattice since the volume is constrained to be divisible by the number of colors. The minimal symmetric choice is when $L_\mu = \sqrt{N_c}$ (i. e. $V = N_c^2$), which is in line with the "effective" lattice induced by twisted BC on gauge fields. [7] In the large-N_c limit the box in which fermion propagates grows indefinitely, but for finite values of N_c we expect to see corrections in the form of finite-volume effects of a lattice of size $L = \sqrt{N_c}$. The choice typically used in practical implementation such as [75] is to take $L_0 = l_0\sqrt{N_c}$ with integer l_0 (typically 2) to improve the signal of the correlator.

7 This choice is also in line with the definitions of the $\Gamma(n)$ matrices in Eq (2.4.12), which are all linearly independent except when n_μ is proportional to $\sqrt{N_c}$, which makes $\Gamma^{\sqrt{N_c}} \propto \mathbb{1}$, implying periodic boundary conditions on a $(\sqrt{N_c})^4$ lattice.

By inserting Eq. (2.4.17) in Eq. (2.4.14), one gets

$$D_w^{\text{fund}} = \Omega \Bigg[\mathbb{1} - \kappa \sum_\mu [(\mathbb{1} - \gamma_\mu) U_\mu \Gamma_\mu^* D_\mu \quad + \\ (\mathbb{1} + \gamma_\mu) U_\mu^\dagger \, {}^t\Gamma_\mu D_\mu^*] \Bigg] \Omega^{-1} \,, \quad (2.4.18)$$

where we made the matrix Ω to act also on spin space and we omitted the tensor product signs. Although a general derivation of the matrices Ω would be necessary, one can easily demonstrate that their effect on almost every practical application of the Dirac matrix is non-relevant. The main observation is that, as one can see in the left-hand side of Eq. (2.4.18), the transformation matrices Ω only implement a change of basis in the space of spinors and therefore left eigenvalues untouched. The transformation also acts as a gauge transformation and therefore all gauge-invariant observable are left untouched. The fermionic observables we are interested in are typically base invariant, as they are the result of a trace or functions of the only eigenvalues. For this reason, from now on we will drop Ω when writing the Dirac matrix.

On the other hand, the matrices D_μ deserve special attention. The first observation is that they are diagonal and unitary and their size depends on the volume of the space in which we let fermion propagate. Furthermore, in the case in which $L_\mu = \sqrt{N_c}$, one can easily see that $D_\mu^{\sqrt{N_c}} = \mathbb{1}$, which implies that the diagonal elements are just repetitions of the $\sqrt{N_c}$ roots of 1. This means that the matrix given by $\Gamma_\mu^* \otimes D_\mu$, is block diagonal and each block is just $z_\mu \Gamma_\mu^*$, being $z_\mu = e^{i\frac{2\pi n}{\sqrt{N_c}}}$ with integer n. Following the properties of the twist group, every solution of the twist equation is unique up to gauge transformation or multiplication of the center, therefore $z_\mu \Gamma_\mu^* = \bar{\Omega} \Gamma_\mu \bar{\Omega}^{-1}$, where the matrix $\bar{\Omega}$ has the same role as Ω in Eq. (2.4.18) and can be safely ignored. We can therefore write the Wilson-Dirac matrix for fundamental fermions as

$$D_w^{\text{fund}} = \mathbb{1} - \kappa \sum_\mu \left[(\mathbb{1} - \gamma_\mu) U_\mu \otimes \Gamma_\mu^* + (\mathbb{1} + \gamma_\mu) U_\mu^\dagger \otimes {}^t\Gamma_\mu \right] \otimes \mathbb{1} \,, \quad (2.4.19)$$

with the caveat that we are omitting the Ω. To obtain this expression we absorbed the factor z_μ inside the definition of Γ_μ^*, which transform D_μ into a unit matrix of the same dimension that can be factored out. We observe that, as it is clear from Eq. (2.4.19), the reduced Dirac matrix is block-diagonal and each block gets repeated V/N_c times. For this reason, the Dirac modes are given by the eigenstates of the inner block, repeated V/N_c times.

In the other relevant case explained before, i. e.when the temporal extent of the fermion lattice is $l_0 \sqrt{N_c}$, we are not entitled to absorb the factor z_μ inside Γ_μ^*, because it would be true only if the global

$\mathbb{Z}_{N_c}$ remains unbroken (and not only $\mathbb{Z}_{\sqrt{N_c}}$). In this case, we would have the same expression of Eq. (2.4.19), but with

$$U_\mu \to U'_\mu = e^{ip_0 \delta_{\mu,0}} U_\mu \,, \quad \text{with } p_0 = \frac{2\pi}{l_0 \sqrt{N_c}} n \,, \tag{2.4.20}$$

being n an integer modulo $l_0\sqrt{N_c}$. It can be useful also to leave the phases z_μ explicit in the formulas. This is also the case that we would obtain when considering the Fourier transform of Eq. (2.4.14). Considering that the momenta take the form of

$$\begin{cases} q_0 = \frac{2\pi}{l_0\sqrt{N_c}} r_0 & \text{with } r_0 \in [0, l_0\sqrt{N} - 1] \\ q_i = \frac{2\pi}{\sqrt{N_c}} r_i & \text{with } r_i \in [0, \sqrt{N_c} - 1] \,, \end{cases} \tag{2.4.21}$$

the Dirac matrix in momentum space would read

$$\tilde{D}^{\text{fund}}_w(q) = \mathbb{1} - \kappa \sum_\mu \left[(\mathbb{1} - \gamma_\mu) e^{iq_\mu} U_\mu \Gamma^*_\mu + (\mathbb{1} + \gamma_\mu) e^{-iq_\mu} U^{\dagger\, t}_\mu \Gamma_\mu \right] . \tag{2.4.22}$$

2.4.1.3 *Dirac spectrum and fermion propagator*

The first relevant observable we can compute is the free-fermion spectrum. We recall that in standard lattice formulation, the spectrum is given by the (inverse of) Eq. (1.2.21). We now want to obtain the corresponding result in our case.

The free-fermion propagator is obtained when the fermion is allowed to propagate in a static background field without interacting with it. This limit can be achieved by using constant vacuum configurations $U_\mu = \Gamma_\mu$ for the gauge field in Eq.(2.4.22):

$$\tilde{D}^{\text{fund, free}}_w(q) = \mathbb{1} - \kappa \sum_\mu \left[(\mathbb{1} - \gamma_\mu) e^{iq_\mu} \Gamma_\mu \Gamma^*_\mu + (\mathbb{1} + \gamma_\mu) e^{-iq_\mu} \Gamma^{\dagger\, t}_\mu \Gamma_\mu \right] , \tag{2.4.23}$$

where, as usual, the product between the (vacuum) link matrices and the twist eaters is to be intended as $\Gamma_\mu \otimes \Gamma^*_\mu$. However, it is easy to prove that the matrices $\bar{\Gamma}_\mu \equiv \Gamma_\mu \otimes \Gamma^*_\mu$ commute among themselves

$$\begin{aligned} \bar{\Gamma}_\mu \bar{\Gamma}_\nu &= (\Gamma_\mu \otimes \Gamma^*_\mu)(\Gamma_\nu \otimes \Gamma^*_\nu) \\ &= \Gamma_\mu \Gamma_\nu \otimes \Gamma^*_\mu \Gamma^*_\nu \\ &= z_{\mu\nu} \Gamma_\nu \Gamma_\mu \otimes z^*_{\mu\nu} \Gamma^*_\nu \Gamma^*_\mu \\ &= z_{\mu\nu} z^*_{\mu\nu} (\Gamma_\nu \otimes \Gamma^*_\nu)(\Gamma_\mu \otimes \Gamma^*_\mu) = \bar{\Gamma}_\nu \bar{\Gamma}_\mu \,, \end{aligned} \tag{2.4.24}$$

and therefore exist another transformation $\bar{\Omega}$ such that

$$\bar{\Gamma}_\mu = \bar{\Omega} \bar{D}_\mu \bar{\Omega}^{-1} \tag{2.4.25}$$

where $\bar{D}_\mu$ is a diagonal matrix. Given the property of the twist eaters that $\Gamma_\mu^{\sqrt{N_c}} = \mathbb{1}$, this also holds for $\bar{\Gamma}_\mu$. Being the dimension of the latter $N_c \times N_c$, the eigenvalues of $\bar{D}_\mu$ can be chosen to be the $\sqrt{N_c}$ roots of the identities e^{iq_μ} with $q_\mu \in \frac{2\pi}{\sqrt{N_c}}[0, \ldots, \sqrt{N_c} - 1]$ repeated $\sqrt{N_c}$ times:

$$\bar{D}_\mu = \operatorname{diag}\left(e^{iq_\mu^{(1)}}, \ldots, e^{iq_\mu^{(\sqrt{N_c})}}\right) \otimes \mathbb{1}_{\sqrt{N_c}}. \tag{2.4.26}$$

When combining the diagonal matrices $\bar{D}_\mu$ and the momenta matrix $e^{\pm iq_\mu}\mathbb{1}$, we observe that the resulting matrix is diagonal and its entries the roots of the identity repeated $\sqrt{N_c}$ times. The global (free) Wilson-Dirac matrix is diagonal in momentum space can be written as

$$\tilde{D}_w^{\text{fund, free}}(q) = \mathbb{1} - \kappa \sum_\mu \left[(\mathbb{1} - \gamma_\mu)e^{iQ_\mu} + (\mathbb{1} + \gamma_\mu)e^{-iQ_\mu}\right], \tag{2.4.27}$$

where Q_μ can be seen as the "generalized momenta

$$Q_\mu = \frac{2\pi}{\sqrt{N_c}} m_\mu + q_\mu^{\text{lat}} \tag{2.4.28}$$

where m_μ are integers modulo $\sqrt{N_c}$ and q_μ^{lat} is given by Eq.(2.4.21). Surprisingly we found that momenta structure for fundamental fermions emerging from reducing the Wilson-Dirac matrix with twisted BC is exactly the one we obtained in Eq. (2.3.10) for gauge fields when discretized on a L^4 lattice with twisted BC.

2.4.2 *Meson correlators and spectroscopy in the reduced model*

In this section, we give technical details about computing meson correlators in both the fundamental and adjoint representation and their subsequent use to obtain the masses of the lowest state with the corresponding quantum numbers. In the literature, there have been extensive studies done previously [76–78] using the same techniques explained in this Thesis.

As a recap of what we saw in this Section, the Dirac matrix for *fundamental* fermion in momentum space is given in Eq. (2.4.22), which we rewrite for completeness using this new compact notation

$$D_w^{\text{fund}}(q) = \mathbb{1} - \kappa \sum_{\mu=1}^{4} \left[(\mathbb{1} - \gamma_\mu) \otimes W_\mu(q) + (\mathbb{1} + \gamma_\mu) \otimes W_\mu^\dagger(q)\right], \tag{2.4.29}$$

where $W_\mu(q)$ are the following $N_c^2 \times N_c^2$ matrices

$$W_\mu(q) = e^{iq_\mu} U_\mu \otimes \Gamma_\mu^*, \tag{2.4.30}$$

while the momenta are quantized in units of $2\pi/L_\mu$ as in Eq. (2.4.21).

For the *adjoint* representation, the reduction of fermions is less involved and the Dirac matrix in momentum space can be obtained by Eq. (2.4.8) with the substitution $U_\mu^{adj} \to e^{iq_\mu} U_\mu^{adj}$, obtaining

$$D_w^{adj}(q) = \mathbb{1} - \kappa_{adj} \sum_{\mu=1}^{4} \left[(\mathbb{1} - \gamma_\mu) \otimes e^{iq_\mu} U_\mu^{adj} + (\mathbb{1} + \gamma_\mu) \otimes e^{-iq_\mu} U_\mu^{adj\dagger} \right], \tag{2.4.31}$$

where the momenta live on the same lattice Λ_q as the one for fundamental fermions. We also remind that fermions in the adjoint representation ψ can be seen as $N_c \times N_c$ matrices, over which the gauge field acts through the bi-fundamental action defined as $U_\mu \psi U_\mu^\dagger$, being U_μ the $N_c \times N_c$ link matrices.

We are now ready to define the meson correlation function. Given some operators acting on the Dirac space, $\mathbf{O}_A$ and $\mathbf{O}_B$ with the quantum numbers of the meson that we are interested in one can use the Wilson-Dirac operators and their inverses to define the corresponding correlator as

$$\hat{C}_{AB}^{ij}(q_0) = \frac{1}{|\Lambda_p|} \sum_{p \in \Lambda_p} \left\langle \mathrm{Tr} \left[\mathbf{O}_A^{(i)} D_W^{-1}(\vec{p}, p_0 + q_0) \mathbf{O}_B^{(j)} D_W^{-1}(p) \right] \right\rangle, \tag{2.4.32}$$

where the trace is over spin, space and color degrees of freedom. In this work, we take the Euclidean time period $l_0 = 2$ so that the temporal momentum takes values $q_0 = \pi m/\sqrt{N}$ with integer m. The symbols A and B specify the spin-parity quantum numbers of the operator and the indices i and j run over a family of operators with the same quantum numbers. The inversion of the Dirac operator is performed using the BiCGStab algorithm or the Conjugate Gradient algorithm whenever the former does not converge. If $|\Lambda_q|$, i. e. the number of elements in Λ_q, is large, this might imply many inversions. In practice, what we do is perform this average stochastically: for each configuration, we generate p randomly and use it to perform the inversion of $D_w(q)$. The Euclidean time correlator is then defined as

$$C_{AB}^{ij}(n_0) = \sum_{q_0} e^{-iq_0 n_0} \hat{C}_{AB}^{ij}(q_0). \tag{2.4.33}$$

Part II

LARGE-N_c SIMULATIONS ON A SINGLE-SITE LATTICE

3

TECHNICAL ASPECTS OF SINGLE SITE SIMULATIONS

In the first part of the Thesis we presented a generic overview of the physical framework we will work in. In this Chapter, we present some technical details of our simulation, leaving results for the next Chapters.

In the first Sections, we deal with the generations of the ensembles of configurations we will use in the next Chapters. In Sec. 3.1 we will first analyze the pure-gauge case ($N_f = 0$), for which different algorithms can be adopted. The common strategy is to adopt the Fabricius-Haan approach [79] together with one of the different existing updating algorithms for unitary groups. In Sec. 3.2 we will then move to the case of Yang-Mills theory coupled with N_f flavors of adjoint fermions. As it is well known, each one of these theories corresponds to distinct computational challenges. The case of $N_f = \frac{1}{2}$ is analyzed in Sec. 3.2.1, where we will deal with the known sign problem we encountered in Sec. 1.2.1.3

Another important topic that we have to discuss is how we deal with autocorrelation in our results, as it influences the determination of the errors in the quantities we will study in the rest of the Thesis. In Sec. 3.3, we will address the problem and discuss the general strategies we will adopt.

Sec. 3.4 is dedicated to the methodology we will employ to perform the scale setting. Our first method is based on Wilson flow techniques combined with a tree-level improvement to treat systematic effects coming from lattice artifacts and finite-N_c effects. Another method we present makes use of Wilson loops and it will be used only in Chapter 5 in the case of $N_f = \frac{1}{2}$.

Sec. 3.5 is a summary of the main formulas concerning meson spectroscopy we will apply in the case of $N_f = \frac{1}{2}$.

3.1 $N_f = 0$: SIMULATING THE TEK MODEL

From a computational perspective, simulating the TEK model amounts to dealing with a Monte-Carlo simulation of a 4-matrix model U_μ distributed according to the exponential of (minus) the TEK action, given in Eq. (2.3.7), which we rewrite for completeness

$$S_{\text{TEK}} = bN_c \sum_{\mu \neq \nu} \text{tr}\left(\mathbb{1} - z_{\mu\nu} U_\mu U_\nu U_\mu^\dagger U_\nu^\dagger\right) \quad z_{\mu\nu} = e^{\frac{2\pi i k}{\sqrt{N_c}}} \text{ for } \mu > \nu \,.$$

In such a simulation, the number of colors N_c, the flux k, and the gauge coupling b are to be intended as "meta-parameters" of the sim-

ulation, in the sense that they are fixed and have to be specified in the preliminary stage of the computation, typically at compiling time.

In standard lattice gauge theory simulations, the pure Yang-Mills theory is simulated by performing local updates of the link variable, i. e. changing the value of a single link while keeping the other frozen. Standard updating algorithms include heat-bath [80, 81], overrelaxation [82] or a combination of the previous two [83]. One particularly efficient method to perform one of the aforementioned updates to a generic $SU(N_c)$ matrix is to adopt the Cabibbo-Marinari subgroup technique [84, 85], where all the $\frac{N_c(N_c-1)}{2}$ diagonal $SU(2)$ subgroups are updated.

Although these algorithms are well-known in the lattice community since the early days of lattice simulations, they cannot be directly applied to the TEK mode since the action is not a linear function of the links U_μ. An early attempt at simulating the EK model made use of the standard Metropolis algorithm [85], while Fabricius and Haan in [79] proposed a heat-bath-inspired algorithm that allowed to overcome the initial problem. In this section, we are just presenting the algorithms used in this Thesis, which are based on the methodology proposed originally in the '80s. A complete and modern review of methodologies and possible choices for the Fabricius-Hann algorithm can be found in [86], which also describes in detail theoretical aspects, algorithmic issues and performance analysis on modern computer making use of parallel computing.

3.1.1 *The Fabricius-Haan algorithm*

The Fabricius-Haan proposal was to introduce auxiliary $d(d-1)/2$ $N_c \times N_c$ matrices $\tilde{Q}_{\mu\nu}$, which are normally distributed.[1] The resulting partition function will be

$$Z \propto \int [dU][d\tilde{Q}] e^{-S_{TEK}[U]} e^{-\frac{1}{2}\sum_{\mu>\nu} \mathrm{tr}\, \tilde{Q}^\dagger_{\mu\nu}\tilde{Q}_{\mu\nu}} . \tag{3.1.1}$$

After performing the change of variables

$$Q_{\mu\nu} = \tilde{Q}_{\mu\nu} + t_{\mu\nu} U_\mu U_\nu + t_{\nu\mu} U_\nu U_\mu, \quad t_{\mu\nu} = \sqrt{2N_c b z_{\mu\nu}} \tag{3.1.2}$$

whose Jacobian is 1, the enlarged action can be written as

$$Z \propto \int [dU][dQ] e^{-S_{TEKQ}[U,Q]} e^{-\frac{1}{2}\sum_{\mu>\nu} \mathrm{tr}\, Q^\dagger_{\mu\nu} Q_{\mu\nu}} , \tag{3.1.3}$$

where

$$S_{TEKQ}[U,Q] = -\sum_{\mu>\nu} \mathrm{Re\ tr}\left[Q^\dagger_{\mu\nu}(t_{\mu\nu} U_\mu U_\nu + t_{\nu\mu} U_\nu U_\mu)\right] . \tag{3.1.4}$$

1 With "normally distributed matrix" we intend a $N_c \times N_c$ matrix whose entries are complex numbers whose real and imaginary parts are sorted from a normal distribution $N(0,1)$ (mean 0, and standard deviation 1).

This action is linear in U_μ, and therefore is suited for the aforementioned updating algorithms.

The general methodology consists in updating first the auxiliary variables $\tilde{Q}_{\mu\nu}$ and then the link matrices U_μ. The update of $\tilde{Q}_{\mu\nu}$ is typically referred to as "refreshing" as it corresponds to a generation of a new set of normally-distributed matrices. On the other hand, the update of the link variables can be achieved using one of the previously mentioned algorithms. The original proposal by Fabricius and Haan used an heat-bath approach through the $SU(2)$ projections proposed by Cabibbo and Marinari. Another possibility is overrelaxation, which can also be achieved by subsequent $SU(2)$ updates.[2] In the configuration used in this Thesis, we used overrelaxation updates through subsequent $SU(2)$-subgroup changes (OR2) to generate configurations.

In general, an update of a single link variable $U_\alpha \to U_\alpha^{\text{new}}$ corresponds to a change in action $\Delta S = S_\alpha[U_\alpha^{\text{new}}] - S_\alpha[U_\alpha]$, being

$$S_\alpha[U_\alpha] = -\text{Re tr}\,[U_\alpha H_\alpha]\,, \tag{3.1.5}$$

where H_α is the sum of "staples" given by

$$H_\alpha = \sum_{\nu\neq\alpha} t_{\alpha\nu} U_\nu Q^\dagger_{\alpha\nu} + t_{\nu\alpha} Q^\dagger_{\alpha_\nu} U_\nu \quad \text{where } Q_{\alpha\nu} \equiv Q_{\nu\alpha} \text{ for } \alpha < \nu\,. \tag{3.1.6}$$

A final version of a possible updating algorithm is described in Alg. 1.

Algorithm 1 Simulation algorithm for TEK model. Details on the updating algorithms can be found in [86].

1: **for** $\alpha \in [0, d-1]$ **do**
2: Generate $d-1$ auxiliary variables $Q_{\alpha\mu}$ according to Eq. (3.1.2)
3: Compute the staple according to Eq. (3.1.6)
4: Update U_α using HB/ORN/OR2
5: **end for**

As a general consideration, when building a simulation code one is typically concerned about the overall performance of the code in terms of timing and memory requirement. It is easy to see that the cost of the updating algorithm scales accordingly to

$$\text{time} \propto \text{memory} \propto \$\$\$ \propto €€€ \propto N_c^3\,, \tag{3.1.7}$$

therefore preferring one choice over another is strongly dependent on the type of data structure, the architecture used for the computation

2 For details of how both algorithms can be implemented, the interested reader can refer to [86] and references therein. In this reference, also an additional overrelaxation update over the entire $SU(N_c)$ group is provided.

and the level of optimization of existing routines. The link matrices (as well as the auxiliary variables) are $N_c \times N_c$ complex dense unitary matrices and writing ad-hoc routines might result in extremely inefficient codes. The best (i. e. coding-time saving) choice is typically to rely on standard libraries that efficiently handle these data structures and allow one to fully exploit the paradigm of parallel computing. In the specific case of the simulation of the TEK model, different update algorithms correspond to different optimal implementations, e. g. $SU(2)$ projections allow for easy vectorization and might benefit from the multi-core structure of the CPU. On the other hand, other algorithms like global overrelaxation updates over the entire $U(N_c)$ only require efficient linear algebra routines like singular value decomposition on top of matrix multiplication, typically offered by linear algebra libraries. Another extremely valid alternative is the usage of graphical processing units (GPU), that in some cases can provide a considerable increase in performance.

In Tab. 2 we provide a complete list of ensembles we will use in the next chapters.

b	(N_c, k)	$\langle P \rangle$	N_{conf}
0.35	(841, 9)	0.52968(4)	500
0.355	(169, 5)	0.5453(1)	800
	(289, 5)	0.545378(57)	800
	(361, 5)	0.545351(60)	400
	(529, 7)	0.545339(31)	400
	(841, 9)	0.545336(25)	800
0.36	(169, 5)	0.557900(89)	800
	(289, 5)	0.558001(49)	800
	(361, 7)	0.558062(72)	321
	(529, 7)	0.557927(39)	400
	(625, 4)	0.558057(45)	360
	(841, 9)	0.558030(17)	1100
0.365	(169, 5)	0.569056(70)	800
	(289, 5)	0.569095(52)	800
	(361, 7)	0.569123(58)	400
	(529, 7)	0.569063(48)	400
	(625, 4)	0.569014(34)	359
	(841, 9)	0.569050(14)	1200
0.37	(169, 5)	0.578861(92)	800
	(289, 5)	0.578960(49)	800
	(361, 7)	0.579008(51)	400
	(529, 7)	0.579010(35)	400
	(625, 4)	0.578981(33)	382
	(841, 9)	0.578927(12)	1400
0.375	(625, 4)	0.588061(35)	300
	(841, 9)	0.588046(12)	1500
0.37	(625, 4)	0.596495(33)	342
	(841, 9)	0.5965021(92)	2500
0.385	(841, 9)	0.6044154(79)	2400

Table 2: List of ensembles for $N_f = 0$ configurations together with the number of configurations and the average value of the plaquette.

The inclusion of dynamical fermions in lattice simulations is an extremely challenging task. Following Eq. (1.2.28), when sea fermions are simulated dynamically, the probability density is

$$p[U] = \frac{e^{-S_{TEK}[U]}}{Z} (\det D_w)^{N_f}, \tag{3.2.1}$$

where we keep considering a generic number of flavors N_f.[3]

As a general consideration, the fermion determinant depends non-locally on the gauge field. A direct single-link update like the one we proposed in the last section is not feasible, and we make use of standard (Rational) Hybrid-Monte Carlo (HMC) techniques adapted for our model. For a review of the HMC algorithm, originally proposed in 1987 in [87], the interested reader can look at the excellent review of computational strategies by Martin Lüscher in [42]. In this section, we will review the algorithm used in our simulations.

First, we consider the hermitian version of the Wilson-Dirac operator, defined as $Q_w \equiv \gamma_5 D_w$. Thanks to γ_5-hermiticity of the Wilson-Dirac operator, $D_w^\dagger = \gamma_5 D_w \gamma_5$, it holds that $D_w^\dagger D_w = Q_w^2$. Using this notation, the power of the fermion determinant can be rewritten in terms of *pseudo-fermion* fields ϕ, i.e. scalar fields with the same quantum number as the fermionic fields. Their usage comes in hand to rewrite the fermion determinant

$$(\det Q_w)^{N_f} = \int [d\phi][d\phi^\dagger] e^{-S_{\text{eff}}\left[Q_w^{-N_f}\right]}. \tag{3.2.2}$$

where the effective action is defined through

$$S_{\text{eff}}\left[Q_w^{-N_f}\right] = \phi^\dagger Q_w^{-N_f} \phi. \tag{3.2.3}$$

The simplest case is for $N_f = 2$ in which the effective action is simply $\phi^\dagger Q_w^{-2} \phi$. Since this pseudo-fermionic effective action is quadratic in ϕ and the matrix Q_w^2 is hermitian and positively defined by definition, the pseudo-fermion fields ϕ can be easily generated with the following procedure: given some random field χ whose components are generated by a standard Gaussian distribution, the fields

$$\phi = Q_w \chi \tag{3.2.4}$$

will be distributed following Eq. (3.2.3).

3 Eq. (3.2.1) is a symbolic notation to indicate all the cases corresponding to different N_f. The equation is the case of a single Dirac fermion is trivially satisfied by setting $N_f = 1$. In the case of $N_f = 2$, the equation corresponds to the case of degenerate masses $m_u = m_d$. The case of one adjoint Majorana fermion ($N_f = \frac{1}{2}$) is to be intended in the sense of Eq. (1.2.30) in Chapter 1, where the square root is to be intended as a square root and an undetermined sign $\pm$. The case of $N_f = \frac{1}{2}$ will be treated in detail in Sec. 3.2.1

On the other hand, in the case of a different number of flavors, Eq. (3.2.2) has to be corrected with the right power of Q_w. For example, in the case of a single Dirac fermion, in order to have $\det Q_w$ one has to generate pseudofermion fields as $\phi = Q_w^{\frac{1}{2}}\chi$. This can be achieved by considering an effective action

$$S_{\text{eff}}\left[R^{(-N_f/2)}(Q_w^2)\right] \equiv \phi^\dagger R^{(-N_f/2)}(Q_w^2)\phi\,, \tag{3.2.5}$$

where the matrix $R^{(-p)}(Q_w^2)$ is a rational approximation of the matrix $(Q_w^2)^{-p}$.[4] Clearly also the generation of pseudofermions has to be performed accordingly as $\phi = R^{(p)}(Q_w^2)\chi$. In this case, the algorithm is called *Rational Hybrid Monte-Carlo* algorithm (RHMC) [88–91].

An additional ingredient is the non-interacting "momentum"-fields $\pi_\mu(x)$. Reminiscent of a classical system, the inclusion of such momenta defines a Hamiltonian

$$H[\pi, U, \phi] = \frac{1}{2}(\partial\pi)^2 + S[U, \phi]\,, \tag{3.2.7}$$

where the action $S[U, \phi] = S_{\text{TEK}} + S_{\text{eff}}$ is a sum of the TEK action and the pseudofermion effective action. With the Hamiltonian, we can rewrite the path integral as

$$\int [dU] e^{-S[U]} (\det D_w[U])^{N_f} \propto \int [d\pi][dU][d\phi][d\phi^\dagger] e^{-H[\pi,U,\phi]}\,, \tag{3.2.8}$$

which does not affect the physics content of the theory. This Hamiltonian drives a dynamic evolution of the system with respect to a fictitious time τ, following the associated Hamilton's equations. In this context, they are typically referred to as *molecular dynamics* equations. The solution of the molecular dynamic equations π_τ and U_τ are uniquely determined and they can be seen as a trajectory in the phase space parameterized by the time τ. After generating the momenta fields π, the newly updated fields in the Monte-Carlo chain are the solution of the molecular dynamic equation after a given time τ. In principle, the MD equations are known to preserve the Hamiltonian of the system, and therefore the updated field does not have to undergo any kind of acceptance-rejection step to ensure detailed

4 Following [78], the matrix $R^{(p)}_{N_R}(Q_w^2)$ is an approximation for $(Q_w^2)^p$ defined through the N_R-th order rational polynomial approximation to x^p for a real number $x \in [a, b]$:

$$x^p \underset{x\in[a,b]}{\simeq} R^{(p)}_{N_R}(x) \equiv \alpha_0^{(p)} + \sum_{j=1}^{N_R} \frac{\alpha_j^{(p)}}{x - \beta_j^{(p)}}. \tag{3.2.6}$$

Using the Remez algorithm, sets of the coefficients $\left\{\alpha^{(p)}_{j=0,\ldots,N_R}, \beta^{(p)}_{j=1,\ldots,N_R}\right\}$ have been prepared and tabulated for various cases: the power $p = 1/8, -\frac{1}{4}$, the dynamic range b/a and the order of the approximation N_R.

balance and ergodicity. Nevertheless, in practice any integrator on the lattice[5] will adopt a step ϵ of finite size and therefore the condition

$$\Delta H \equiv H[\pi', U', \phi'] - H[\pi, U, \phi] = 0 \tag{3.2.9}$$

is only satisfied approximately and gets corrected at some order in ϵ. In the equation, the primed quantities represents the fields after the integration of the MD equations. For this reason, after MD equations are integrated and a field variable U' is proposed for the update, a Metropolis accept-reject step is employed to ensure detailed balance. Overall, a general summary of the algorithm is given in Alg. 2

Algorithm 2 Summary of the HMC algorithm.

1: Generate randomly momentum fields π and fields η, both following a Gaussian distribution.
2: Create the pseudo-fermion from the field η following the distribution given by Eq. (3.2.3), or Eq. (3.2.5) in case of rational approximation.
3: Integrate molecular dynamics equations from (Hamiltonian) time $\tau = 0$ to some time $\tau = \tau_{MD}$ taking π_μ and U_μ as initial values of the field.
4: The gauge fields are updated to U_τ with probability

$$P_{acc}(\pi, U) = \min[1, e^{-\Delta H}]$$

otherwise, the updated field is set to $U_{\tau=0}$.

3.2.1 $N_f = \frac{1}{2}$: *One adjoint Majorana fermion*

The case of a single Majorana fermion is complicated by the presence of a sign-problem. As we saw in Sec. 1.2.1.3 of Chapter 1, the path integral weight of a single configuration is given by

$$\frac{e^{-S_{TEK}[U]}}{Z} \mathrm{Pf}(\not{D}_w)\,, \tag{3.2.10}$$

which cannot be taken as a probability distribution as the Pfaffian is not positive definite. In general, we can rewrite the pfaffian isolating its oscillatory sign as

$$\mathrm{Pf}(\not{D}_w) = \mathrm{sign}(\mathrm{Pf}(\not{D}_w))|\det Q_w^2|^{\frac{1}{4}}\,. \tag{3.2.11}$$

The methodology thus consists in generating an ensemble of configurations with

$$p[U] = \frac{e^{-S_{TEK}[U]}}{Z}|\det Q_w^2|^{\frac{1}{4}} \tag{3.2.12}$$

5 A widely used choice is the *leap-frog* integrator, which is explained in detail in [43]. Other suitable integrators can be found in the literature under the name of *symplectic* integrator.

κ_{adj}	plaquette	N_{conf}
0.100	0.53159(12)	500
0.110	0.53256(14)	500
0.120	0.534148(81)	500
0.130	—	500
0.140	—	500
0.150	—	495
0.155	0.544957(99)	500
0.160	0.547599(84)	500
0.165	0.550819(77)	492
0.175	0.558961(80)	500

κ_{adj}	plaquette	N_{conf}
0.100	0.55946(11)	500
0.110	0.560129(86)	500
0.120	0.56116(11)	500
0.130	0.562683(74)	500
0.140	0.564782(77)	500
0.150	0.567829(70)	500
0.155	0.569670(77)	500
0.160	0.571896(76)	500
0.165	0.574812(60)	500
0.175	0.58233(16)	80

Table 3: Ensemble of "heavy" configurations generated for $N_f = \frac{1}{2}$ for $(N_c = 289, k = 5)$. (*left:* $b = 0.35$, *right:* $b = 0.36$).

using the RHMC algorithm with $p = -\frac{1}{4}$ and by taking the absolute value of the pfaffian and then reweighting the negative sign directly in the observables by following

$$\langle \mathcal{O} \rangle = \frac{\langle \mathcal{O}\, \mathrm{sign}(\mathrm{Pf}(\mathcal{C}D_w)) \rangle_{p[U]}}{\langle \mathrm{sign}(\mathrm{Pf}(\mathcal{C}D_w)) \rangle_{p[U]}} \tag{3.2.13}$$

A dynamical algorithm to simulate gluinos on the lattice was first proposed in [92]. On the line of this algorithm, we adopted the same choice for our simulation as explained in the introduction of this section. In Tab. 3 and Tab. 4 and we report a list of all the ensemble we generated for $N_f = \frac{1}{2}$, technical details of the algorithm employed can be found in [78]. After computing the configuration, one has to deal with the effect of the sign of the Pfaffian in Eq. (3.2.11) by means of the reweighting method as in Eq. (3.2.13). To compute the sign of the Pffafian for our configurations we make use of the results [40, 93–95], according to which, the sign can be determined by counting the number of negative real eigenvalues of D_w. To perform this search, we carried out a complete determination of all the complex eigenvalues of D_w near the origin of the complex plane, using the `ARPACK` library [96]. The shift invert mode with the shift parameter $\sigma = -0.1$, which computes the extreme eigenvalues of $(D_w - \sigma)^{-1}$, is used so that the eigenvalues having negative real part can be captured. Fig. 2 shows, for all configurations, the 100 complex eigenvalues of D_w closest to $z = -0.1$ in the complex plane. Given the symmetry of $(\mathcal{C}D_w)^t = -(\mathcal{C}D_w)$, each point represents a two-folded eigenvalue. For heavy gluino masses, we are not expecting flips of sign of the Pfaffian. Hence, our analysis focused on the lightest adjoint fermion masses at each b and N_c. We did not observe any negative-real eigenvalues in the spectrum. This absence was also checked for several

(N_c, k)	b	κ_{adj}	plaquette	$\langle\lvert\lambda_{min}\rvert\rangle$	N_{confs}
$(361, 7)$	0.350	0.17750	0.561689(73)	0.049554(65)	600
		0.18000	0.564610(70)	0.038933(51)	600
		0.18250	0.568020(55)	0.028445(42)	600
		0.18500	0.571769(42)	0.018722(79)	607
		0.18750	0.576334(91)	0.011781(77)	600
	0.345	0.18000	0.55072(10)	0.049524(85)	600
		0.18400	0.556355(81)	0.032503(57)	712
		0.18680	0.561253(71)	0.020603(59)	600
		0.18960	0.567106(91)	0.011117(97)	600
	0.340	0.18500	0.541414(99)	0.040589(71)	640
		0.18750	0.546237(83)	0.029619(64)	638
		0.18900	0.549479(88)	0.023011(64)	604
		0.19100	0.55419(10)	0.014393(64)	660
		0.19300	0.560145(74)	0.008346(73)	625
$(289, 5)$	0.360	0.176000	0.583233(62)	0.039755(62)	516
		0.178000	0.585296(89)	0.031968(77)	800
		0.180000	0.587629(60)	0.024920(65)	600
		0.182000	0.590255(64)	0.019453(67)	720
		0.183172	0.591912(75)	0.017702(68)	600
		0.184000	0.593188(51)	0.017090(80)	800
	0.350	0.177500	0.561674(93)	0.050168(76)	680
		0.180000	0.564575(72)	0.039760(56)	600
		0.182500	0.568034(85)	0.029459(77)	600
		0.185000	0.57191(10)	0.020167(95)	600
		0.186378	0.57421(10)	0.016132(79)	600
		0.187500	0.576383(73)	0.01427(11)	680
	0.345	0.180000	0.55045(12)	0.050209(83)	624
		0.184000	0.55636(10)	0.033087(77)	600
		0.186800	0.56126(11)	0.021689(91)	600
		0.189600	0.567256(95)	0.013094(99)	600
	0.340	0.185000	0.541611(88)	0.040868(72)	610
		0.187500	0.546422(99)	0.029998(74)	600
		0.189000	0.54981(14)	0.02343(10)	608
		0.191000	0.554363(99)	0.015480(69)	600
		0.192067	0.557248(99)	0.011992(77)	610
		0.193000	0.56039(14)	0.010557(92)	630
$(169, 5)$	0.350	0.1775	0.56191(18)	0.05322(12)	600
		0.1800	0.56479(16)	0.04353(10)	600
		0.1825	0.56834(15)	0.034286(94)	600
		0.1850	0.57194(14)	0.02676(11)	700
		0.1875	0.57680(12)	0.022537(83)	600
	0.340	0.1850	0.54165(23)	0.04309(15)	600
		0.1875	0.54666(23)	0.03270(17)	600
		0.1890	0.55007(19)	0.02691(11)	610
		0.1910	0.55495(17)	0.020784(92)	610
		0.1930	0.56003(28)	0.017592(78)	600

Table 4: List of "light" configurations for $N_f = \frac{1}{2}$. For each value of N_c, b and κ_{adj} we list the expectation value of the plaquette $\langle P \rangle$, and $\langle\lvert\lambda_{min}\rvert\rangle$, with λ^2_{min} the lowest eigenvalue of $Q^2_w = (D_w\gamma_5)^2$.

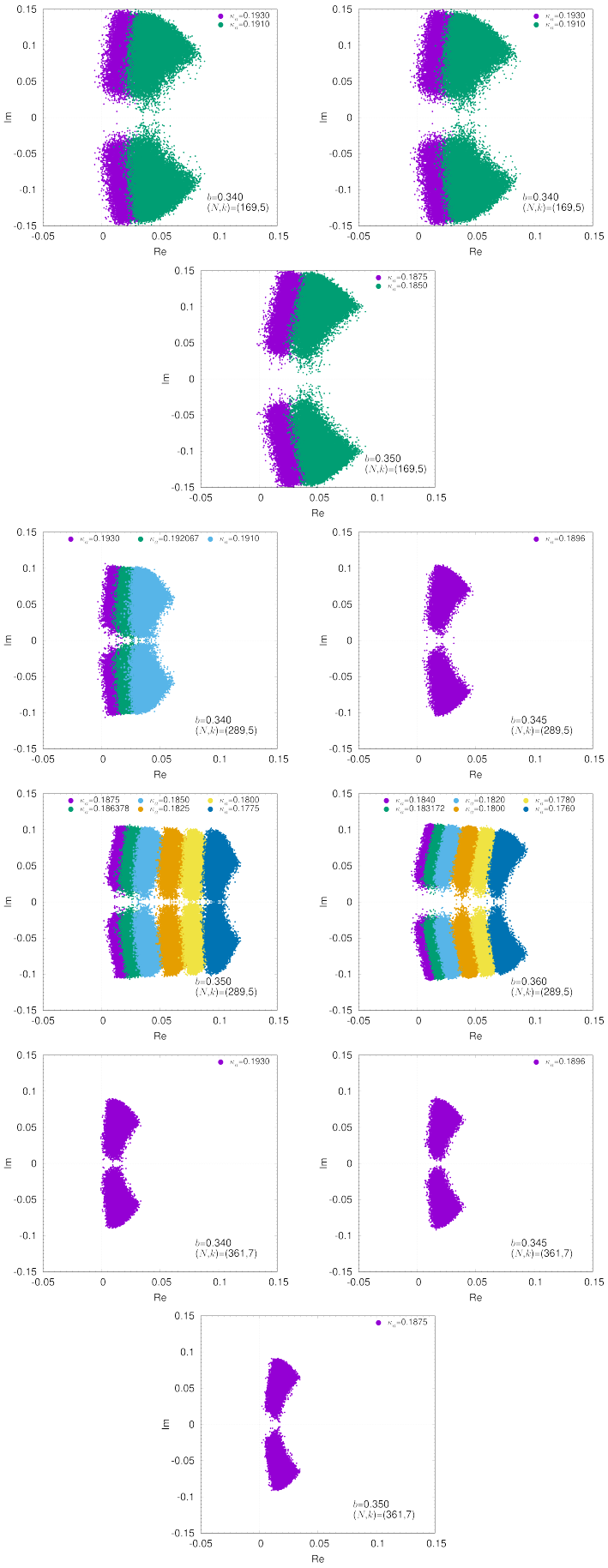

Figure 2: We display in the complex plane and for a subset of our simulation parameters at various values of N, the 100 eigenvalues of the Wilson-Dirac operator D_w closest to -0.1. Figure taken from [78].

κ_{adj}	N_{conf}
0.050	495
0.100	495
0.110	495
0.120	250
0.130	500
0.140	500
0.150	500
0.155	495
0.160	500
0.165	495
0.170	500
0.172	300
0.175	300
0.180	340

κ_{adj}	N_{conf}
0.050	495
0.100	495
0.120	250
0.130	250
0.140	500
0.150	500
0.155	995
0.160	500
0.165	500
0.170	500
0.172	300
0.175	300

Table 5: Ensemble of configurations generated for $N_f = 1$ for $(N_c = 289, k = 5)$. (*Left:* $b = 0.35$, *right:* $b = 0.36$).

heavier fermion masses. Therefore we conclude that the sign of the Pfaffian is always positive for the model parameters we employed, simplifying the reweighting method by validating the distribution using the absolute value of the Pfaffian. Similar results showing that the negative sign of the Pfaffian is rare even with moderately light adjoint masses have been observed in lattice SUSY models [38, 97].

3.2.2 $N_f = 1, 2$ *adjoint Dirac fermions*

The case of $N_f = 1, 2$ adjoint Dirac fermions is more standard and the generation of configurations for the case of $N_f = 2$ was detailed in [74] to which we refer to any technical details. The case of $N_f = 1$ follows the explained methodology and employs the standard RHMC algorithm we mentioned in the previous section. A list of the ensembles available for the case of $N_f = 1$ and $N_f = 2$ are given in Tab. 5 and Tab. 6, respectively.

3.3 DEALING WITH AUTOCORRELATION

A crucial issue we have to take into account when analyzing the results of the simulations is the so-called *autocorrelation*. We shortly present here the problem and how it affects our ensembles of configurations.

κ_{adj}	N_{conf}
0.100	500
0.105	495
0.110	500
0.115	495
0.120	500
0.125	495
0.130	500
0.135	495
0.140	500
0.145	495
0.150	500
0.155	495
0.160	500

κ_{adj}	N_{conf}
0.100	500
0.105	495
0.110	500
0.115	495
0.120	250
0.125	495
0.130	500
0.135	495
0.140	500
0.145	495
0.150	500
0.155	495
0.160	500

Table 6: Ensemble of configurations generated for $N_f = 2$ for $(N_c = 289, k = 5)$. (*Left:* $b = 0.35$, *right:* $b = 0.36$).

After an MC run, one is left with N_{MC} configurations from which are determined *primary observables*[6]

$$\mathcal{O}_t, \quad t = 1, \dots, N_{conf}\,, \tag{3.3.1}$$

where t labels the Monte-Carlo time in the Markov chain.

Following a naive statistical treatment of these MC data, assuming that the distribution of these observables can be approximated with a simple gaussian $\mathcal{N}(\bar{\mathcal{O}}, \sigma_{\mathcal{O}})$, estimates for the real observable are estimated with the average over the measurements

$$\bar{\mathcal{O}} = \frac{1}{N_{MC}} \sum_{t=1}^{N_{MC}} \mathcal{O}_t\,, \tag{3.3.2}$$

and the uncertainty through the standard deviation of the gaussian distribution divided by the square root of the number of statistically independent samples

$$\delta_{\mathcal{O}} = \frac{\sigma_{\mathcal{O}}}{\sqrt{N_{MC}}}, \quad \sigma^2_{\mathcal{O}} = \frac{1}{N_{MC}} \sum_{t=1}^{N_{MC}} (\mathcal{O}_t - \bar{\mathcal{O}})^2\,. \tag{3.3.3}$$

6 With the term "primary" we intend that the observable $\mathcal{O}$ is obtained just through elementary linear-algebra operations of the link matrices, such as multiplications, sums, traces and determinants and not the results of fit, extrapolations or interpolations. Examples of such observables could be the plaquette, and Wilson loops but also the exponential decay of a correlator.

The final result for the lattice estimate will be quoted as $\bar{\mathcal{O}} \pm \delta_{\mathcal{O}}$. Nonetheless, this procedure relies on several assumptions we are going to briefly discuss.

The statement of the distribution of the data being gaussian is somewhat justified, although not always true. In fact, primary observables are typically the result of several averaging procedures[7] that tend to produce a normal distribution, by means of the central limit theorem. This assumption though is not always verified. For example, some observables might have an asymmetric distribution due to their definition: plaquettes and Wilson loops for example are bounded and they cannot be bigger than 1. In this case, a simple average like that in Eq. (3.3.2), might introduce some bias in the final results, although most of the time is included in the statistical error.

The other loose point in the naive description we presented is that we assumed that in the ensemble we generate all the configurations are statistically independent. It is known that subsequent MC measurements are not independent and thus the error given by Eq. (3.3.3) is underestimated. A quantitative statement about how much our computations are affected by autocorrelation can be made by means of the *autocorrelation function*, defined as

$$\Gamma(t) = \frac{1}{N_{MC} - t} \sum_{t'=1}^{N_{MC}-t} (\mathcal{O}_{t+t'} - \bar{\mathcal{O}})(\mathcal{O}_{t'} - \bar{\mathcal{O}}) \,, \tag{3.3.4}$$

which quantifies how much the signal at t is correlated on average with every other MC time. In a normal situation, the normalized autocorrelation time behaves exponentially at large t

$$\frac{\Gamma(t)}{\Gamma(0)} \sim e^{-\frac{t}{\tau_{exp}}} \,, \tag{3.3.5}$$

where τ_{exp} is called *exponential autocorrelation time*. Empirically, one could say that the number of independent configurations is given by

$$N_{\text{ind. conf}} = \frac{N_{MC}}{2\tau_{exp}} \,, \tag{3.3.6}$$

and thus a more fair estimate of the error on the observable is given by

$$\hat{\delta}_{\mathcal{O}} = \frac{\sigma_{\mathcal{O}}}{\sqrt{N_{\text{ind. conf}}}} = \sqrt{\frac{2\tau_{exp}}{N_{MC}}}\sigma_{\mathcal{O}} \tag{3.3.7}$$

In the vast literature of Monte-Carlo Markov Chains, the interested reader can find several detailed discussions on how to compute this exponential autocorrelation time (i. e.the slowest mode of the Markov

7 Plaquettes and loops are averaged over the different planes and then the trace is taken, which can be seen as a "color average". Correlators, on the other hand, are "averages" over the spatial volume of the effective lattice.

operator), but a simple practical implementation of τ_{exp} can be given by the *integrated autocorrelation time*, defined as

$$\tau_{int}(W) = \frac{1}{2} + \sum_{t=1}^{W} \frac{\Gamma(t)}{\Gamma(0)} \tag{3.3.8}$$

In the limit in which the parameter W, called *summation window*, is large compared to τ_{exp}, we can safely assume that $\tau_{int} \approx \tau_{exp}$ and use it to calculate the corrected error as in Eq. (3.3.7).

In our analysis, when performing the estimation of errors of primary observables, we take into account the autocorrelation using two distinct methods we are briefly going to summarize here.

- The so-called Γ-*method*. We directly estimate the integrated autocorrelation time (3.3.8) and assign $\hat{\delta}$ defined in Eq. (3.3.7) as an error associated with the observable $\mathcal{O}$. In practical implementations, one has to adopt a choice for the summation window W. In [98], one of the first implementations of the Γ-method advocates an optimal algorithm to choose the summation window. We are not going into the details of this *automatic windowing*, but it is based on the observation that the error coming from the truncation of the sum in the autocorrelation function is approximately $e^{-\frac{W}{\tau_{exp}}}$, while the "relative error on the error" can be estimated as $2\sqrt{W/N_{MC}}$. The optimal window is then chosen to minimize the quantity

  $$E(W) = e^{-\frac{W}{\tau_W}} + 2\sqrt{\frac{W}{N_{MC}}} \quad \text{where } \tau_W \approx 4\tau_{int}\,. \tag{3.3.9}$$

  In our analysis, the estimation of errors by the Γ-method is implemented through `ADerrors` [99], which combines the estimation of the integrated autocorrelation time with the propagation of errors on derived observables following the paradigm of *automatic differentiation*. This is not the only viable option. Other solutions, which rely on prior knowledge of the exponential autocorrelation time, can be found in [100, 101].

- *Jackknife* resampling. Out of the N_{MC} initial measurements of the observable $\mathcal{O}$, we build N_{MC} subsets by removing the n-th entry of the original sets ($n = 1, \ldots, N_{MC}$) and determining the average $\mathcal{O}_n$ for each set. An estimate of the true standard deviation is given by the square root of

  $$\sigma^2_{\mathcal{O}} = \frac{N_{MC} - 1}{N_{MC}} \sum_{n=1}^{N_{MC}} \left(\mathcal{O}_n^2 - \bar{\mathcal{O}}^2\right), \tag{3.3.10}$$

  being $\bar{\mathcal{O}}$ the total average. Often jackknife is combined with blocking techniques, where instead of applying the procedure

directly on the measurements, they are first divided into groups or *bins* of length N_{bin} and averaged inside each bin. In order for the method to be effective, the size of the bin should satisfy $N_{bin} \gtrsim \tau_{exp}$ and use

$$\sigma_{\mathcal{O}}^2 = \frac{N_{bin} - 1}{N_{bin}} \sum_{n=1}^{N_{bin}} \left(\mathcal{O}_n^2 - \hat{\mathcal{O}}^2 \right), \tag{3.3.11}$$

where $\mathcal{O}_n$ here represent the average inside the n-th bin.

3.4 SCALE SETTING

Scale setting is a standard and rather crucial step one has to face in lattice gauge theories. In simulations, the lattice spacing a can be seen as a natural unit length (or energy) scale one can use to define the numerical value of any other observables. Any dimensionful observable with the right energy dimensions is a candidate to fix the scale. In theories with a massive spectrum, one could simply take one of the masses as a unit. For QCD or Yang-Mills theory the lowest glueball mass, the vector meson mass or the square root of the string tension are typical units of this kind. A unit must be of the appropriate size for the objects to be measured, it should be precise, easy to compute and as insensitive as possible to typical statistical or systematic errors. From that point of view, the natural type of units mentioned earlier might not be optimal, since they involve taking asymptotic limits. Another possible family of choices involves dimensionless monotonous functions of an energy scale. The unit of energy is taken to be the value at which the function takes a particular numerical value. To this class belong some of the most common scales used nowadays by the lattice community such as the Sommer scale [102], based on the quark-antiquark potential, and those relying on the use of the gradient flow such as t_0 [103] or w_0 [104]. For a review of these and other common methods to fix the scale, the interested reader can consult [105]. In the following, we are going to provide a general discussion about scale setting techniques that are not only valid in the case of the single site lattice. At the end of each part, we will underline which formulas are going to be directly applied to our case.

3.4.1 *Scale setting with the Wilson flow scale*

The gradient flow [103, 106, 107] is a smoothing technique that has received much attention in recent years. The idea is to replace the original gauge fields $A_\mu(x)$ with a set of flow-time dependent fields obtained by solving the gradient flow equations:

$$\partial_t B_\mu(x;t) = D_\nu G_{\mu\nu}(x;t), \tag{3.4.1}$$

with $B_\mu(x;0) = A_\mu(x)$ and leading to effective smearing of the gauge fields over a length scale $\sqrt{8t}$. The flow time, having physical dimensions of a length squared, induces natural candidates for scale setting; one just has to find a dimensionless, flow-time dependent, quantity and determine the flow time at which it equals a particular pre-fixed value. The most common choices used for this purpose are based on the quantity:

$$\Phi(t) = \left\langle \frac{t^2 E(t)}{N_c} \right\rangle , \tag{3.4.2}$$

where $E(t)$ stands for the *flowed energy density*:

$$\langle E(t) \rangle = \frac{1}{2} \langle \mathrm{Tr}\, G_{\mu\nu}(x,t) G_{\mu\nu}(x,t) \rangle \, . \tag{3.4.3}$$

Particular examples are the ones obtained by solving either of the two following implicit equations:

$$\Phi(t)\Big|_{t=t_s} = s, \tag{3.4.4a}$$

$$t\frac{d}{dt}\Phi(t)\Big|_{t=w_s^2} = s, \tag{3.4.4b}$$

where $s = 0.1$ corresponds to the standard choices in the literature denoted by t_0 [103] and w_0 [104]. These definitions differ from the standard ones used in lattice QCD simulations due to the extra, N_c-dependent, factor, required to have a well-defined large N_c limit of these quantities.

The perturbative expansion of the infinite volume flow in terms of the 't Hooft coupling in the $\overline{\mathrm{MS}}$ scheme at scale $\mu = 1/\sqrt{8t}$ is given by [103]

$$\Phi_\infty(t, N_c) = \mathcal{K}(N_c) \lambda_{\overline{\mathrm{MS}}}(\mu) \left(1 + c_1 \lambda_{\overline{\mathrm{MS}}}(\mu)\right)\Big|_{\mu = \frac{1}{\sqrt{8t}}} , \tag{3.4.5}$$

where

$$\mathcal{K}(N_c) = \frac{3(N_c^2 - 1)}{128\pi^2 N_c^2} \, . \tag{3.4.6}$$

This expression is used to define the *gradient flow* (GF) coupling constant [103]:

$$\lambda_{\mathrm{gf}}\left(\mu = \frac{1}{\sqrt{8t}}\right) \equiv \frac{\Phi_\infty(t)}{\mathcal{K}(N_c)} = \lambda_{\overline{\mathrm{MS}}}(\mu)\left(1 + c_1 \lambda_{\overline{\mathrm{MS}}}(\mu)\right) , \tag{3.4.7}$$

showing that c_1 stands for the finite one-loop renormalization constant that relates the Λ parameters in the two schemes. So far our discussion of the flow observables has been in the continuum. A generalization to the lattice is rather straightforward, one has to select a

discretization of the energy density and the flow equations. We adopt the clover version of the field strength which, in our one-site reduced lattice, leads to a discretized version of Eq. (3.4.3) given by:

$$\hat{E} = -\frac{1}{128}\sum_{\mu,\nu} \mathrm{tr}\Big[z_{\mu\nu}\Big(U_\nu U_\mu U_\nu^\dagger U_\mu^\dagger + + U_\mu U_\nu^\dagger U_\mu^\dagger U_\nu + U_\nu^\dagger U_\mu^\dagger U_\nu U_\mu + U_\mu^\dagger U_\nu U_\mu U_\mu^\dagger\Big) - \mathrm{h.c.}\Big]^2 . \quad (3.4.8)$$

As for the flow, the flow time is discretized in units of the lattice spacing as $t = Ta^2$, where we will from now on use capital letters to denote lattice, dimensionless quantities. We integrate the discretized flow equations by using a 3rd order Runge-Kutta integrator with constant time interval $\Delta T = 0.03125$. We have checked that changing the time step does not produce any sizeable difference in the integrated flowed observable, resulting only in a different computational cost for different lattice spacings. In terms of $\hat{E}(T)$, the naive dimensionless flowed energy density can be estimated on the lattice from:

$$\Phi_L(T, b, N_c) \equiv \left\langle \frac{T^2\,\hat{E}(T)}{N_c} \right\rangle . \quad (3.4.9)$$

3.4.1.1 *Finite-"size" effects in the gradient flow*

All these definitions we gave, take place in infinite volume. However, numerical simulations are typically implemented on a L-site lattice of finite physical size $l = aL$, a fact that leads to finite size effects in the determination of the scale whenever the flow radius extends over a significant fraction of the box size. One can derive an analogous expression for the finite volume flow. In our case, on a box of size l^4 with twisted boundary conditions, one obtains at second order in the coupling [72]:

$$\Phi(t, l, N_c) = \mathcal{N}(c(t), N_c)\lambda_{\overline{MS}}(\mu)[1 + c_1\lambda_{\overline{MS}}(\mu) + + \mathcal{C}(c(t), N_c)\lambda_{\overline{MS}}(\mu)]|_{\mu=\frac{1}{\sqrt{8t}}} , \quad (3.4.10)$$

where finite volume effects depend on the dimensionless variable:

$$c(t) = \frac{\sqrt{8t}}{\tilde{l}}, \quad \tilde{l} \equiv \sqrt{N_c}\,l , \quad (3.4.11)$$

and are encoded in the functions $\mathcal{N}(c(t), N_c)$ and $\mathcal{C}(c(t), N_c)$. The former has a simple expression in terms of Jacobi θ_3 functions and reads:

$$\mathcal{N}(x, N_c) = \frac{3x^2}{128}\left(\theta_3^4(0, i\pi x) - \theta_3^4(0, i\pi N_c x)\right) , \quad (3.4.12)$$

with:

$$\theta_3(0,ix) = \sum_{m\in\mathbb{Z}} e^{-\pi x m^2} \equiv \frac{1}{\sqrt{x}} \sum_{m\in\mathbb{Z}} e^{-\pi m^2/x}\,. \tag{3.4.13}$$

In the large volume limit, taken by sending l to infinity at fixed flow time, i.e. by sending $c(t)$ to zero, this normalization factor tends to the infinite volume one, i. e. Eq. (3.4.6). The function $\mathcal{C}(c(t), N_c)$ goes to zero in this limit and the infinite volume expansion of the flow presented above is recovered.

Let us also mention that, on account of volume independence, the same expressions can be obtained for $SU(\infty)$ by taking the $c(t) \to 0$ limit differently, i.e. by sending N_c to infinity at fixed torus size l (in the particular case of the one-point lattice, $l = a$). In that limit, the explicit N_c dependence of the normalization $\mathcal{K}(N_c)$ factor disappears.

These considerations indicate a simple way to correct the flow at leading order in the coupling. Indeed, we introduce the following definition of the coupling

$$\hat{\lambda}(t, l, N) \equiv \frac{1}{\mathcal{N}(c(t), N_c)} \Phi(t, l, N_c)\,, \tag{3.4.14}$$

which, at the leading order in the coupling, has the correct perturbative expansion. Consequently, by "inverting" Eq. (3.4.14), we can define a modified flowed energy density given by:

$$\hat{\Phi}(t, l, N_c) = \mathcal{K}(N_c)\hat{\lambda}(t, l, N_c)..\tag{3.4.15}$$

At the second order in λ, the remnant volume dependence comes from the $c(t)$ dependence of the function $\mathcal{C}(c(t), N_c)$, which has not yet been computed in perturbation theory for a general number of fermions. As we will see, finite volume (finite N_c in our set-up) effects are considerably reduced with this choice. Our scale definitions are then obtained by replacing Φ by $\hat{\Phi}$ in Eq. (3.4.4), which at infinite volume coincide with the standard ones. In the next paragraph, we are going to see how this can be implemented in lattice observables.

In order to correct the scale with the normalization factor, we have to find an analogous correction, which in addition takes into account lattice artifacts, to be derived by computing the tree level factor $\mathcal{N}(c(t), N_c)$ in lattice perturbation theory. For our choice of the clover discretization of the energy density and the one-point lattice [71]:

$$\mathcal{N}_L(x, N_c) = \frac{x^4}{128} \sum_{\mu\neq\nu} {\sum_q}' \frac{e^{-\frac{N_c x^2}{4}\hat{q}^2}}{\hat{q}^2} \sin^2(q_\nu)\cos^2\left(\frac{q_\mu}{2}\right), \tag{3.4.16}$$

where the lattice momentum is given by $\hat{q}_\mu = 2\sin(q_\mu/2)$, with q_μ taking values:

$$q_\mu = \frac{2\pi m_\mu}{\sqrt{N_c}}\,, \tag{3.4.17}$$

for $n_\mu = 0, \cdots, \sqrt{N_c} - 1$. The prime in the sum excludes the zero momentum mode, with $n_\mu = 0$, $\forall \mu$. One advantage of using the lattice determined instead of the continuum norm is that one corrects finite lattice artifacts on top of finite size effects at tree level. On the other hand, the normalization factor corresponding to the plaquette discretization of the energy density simply corresponds to

$$\mathcal{N}_L^{(\mathrm{plaq})}(x, N_c) = \frac{3x^4}{128} \sum_q{}' e^{-\frac{N_c x^2}{4} \hat{q}^2} \,. \tag{3.4.18}$$

With all this, our final formula for the discretized version of the flow is given by the following observable

$$\hat{\Phi}_L(T, b, N_c) \equiv \frac{3}{128\pi^2 \mathcal{N}_L\left(\sqrt{\frac{8T}{N_c}}, N_c\right)} \left\langle \frac{T^2 \hat{E}(T)}{N_c} \right\rangle , \tag{3.4.19}$$

with $\mathcal{N}_L(x, N_c)$ given by eq. (3.4.16). Before directly applying our scale-setting procedure to our ensembles, it is worthwhile to make some general considerations about the applicability of the method we are about to use.

As we will observe, finite-N_c corrections are a sizable source of systematics. We expect that the usage of Eq. (3.4.19) will considerably improve the determination of the scale reducing these systematic effects. This method is expected to work within a *scaling window*, whose lower bound is determined by limiting the effects of lattice artifacts and the higher bound by remnant finite-size effects. In particular, the effective parameter that governs the validity of our method is the ratio $c(t) = \sqrt{\frac{8T}{N_c}}$, which determines the fraction of the effective box occupied by the smearing radius. The bounds of the scaling limit can be empirically set to be

$$T \in \left[1.25, \gamma^2 \frac{N_c}{8}\right] \tag{3.4.20}$$

where γ is a value to be chosen.

There is an additional consideration that has to be made. To have a precise determination of the scale it is important that the value of $T_s = {}^{t_s}/_{a^2}$ in the lattice counterpart to Eq. (3.4.4) falls well within the scaling window given by Eq. (3.4.20) and can therefore be reached by interpolation. As will become clear in the next sections, this is best attained by choosing $s = 0.05$ instead of the commonly used value of $s = 0.1$. The corresponding lattice scales will be denoted by T_0 ($s = 0.1$) and T_1 ($s = 0.05$) from now on.

3.4.1.2 *Scale setting with Wilson loops*

A particular version of these techniques was used to set the scale in large N_c pure Yang-Mills theory [108]. In this section, we are going to

provide an alternative way to set the scale. Standard physical quantities such as string tension or glueball masses are difficult observables to measure as they involve taking asymptotic limits. This makes them more affected by corrections and systematic uncertainties. It is in this spirit that Sommer scale [102], which is based on the quark-antiquark potential but not at infinite separation, is superior. However, the Sommer scale still involves the study of loops that are asymptotically long in time. Our proposal is based on fixed aspect ratio Wilson loops and hence it involves no limit.

Ultimately all gluon observables are based on Wilson loop expectation values. However, the Wilson loops themselves are UV divergent quantities and thus not suitable observables. Our proposal is based on the following observable function

$$F(r,r') = -\frac{\partial^2 \log \mathcal{W}(r,r')}{\partial r \partial r'}, \tag{3.4.21}$$

where $\mathcal{W}(r,r')$ are expectation values for rectangular $r' \times r$ Wilson loops. The double derivative gets rid of perimeter and corner singularities and one gets a well-defined continuum quantity depending on two scales. We can reduce it to a single scale by fixing the aspect ratio r'/r. Different choices give different definitions. Notice that the Sommer scale involves the limit $r \gg r'$. Here we will restrict ourselves to the opposite limit given by symmetric loops $r = r'$ (a restriction taken after the derivative is evaluated).

Indeed we claim that $F(r,r)$ is a very interesting physical quantity for $SU(N_c)$ Yang-Mills theory, which has been computed in [108] both for finite and infinite N_c. Obviously, the string tension is given by

$$\sigma = \lim_{r \longrightarrow \infty} F(r,r). \tag{3.4.22}$$

However, it is better not to fix the scale in terms of the string tension. For that purpose, one notices that $F(r,r)$ has dimensions of energy square, so we consider the dimensionless observable $G(r) = r^2 F(r,r)$. A physical scale $\bar{r}(f_0)$ can be defined, á-la Sommer, as follows

$$G(\bar{r}(f_0)) = r^2 F(r,r)\Big|_{r=\bar{r}} = f_0, \tag{3.4.23}$$

where f_0 is some numerical value that can be chosen arbitrarily. This is essentially the method used in [108] to fix the scale with $f_0 = 1.65$. Here we will consider a variant of the method that makes use of the gradient flow and results advantageous from the point of view of the lattice implementation.

One can use the gradient flow to construct flow-time dependent Wilson loops $\mathcal{W}_t(r,r')$ and use them to define a function $F_t(r,r)$, in analogy to Eq. (3.4.21). Our new proposal is to use the flowed functions at non-zero flow time to set the scale. To define a function of a

single energy scale in the problem, we fix the flow smearing radius to be proportional to the loop size: $\sqrt{8t} = \sqrt{8\bar{t}(r,s)} \equiv sr$. This amounts to defining Wilson loops having fat edges with thickness proportional to the size of the loop. This choice defines a dimensionless function of a single length r

$$\hat{G}(r;s) = r^2 F_{\bar{t}(r,s)}(r,r)\,. \tag{3.4.24}$$

Applying now the prescription we can define a physical scale $\bar{r}(f_0,s)$ as follows

$$\hat{G}(\bar{r}(f_0,s);s) = f_0, \tag{3.4.25}$$

Any choice of f_0 and s defines a different scale, but they should all be proportional to each other. The concrete choice of s and f_0 is dictated by practical reasons of accessibility and insensitivity of the corresponding lattice observable to different error sources. From that viewpoint, the choice used previously $\bar{r}(1.65,0)$ is not the most adequate here.

On the lattice, the counterparts of the observables $F(r,l)$ are the so-called *Creutz ratios*, defined as follows:

$$\chi(R,R') = -\log \frac{W(R+0.5,R'+0.5)W(R-0.5,R'-0.5)}{W(R+0.5,R'-0.5)W(R-0.5,R'+0.5)}\,. \tag{3.4.26}$$

In this formula, $W(R,R')$ is the lattice Wilson loop evaluated for a rectangle of size $r \times r'$, where $r = aR$ and $r' = aR'$ are integer multiples of the lattice spacing a. Thus, in our definition of $\chi(R,R')$, the arguments take half-integer values. Taylor expanding the Wilson loops we see that

$$\chi(R,R') = a^2 F(aR,aR') - \frac{a^4}{12}\frac{\partial^4 \log \mathcal{W}(r,r')}{\partial r^3 \partial r'} + \dots\,. \tag{3.4.27}$$

Thus, in the continuum limit one has

$$G_L(R) \equiv R^2\chi(R,R) \xrightarrow{a\to 0} r^2 F(r,r) + \mathcal{O}\left(\frac{a^2}{r^2}\right). \tag{3.4.28}$$

Notice that the first term is universal, being independent of the lattice bare coupling, once r is measured in units of an implicitly defined $\bar{r}$. A practical problem that appears when implementing this method is that Creutz ratios $\chi(R,R')$ are very noisy quantities for R and R' large. To face this issue one can use the gradient flowed equivalents of these observables: $\mathcal{W}_t(r',r)$, $F_t(r,r)$ and $G_t(r)$. Analogously to what is done for the flowed energy density in the Wilson flow, we have to give a definition of a lattice equivalent to $\hat{G}(r;s)$. In Chapter 5, we are going to give technical details of the lattice implementation and a discretized version which will be called $\hat{G}_L(R;s)$. In this case, the flow time in lattice units is fixed in terms of R as follows: $\sqrt{8T} = sR$. Although, this function is well-defined in the limit $s \to 0$, performing

this extrapolation as in [108] is unnecessary. For an effective statistical error reduction it is enough to keep s larger than 0.1 and smaller than 1. Notice that intuitively our lattice observables are square Creutz ratios obtained from fat (i. e. smeared) links of thickness proportional to their edge length.

3.5 SPECTROSCOPY ON A SINGLE-SITE LATTICE

In this last Section, we are going to review the main techniques that will be employed to perform spectroscopy in the single-site lattice setup. At the end of Chapter 2 we discussed how reduction can be applied to the case of fermions. The formula for the correlator of operators acting on the Dirac space $\mathbf{O}_A$ and $\mathbf{O}_B$ with the quantum numbers of the meson that we are interested is given by Eq. (2.4.32), which we rewrite for completeness

$$\hat{\mathcal{C}}^{ij}_{AB}(q_0) = \frac{1}{|\Lambda_p|}\sum_{p\in\Lambda_p}\left\langle \mathrm{Tr}\left[\mathbf{O}^{(i)}_A D^{-1}_W(\vec{p}, p_0+q_0)\mathbf{O}^{(j)}_B D^{-1}_W(p)\right]\right\rangle ,$$

We recall that the symbols A and B specify the spin-parity quantum numbers of the operator and the indices i and j run over a family of operators with the same quantum numbers. The Euclidean time correlator is then defined as

$$\mathcal{C}^{ij}_{AB}(n_0) = \sum_{q_0} e^{-iq_0 n_0}\hat{\mathcal{C}}^{ij}_{AB}(q_0)\,.$$

Now we have to specify the selection of operators used to obtain the masses. The easiest choice is to use ultralocal operators $\mathbf{O}^{(i)}_A \equiv \gamma_A$, being γ_A the corresponding fermion bilinear. We will be mainly interested in the pseudoscalar (0^{-+}), axial (1^{++}) and vector (1^{--}) channels for which the quantum numbers are given by γ_5, $\gamma_0\gamma_5$ and $\gamma_i\gamma_5$. Apart from ultralocal operators, we are interested in having a full set of operators having the same quantum numbers. This is obtained by applying Wuppertal smearing [109–111] to the bilinear operator combined with three-dimensional APE smearing to the link variables [112]. This amounts to replacing the ultralocal operator γ_A as follows

$$\gamma_A \longrightarrow \mathbf{O}^{(i)}_A \equiv \gamma_A\left(\tilde{M}(\boldsymbol{p})\right)^{s_i}, \tag{3.5.1}$$

where the single-step smearing operator is given by

$$\tilde{M}(\boldsymbol{p}) = \frac{1}{1+6c}\left[\mathbf{I} + c\sum_{k=1}^{3}\left[e^{ip_k}\bar{U}_k + e^{-ip_k}(\bar{U}_k)^\dagger\right]\right], \tag{3.5.2}$$

and the s_i are integers. In this equation, $\bar{U}$ indicates smeared gauge field in a generic representation. In the fundamental representation

this amounts to $\bar{U}_k \equiv \bar{U}_k \otimes \Gamma_k^*$, while in the adjoint representation this is simply $\bar{U}_i \equiv \bar{U}_k^{adj}$. In this work, we have used $c = 0.5$ and the following list of values:

i	0	1	2	3	4	5	6	7	8	9
s_i	0	1	4	16	36	64	100	144	196	256

In the case of adjoint fermions, we only used up to 6 operators, while for fundamental ones we used up to 9. The symbol $\bar{U}_k$ appearing in eq. (3.5.2) corresponds to the 10 times APE-3d smeared link to be explained below. The smearing procedure is an iterative one which in our case maps three spatial $SU(N_c)$ matrices onto new ones:

$$U_i^{(s)} \longrightarrow U_i^{(s+1)} = P\Big[(1-f)U_i^{(s)} + \\ + \frac{f}{4}\sum_{j\neq i}\left(z_{ji}^* U_j^{(s)} U_i^{(s)} U_j^{(s)\dagger} + z_{ji} U_j^{(s)\dagger} U_i^{(s)} U_j^{(s)}\right)\Big], \quad (3.5.3)$$

where $\mathcal{P}$ is an operator projecting on $SU(N_c)$. The starting point of the iteration is the link matrices $U_i^{(0)} \equiv U_i$. For the case of adjoint fermion correlators, we chose $f = 0.081$ and stopped after 10 iterations $\bar{U}_i = U_i^{(10)}$, which is then transformed into the adjoint representation and replaced in eq. (3.5.2). For the adjoint fermion, the projection to $SU(N_c)$ matrix is not required and it is enough to project onto $U(N_c)$ as follows

$$P(W) = W(W^\dagger W)^{-1/2}. \quad (3.5.4)$$

For the case of fundamental meson correlators, we applied the same method using $f = 0.15$.

3.5.0.1 *GEVP methodology*

As we argued in Eq. (1.2.45) in Sec. 1.2.3.2 of Chapter 1, we expect the signal to decay in time as an (infinite) sum of exponentials, corresponding to the contribution of the ground state plus other heavier excited states. Given the typical hierarchy in the mass spectrum, we expect the excited states to decay faster than the ground state, whose signal dominates for large enough time separation. We want to extract the mass of the ground state from an exponential fit in a region where excited states give no systematic contribution. In order to do so, one has to maximize the projection onto the ground state to have a single-exponential decay setting in early on. Fermion smearing in Eq. (3.5.1) should provide an improvement in this regard since it increases the overlap onto the ground state wave function. Beyond that, we make use of a variational approach, in the same philosophy of ref. [77]. Using the definition of the correlator matrix given in eq. (2.4.32), where

the index i and j run over the smearing levels, we applied the so-called GEVP method. Given two timeslices τ_0 and τ_1 (with $\tau_0 < \tau_1$) (not to be confused with gradient flow scales) we solve numerically the generalized eigenvalue problem (GEVP)

$$\mathcal{C}^{ij}(\tau_1)\boldsymbol{v}_j^{(n)} = \lambda^{(n)}\mathcal{C}^{ij}(\tau_0)\boldsymbol{v}_j^{(n)} \quad \text{at fixed } \tau_0, \tau_1, \tag{3.5.5}$$

where $\boldsymbol{v}^{(n)}$ and $\lambda^{(n)}$ are the eigenvectors and the eigenvalues, respectively for a given choice of τ_0 and τ_1 (in order to lighten the notation, we also omitted the indices A and B that appeared in eq. (2.4.32)). In this work we used $\tau_0 = a$ and $\tau_1 = 2a$. Among the basis composed by the eigenvectors $\boldsymbol{v}^{(n)}$, we choose the one whose corresponding eigenvalue is the biggest among the others. Let us denote this maximum eigenvector with $\boldsymbol{v}^{\max}$, which we use to define an *optimal* operator by rotating the original correlator-matrix

$$\mathcal{C}_{\text{opt}}(n_0, \tau_1, \tau_0) = \boldsymbol{v}_i^{\max *}\mathcal{C}^{ij}(n_0, \tau_1, \tau_0)\boldsymbol{v}_j^{\max}. \tag{3.5.6}$$

The ground state mass is extracted from the exponential decay at large time of this correlator.

4

RESULTS FOR YANG-MILLS THEORY AT LARGE-N_c

This Chapter is dedicated to the results we obtained from our simulations of Yang-Mills theory at large-N_c through TEK volume reduction, whose configurations were generated according to what is stated in Chapter 3.

In Sec. 4.1 we apply the Wilson flow technique to set the scale in our ensembles of configurations. We will study the systematic effects coming from lattice artifacts and finite-N_c.

In Sec. 4.2 we use the Wilson flow scales calculated in the previous sections and confront them with the ones obtained from the string tension from previous results. Since our ensembles span many different gauge couplings also to values close to the region where perturbation theory can be applied, we will use the corresponding scales to attempt an extrapolation of the Λ-parameter of Yang-Mills theory in the large-N_c limit exploiting asymptotic scaling.

In Sec. 4.3 we discuss the computation of the chiral condensate of Yang-Mills theory in the large-N_c limit. We will use two different methodologies, one coming from the dependence of the pion mass on the fermion mass and the other from the analysis of the low modes of the Dirac spectrum.

4.1 $N_f = 0$: THE SCALE OF YANG-MILLS THEORY AT LARGE-N_c

In this section, we apply the methodology explained in the previous Chapter to the ensembles of configurations we have for the case of pure Yang-Mills theory $N_f = 0$. We will start by analyzing the effect of the norm correction on lattice artifacts and finite-size effects.

The first step is to integrate the Wilson flow equations and apply the norm correction to obtain the improved flow function $\hat{\Phi}_L(T, b, N_c)$ as in Eq. (3.4.19) and then extract the scales T_0 and T_1. We recall that we define as $\hat{\Phi}_L(T, b, N_c)$ the integrated flowed energy density whose definition can be found in Eq. (3.4.19). The improvement of the flow through the norm corrections is thought to treat simultaneously lattice artifacts and finite-volume effects. Since we have at our disposal several values of the gauge coupling b and N_c we can study how our method works to reduce the aforementioned systematic effects. We recall also that the norm correction is expected to work within a window determined on the low side by lattice artifacts and on the upper one by finite volume effects.

To illustrate the role of lattice artifacts, we select the cases of $(N_c = 289, b = 0.36)$ and $(N_c = 841, b = 0.38)$. This choice is driven by

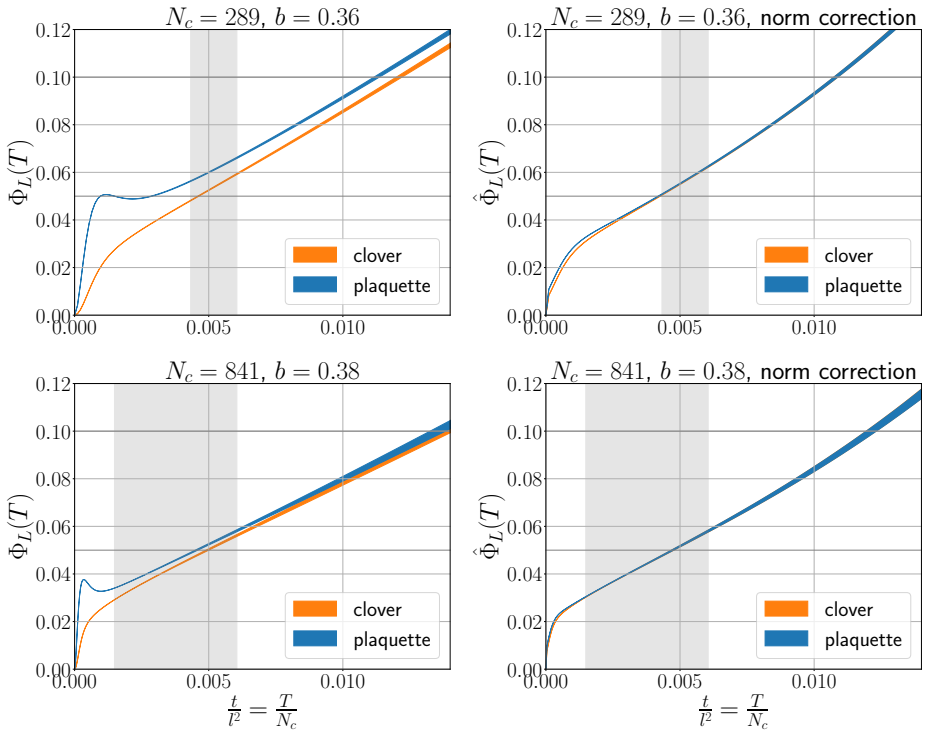

Figure 3: Flowed energy density at $b = 0.36$ for $N_c = 289$ (upper panels) and $N_c = 841$ (lower panels) before (left-hand panels) and after (right-hand panels) the norm correction as in Eq. (3.4.19). Different colors correspond to different discretizations of $\Phi(T)$ on the lattice ("clover" refers to Eq. (3.4.8)). The reference scale $s_1 = 0.05$ and $s_0 = 0.1$ are represented as horizontal grey lines and the scaling window $[1.25, \gamma^2 N_c/8]$ (with $\gamma = 0.22$) is represented as a vertical grey band. The value of the physical volume in units of $\sqrt{8t_1}$ is approximately the same for the two (b, N_c) values showed, as indicated in the text.

the observation that the effective volume $l^4 = (a\sqrt{N_c})^4$ in the two cases is approximately the same ($\sqrt{N_c}/\sqrt{8t_1} \simeq 5.424(13)$ and $5.143(25)$, respectively). In such a case the two curves should display similar finite volume/N_c effects at large flow time, while the curve at $b = 0.38$ should be less affected by lattice artifacts at small T since this value of b corresponds to our finest lattice. To compare these two cases directly, we plot in Fig. 3 the respective flowed energy densities as functions of $\frac{T}{N_c} = \frac{t}{l^2}$. In the same plot, we display the scaling window as a vertical colored band. By looking at the plot we can make several observations. In the left-hand panels we show the uncorrected flowed energy density $\Phi_L(T)$ using two different choices for the lattice version of the flowed energy density: the simple plaquette and the clover from Eq. (3.4.8). The clover discretization is better behaved in the region of small T, where we expect the effect of lattice artifacts to be more sizeable. The plaquette discretization shows indeed a small

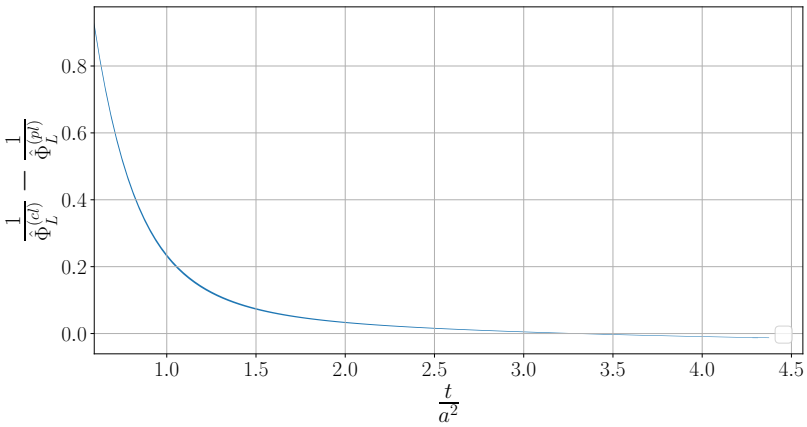

Figure 4: Difference between the (inverse of the) of plaquette and clover flow after the norm correction.

"bump" which in the case of $N_c = 289$ induces a large systematic uncertainty in the direct determination of the corresponding $\sqrt{8T_1}$. The same behavior is present also in the finer lattice at $b = 0.38$, but does not influence the determination of the scale, as expected. On the other hand, this systematic effect is completely absent in the clover flow, as the curve shows a monotonous behavior. An additional effect captured by the different discretizations of $\Phi(T)$ is a relative horizontal shift between the plaquette and the clover curve, which can be also attributed to the effects of lattice artifacts. In the right-hand panels of Fig. 3, we repeat the same plot but after the application of the norm correction as in Eq. (3.4.19). Note that the norm correction factor changes depending on the lattice discretization of the energy density: the norm associated with the clover is given by Eq. (3.4.16), while the one for the plaquette by Eq.(3.4.18). As it is evident, the norm correction gets rid of the bump in the plaquette flow and makes the clover and the plaquette flow overlap almost completely above the lower end of the scaling window. In Fig. 4 we depict the difference between the inverse of the plaquette and the clover flow after the application of the norm correction. The difference grows sizeably big in the region of small flow times, signaling additional lattice artifacts effects. For better visualization, in Fig. 5 we depict for $N_c = 289$, $b = 0.36$ and $N_c.841$ $b = 0.38$ the flowed energy density before and after the application of the norm correction, making the flow $\Phi_L(T)$ and its corrected version $\hat{\Phi}_L(T)$ to overlap. The additional conclusion we make from this plot is that the norm correction induces a horizontal shift of the curves, which we are going to analyze in the following.

The other systematic effect we target is the one produced by finite-N_c. In Fig. 6, we illustrate the effect of the norm correction for several values of N_c (13^2, 17^2, 19^2, 23^2, 25^2, 29^2) in the case $b = 0.37$. In the left-hand panel of Fig. 6 we display the flow curves before the applica-

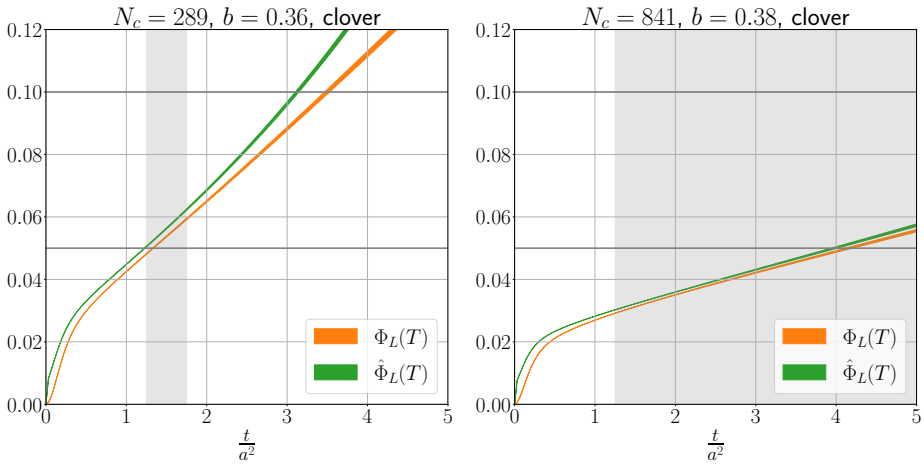

Figure 5: Effect of the norm correction to the flowed energy density in the case of $b = 0.36$ for $N_c = 289$ and $N_c = 841$ for the clover flow. The reference scale $s_1 = 0.05$ and $s_0 = 0.1$ are represented as horizontal grey lines and the scaling window $[1.25, \gamma^{2N_c}/8]$ (with $\gamma = 0.22$) is represented as a vertical grey bands.

tion of the norm correction, and the two reference scales $s_0 = 0.1$ and $s_1 = 0.05$ depicted with corresponding horizontal grey lines. As it is evident from the magnification in the plot, each curve corresponding to a different N_c intersects the line corresponding to s_1 at a different value of the lattice flow time T. The values of the scales $\sqrt{8T_1}$ are 4.847(74), 4.464(22), 4.393(29), 4.367(21), 4.359(17), 4.328(13), ordered for all the values of N_c quoted previously. In the right-hand panel, we apply the norm correction to the flowed energy densities for each value of N_c and we depict the results of the right-hand side of Fig. 6. The corresponding value of $\sqrt{8T_1}$ are 4.134(29), 4.222(17), 4.222(24), 4.251(19), 4.257(16), 4.240(12). In the plot, each different color corresponds to a different N_c and the different scaling windows are represented as colored vertical bands. It is visible to the eye that inside each scaling window all the different flow curves collapse, indicating that the norm corrections effectively remove finite-N_c effects within the region described by Eq. (3.4.20).

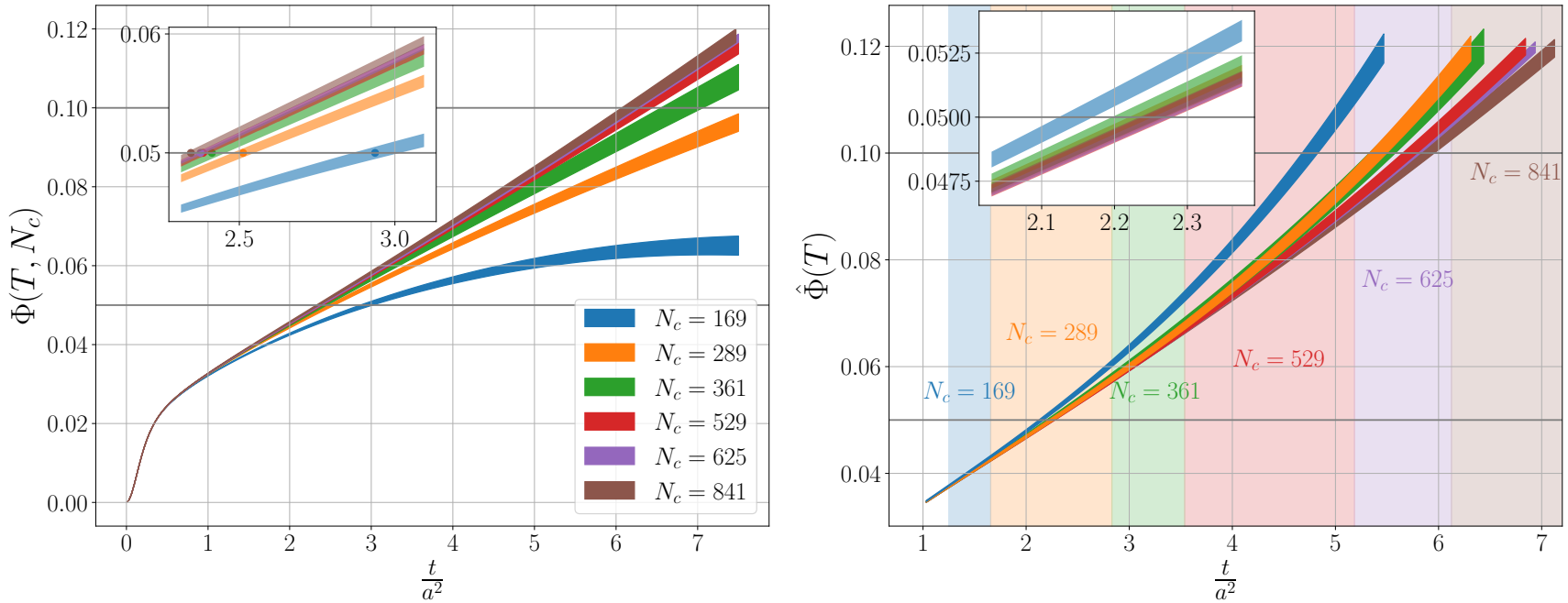

Figure 6: Left-hand side: Flowed dimensionless energy density $\Phi(b, N_c)$ (c.f. Eq. (3.4.9)) for pure Yang-Mills for different numbers of colors at $b = 0.37$. Right-hand side: Same flow curves with the norm correction applied, c.f. Eq. (3.4.19). The scaling windows in Eq. (3.4.20) with $\gamma = 0.28$ are represented with a vertical stripe of the same color as the flow curve they are associated with. They all start at $T = 1.25$ but in the region where two window overlaps, it is only depicted the ones with the smallest N_c.

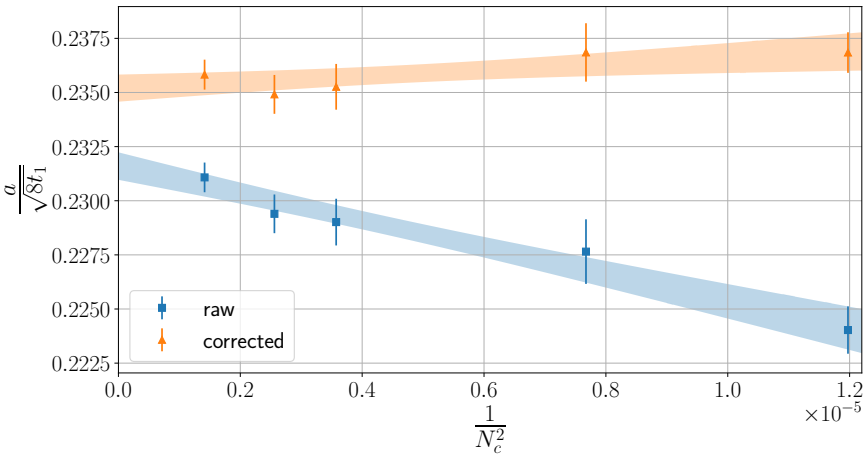

Figure 7: N_c dependence at $b = 0.37$ of the lattice scales $\sqrt{8T_1}$ extracted from the clover flowed energy density before ("raw") and after ("corrected") the application of the norm correction. The plot shows a linear extrapolation to the large-N_c limit of both cases. The values of the scales before the application of the norm corrections are reported in the text, while the ones after are in Tab. 7.

Nevertheless, it is interesting to compare the results obtained with and without the norm correction. In Fig. 7 we display the lattice scales $\frac{a}{\sqrt{8t_1}}$ determined in both cases ("raw" and "corrected" in the caption) as a function of $1/N_c^2$ and we perform a linear extrapolation to the limit of large-N_c. We first observe that the N_c dependence is milder for the norm-corrected scales, which are compatible with a constant value. Although both linear extrapolations have a good χ^2/dof (~ 0.2 in both cases), the extrapolated values do not coincide.

To explore this in more detail, we analyzed how this discrepancy varies with the values of b. Let us call with $T_1^{\text{raw}}(b)$ the value of T_1 extracted from the clover flow without the norm correction and then linearly extrapolated in $1/N_c^2$ to the limit $N_c \to \infty$ as in Fig. 7. By calling $T_1(b)$ the extrapolated value of the clover flow after applying the norm correction, we can define the ratio $R(b) = \frac{a_{\text{corr}}(b)}{a_{\text{raw}}(b)} = \sqrt{\frac{T_1^{\text{raw}}(b)}{T_1(b)}}$. In Fig. 8 we plot the number $R(b)$ as a function of the lattice spacing calculated as $\frac{a}{\sqrt{8T_1}}$ leaving out the case of $b > 0.37$ for which we do not have enough values of N_c to perform a large-N_c extrapolation. As one can see from the plot, the number $R(b)$ extrapolates to 1 within errors in the continuum limit, confirming that the discrepancy we observed is an effect due to lattice artifacts. Although the values of $T_1(b)$ are obtained through a large-N_c extrapolation, a constant fit gives almost always a good χ^2 as the dependence on N_c is efficiently captured and neutralized by the norm correction. Moreover, the extrapolated values are always compatible with the values $T_1(b, N_c = 841)$ and therefore in the following we will always use

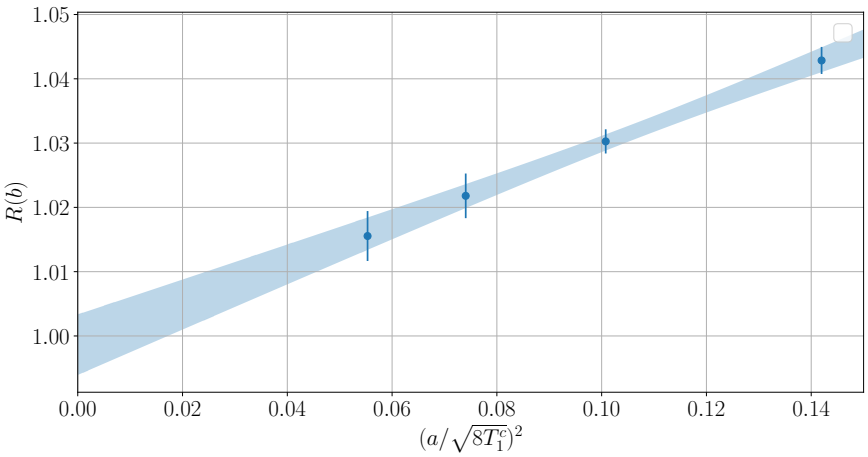

Figure 8: Extrapolation of $R(b) = \sqrt{T_1^{raw}(b)/T_1^{corr}(b)}$ to the continuum limit. The lattice spacing in the x-axes is expressed in units of T_1^{corr}.

them to fix the scale. All the values of T_1 obtained after applying the norm corrections are reported in Tab. 7.

4.1.1 *Outside the window*

One important issue that we have to address is the choice of the upper limit of the scaling window, set to $T_{max} = \gamma^2 \frac{N}{8}$. We remind that, as commented in Sec.3.4.1 of Chapter 3, the physical parameter that governs finite volume effects is $c(T) = \sqrt{\frac{8T}{N_c}}$, i.e. the fraction of the effective length occupied by the flow smearing range. In order to give a quantitative prescription, we have to analyze the behavior of the norm correction. In Fig. 9, we plot the correction factor of the flow (subtracted by 1), for different values of N_c versus the parameter c. At small values of c, the differences between the corrections factor are associated with lattice artifacts effects, which for fixed physical volume $l = a\sqrt{N_c}$ are given in terms of $l/\sqrt{N_c}$. As the parameter c grows, the effect of the norm correction tends to be the same, irrespective of the value of N_c. We also notice that the correction grows rapidly as one goes beyond the region having $c \sim 0.3$, indicating that finite volume corrections are expected to be severe. In Fig. 10, we display the relative difference between the norm-corrected clover flows for $N_c = 841$ and $N_c = 169$, corresponding to the biggest and smallest effective lattice volume, respectively. This helps to identify the region in T in which the corrections treat effectively finite-N_c effects: as one can see from the plot, choosing $\gamma \sim 0.22$ ensures that the relative difference is of the order of a few percent.

An important observation is that for the majority of the cases (except for $N_c = 169$) the scale selected at the reference value $s_1 = 0.05$ falls before the upper limit of the scaling window $T_{max} = \gamma^2 \frac{N_c}{8}$ with

b	(N_c, k)	$\frac{\sqrt{8t_1}}{a}$	$\frac{\sqrt{8t_1}}{a}$ (g. fit)	$\frac{\sqrt{8t_0}}{a}$	$\frac{\sqrt{8t_0}}{a}$ (g. fit)
0.35	(841, 9)	2.1819(23)	2.2014(43)(78)	3.5932(62)	3.578(68)(35)
0.355	$(169,5)^{\dagger}$	2.6243(89)	–	4.154(19)	–
	$(289,5)^{\dagger}$	2.6451(44)	2.6511(53)(54)	4.2784(94)	4.31(1)(65)
	$(361,7)^{\dagger}$	2.6513(44)	2.6697(56)(59)	4.334(10)	4.3393(90)(37)
	(529, 7)	2.6504(37)	2.6693(66)(76)	4.34(11)	4.339(11)(1)
	(841, 9)	2.6533(44)	2.6803(82)(74)	4.359(14)	4.356(13)(1)
0.36	$(169,5)^{*,\dagger}$	3.093(11)	–	4.800(24)	–
	$(289,5)^{\dagger}$	3.1341(77)	3.1333(83)(14)	4.999(17)	5.09(1)(77)
	$(361,7)^{\dagger}$	3.1384(96)	3.139(11)(2)	5.044(20)	5.102(2)(12)
	$(529,7)^{\dagger}$	3.1377(43)	3.1401(64)(50)	5.094(12)	5.104(11)(8)
	(625, 4)	3.1558(62)	3.1637(89)(68)	5.141(16)	5.142(15)(5)
	(841, 9)	3.1492(47)	3.1610(68)(87)	5.138(12)	5.138(12)(1)
0.365	$(169,5)^{*,\dagger}$	3.577(19)	–	5.410(39)	–
	$(289,5)^{\dagger}$	3.678(12)	3.67876(93)(86)	5.777(28)	5.98(2)(90)
	$(361,7)^{\dagger}$	3.649(13)	3.6486(6)(36)	5.769(28)	5.930(21)(23)
	$(529,7)^{\dagger}$	3.663(11)	3.655(13)(3)	5.868(26)	5.940(21)(19)
	$(625,4)^{\dagger}$	3.6801(97)	3.676(11)(3)	5.938(24)	5.975(19)(15)
	(841, 9)	3.682(14)	3.684(23)(8)	5.986(43)	5.988(39)(6)
0.37	$(169,5)^{*,\dagger}$	4.134(29)	–	6.150(52)	–
	$(289,5)^{*,\dagger}$	4.222(17)	4.2322(37)(56)	6.529(37)	6.88(2)(100)
	$(361,7)^{*,\dagger}$	4.222(24)	4.2345(35)(57)	6.598(66)	6.883(25)(30)
	$(529,7)^{\dagger}$	4.251(19)	4.247(18)(2)	6.762(50)	6.903(30)(24)
	$(625,4)^{\dagger}$	4.257(16)	4.251(16)(2)	6.798(35)	6.910(26)(23)
	$(841,9)^{\dagger}$	4.240(12)	4.231(15)(2)	6.837(36)	6.877(26)(20)
0.375	$(625,4)^{\dagger}$	4.854(30)	4.862(22)(8)	7.621(75)	7.902(39)(36)
	$(841,9)^{\dagger}$	4.853(16)	4.849(16)(5)	7.761(38)	7.881(26)(30)
0.38	$(625,4)^{*,\dagger}$	5.508(44)	5.558(7)(16)	8.52(12)	9.034(47)(52)
	$(841,9)^{\dagger}$	5.639(27)	5.618(19)(3)	9.03(07)	9.131(31)(26)
0.385	$(841,9)^{\dagger}$	6.311(59)	6.342(26)(13)	9.84(14)	10.307(42)(51)

Table 7: List of Wilson flow scales for TEK model for each value of (N_c, b). Those ensembles whose scale T_0 (after norm correction) falls at the right of the scaling window with $\gamma = 0.22$ are marked with an $\dagger$, while the same cases for T_1 are marked with a $*$. The scales in the 3^{rd} and 5^{th} columns are extracted by simple interpolation, and errors are evaluated with the Γ method. The scales in the 4^{th} and 6^{th} columns are extracted with the global fit procedure, the first reported error is statistical, the second in systematical.

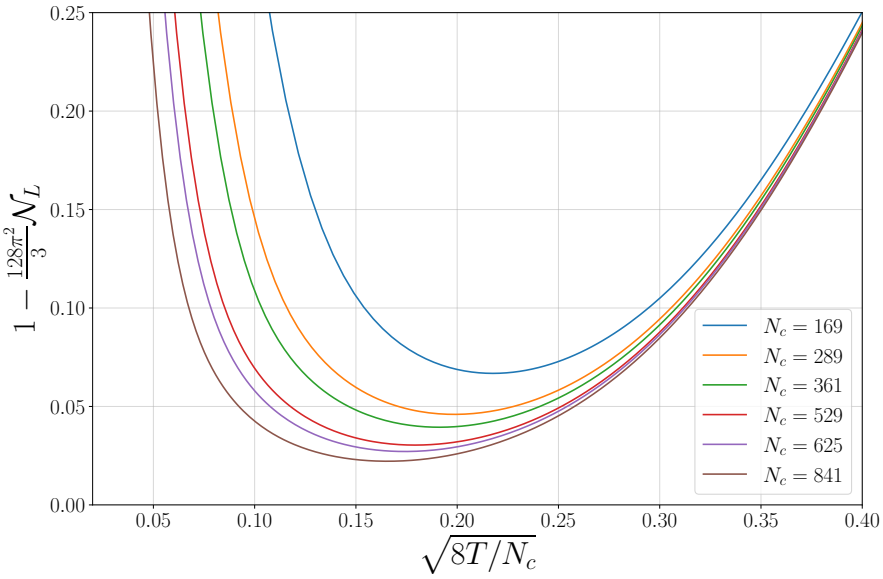

Figure 9: Norm correction of the clover flow subtracted by 1 versus the parameter $c(T) = \sqrt{8T/N_c}$ indicating the portion of the effective size occupied by the flowed smearing region.

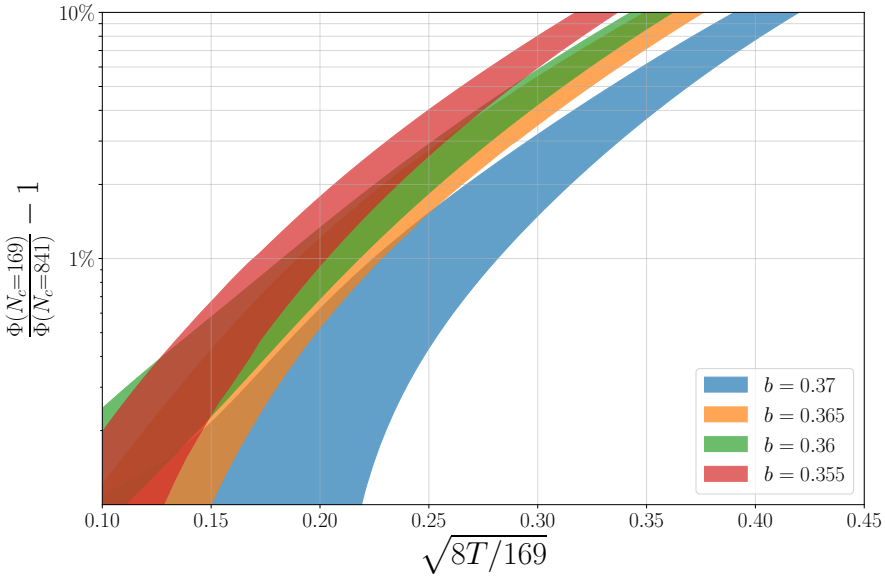

Figure 10: Relative difference between the corrected flow for the biggest ($N_c = 841$) and the smallest effective volume ($N_c = 169$) for different values of b in logarithmic scale.

$\gamma = 0.22$, therefore $\sqrt{8T_1}$ can be safely estimated through an interpolation. This is not generally true for $s_0 = 0.1$, which falls out of the scaling windows (except for $N_c = 841$ for some b values), and therefore can suffer from systematic effects coming from finite-volume/N_c corrections. Conversely, the flow curve may intersect the reference value at a value of $T < 1.25$. This is also a case in which the scale falls outside the scaling window, although the systematic effect felt in this case is due to lattice artifacts. In both cases, the scale should not be extracted by interpolating the curve, but rather by fitting it inside the scaling window and then extrapolating (backward or forward) the values at the reference scale. In Tab. 7, we indicate which ensembles have a T_1 or T_0 falling outside the scaling window and for which, in principle, one would need to extrapolate. We will detail below how to handle these cases.

We make use of a parameterization of the flow-time dependence which relies on the connection between the infinite volume flow and the gradient flow renormalized coupling constant λ_{gf}, c.f. Eq. (3.4.7). Starting from the renormalization group equation defining the β function and integrating it between two different reference scales t_s and t one arrives at:

$$\int_{\lambda_{gf}(t_s)}^{\lambda_{gf}(t)} \frac{dx}{\beta(x)} = \frac{1}{2} \log\left(\frac{t_s}{t}\right). \tag{4.1.1}$$

The left-hand side of this equation can be easily integrated in our range of couplings using the following parameterization of the β-function:

$$\beta(\lambda_{gf}) = -\frac{b_0 \lambda_{gf}^2}{1 - \sum_{k=0}^{n_b} a_k \lambda_{gf}^{k+1}}, \tag{4.1.2}$$

with coefficients chosen to reproduce the universal expansion of the β-function to second order in λ_{gf}, given by

$$\beta(\lambda_{gf}) = -b_0 \lambda_{gf}^2 - b_1 \lambda_{gf}^3 + \mathcal{O}\left(\lambda_{gf}^4\right), \tag{4.1.3}$$

where

$$b_0 = \frac{1}{(4\pi)^2} \frac{11 - 4N_f}{3} \tag{4.1.4a}$$

$$b_1 = \frac{1}{(4\pi)^4} \frac{34 - 32N_f}{3}. \tag{4.1.4b}$$

where a_0 is set to b_1/b_0 and we allowed for a generic number of flavors N_f. For the time being, we will set $N_f = 0$, although the same method can be trivially extended to the case of dynamical fermions by allowing the global function to be a function of $T/T_s(b, N_c, \kappa_{adj})$ and considering the appropriate N_f factor in Eq. (4.1.4). The advantage of using such a parameterization is that it constrains the small-time

behavior of the flow to the expected one in PT and the large-time flow to those given by "safe" interpolations. After integration, one arrives at the following equation

$$\frac{b_0}{2}\log\frac{t}{t_s} = -\left(\frac{1}{\lambda_{gf}(t)} - \frac{1}{\lambda_{gf}(t_s)}\right) + \\ - a_0 \log\left(\frac{\lambda_{gf}(t)}{\lambda_{gf}(t_s)}\right) - \sum_{k=1}^{n_b} \frac{a_k}{k}\left(\lambda_{gf}^k(t) - \lambda_{gf}^k(t_s)\right), \quad (4.1.5)$$

which can be used to fit the numerical results for the flow, leaving as free parameters the non-universal coefficients of the β-function and the t_s scale.[1] To be more specific about the procedure, we recall that the flow and the gradient flow coupling in the continuum differ for a multiplicative factor $\lambda_{gf}(t) = \Phi_\infty(t)/\mathcal{K}(\infty)$. According to Eq. (4.1.5), we can define a function $\hat{H}$ as

$$\hat{H}(T) = \frac{b_0}{2}\log T_s - \mathcal{K}(\infty)\left(\frac{1}{\hat{\Phi}(T)} - \frac{1}{s}\right) + \\ - a_0 \log\left(\frac{\hat{\Phi}(T)}{s}\right) - \sum_{k=1}^{n_b} \frac{a_k}{k\mathcal{K}(\infty)^k}\left(\hat{\Phi}(T)^k - s^k\right), \quad (4.1.6)$$

which is a function of the flow $\hat{\Phi}$ and of some free coefficients $\{a_k\}$ and one free parameter T_s for each b and N_c, $\hat{H}\left(\hat{\Phi}(T);\{a_k\},T_s\right)$. We thus extract the scale and the parameters by minimizing the following cost function

$$\chi^2(T_s,\{a_k\}) = \sum_T \left(\frac{\hat{H}\left(\hat{\Phi}(T);\{a_k\},T_s\right) - \frac{b_0}{2}\log T}{\delta H}\right)^2, \quad (4.1.7)$$

where δH is the uncertainty on H, linearly propagated from the one on $\hat{\Phi}$:

$$\delta H = \frac{dH}{d\hat{\Phi}}\sigma_\Phi = \left(\frac{\mathcal{K}(\infty)}{\hat{\Phi}^2} - \frac{a_0}{\hat{\Phi}}\right)\sigma_\Phi, \quad (4.1.8)$$

where σ_Φ identifies the Monte-Carlo error we calculated on the flow Φ.

Let us apply now this procedure to our data. First of all, we test our methodology by applying this global fit procedure to extract T_1 and compare it to the values we obtained before. To obtain good χ^2/dof in the global fit, we adopt the following choices: we consider a scaling window of $[1.25, 0.22^2\frac{N_c}{8}]$, we exclude the case of $N_c = 169$, and fit the curves in the region where $\hat{\Phi}_L < 0.11$. As previously mentioned we fit together all the curves with different b and N_c and allow T_s to depend on both these parameters. In the fourth column of Tab. 7, we

1 An analogous procedure can be found in [113] where it is used to parameterize the step scaling function.

b	$a\sqrt{\sigma}$	$\frac{a}{\sqrt{8t_1}}$
0.355	0.2410(30)	0.37689(62)
0.360	0.2058(25)	0.31754(47)
0.365	0.1784(17)	0.2716(10)
0.370	0.1573(19)	0.23582(69)
0.375	0.1361(17)	0.20605(69)
0.380	0.1191(17)	0.17734(86)
0.385	0.1049(11)	0.1584(15)

Table 8: Lattice scale in units of the string tension (taken from [108]) and the Wilson flow improved scale.

report the values of $\sqrt{8T_1}$ obtained following this methodology. We also associate a systematic error calculated as the dispersion of the results of the global fit by varying the number of free coefficients in the β-function expansion, and the limit of the scaling window. We observe that the values we obtain are perfectly compatible with the ones obtained through interpolation, also for some of those few cases whose interpolated T_1 fell right above the upper end of the the scaling window with 0.22. This is a confirmation of the fact that, although needed to have a good fit, $\gamma = 0.22$ is a somewhat "strict" parameter and for T_1 a global fit is not needed. Given this compatibility, we proceed to apply the procedure to extract the values of $\sqrt{8T_0}$. We perform again the same global fit procedure, this time using $s_0 = 0.1$ as a reference value, and we report the values in Tab. 7.

4.2 TESTING (ASYMPTOTIC) SCALING AT LARGE-N_c

In this section, we are going to confront the lattice scale extracted in the previous section with the one extracted in units of the string tension $\sqrt{\sigma}$ obtained from a previous determination. In particular, we will refer to [108] in which the authors extract the string tension of Yang-Mills theory in the large-N_c limit, by using Creutz ratios method introduced in Sec. 3.4.1.2 of Chapter 3. In Tab. 8, we report the values of the lattice spacing in units of the string tension taken from [108] and the Wilson flow improved scale and their dimensionless ratio $R = \sqrt{\sigma}\sqrt{8t_1}$. In Fig. 11, we depict each value of the ratio as a function of $(a/\sqrt{8t_1})^2$. A simple fit to a constant gives the value of 0.6566(78) with a $\chi^2/\#\text{dof} = 1.6$, mainly spoiled by the value at the coarsest point. Nevertheless, we notice that a linear fit in $(a/\sqrt{8t_1})^2$ gives an extrapolated value of 0.6742(83) with a $\chi^2/\#\text{dof} = 0.24$ may accounts better for scaling violations. As a final value, we will consider 0.674(8)(18) where the systematical error is the dispersion between the two previously obtained values. This comparison with the

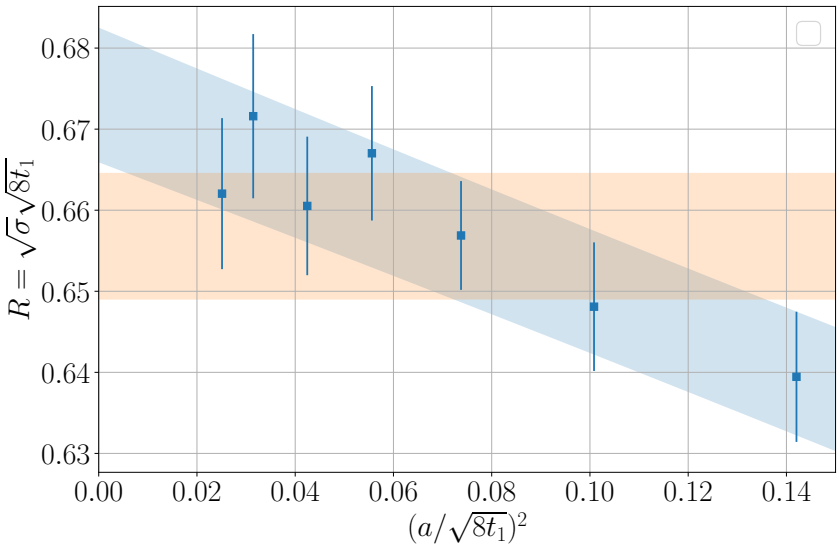

Figure 11: Ratio of the string tension on the lattice and the Wilson flow scale for each value of the gauge coupling b. The horizontal band corresponds to the fit to a constant, giving the value of $0.6566(78)$, while the linear fit gives a value of $0.6742(83)$ for the extrapolated value.

string tension is a remarkable confirmation of the validity of scaling for a wide range of 't Hooft couplings which gets small violations in the case of the coarsest ensembles. Furthermore, our new determination of the scale has smaller errors than the one previously extracted using the string tension.

In the next subsection, we will exploit this feature to extract the Λ-parameter of the Yang-Mills theory in the large-N_c limit. We recall that what is going to be presented in the next sections is the result of a preliminary analysis, and there is ongoing work that is not included. The final results will be presented in a future publication.

4.2.1 *The Λ-parameter*

As already mentioned in Sec. 1.2.3.3 of Chapter 1, in a generic renormalization scheme labeled with s, the Renormalization Group (RG) equation for the bare coupling dependence on the cutoff scale a reads

$$\beta_s(\lambda_s) = -\frac{d\lambda_s}{d\log a^2}\,, \tag{4.2.1}$$

which, upon integration, leads to

$$a\Lambda_s = (b_0\lambda(a))^{-\frac{b_1}{2b_0^2}} e^{-\frac{1}{2b_0\lambda(a)}} \times \\ \times e^{-\int^{\lambda(a)} dx \left(\frac{1}{2\beta(x)} + \frac{1}{2b_0 x^2} - \frac{b_1}{2b_0^2 x}\right)} \tag{4.2.2}$$

where Λ_s is the integration constant which is scheme-dependent. We recall that Eq. (4.2.2) is an exact integral of the first-order differential RG equation and the equal sign holds when the integral is performed with the exact β-function. On the other hand, it is well-known that the β-function has the following perturbative expansion around $\lambda_s \sim 0$

$$\beta(\lambda_s) \sim -b_0\lambda_s^2 + b_1\lambda_s^3 + b_2^{(s)}\lambda_s^4 + \mathcal{O}(\lambda_s^5)\,, \tag{4.2.3}$$

where b_0 and b_1 are known to be universal (scheme independent) and in a pure Yang-Mills theory they amount to[2]

$$b_0 = \frac{11}{3(4\pi)^2} \approx 0.02321943791803574 \tag{4.2.5}$$

$$b_1 = \frac{34}{3(4\pi)^4} \approx 0.0004544835894000 8786\,, \tag{4.2.6}$$

while higher-order coefficients are known to be dependent on the scheme chosen. In the $\overline{\text{MS}}$-scheme the second coefficient is given by [114]

$$b_2^{\overline{\text{MS}}} = \frac{1}{(4\pi)^6}\frac{2857}{54} \approx 0.000013435607137976756\,. \tag{4.2.7}$$

On the lattice using the Wilson action, the coefficient in the large-N_c limit is given by [115, 116]

$$b_2^{w} \approxeq b_2^{\overline{\text{MS}}} + 0.16995599 b_1 - 0.0079101185 b_0 \approx -0.00009299069\,, \tag{4.2.8}$$

which will be referred to as the "Wilson scheme". Using a fully perturbative β-function truncated at $\mathcal{O}(\lambda^3)$, we can easily calculate the coefficient of the linear term of the expansion of the integral. In terms of the Wilson flow scale $\sqrt{8t_1}$, we obtain the following formula

$$-\log\frac{a}{\sqrt{8t_1}} = \log\Lambda_s\sqrt{8t_1} + \frac{1}{2b_0\lambda_s(a)} + \\ + \frac{b_1}{2b_0^2}\log(b_0\lambda_s(a)) + \frac{c_1^{(s)}}{2b_0}\lambda_s(a) + \mathcal{O}(\lambda_s^2)\,, \tag{4.2.9}$$

2 We are giving our definitions using the 't Hooft coupling $\lambda \equiv g^2 N_c$, since we are interested in the large-N_c limit of Yang-Mills theories. Although in the literature it is more common to use g^2 to define the β-function, the formulas we are going to review here are easily generalizable. The coefficients of the standard $\beta(g^2)$ are typically indicated with the Greek letters β_i. The conversion between the two definitions reads

$$b_i = \frac{\beta_i}{N_c^{i+1}}\,. \tag{4.2.4}$$

where the coefficient of the linear term is given by

$$c_1^{(s)} = \frac{b_2^{(s)}}{b_0} - \frac{b_1^2}{b_0^2}\,, \tag{4.2.10}$$

and is scheme dependent, as well as the Λ-parameter itself.

On the lattice, several approaches can be followed to calculate the Λ-parameter. Among the different possible schemes, we recall that the twisted gradient flow we analyzed in detail in Sec. 3.4.1 of Chapter 3, provides a well-defined scheme for the coupling. One possible approach is to combine twisted BC with standard step-scaling techniques which allows one to fix the energy scale $\mu = (\sqrt{8t})^1$ and link it to the inverse of the physical size of the effective lattice $\tilde{l}$ as $\tilde{l} = (c\mu)^{-1}$, being c a parameter that is usually chosen to be 0.3. By confronting the results of simulations of several values of $\tilde{l}$, one can run the coupling to match the lattice results to perturbation theory. This is the line followed by [71, 117], in which twisted gradient flow on an extended lattice with twisted BC is combined with step-scaling techniques to determine the Λ-parameter in $SU(3)$ Yang-Mills theory.[3]

Another possible approach is the one whose philosophy follows the one in [108, 118], which we are going to briefly review here.

Given a change in the coupling

$$\lambda' = \lambda_s(1 + \gamma_1\lambda_s + \gamma_2\lambda_s^2) + \mathcal{O}\left(\lambda_s^4\right), \tag{4.2.11}$$

we can easily relate the definition of the scheme dependent quantities (the Λ-parameter and $c_1^{(s)}$) with a one-loop calculation as

$$\frac{\Lambda'}{\Lambda_s} = e^{\frac{\gamma_1}{2b_0}} \tag{4.2.12}$$

$$c_1' = c_1 + \gamma_1^2 - \gamma_2 + \frac{b_1}{2b_0}\gamma_1\,. \tag{4.2.13}$$

which allows us to confront different schemes. The coupling scheme we have direct access to is the lattice one given by the Wilson action $\lambda_w \equiv 1/b$, which is known to have large higher-order perturbative corrections. In fact, the ratio between the Wilson's and the $\overline{\text{MS}}$ scheme is known to be [70, 119]

$$\frac{\Lambda_{\overline{\text{MS}}}}{\Lambda_w} = 38.853\,. \tag{4.2.14}$$

Nonetheless, this is to be expected: in the range of b in which typical lattice simulations are performed, it is well known that asymptotic scaling has large corrections when using the naive Wilson coupling constant. However, it is well known that adopting a different "improved" definition of the coupling as in Eq. (4.2.11) can mitigate the problem of large higher-order correction and improve the convergence with perturbation theory. In the following, we give three differ-

3 In [71], the physical size of the lattice is set to $\tilde{l} = a\sqrt{N_c}$.

symbol	definition	$\frac{\Lambda_w}{\Lambda'}$	c_1
λ_w	$\frac{1}{b}$	1	-0.00438798235
λ_I	$\frac{\lambda_w}{P(\lambda_w)}$	0.0677656398	-0.00172791
λ_E	$8(1-P(\lambda_w))$	0.4148791463	-0.0005030
$\lambda_{E'}$	$-8\log P(\lambda_w)$	0.1080025976	-0.00042426

Table 9: Possible definitions for the gauge coupling on the lattice.

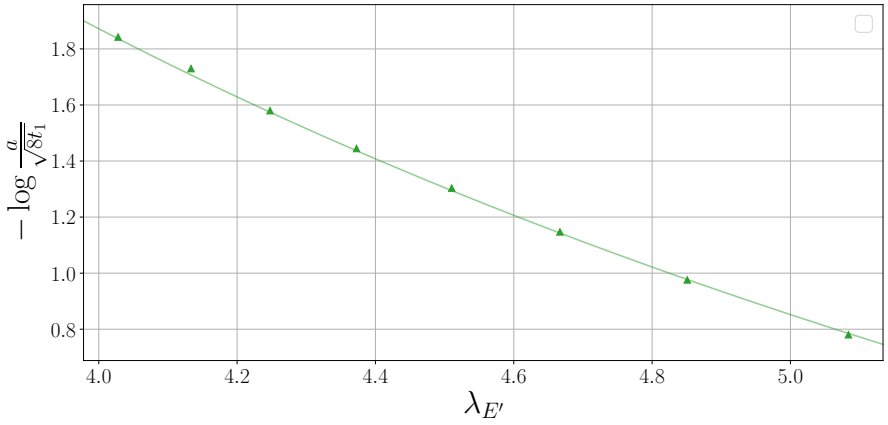

Figure 12: Logartihm of the lattice spacing in units of the Wilson flow scale $\sqrt{8t_1}$ listed in 8 as a function of the improved coupling $\lambda_{E'}$ defined in Tab. 9. The green line is the result of a fit to Eq. (4.2.9).

ent possibilities that will be adopted: λ_I (from [118]), λ_E (from [120, 121]) and $\lambda_{E'}$. We report their definition in Tab. 9. All of them rely on the usage of the plaquette, which in the case of TEK action is known to $\mathcal{O}(\lambda_w^3)$ in PT [52]

$$P(\lambda_w) = 1 - \omega_1\lambda_w - \omega_2\lambda_w^2 - \omega_3\lambda_w^3\,, \tag{4.2.15}$$

where $\omega_1 = 1/8$, $\omega_2 \approx 0.0051069297$ and $\omega_3 \approx 0.00079425$. By employing these three different improved couplings, in the following, we proceed with the extraction of the corresponding Λ-parameter.

Having at our disposal such a large range of values for the 't Hooft coupling we can explore non-perturbatively a region close to the weak coupling limit. To illustrate the effectiveness of the usage of the improved couplings, in Fig. 12 we depict the logarithm of the lattice spacings in units of $\sqrt{8t_1}$ as a function of $\lambda_{E'}$ and a fit of Eq. (4.2.9) leaving the Λ-parameter term free. Although when looking at the plot the accordance with theoretical prediction is quite striking, the direct fit of Eq. (4.2.9) to our data does not give a good χ^2. This is to be expected, given the small size of the error and the large range of values of the coupling covered by our data.

4.2.1.1 *Λ-parameter of Yang-Mills theory at large-N_c*

As explained in the previous subsection, the goal is to determine the Λ-parameter in the $\overline{\text{MS}}$ scheme in units of the improved Wilson flow scale $\sqrt{8t_1}$ by exploiting asymptotic scaling. The main formula is Eq. (4.2.9), which dictates the dependence of the lattice spacing on the 't Hooft coupling in units of $\sqrt{8t_1}$ in a given renormalization scheme. Scaling implies that we can define the Λ-parameter in the $\overline{\text{MS}}$ scheme in the continuum as

$$\Lambda_{\overline{\text{MS}}}\sqrt{8t_1} = \lim_{\lambda_s\to 0} \frac{\Lambda_{\overline{\text{MS}}}}{\Lambda_s} f_s(\lambda_s)\sqrt{8T_1}\,, \tag{4.2.16}$$

where we defined

$$f_s(\lambda_s) = e^{-\left(\frac{1}{2b_0\lambda_s}+\frac{c_1^{(s)}}{2b_0}\lambda_s\right)}(b_0\lambda_s)^{-\frac{b_1}{2b_0^2}} \tag{4.2.17}$$

from Eq. (4.2.9) and the ratio between the corresponding Λ-parameters is known by taking the product

$$\frac{\Lambda_{\overline{\text{MS}}}}{\Lambda_s} \equiv \frac{\Lambda_{\overline{\text{MS}}}}{\Lambda_w}\frac{\Lambda_w}{\Lambda_s}\,, \tag{4.2.18}$$

where the separate factors can be calculated from Eq. (4.2.14) and Eq. (4.2.12).

We depict in Fig. 13 the calculated values of $\Lambda_{\overline{\text{MS}}}$ in units of $\sqrt{8t_1}$ at fixed lattice spacing. We observe that the point corresponding to $b = 0.38$ is unexpectedly displaced. For this value of the coupling, the flowed energy density suffers from large autocorrelation time which might bias the central value of the distribution. For the sake of visualization, we depict in Fig. 14 the Monte-Carlo history of T_1, and the relative histogram. The origin of this large autocorrelation is yet to be explored and analyzed, although it is similar to what is observed in other similar works in the literature [122, 123]. For the moment, we exclude this point from the following analysis. A more complete treatment of this behavior will be issued in a future publication. We perform a quadratic extrapolation to $a/\sqrt{8t_1} = 0$ for each one of the improved couplings, excluding the one at $b = 0.38$, obtaining good reduced χ^2, reported in the caption of Fig. (13). The extrapolated value of $\Lambda_{\overline{\text{MS}}}$ in units of $\sqrt{8t_1}$ are 0.3682(47), 0.3620(46) and 0.3652(47) for λ_I, λ_E and $\lambda_{E'}$, respectively. We also notice that the extrapolated values do not change significantly if we also include the point at $b = 0.38$, although the χ^2 grows bigger. To quote a final estimate of the Λ-parameter for the Yang-Mills theory at large-N_c in the $\overline{\text{MS}}$ scheme, we give the mean values between the previous results and assign the dispersion as a systematical error. We report the final value in units of $\sqrt{8t_1}$ and of $\sqrt{\sigma}$[4]

$$\Lambda_{\overline{\text{MS}}} = 0.3618(47)(29)\left(\sqrt{8t_1}\right)^{-1} = 0.5366(94)(120)\sqrt{\sigma}\,, \tag{4.2.19}$$

4 We convert the result using the dimensionless ratio $R = \sqrt{8t_1}\sqrt{\sigma} = 0.674(8)(12)$ we previously found.

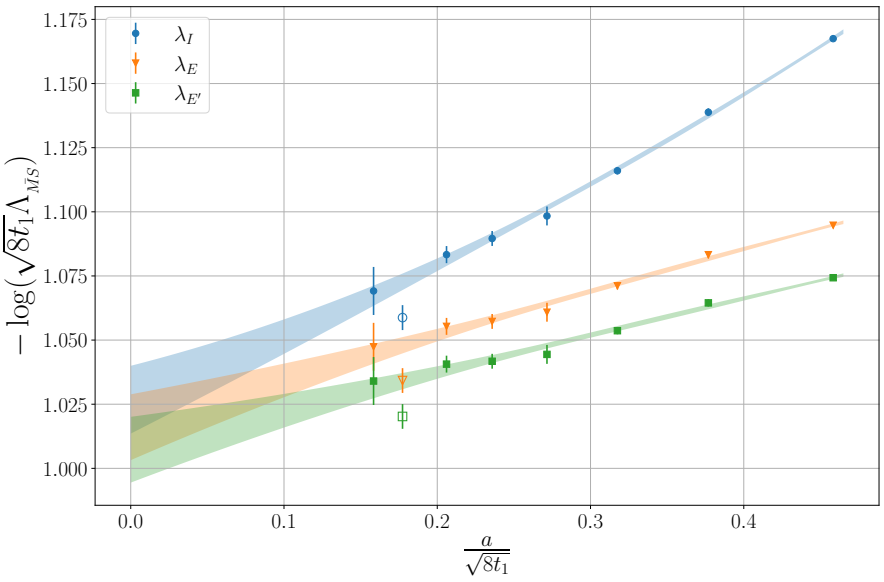

Figure 13: (Logarithm of the) Λ-parameter in the $\overline{\text{MS}}$ scheme in units of $\sqrt{8t_1}$ versus the lattice spacing in the same units using three different improved couplings in Tab. 9. We also depict the corresponding quadratic continuum extrapolations. In the fit, we excluded the point corresponding to $b = 0.38$ (whose points are depicted with an empty marker), obtaining $\chi^2/\#\text{dof} = 0.49, 0.61, 0.62$ for λ_I, λ_E and $\lambda_{E'}$, respectively.

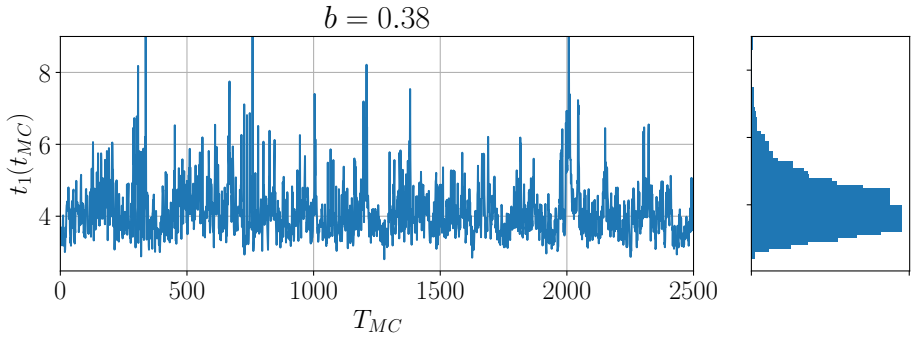

Figure 14: Monte-Carlo history of the value at which the flowed energy density at $N_c = 841$, $b = 0.38$ crosses $s = 0.05$ and relative histogram.

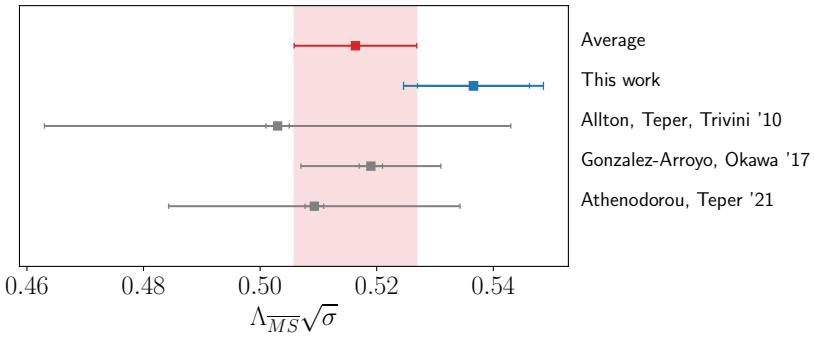

Figure 15: Values of $\Lambda_{\overline{\text{MS}}}$ present in the literature compared. The red band represents a weighted average.

where the systematical error is a sum in quadrature between the systematical uncertainty on Λ and the one on R. which results to be in accordance with the large-N_c value $0.503(2)(40)\sqrt{\sigma}$ in [118] and with the result $0.525(2)$ in the TEK model from [108] and also with the number of $0.5093(15)(250)$ given in [124]. To collect and compare visually all these results we plot all the values in Fig. 15 in a FLAG-style plot.

4.3 THE CHIRAL CONDENSATE OF YANG-MILLS THEORY AT LARGE-N_c

In this section, we present the result concerning the extraction of the chiral condensate for fermions in the fundamental representation. As mentioned in Sec. 1.1.2.1 of Chapter 1, the fermion condensate is the order parameter of the spontaneous breaking of chiral symmetry in the vacuum. Under the assumption that this mechanism survives the large-N_c limit, our goal is to perform a quantitative calculation of the chiral condensate in Yang-Mills at large-N_c. We recall that in the large-N_c limit, fundamental fermions are naturally quenched and thus pure gauge configurations can be directly employed and no additional computational cost, excluding the ones needed to compute fermionic observables. Although a computation of the chiral condensate has never been attempted in the TEK model, a lot of effort has been put into computing the meson spectrum in the large-N_c limit in [75], where the authors also provide the data of a large number of observables at several values of b and N_c. We will follow two different strategies to compute the chiral condensate in our setup. The first one, presented in Sec. 4.3.1 makes use of the GMOR relation on the lattice, i. e. the dependence of the pion mass on the renormalized fermion mass that can be read directly from [75] at no additional computing cost. The second one, presented in Sec. 4.3.2, is based on the study of the spectral density of the Dirac operator following the

Banks-Casher relation for which we will need to perform an explicit computation of the eigenspectrum of the Dirac operator.

The material presented in this Section has to be intended as a preliminary analysis that will be presented in a future publication.

4.3.1 *The condensate from the GMOR relation*

The first methodology makes use of the Gell-Mann-Oakes-Renner relation (cfr. Eq. (1.1.38)), which states that in the continuum the squared pion mass m_π^2 is equal to the renormalized fermion mass m_r multiplied by a combination of the renormalized chiral condensate Σ_r and the pion decay constant f_π,

$$m_\pi^2 = \frac{2\Sigma_r}{f_\pi^2} m_r \,. \tag{4.3.1}$$

As mentioned in the introduction of this section, we can use the data provided in [75] for $N_c = 289$ and 4 different values of b. More specifically, when dealing with pion spectroscopy, the authors provide data for the slope (divided by $\sqrt{\sigma}$) of the relation between the pion mass squared in units of the string tension versus the bare subtracted quark mass $(m_\pi/\sqrt{\sigma})^2 \propto (2\kappa)^{-1}$. We can compare this formula to the GMOR relation, by dividing both sides of Eq. (4.3.1) for $\sqrt{\sigma}^2$ and expressing the renormalized pion mass in terms of the subtracted mass m_q, defined through

$$m_q = \frac{1}{a}\left(\frac{1}{2\kappa} - \frac{1}{2\kappa_c}\right) = Z_S m_r \,. \tag{4.3.2}$$

We thus obtain the relation

$$\frac{\text{slope}}{\sqrt{\sigma}} = \frac{2\Sigma_R}{Z_S f_\pi^2 \sqrt{\sigma}} \,, \tag{4.3.3}$$

whose corresponding numbers are reported in [75] for several values of b and N_c. To extract a value for the condensate, we need to have the values of the pion decay constant f_π and the renormalization factor Z_S. The pion decay constant is given in terms of the matrix element of the axial current A_μ between the vacuum and the pion states and, given its scaling in color as $\sqrt{N_c}$, it can be defined to coincide with the $N_c = 3$ case as

$$F_\pi \equiv \sqrt{\frac{3}{N_c m_\pi^2}} \langle 0|A_0(0)|\pi; \mathbf{p} = 0\rangle = \sqrt{\frac{3}{N_c}} f_\pi \,. \tag{4.3.4}$$

In [75], the calculation of F_π is tackled from several measurements, including a separate calculation using twisted mass Wilson fermions to have a determination independent of the normalization factor Z_A. The final result is given by a fit to the general formula

$$F(m_\pi) + B(m_\pi) e^{-Cl\sqrt{\sigma}} \,, \tag{4.3.5}$$

where the functions F and B are well described by second degree polynomials in m_π and $l = a\sqrt{N_c}$. $F(m_\pi)$ gives the estimate of the pion decay constant at infinite volume and infinite N_c. We are interested in the limit of zero pion mass, as the GMOR relation describes the behavior of the pion mass in the chiral limit, given by

$$\frac{f_\pi}{\sqrt{N_c}\sqrt{\sigma}} = \frac{0.232(6)}{\sqrt{3}}\,. \tag{4.3.6}$$

This value has to be intended in the continuum limit, therefore it will be used just as an overall numerical factor. The last missing ingredient would be the explicit value of the renormalization factor Z_S, which is known to be a cumbersome quantity to calculate on the lattice. On the other hand, we have direct access to the ratio Z_P/Z_S, derived from the ratio $Z_P/Z_S Z_A$ (i. e. the slope of m_{pcac} versus the bare quark mass) and Z_A, obtained by confronting the different determinations of F_π. Combining Eq. (4.3.3) and Eq. (4.3.6) we obtain a definition of the chiral condensate (divided by N_c) and in units of the renormalization factor Z_P

$$\frac{\Sigma_r}{N_c Z_P} = \frac{1}{2}\left(\frac{0.232(6)}{\sqrt{3}}\right)^2\left(\frac{\text{slope}}{\sqrt{\sigma}}\right)\frac{Z_S}{Z_P}(\sqrt{\sigma})^3\,. \tag{4.3.7}$$

In Fig. 16 we depict the values of the condensate as in Eq. (4.3.7) versus the lattice spacing in units of $\sqrt{\sigma}$ converted to MeV through $\sqrt{\sigma} = 440$ MeV. A meaningful extrapolation of the chiral condensate to the continuum limit with the data in Fig. 16 would need the exact non-perturbative values of the renormalization constant $Z_P(a)$, which unfortunately are not available at the moment of the writing of this Section. For this reason, we will take the point with the finest lattice spacing as a result, which gives

$$\left(\frac{\Sigma_r}{Z_P N_c}\right)^{\frac{1}{3}} = 0.514(14)/\sqrt{\sigma} \quad \text{at } b = 0.37\,, \tag{4.3.8}$$

which, converted in MeV through $\sqrt{\sigma} = 440$ MeV, gives a value of 226(6) MeV.

4.3.2 *The chiral condensate from the Banks-Casher relation*

As mentioned in Sec. 1.1.2.1 of Chapter 1, one way to see the mechanism of spontaneous symmetry breaking is the condensation of the low-lying modes of the Dirac operator á-la Banks-Casher, whose relation states that the spectral density $\rho(\lambda)$ of the massless continuum theory has a non-vanishing value for the lowest mode in the thermodynamic limit, which is directly related to the quark condensate

$$\lim_{\lambda\to 0}\lim_{m\to 0}\lim_{V\to\infty}\rho(\lambda, m) = \frac{\Sigma}{\pi}\,, \tag{4.3.9}$$

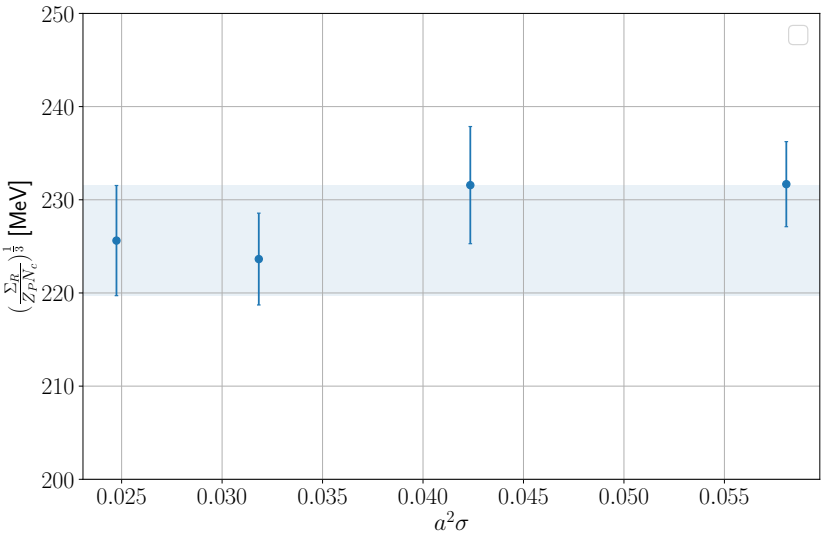

Figure 16: Chiral condensate from the GMOR relation in units of Z_P versus the squared lattice spacing in units of the string tension. The values of the condensate have been converted to MeV using the relation $\sqrt{\sigma} = 440$ MeV. The blue horizontal band represents the value of the point corresponding to the ensemble with the finest lattice spacing.

being Σ the quark condensate of the infinite-volume massless theory. We remind that λ are the eigenvalues of the Euclidean massless Dirac operator D and m is the quark mass. In the infinite volume limit, as found in [125] chiral perturbation theory dictates the behavior of the spectral density as a power series of the fermion mass (and the eigenvalue λ). The leading term in the expansion is given by the Banks-Casher formula, where the "effective condensate" reads

$$\Sigma = \frac{\pi}{2} \frac{\nu(M, m)}{\Lambda V}, \tag{4.3.10}$$

where $\nu(M, m)$ is the *mode number*, i. e. the average number of eigenmodes of the massive hermitian operator $D^\dagger D + m^2$ with eigenvalues $\alpha \leqslant M^2$,

$$\nu(M, m) = V \int_{-\Lambda}^{\Lambda} d\lambda \, \rho(\lambda, m), \quad \text{where } \Lambda = \sqrt{M^2 - m^2}\,. \tag{4.3.11}$$

At the next-to-leading order, the formula receives corrections directly proportional to the fermion mass.

The definitions that we gave of the quantities related to the mode number can be translated on the lattice once one is careful to correctly identify meaningful observables. As pioneered in [126], the mode number itself can be estimated through the average number $\langle \nu(M, m_q) \rangle$ of eigenmodes of the hermitian operator $D_w^\dagger D_w$ with

eigenvalue $\alpha \leqslant M^2$, where M^2 is a bare mass threshold. There are different methods one can adopt to evaluate the average mode number $\langle \nu \rangle$. A popular one employs the usage of *spectral projectors*: the eigenmodes of the Dirac operator with $\alpha \leqslant M^2$ are "filtered" through a projection operator, then the mode number is evaluated stochastically by a trace over the filtered subspace.[5] On the other hand, our approach is somewhat simpler. We proceed with the direct extraction of the 100 lowest magnitude eigenvalues Q_w using `ARPACK` routines for a sample of 100 configurations at $N_c = 289$ maximally spaced in MC time to minimize autocorrelations, for several values in the (b, κ) parameter space. By calling λ_Q the extracted eigenvalues, we define $\alpha \equiv (\frac{\lambda_Q}{2\kappa})^2$ which has the right naive continuum limit and thus can be considered the lattice version of the eigenvalue of the operator $D^\dagger D + m^2$.

To extract the mode number we perform the counting of eigenvalues in terms of renormalized quantities. We recall that the mass threshold, as well as the eigenvalues, renormalize as $M = Z_P M_r$ (or $\lambda = Z_P \lambda_r$), while the bare subtracted fermion mass $m_q = Z_S m_r$ can be expressed in terms of the PCAC mass m_{PCAC}. We can thus define the ratios

$$\frac{M_r}{m_r} = \frac{M}{Z_A m_{PCAC}}, \quad \frac{|\lambda_r|}{m_r} = \frac{\sqrt{\alpha}}{Z_A m_{PCAC}}, \tag{4.3.12}$$

where the PCAC masses and the renormalization factor Z_A can be directly taken from [75]. Nevertheless, it is worth noticing that, as formally demonstrated in in [126], the mode number is a RG invariant quantity, i. e. $\nu_r(M_r, m_r) = \nu(M, m_q)$ and thus can be calculated by counting the number of eigenstates having $\frac{|\lambda_r|}{m_r}$ below a certain threshold given in physical units i. e.

$$\nu_r(m_r, M_r) = \sum_{\frac{|\lambda_r|}{m_r} \leqslant \frac{M_r}{m_r}} 1 \,. \tag{4.3.13}$$

As predicted by chiral perturbation theory, the mode number shows a linear behavior starting from above the threshold region $M_r \simeq m_r$, from which we fit the slope. Given this linear behavior, following the methodology suggested in [126], we define the mass-dependent effective condensate as

$$\frac{\bar{\Sigma}}{N_c} = \frac{\pi}{2V} \sqrt{1 - \left(\frac{m_r}{M_r}\right)^2} \frac{\partial \nu_r(M_r, m_r)}{\partial M_R} \tag{4.3.14}$$

which coincides with the leading term of the condensate in chiral perturbation theory. We notice that the N_c factor in the effective condensate comes naturally from the definition of our Dirac operator. If

5 The original method was already employed in [126]. Later in the years, the same approach has been endowed with more efficient filtering operators [127–129].

we let fermions propagate in a $(\sqrt{N_c})^4$ box, the Dirac operator becomes block diagonal where each block gets repeated N_c times (cfr. Eq. (2.4.19)). Since we calculate the eigenvalues of one block, we automatically obtain the right multiplicity factor. We will repeat this procedure for several values of the lattice coupling and the fermion mass.

Since the Banks-Casher relation is a statement in the continuum and the chiral limit, to recover the value of the condensate through Eq. (4.3.14) we use the following procedure.

- We identify 3 lines of constant physics in the parameter space (b, κ), in which the pion mass in units of the string tension is approximately constant. For each one of the 4 values of the lattice spacing ($b = 0.355$, 0.36, 0.365, 0.370), we use the data in [75] to find the linear dependence of the pion mass squared on $1/2\kappa$. We then select 3 values of the pion mass squared in units of the string tension $m_\pi/\sqrt{\sigma} \simeq 1.05, 1.25, 1.563$ and use this dependence to extract at each b the values of κ corresponding to each one of the values of the fixed pion mass. Using the data provided in [75], we are also able to extract the dependence of m_{PCAC} on κ, which can be combined with Z_A to give $m_r Z_P \equiv Z_A m_{PCAC}$. We report the values of (b, κ) and the corresponding value of $Z_A m_{PCAC}$ in Tab. 10.

- We thus proceed to calculate the mode number for each value of (b, κ) in Tab. 10 by counting the number of eigenvalues as in Eq. (4.3.13), obtaining the value of the $\langle \nu_r \rangle$ as a function of M_r/m_r.

- We identify a linear region in the dependence $\langle \nu_r(M_r/m_r) \rangle$, we fit the following linear relation to our obtained data

$$\left\langle \nu_r\left(\frac{M_r}{m_r}\right)\right\rangle = p_0 + p_1 \frac{M_r}{m_r}$$

  We then use the slope p_1 and the relation between the PCAC mass and Z_A to calculate

$$\frac{p_1}{Z_A m_{PCAC}} = \frac{p_1}{Z_P m_r}$$

- We calculate the effective condensate as in Eq. (4.3.14) as

$$\frac{\bar{\Sigma}}{Z_P N_c} = \frac{\pi}{2V}\sqrt{1-\left(\frac{m_r}{M_r}\right)^2}\,\frac{p_1}{Z_P m_r}$$

  where in the square root factor we use the value m_r/M_r evaluated at the middle of the fitting interval.

b	κ	$Z_P m_r$	$\left(\frac{\bar{\Sigma}}{Z_P N_c}\right)^{\frac{1}{3}} \sqrt{8t_0}$
0.355	0.1600	0.03785(38)	0.6084(79)
0.360	0.1580	0.03055(52)	0.638(10)
0.365	0.1565	0.02279(43)	0.629(10)
0.370	0.1550	0.02045(63)	0.638(12)
0.355	0.1610	0.02426(33)	0.6061(70)
0.360	0.1588	0.01897(56)	0.6221(96)
0.365	0.1573	0.01069(53)	0.592(13)
0.370	0.1556	0.01085(58)	0.612(15)
0.355	0.1615	0.01752(34)	0.5976(69)
0.360	0.1592	0.01323(62)	0.595(16)
0.365	0.1576	0.00618(58)	0.587(22)
0.370	0.1559	0.00607(60)	0.608(23)

Table 10: Values of $Z_P m_r$ (calculated as $Z_A m_{PCAC}$) and the effective chiral condensate in units of Z_P at fixed b and κ obtained from the slope of the mode number on the mass threshold in units of $\sqrt{8t_0}$. Inside each horizontal block, the values of (b, κ) correspond to a fixed value of the pion mass in units of the string tension, respectively $1.05, 1.24, 1.57$.

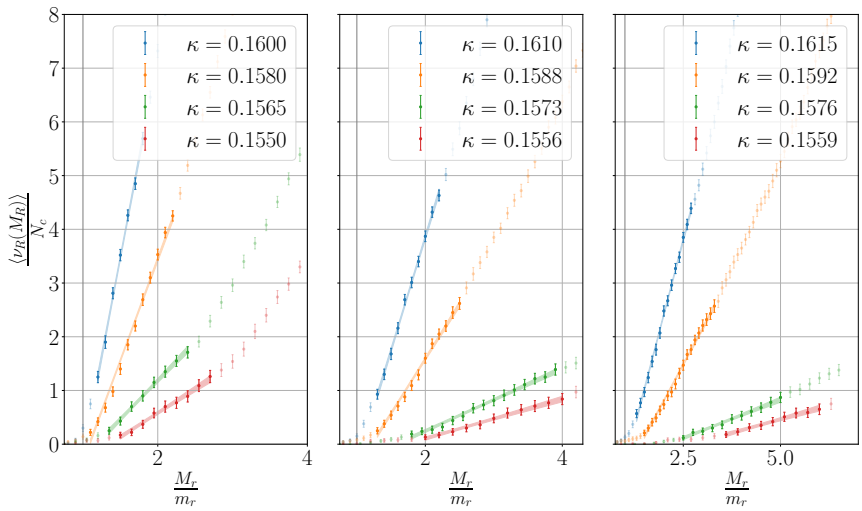

Figure 17: Renormalized mode number versus M_r/m_r for each value of (b, κ). The value of κ is reported in the caption, while the color reflects the value of b (blue, orange, green, red corresponding to $b = 0.355, 00.36, 0.365, 0.37$). Each panel contains the mode number calculated for values of (b, κ) having approximately a constant value of $m_\pi/\sqrt{\sigma} \simeq 1.05, 1.25, 1.563$, respectively. The solid points represent the one for which we performed a linear to extract the value of the effective condensate reported in Tab. 10

.

In Fig. 17 we depict the mode number as a function of the ratio M_r/m_r for every value of (b, κ) and we report the values of the effective condensate in Tab. 10 using $\sqrt{8t_0}$, whose values have been taken from the fifth column of Tab. 7 for $N_c = 841$.

The final value of the chiral condensate needs to be extrapolated first to the continuum limit and then to the chiral limit. Unfortunately, analogously to the last Section, we cannot perform a direct extrapolation to the continuum limit since the values of the renormalization constant Z_P are not available. Using the numbers we obtained at the finest lattice spacing, we can use the corresponding value of the condensate to take the chiral limit using the pion masses extracted from [75]. In Fig. 18 we depict the points corresponding to $b = 0.37$ and the linear extrapolation to the chiral limit. The final value we obtain is

$$\left(\frac{\Sigma_r}{Z_P N_c} \right)^{\frac{1}{3}} = 0.573(36)/\sqrt{8t_0}\,, \tag{4.3.15}$$

which results be compatible with the value of $0.546(15)/\sqrt{8t_0}$ we previously found in the last subsection from the GMOR relation, after the conversion factor $R = \sqrt{8t_0}\sigma = 1.0631(67)$ has been applied. For the sake of completeness, we report in Tab. 11 the values of the ex-

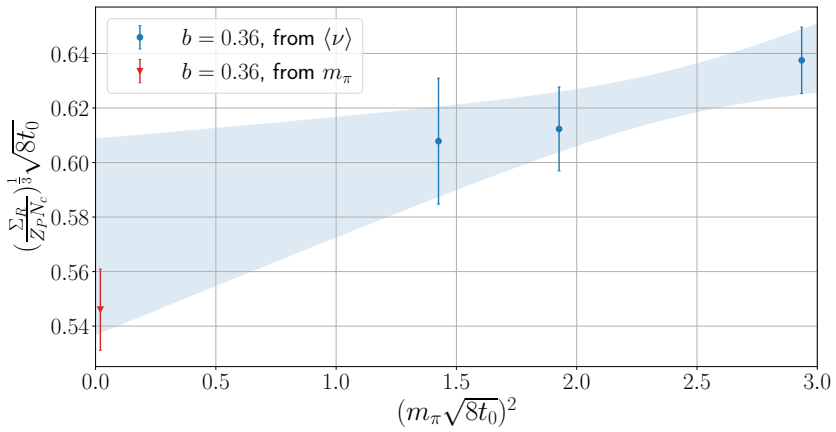

Figure 18: Chiral condensate in units of Z_P at $b = 0.37$ versus the pion mass squared in units of $\sqrt{8t_0}$. The blue band represents the result of the linear fit. The red point corresponds to the value in Eq. (4.3.8) converted in units of $\sqrt{8t_0}$ using the ratio $R = \sqrt{8t_0}\sigma = 1.0631(67)$.

b	$(\frac{\Sigma_R}{Z_P N_c})^{\frac{1}{3}}\sqrt{8t_0}$
0.355	0.591(13)
0.360	0.579(22)
0.365	0.549(26)
0.370	0.573(36)

Table 11: Values of the chiral condensate at large-N_c limit in units of $\sqrt{8t_0}$ extrapolated at zero pion mass at fixed lattice spacing.

trapolated condensate at zero pion mass for the other values of the lattice spacing.

The last point needed would be a comparison with other results in the literature. Unfortunately, this is not possible since our results, as well as the majority of those found in the literature, are calculated at a fixed value of the lattice spacings and do not take into account the value of a Z_P factor, which depend on the cut-off scale as well as the lattice action.

We just limit ourselves to quoting the references where other determinations of the chiral condensate have been performed. In [126], Giusti and Lüscher calculate a value of the condensate from the mode number for SU(3) and $N_f = 2$ configurations with $\mathcal{O}(a)$-improved fermions, obtaining a value of 191(4) MeV, after a trivial rescaling with $3^{\frac{1}{3}}$. Applying our conversion factor $R = \sqrt{8t_0}\sigma = 1.0631(67)$, the value we obtain is 0.4644(97). Another result in the literature comes from [130], whose lattice simulations are done with the Iwasaki action and $\mathcal{O}(a)$-improved Wilson fermions at generic values of N_c. Al-

though the authors do not directly give a value for the condensate, we can calculate it from the data related to the slope of the pion mass squared $\Sigma/(F_\pi^2 Z_P)$, for which they provide two numbers for the large-N_c quantity coming from two different fitting functions, an average of the two being $1.71(7)$ in lattice units. Since the value of the lattice spacing in $\sqrt{t_0}$ units as well as the one of F_π in physical units are also provided, we obtain a condensate of $0.585(25)$. As previously mentioned these numerical values cannot be directly compared with our result as they are obtained for a different lattice spacing, a different lattice discretization and they do not include Z_P. Nevertheless, we observe that all these values are in the same ballpark, which sounds extremely promising. A more precise comparison will be issued in a future publication.

5

RESULTS FOR YANG-MILLS THEORY COUPLED WITH $N_f = \frac{1}{2}$ ADJOINT FERMIONS

This Chapter is dedicated to the results we obtained for our simulations of a Yang-Mills theory coupled with adjoint dynamical fermions in the large-N_c limit. The majority of our results concerns the theory with one adjoint Majorana fermion ($N_f = \frac{1}{2}$), i. e. $\mathcal{N} = 1$ SUSY Yang-Mills (SYM), introduced in Sec. 1.1.3 and 1.2.2 of Chapter 1.

In Section 5.1 we will perform the scale setting of the $\mathcal{N} = 1$ SUSY theory using the Wilson flow techniques we developed in Chapter 4 for the case of pure Yang-Mills theory. The method corresponds to the application of the tree-level improved norm correction to the flow function, combined with the global fit procedure.

In Section 5.2 we perform scale setting using two additional definitions of the scale. The first one is related to quantities built from Wilson loops, while the second employs the fundamental light meson spectrum in the fundamental chiral limit. The compatibility of different results confirms the solidity of our results.

Section 5.3 is dedicated to the study of the supersymmetric limit of the theory. As explored in Sec. 1.2.2 of Chapter 1, the lattice discretization breaks SUSY, which is claimed to be restored to the limit in which the physical mass of the gluino vanishes. We will explore this limit by studying the PCAC mass and the low-lying spectrum of the Dirac operator.

Once the scale has been extracted and we define a meaningful way to perform a limit to the supersymmetric theory, in Section 5.4 we test our results for the scale extrapolated to the vanishing gluino mass against theoretical prediction for the bare β-function.

Finally, Section 5.5 is dedicated to the scale setting of the theory with $N_f = 1, 2$, using the Wilson flow improved methodology. Having at our disposal ensembles at several values κ_{adj}, we can explore the dependence of the scale on the adjoint fermion mass.

5.1 THE WILSON FLOW SCALE

As a reminder of Sec. 3.2.1 of Chapter 3, we generated gauge configurations with one dynamical gluino for a large number of values of the parameter (b, κ_{adj}). A summary can be found in Tab. 3 and Tab. 4.

The procedure to extract the scale consists of the application of the norm correction as in Eq. (3.4.19) and the global fit procedure. We also remind the reader that, unlike the case of pure gauge configurations, the scale now acquires a dependence on the gluino mass. We simulta-

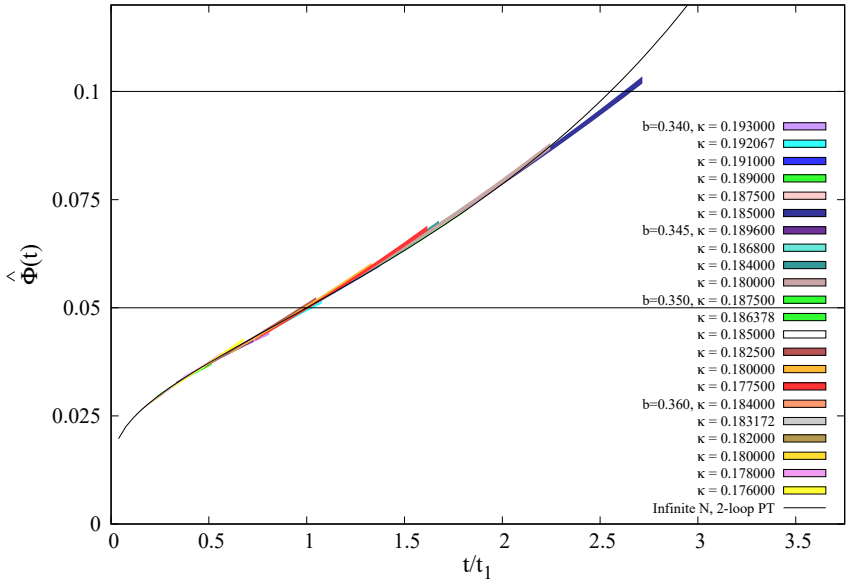

Figure 19: We display $\hat{\Phi}(t)$ as a function of t/t_1 for all our datasets with $N_c = 289$. The width of the colored bands indicates the error in the different quantities. The black line on the plot corresponds to the two-loop infinite N_c (infinite volume) perturbative prediction for the flow-time dependence of $\hat{\Phi}(t)$.

neously fit our data to a single universal curve whose only argument is $T/T_1(b, N_c, \kappa_{adj})$. Our combined data covers a window that runs from the perturbative small flow-time region up to values around T_0. In playing this game we are neglecting violations of universality that may come from lattice artifacts, remnant finite size effects or dependence of the flow on the gluino mass. As we will see below, these assumptions are well satisfied by our results. To serve the purpose of illustrating how well universality holds, we display in Fig. 19 the dependence of $\hat{\Phi}(T)$ on T/T_1 for $N_c = 289$. The different data displayed in the plot correspond to different values of b and κ_{adj} restricted to the scaling window Eq. (3.4.20) with $\gamma = 0.28$. The values of T_1 have been obtained from a universal fit to the data as the one described by Eq. (4.1.5) with three parameters of the β-function, in addition to the two universal ones corresponding to $\mathcal{N} = 1$ Supersymmetric Yang-Mills, and gives a χ^2/dof per degree of freedom of 1.2 (we obtain $\chi^2/dof = 3.1$ for the datasets with $N_c = 361$). As becomes evident from the plot, the advantage of the joint fit is that it allows constraining the time dependence of the flow in a region of scales much larger than the actual fitting window and permits to determine T_1 even when it falls outside it. Finally, we also display for comparison the prediction

of two loop perturbation theory at infinite N_c, given by the black line in the plot, which describes quite well our results in a large window of flow times.

We now present our results. To have an additional check on the effective reduction of finite N_c effects, we have fitted separately the $N_c = 289$ and 361 data sets, obtaining compatible results within errors. Our final values for T_1 are given in Tab. 15, the first quoted error is statistical and the second systematic. The latter is determined to cover various determinations of the scale corresponding to different fitting functions and ranges.

We end this section by discussing the relation of the scale t_1 to those more common in the literature, such as t_0 or w_0. We have already mentioned that in most of our simulations, t_0 falls out of the scaling window. Nevertheless, and under the assumption of scaling, we can use the universal fitting functional describing the flow to obtain a determination of the ratio $R = \sqrt{\frac{T_0}{T_1}}$. The result is $R = 1.624(50)$ and $R = 1.631(70)$ for $N_c = 361$ and 289 respectively. This is in perfect agreement with the ratios obtained in the few cases where we can determine T_0 directly by interpolation. The error quoted in all cases covers the systematics in the fitting functional and fitting ranges following the same procedure used to determine t_1.

Finally, we have also determined the scales w_1 and w_0 derived by solving the implicit equation Eq. (3.4.4) with $s = 0.05$ and $s = 0.1$ respectively. The strategy to determine these scales is very similar to the one used for t_1. We rely on the universality of the flow and fit $t\frac{d\hat{\phi}(t)}{dt}$ as a function of t/a^2 simultaneously for all our datasets within the scaling window corresponding to $\gamma = 0.28$. In this case, we use a degree-two polynomial fit, with the systematic error obtained by varying the fitting range. The resulting scales can be compared to t_1. Excluding the sets at $b = 0.36$, which have very large systematic errors and give nevertheless results consistent within errors, and restricting to a region "safe" from finite-volume effects,[1] a fit of the dimensionless ratio of scales to a constant gives $w_1/\sqrt{8t_1} = 0.4535(49)$ and $w_0/\sqrt{8t_1} = 0.586(10)$ with χ^2 per degree of freedom equal to 0.24 and 0.15 respectively.

We collect our final results for the ratio of $\sqrt{8t_0}$, w_0 and w_1 to $\sqrt{8t_1}$ in Tab. 12. These ratios can be used to convert all the results given in this section, in particular, the values of the lattice spacing as a function of the bare coupling and gluino mass, to the other more standard units used in the literature.

1 To determine such a region, we rely on the PCAC mass m_{pcac} we defined in Chapter 1 from Eq. (1.2.37), and select those ensemble having $m_{pcac}\sqrt{8t_1} > 0.3$. Further details on the computation of m_{pcac} will be given in the next Section.

$\sqrt{\frac{t_0}{t_1}}$	$\frac{w_1}{\sqrt{8t_1}}$	$\frac{w_0}{\sqrt{8t_1}}$
1.627(50)	0.4535(49)	0.586(10)

Table 12: Different scales determined from the flow expressed in units of $\sqrt{8t_1}$. Scales $t_1(t_0)$ and $w_1(w_0)$ are derived respectively from Eq. (3.4.4) setting $s = 0.05(0.1)$.

b	κ_{adj}	$\frac{\sqrt{8t_1}}{a}(N_c = 289)$	$\frac{\sqrt{8t_1}}{a}(N_c = 361)$
0.34	0.185	2.878(2)(46)	2.883(2)(58)
	0.1875	3.209(3)(68)	3.188(3)(90)
	0.189	3.514(3)(65)	3.488(3)(88)
	0.191	4.049(4)(37)	4.042(4)(58)
	0.192067	4.568(6)(58)	–
	0.193	5.273(7)(161)	5.244(8)(175)
0.345	0.18	3.166(3)(74)	3.145(2)(93)
	0.184	3.664(4)(77)	3.645(3)(98)
	0.1868	4.294(5)(40)	4.274(5)(55)
	0.1896	5.559(8)(154)	5.614(8)(201)
0.35	0.1775	3.730(3)(97)	3.737(3)(105)
	0.18	4.109(4)(75)	4.003(7)(109)
	0.1825	4.634(6)(70)	4.516(5)(64)
	0.1850	5.364(8)(144)	5.323(7)(65)
	0.186378	5.909(9)(192)	–
	0.1875	6.608(11)(249)	6.582(12)(287)
0.36	0.1760	5.77(1)(32)	–
	0.1780	6.32(1)(31)	–
	0.18	7.05(1)(31)	–
	0.1820	7.85(2)(35)	–
	0.183172	8.68(2)(44)	–
	0.184	9.16(2)(52)	–

Table 13: Values of the inverse lattice spacing for $N_f = \frac{1}{2}$ in units of the Wilson flow scale T_1, the first error is statistical, and the second is systematic.

5.2 OTHER DETERMINATIONS OF THE SCALE $N_f = \frac{1}{2}$

The case of $N_f = \frac{1}{2}$ has to be analyzed with special care. The list of the ensembles we generated is vast and very fine in the region of light gluino masses. Having ensembles in this region was crucial to have good control over the extrapolation of the lattice scale in the supersymmetric limit in Sec. 5.3. In this region, the effect of finite-N_c effects are particularly evident, especially when considering the ensembles for the finest lattice spacing at $b = 0.36$. For this reason, following [78], we are going to perform scale setting with other two methods.

The first, a variant of which has been already used in large-N_c pure Yang-Mills theory [108], is analogous to the Sommer scale but involves Wilson loops of fixed aspect ratio. The advantage of this is that the extrapolation to asymptotically large times needed to compute the quark-antiquark potential is no longer required.

The third method involves the usage of the spectra of mesons made of quarks in the fundamental representation to set the scale. In the large-N_c limit, fundamental fermion loops are suppressed and the quenched approximation is exact. The computation of the meson spectrum can therefore be determined at no additional cost on our set of dynamical adjoint fermion configurations. These meson masses depend on an additional scale, which is the fundamental quark mass, but in the zero mass limit this dependence disappears and the mass of the lightest non-singlet vector meson becomes a natural scale for SUSY Yang-Mills.

Finally, we will compare the three different determinations of the scale. We emphasize that the methods presented in the following subsections can also be used at finite N_c and for other gauge theories and are particularly well-suited when finite size effects are an important source of concern.

5.2.1 *The scale from Wilson loops*

This scale setting procedure was spelled out in Sec. 3.4.1.2 in Chapter 3. As a reminder, we recall that it is based on Creutz rations, which on the lattice can be defined as

$$\chi(R, R') = -\log \frac{W(R+0.5, R'+0.5)W(R-0.5, R'-0.5)}{W(R+0.5, R'-0.5)W(R-0.5, R'+0.5)}\,, \quad (5.2.1)$$

where $W(R, L)$ are the lattice Wilson loop evalutated for a rectangle of size $r \times l$, being $r = aR$ and $l = aL$. Creutz ratios can be used to define the following lattice quantity

$$G_L(R) \equiv R^2 \chi(R, R)\,, \quad (5.2.2)$$

which continuum limit has been spelled out in Eq. 3.4.28. In order to practically treat Wilson loops, which are known to be noisy quanti-

ties, we employ a smeared version $\hat{G}_L(R;s)$, in which Wilson loops are calculated on configurations on which the Wilson flow has been integrated up to flow time s.

Having defined the lattice observables to be used, we will now describe the process leading to the determination of the lattice spacing in units of $\bar{r}(f_0,s)$, c.f. eq. (3.4.25).

- For each configuration of our simulation parameters (b, κ_{adj}, N_c) we evolve the lattice link variables using the same discretized flow that was explained earlier.

- At each flow time T we compute the Wilson loops and Creutz ratios for $R = R' = 1.5, 2.5, 3.5, 4.5$ and 5.5, and determine from them the corresponding value of $\hat{G}_L(R;s)$ and its error by averaging over configurations having the same simulation parameters.

- We investigated the N_c dependence of these values for those cases in which we have at least two values of N_c. As expected the sensitivity depends on the quantity $R/\sqrt{N_c}$ giving the ratio of the loop size to the effective lattice size. This is indeed what happens when computing these quantities in perturbation theory at finite volume. To keep the finite volume correction smaller than $1-2\%$, one should set $R/\sqrt{N_c} \leqslant 0.25$. Our largest value of $R_{max} = 5.5$ gives ratios of 0.29, 0.32 and 0.49 for $N_c = 361, 289$ and 169 respectively, which are larger than 0.25. Indeed, for $\hat{G}_L(5.5;s)$ the difference between the value at $N_c = 289$ and $N_c = 361$ can reach up to 10%. Thus, to process the results we first extrapolate to $N_c = \infty$ using the $N = 289$ and 361 data and assuming a $1/N_c^2$ dependence as predicted by perturbation theory for large enough N_c. In practice, this limits our determination of the scale to the cases in which there is $N = 361$ data available.

- To extract the value of $a/\bar{r}(f_0,s)$ one should deal with two additional issues. The first is that the values of r obtained on the lattice are multiples of the lattice spacing. Determining the value $\bar{r}$ at which $\hat{G}(\bar{r};s) = f_0$ must be done by interpolation. The second is that $\hat{G}_L$ differs from the continuum function $\hat{G}$ by terms of order a^2 as described in Eq. (3.4.28). One can deal with both issues simultaneously by a method that gives a more robust determination of the scale. It involves a simultaneous fit to all our data points with $2.5 \leqslant R \leqslant 5.5$ by a function

$$G_L(R,s) = \alpha\left(\frac{R}{\bar{R}}\right)^2 + 2\gamma + 4\left(\frac{\bar{R}}{R}\right)^2\left(\frac{f_0-\alpha-2\gamma}{4} + \frac{\delta}{\bar{R}^2}\right), \quad (5.2.3)$$

  where α, γ and δ only depend on the value of s and f_0, and $1/\bar{R} = a(b,\kappa_{adj})/\bar{r}(f_0,s)$ expresses the lattice spacing in $\bar{r}(f_0,s)$

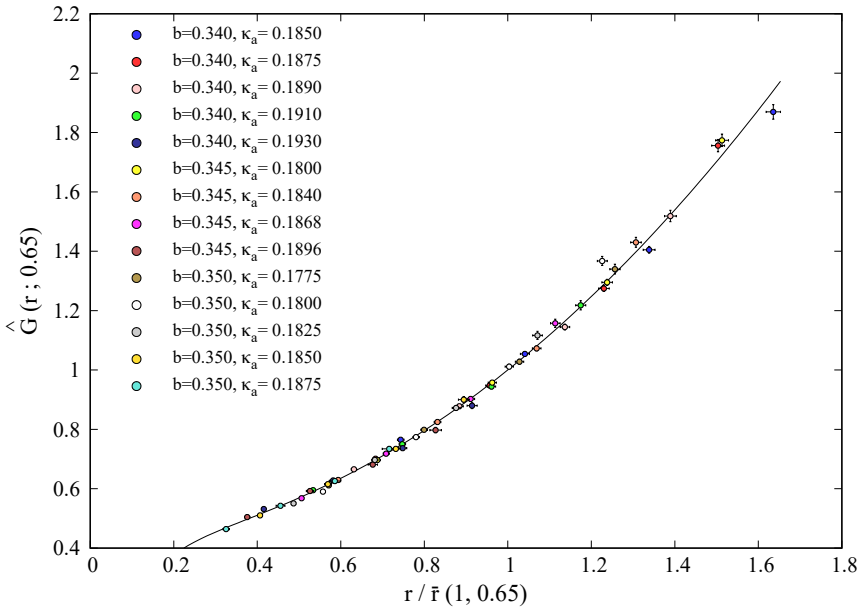

Figure 20: For all our $N_c = 361$ data samples, we display $\hat{G}(r;0.65)$ as a function of $r/\bar{r}(1,0.65)$, where $\bar{r}(1,0.65)$ is the scale determined using eq. (3.4.25) setting $f_0 = 1$ and $s = 0.65$. The black line is obtained by doing a joint fit of all the data with $R > 1.5$ to eq. (5.2.3), as described in the text.

units. Thus, the fitted data contains 4 values of R for each of the 14 total simulation parameters, and the fit parameters are the 14 values of $\bar{R}$ and the three additional parameters α, γ and δ. The rationale behind the parameterization is given by the flowed equivalent to eq. (3.4.28). The universal function $F_{\bar{t}(r;s)}(r,r)$ is well described by a second order polynomial in $(\bar{r}(f_0,s)/r)^2$ forced to be equal to f_0 for $\bar{r}(f_0,s)/r = 1$. This parameterization is inspired by the results at $s = 0$ in which α is given by the string tension $\sigma\bar{r}^2(f_0,s)$ and γ by a Lüscher-type term. The parameter δ is introduced to account for the a^2 correction appearing in eq. (3.4.28).

The procedure can be performed for various values of s and f_0 and the results should be compatible up to a change in the unit. In particular, we chose two values of f_0 (0.65 and 1) and two values of s (0.5 and 0.65) to check consistency. The results for different f_0 are perfectly compatible since they involve fitting the same data points. The data just predicts the ratio $\bar{r}(1,0.65)/\bar{r}(0.65,0.65) = 1.611$ and $\bar{r}(1,0.50)/\bar{r}(0.65,0.50) = 2.045$. On the other hand a change in s involves data at different flow times so that the comparison serves to check the independence of this choice. If we fit the ratio of scales

to a constant we get perfect compatibility with a constant value of $\bar{r}(1, 0.65)/\bar{r}(1, 0.50) = 1.120(6)$.

Finally, we will express our lattice spacing in units of $\bar{r}(1, 0.65)$ which are the ones affected by smaller errors. The results are given in Tab. 15. Notice that the final values come from a global fit to the data which assumes scaling. Hence, the errors do include a part associated with the amount of scaling violation present in our data. A visual determination of how well our data satisfies scaling can be obtained by plotting the best fit to the continuum function $\hat{G}(r; 0.65)$. This is given in Fig. 20. Together with the function we plot all our data points after subtraction of the lattice artifact δ term. The horizontal errors come from the errors in the determination of the scales $\bar{R}$. The overall agreement is very good.

5.2.2 *The scale from fundamental meson spectrum*

As mentioned in Sec 1.1.1, fermions in the fundamental representation play a different role than adjoint ones in the large-N_c limit. If the number of flavors is fixed when taking N_c to infinity, fundamental-quark loops are suppressed and the quenched approximation is exact. Nevertheless, these fundamental fermions give rise to a spectrum that can be used to set the scale for the $\mathcal{N} = 1$ SUSY Yang-Mills theory at large N_c. Fundamental pions can be considered pseudo-Goldstone bosons associated with the spontaneous breaking of the fundamental chiral symmetry, and the PCAC relation should hold as we approach the limit of vanishing fundamental fermion mass. The ρ-meson remains massive in the fundamental chiral limit, and its mass can be used as a scale for the massless (supersymmetric) theory. To achieve our final goal we compute the correlation functions of bilinear quark operators for pseudoscalar, axial and vector channels. The next step is to determine the mass of the lightest state having the corresponding quantum numbers for various values of the fundamental quark mass. Then we extrapolate those masses to the fundamental chiral limit.

In order to compute m_{pcac}, m_π and m_ρ on the lattice we perform a spectroscopy calculation according to the method defined the last Section of Chapter 2. As an example of the outcome of the method, we display in Fig. 21 the correlators of the optimal operators in the pseudoscalar and vector channels for the case $b = 0.35$, $\kappa_{adj} = 0.1825$, $\kappa_f = 0.1525$, with κ_f the fundamental hopping parameter. The time-dependence of these correlators shows a clear exponential decay from which the mass of the π-meson (pseudoscalar) and ρ-meson (vector) can be extracted. The numbers obtained and the χ^2 of the fits to an exponential are also displayed in the figure. We also show the signal that allows one to extract the fundamental PCAC mass m^f_{pcac}, defined as in eq. (5.3.2). Summing up, the procedure to extract the masses goes as follows. It amounts to determining the optimal operator and then

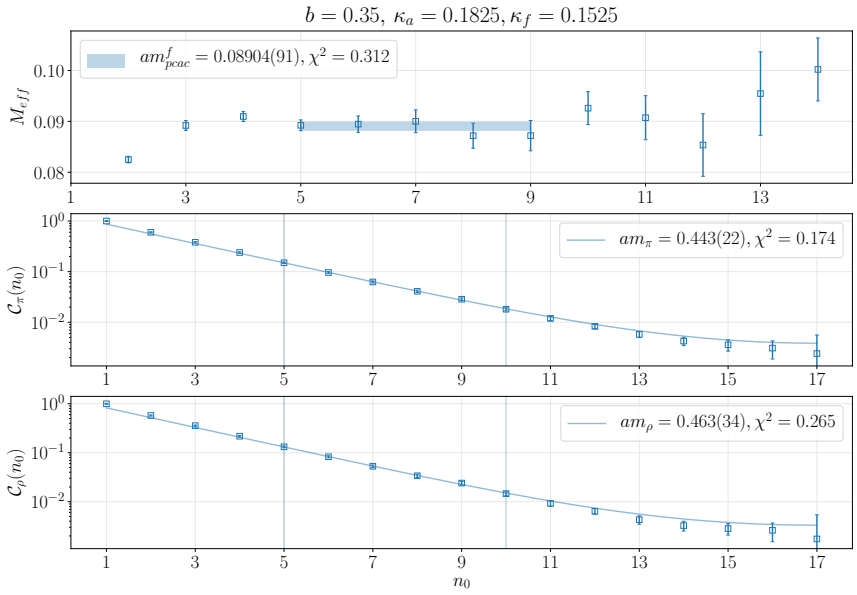

Figure 21: Stack plot of the correlators in this analysis for one example case. The first one shows the signal for am^f_{pcac} as an effective mass. The blue band is the result of the fit, the length corresponds to the time slices used to fit the mass, while the width corresponds to the error. The second and the third display the pion and the rho correlator signal, respectively. The blue line is the result of the fit performed in the region between the vertical lines.

fitting the corresponding correlator in a certain interval to an exponential (rather to a hyperbolic cosine function, taking into account the periodic nature of the temporal direction). There are of course some specific details that reflect the selection of the operator and the choice of fitting interval that affect the final numerical value for the mass. In the end, variations of these types which are of similar statistical significance are accounted for as a systematic error of the determination. Here we will comment briefly on the choice of the fitting interval. The main points to be taken into account in this selection are finite volume effects, lattice artifacts and the contamination of excited states. Typically, finite-size effects are more relevant close to the chiral limit, as the pion mass goes to zero and its Compton wavelength becomes comparable to the effective volume. To avoid too severe effects our selected values of the hopping parameter should stay sufficiently far from the chiral limit. In particular, in our data, the lightest cases still had $m_\pi a\sqrt{N} \sim 3.4$. Nonetheless, finite-size effects may still reflect in the appearance of a constant term in the correlator arising from the propagation of quarks wrapping around the finite extent of the lattice [131]. Although this effect disappears in the large volume (large N_c) limit, we have observed that in some cases the addition of a small constant to the hyperbolic cosine was required to obtain a good fit.

b	κ_{adj}	κ_f	am^f_{pcac}	am_π	am_ρ
0.34	0.189	0.15500	0.09711(88)	0.507(12)	0.549(20)
		0.15700	0.05755(89)	0.381(17)	0.434(31)
		0.15800	0.0392(11)	0.350(14)	0.421(27)
		0.15920	0.0149(11)	0.248(39)	0.336(56)
	0.191	0.15250	0.1253(11)	0.545(16)	0.570(21)
		0.15500	0.07464(76)	0.423(17)	0.450(29)
		0.15580	0.05929(86)	0.370(14)	0.416(22)
		0.15700	0.03601(89)	0.345(33)	0.373(54)
	0.192	0.15380	0.08564(87)	0.430(20)	0.458(27)
		0.15550	0.05090(88)	0.368(21)	0.405(32)
		0.15650	0.03086(75)	0.336(21)	0.379(34)
	0.193	0.15240	0.1000(12)	0.443(21)	0.450(30)
		0.15380	0.06932(92)	0.318(24)	0.317(30)
		0.15530	0.03904(60)	0.301(21)	0.299(27)
		0.15630	0.01982(96)	0.288(34)	0.283(46)
0.35	0.1775	0.15000	0.1730(11)	0.701(16)	0.741(22)
		0.15250	0.11939(90)	0.558(13)	0.599(20)
		0.15500	0.06896(73)	0.425(15)	0.480(27)
		0.15625	0.04288(45)	0.328(18)	0.382(28)
	0.18	0.15000	0.15806(93)	0.608(12)	0.626(15)
		0.15250	0.10532(64)	0.488(13)	0.514(19)
		0.15500	0.05327(78)	0.343(14)	0.377(24)
		0.15625	0.02986(60)	0.323(18)	0.409(33)
	0.1825	0.14700	0.2093(16)	0.719(18)	0.731(21)
		0.15000	0.1457(13)	0.560(19)	0.582(25)
		0.15250	0.08904(91)	0.443(22)	0.463(34)
		0.15500	0.03765(92)	0.306(30)	0.303(50)
		0.15580	0.02157(81)	0.314(22)	0.319(43)
	0.185	0.14930	0.1410(19)	0.533(26)	0.537(33)
		0.15100	0.1025(13)	0.430(24)	0.432(32)
		0.15250	0.0704(12)	0.351(25)	0.346(34)
		0.15380	0.0428(10)	0.288(30)	0.277(42)
		0.15500	0.0176(11)	0.259(42)	0.262(78)
	0.1875	0.14180	0.1538(23)	0.496(32)	0.495(39)
		0.15000	0.1106(17)	0.447(28)	0.452(35)
		0.15100	0.0882(14)	0.397(29)	0.401(36)
		0.15250	0.0547(12)	0.323(34)	0.323(45)
		0.15380	0.0258(11)	0.253(52)	0.249(68)
0.36	0.1831	0.14750	0.1194(20)	0.413(28)	0.406(33)
		0.15000	0.0630(14)	0.282(39)	0.282(46)
		0.15100	0.0430(12)	0.289(55)	0.282(67)

Table 14: The values of m^f_{pcac}, m_π and m_ρ for fermions in the fundamental representation and for each $(b, \kappa_{adj}, \kappa_f)$ value at $N = 289$ are given. The fitting procedure is the one described in sec. **??**, from which we obtained χ^2 per degrees of freedom in general smaller than one.

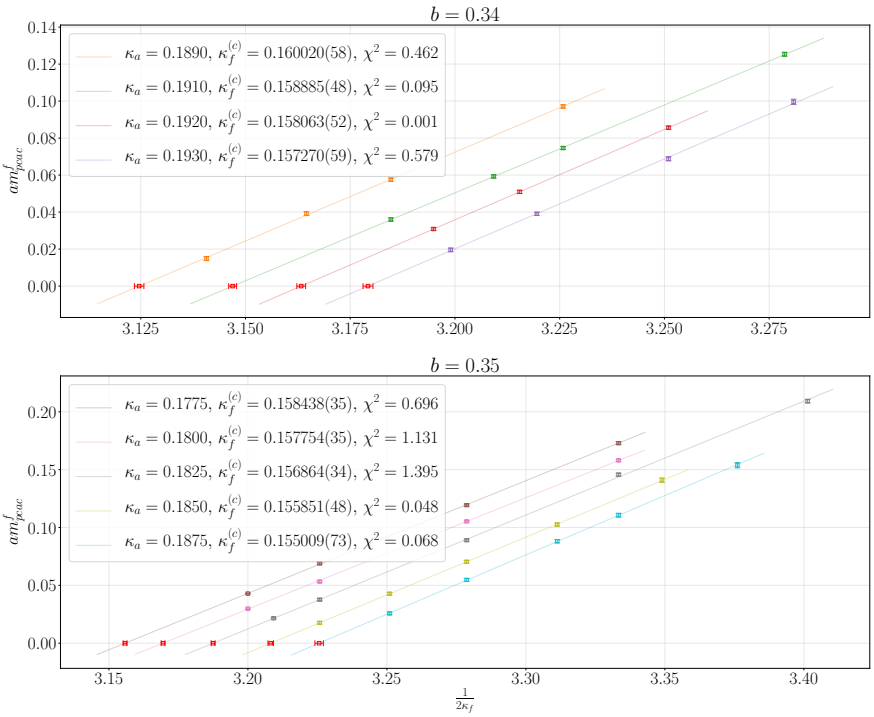

Figure 22: Extrapolation of am^f_{pcac} to 0. In the labels, we report the corresponding value of $\kappa_f^{(c)}$ extracted from the fit and the corresponding χ^2 per degree of freedom. Errors are calculated using standard jackknife techniques.

The results we obtained for the PCAC mass, the pion mass and the vector meson mass of fundamental fermions are reported in lattice units in Tab.14. We use these results to explore the (fundamental) chiral limit of the theory. The first check we do is to analyze the dependence of the PCAC mass on the fundamental hopping parameter κ_f. To determine the critical hopping parameter where the fundamental fermions become massless we follow the same strategy as for gluinos, i. e. we analyze the dependence of the PCAC mass on κ_f and determine the critical hopping parameter as the point where the fundamental PCAC mass vanishes. In Fig. 22 we plot am^f_{pcac} as a function of $1/(2\kappa_f)$. Performing separate linear fits for each value of (b, κ_{adj}), we extracted in each case the critical value of the hopping parameter $\kappa_f^{(c)}$. As signaled by the χ^2 per degree of freedom reported in the legend of the plot, the observed linear dependence is very good and confirms what one would expect from chiral symmetry restoration in the limit of vanishing quark masses for Wilson fermions.

We finally come to the determination of the scale based on the vector meson mass. To determine the chiral extrapolation of this quan-

tity we perform a global fit of am_ρ as a linear function of am^f_{pcac} for each value of (b, κ_{adj}), by imposing a common slope and extracting $am^\chi_\rho(b, \kappa_{adj})$ as the intercept at vanishing PCAC mass. We obtain a χ^2 per degree of freedom of 0.56. The final values of the inverse lattice spacing in units of m^χ_ρ obtained in this way are the ones used in Chapter 4 to determine the scale in the SUSY theory and were reported in Tab. 15.

5.2.3 *Scales comparison*

b	κ_{adj}	$\frac{\sqrt{8t_1^{2S}}}{a}$	$\frac{\sqrt{8t_1^{3GT}}}{a}$	$\frac{\bar{r}(1,0.65)}{a}$	$\frac{1}{am^\chi_\rho}$
0.34	0.185	2.878(2)(46)	2.883(2)(58)	3.362(36)	–
	0.1875	3.209(3)(68)	3.188(3)(90)	3.658(37)	–
	0.189	3.514(3)(65)	3.488(3)(88)	3.959(40)	3.10(13)
	0.191	4.049(4)(37)	4.042(4)(58)	4.682(48)	3.53(17)
	0.192067	4.568(6)(58)	–	–	3.54(28)
	0.193	5.273(7)(161)	5.244(8)(175)	6.014(78)	4.86(51)
0.345	0.18	3.166(3)(74)	3.145(2)(93)	3.635(37)	–
	0.184	3.664(4)(77)	3.645(3)(98)	4.208(41)	–
	0.1868	4.294(5)(40)	4.274(5)(55)	4.939(51)	–
	0.1896	5.559(8)(154)	5.614(8)(201)	6.649(111)	–
0.35	0.1775	3.730(3)(97)	3.737(3)(105)	4.377(43)	3.08(14)
	0.18	4.109(4)(75)	4.003(7)(109)	4.485(43)	3.65(17)
	0.1825	4.634(6)(70)	4.516(5)(64)	5.135(56)	3.94(26)
	0.1850	5.364(8)(144)	5.323(7)(65)	6.187(108)	5.06(37)
	0.186378	5.909(9)(192)	–	–	–
	0.1875	6.608(11)(249)	6.582(12)(287)	7.681(180)	5.34(71)
0.36	0.1760	5.77(1)(32)	–	–	–
	0.1780	6.32(1)(31)	–	–	–
	0.18	7.05(1)(31)	–	–	–
	0.1820	7.85(2)(35)	–	–	–
	0.183172	8.68(2)(44)	–	–	6.99(87)
	0.184	9.16(2)(52)	–	–	–

Table 15: Values of the inverse lattice spacing in units of the three different scales determined in this work. For flow-related scales, the first error is statistical, the second is systematic.

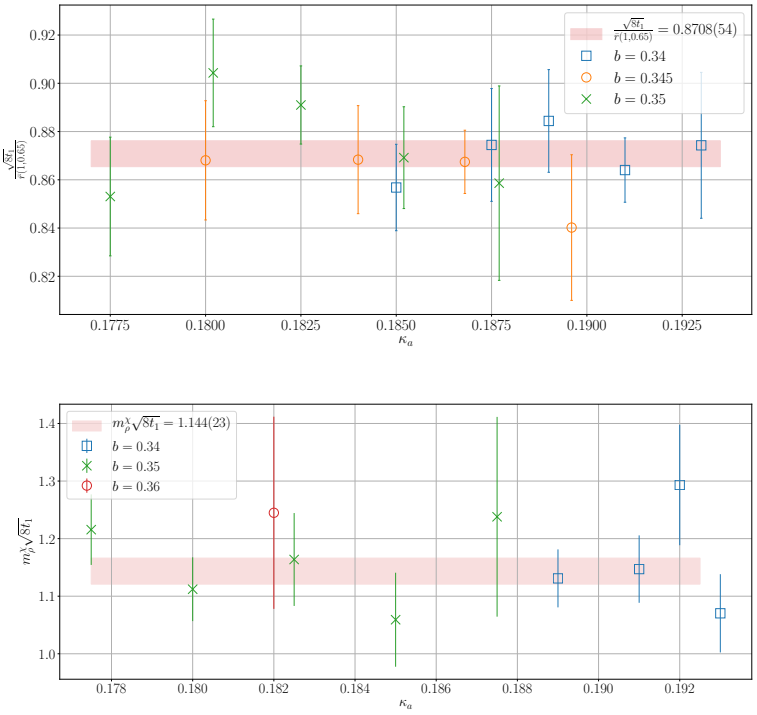

Figure 23: Comparison of scales as a function of the adjoint hopping parameter κ_{adj} for different gauge couplings. In the top panel it is displayed the ratio $\sqrt{8t_1}/\bar{r}(1, 0.65)$, in the bottom one $m_\rho^\chi\sqrt{8t_1}$. The red bands represent the average weighted over the errors, while their width represents the statistical uncertainty over the average ratio. When needed, points corresponding to the same κ_{adj} have been slightly shifted in the x-axes to avoid overlapping.

We dedicate this last part of the section to the comparison of the results obtained with the three different scale setting methods which are summarized in Tab. 15, which reports the lattice spacing in terms of $\frac{a}{\sqrt{8t_1}}$, $\frac{a}{\bar{r}}$ and am_ρ^χ. Although each of these quantities changes considerably when we change b (the inverse lattice 't Hooft coupling) and the hopping parameter κ_{adj} (related to the gluino mass), scaling dictates that the ratio should stay constant and be given by the ratio of the corresponding units of energy. In Fig. 23 we display the two independent ratios $\sqrt{8t_1}/\bar{r}(1, 0.65)$ and $m_\rho^\chi\sqrt{8t_1}$ for all the cases in which it is available. For the case of $a/\sqrt{8t_1}$ we have used an average of the results of $N_c = 289$ and $N_c = 361$ with errors that are dominated by the systematic ones. The results are compatible with being a constant within errors. From the best fit, we estimate that the conversion factor between the two units $\sqrt{8t_1}$ and $\bar{r}(1, 0.65)$ is 0.8708(54), while between $\sqrt{8t_1}$ and $1/m_\rho^\chi$ it is 1.144(23). A more visual impression of how scaling works can be seen in Fig. 24 where the three lattice spacing determinations of the inverse of the lattice spacing are displayed side by side after applying the conversion factors determined earlier.

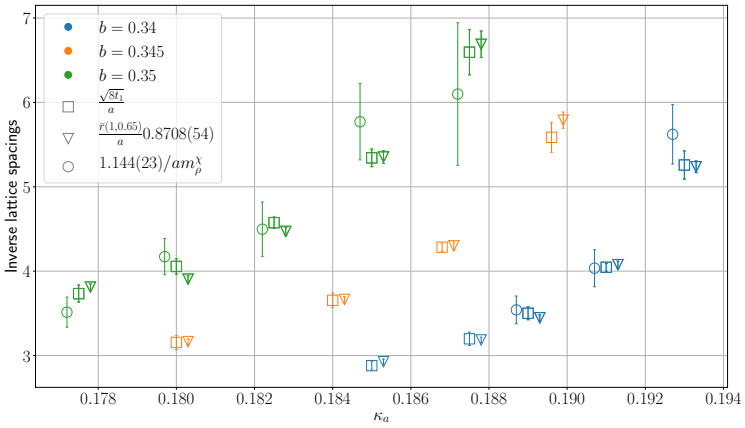

Figure 24: The inverse lattice spacing for the different values of (b, κ_{adj}). The quantities $\bar{r}(1, 0.65)/a$ and $1/am_\rho^\chi$ have been rescaled with the conversion factor indicated in the legend to match the value of $\sqrt{8t_1}/a$.

All datasets for which $\bar{r}(1, 0.65)$ was available are displayed. The figure shows how the three scales change considerably within all the datasets following the same trend in a consistent way. One can also notice the relative size of the errors of the three determinations of the lattice spacing. It looks as if the scale based on the Creutz ratios is the most precise, but the N_c dependence had to be corrected for systematic errors and might be underestimated.

5.3 THE SUPERSYMMETRIC LIMIT

In this Section, we want to explore the limit of massless gluinos, where the theory is expected to retrieve supersymmetry. As a recap of what is explained in Chapter 1, the typical methodology requires tuning the parameters of the theory to the vanishing gluino mass limit. The way this tuning is done in QCD takes advantage of the fact that pions are pseudo-Goldstone bosons for the spontaneous breaking of chiral symmetry, and their mass is proportional to the square root of the renormalized quark mass. On the other hand, in $\mathcal{N} = 1$ SUSY Yang-Mills, the chiral-symmetry breaking pattern is different, and no Goldstone excitation appears in the spectrum, one has instead an excitation analogous to the QCD η'. Several methods have been proposed in the literature to attain in this case the limit where SUSY is restored. One of them is to define a renormalized gluino mass using the supersymmetric Ward identities regularized on the lattice and tune this mass parameter to zero [37]. Another possibility is to use the connected part of the adjoint-η' correlator, this leads to a non-singlet adjoint-pion correlator that can be seen as composed

of the gluino and a quenched Majorana fermion. On the basis of partially-quenched chiral perturbation theory [39], this adjoint-pion is a pseudo-Goldstone boson for the spontaneous breaking of the "partially quenched" chiral-symmetry and can be tuned to vanishing mass to restore supersymmetry [36, 38]. In this Section, the strategy used to determine the point of SUSY restoration consists of two very different methods.

The first one is in the same spirit as the aforementioned adjoint-pion mass tuning. Although in the target supersymmetric theory, the gluino field is described by a single flavor, we make use of an additional "quenched" flavor which allows us to define a pseudoscalar $P = \bar{\Psi}\gamma_5\Psi$ and an axial current $A_\mu = \bar{\Psi}\gamma_\mu\gamma_5\Psi$. We can therefore define an analog of the PCAC mass as in Eq. (1.2.37) though

$$2m_{\text{pcac}} = \frac{\langle 0|\partial_\mu A_\mu|\pi\rangle}{\langle 0|P|\pi\rangle}, \tag{5.3.1}$$

where $|\pi\rangle$ stands for a generic state with the quantum numbers of the adjoint-pion. On the basis of partially-quenched chiral perturbation theory, we expect this mass to be directly proportional to the renormalized gluino mass and we tune it to zero to find the SUSY restoration limit. As in Eq. (1.2.38), the PCAC mass is then determined by fitting to a constant the ratio of correlation functions:

$$am_{\text{pcac}} = \frac{\mathcal{C}_{\gamma_0\gamma_5,\gamma_5}(x_0+a) - \mathcal{C}_{\gamma_0\gamma_5,\gamma_5}(x_0-a)}{4\,\mathcal{C}_{\gamma_5,\gamma_5}(x_0)}, \tag{5.3.2}$$

The values of the PCAC masses extracted in this way are provided in Tab. 16. We include in the table results for our datasets with $N_c = 289$ and 361. The general agreement, within errors, of the results for the two different values of N_c indicates the small influence of finite N_c effects on this quantity.

The second one makes use of the analysis of the eigenvalues of the Wilson-Dirac matrix, whose calculation has already been tackled in Sec. 3.2.1 of Chapter 3. Let us call λ^2_{min} the minimum eigenvalue of Q^2_w. At infinite volume, we expect this quantity to vanish in the chiral limit. In our case, this corresponds to it vanishing at large N_c, as already observed in the context of Yang-Mills theories with $N_f = 2$ Dirac flavors [132]. Hence, we can use its dependence on the fermion mass to define a proper massless gluino limit.

5.3.1 *Determination from the PCAC mass*

Contrary to what happens in standard lattice simulations, and due to the form in which it is computed in the reduced setup, the signal-to-noise ratio in the adjoint-pion correlation function deteriorates significantly at large time [76]. For this reason, it turns out to be more convenient to do the tuning in terms of the PCAC mass which can

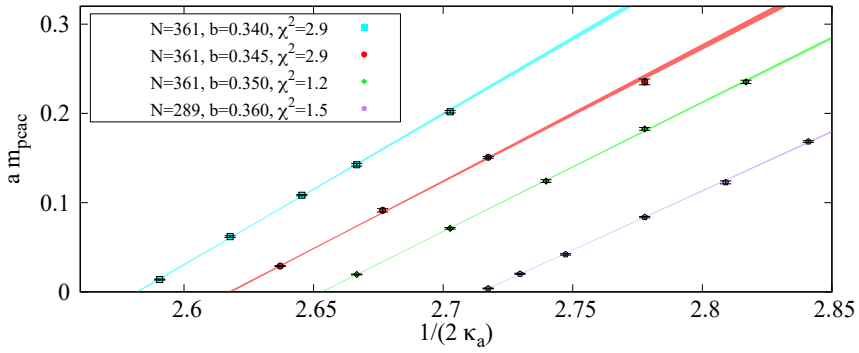

Figure 25: Dependence of the PCAC adjoint fermion mass on $1/(2\kappa_{adj})$ for all the values of the bare coupling b and the largest value of N_c within out set of simulations. The bands are linear fits at a fixed value of b used to determine the critical value of the adjoint hopping parameter κ^c_{adj}, with the width indicating the error in the fit. The χ^2 per degree of freedom of each of the fits is indicated in the legend.

be determined with very good precision, and this is the choice we have used in this Thesis. As we will see below, the results obtained in this way turn out to be consistent with the less precise determination from the adjoint-pion mass.

In the chiral limit, the PCAC mass is expected to be proportional to the fermion mass. This implies that close to this limit m_{pcac} should depend linearly on $1/\kappa_{adj}$ and vanish at the critical value. Indeed, in Fig. 25 we display our results, for the datasets with the larger value of N_c, together with a fit to a linear function of $1/(2\kappa_{adj})$. We see that the straight line provides a very good qualitative description of the data. Given the small errors, an additional quadratic term is needed in some cases to get a fit with χ^2 per degree of freedom of the order of one, if we include also the largest masses. In any case, to determine the point of vanishing of the PCAC mass both fits give identical results.

Our final results for the critical value of κ_{adj}, corresponding to the largest value of N_c simulated in each case, are collected in Tab. 17. The values obtained are in remarkable agreement with the determination based on the eigenvalues of the Dirac operator. In the rest of this work, the vanishing of the PCAC mass will be used as the criteria to tune all other quantities to the zero gluino mass limit.

Finally, to check for the consistency of our approach, we have as well determined the adjoint-pion mass and analyzed its dependence on the hopping parameter κ_{adj}. Results are collected in table 16. Fig. 26 displays m_π^2 vs $1/2\kappa_{adj}$. The colored lines shown in the plot correspond

b	κ_{adj}	am_{pcac}^{289}	am_{pcac}^{361}	am_{π}^{289}	am_{π}^{361}
0.340	0.1850	0.1957(21)	0.2018(14)	0.970(6)	0.977(4)
0.340	0.1875	0.1426(14)	0.1424(15)	0.814(7)	0.819(7)
0.340	0.1890	0.1041(12)	0.1083(7)	0.699(5)	0.719(4)
0.340	0.1910	0.0603(9)	0.0619(9)	0.534(6)	0.540(5)
0.340	0.192067	0.0344(8)	–	0.397(4)	–
0.340	0.1930	0.0120(3)	0.0138(6)	0.258(6)	0.263(13)
0.345	0.1800	0.2390(60)	0.2352(32)	1.040(17)	1.043(6)
0.345	0.1840	0.1477(22)	0.1507(11)	0.814(16)	0.821(5)
0.345	0.1868	0.0901(7)	0.0913(18)	0.630(7)	0.631(6)
0.345	0.1896	0.0275(5)	0.0289(5)	0.349(6)	0.353(5)
0.350	0.1775	0.2363(29)	0.2353(19)	1.013(12)	1.001(7)
0.350	0.1800	0.1805(25)	0.1826(16)	0.878(9)	0.883(7)
0.350	0.1825	0.1242(24)	0.1242(15)	0.719(13)	0.733(6)
0.350	0.1850	0.0733(14)	0.0712(10)	0.534(6)	0.540(6)
0.350	0.1864	0.0427(9)	–	0.433(7)	–
0.350	0.1875	0.0192(7)	0.0195(4)	0.291(8)	0.293(6)
0.360	0.1760	0.1684(9)	–	0.804(7)	–
0.360	0.1780	0.1227(17)	–	0.689(15)	–
0.360	0.1800	0.0837(8)	–	0.541(15)	–
0.360	0.1820	0.0420(7)	–	0.370(7)	–
0.360	0.1832	0.0202(6)	–	0.270(19)	–
0.360	0.1840	0.0038(5)	–	0.249(17)	–

Table 16: Values of the PCAC and adjoint-pion masses determined for all values of the bare coupling and adjoint hopping parameter in our set of simulations with $N_c = 289$ and $N_c = 361$.

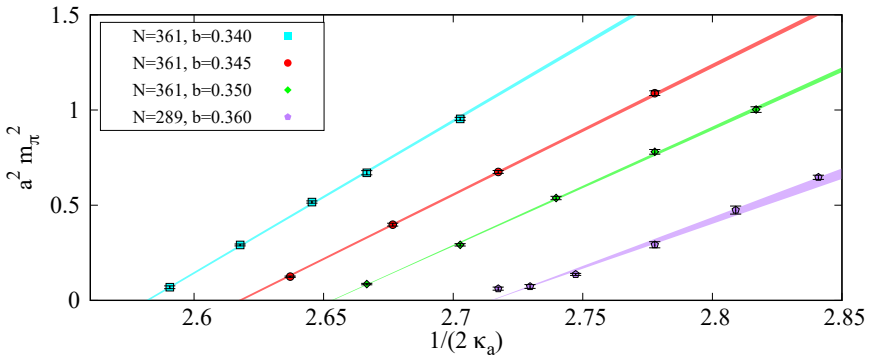

Figure 26: Dependence of the adjoint pion mass on $1/(2\kappa_{adj})$. The bands are fits to the data at a fixed value of b with the critical hopping parameter fixed to the one extracted from the vanishing of the PCAC mass, as determined from Fig. 25.

to linear fits where, for each value of the bare coupling b, the critical value of the hopping parameter is fixed to the one determined from the PCAC mass; only the slope is left as a free parameter. Linearity works very well in all cases, giving χ^2 per degree of freedom of the order of one, except on the smallest lattice with bare coupling $b = 0.36$, where a deviation is observed for the lighter masses (the two lightest ones are excluded from the fit). This difference can be due to finite size effects, which come out more pronounced for the pion mass than for the PCAC mass. For this reason, it is also preferable to use the latter to determine the point of SUSY restoration.

5.3.2 *Determination from the eigenvalues of* Q_w

As already mentioned, the second method that we have used to determine the point of SUSY restoration is based on the eigenvalues of the Dirac matrix. In the continuum limit the minimum eigenvalue of the massive Dirac operator at infinite volume goes to zero linearly with the fermion mass. On the lattice one expects a similar behavior for the operator D_w/κ_{adj} which tends to the continuum one up to a renormalization factor. As explained earlier the lowest lying spectra of $Q_w = D_w\gamma_5$ have been determined for all our configurations. This includes $|\lambda_{min}|$, whose average value is listed in Tab. 4 for all our datasets. Notice that this quantity has very small errors, making it a perfect observable for the determination of the zero mass point. Indeed, the aforementioned continuum behaviour implies that $\langle|\lambda_{min}|\rangle/\kappa_{adj}$ should depend linearly on $1/2\kappa_{adj}$ and vanish at $\kappa_{adj} = \kappa^c_{adj}$, signalling the point of vanishing gluino mass. Since finite N_c corrections amount to finite volume effects, this behavior is only expected

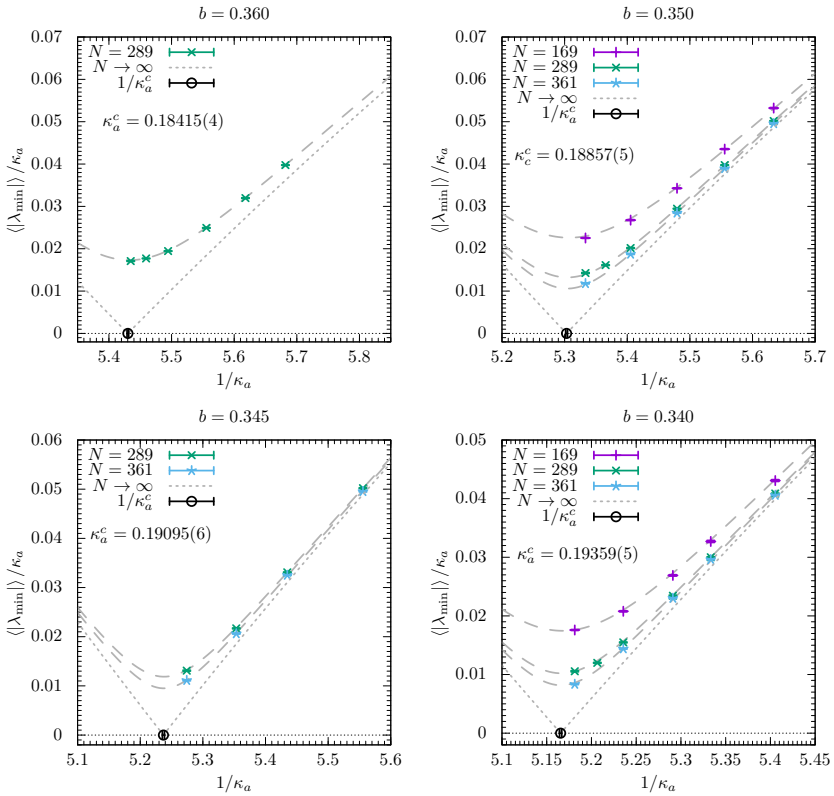

Figure 27: Dependence, for the 4 values of the bare coupling used in this work, of $\langle|\lambda_{\min}|\rangle/\kappa_a$ on $1/(2\kappa_{adj})$, where $\lambda^2_{\min}$ stands for the minimum eigenvalue of Q^2_w. The dashed lines in the various plots correspond to fits to eq. (5.3.3), while the dotted lines represent the infinite N_c extrapolations, allowing to determine the value of the critical hopping parameter $\kappa^c_{adj}(b)$.

to hold at infinite N_c. Building on this analogy we would expect a dependence of the following form:

$$\left(\frac{\langle|\lambda_{\min}|\rangle}{\kappa_{adj}}\right)^2 = A\left(\frac{1}{2\kappa_{adj}} - \frac{1}{2\kappa^c_{adj}}\right)^2 + \delta\left(\frac{1}{N_c^2}\right). \tag{5.3.3}$$

where the function $\delta(1/N_c^2)$ should vanish at large N_c. A correction of this type was observed earlier [132] for the large N_c reduced model coupled to two flavors of adjoint fermions. In our case, the formula describes our data very well as shown in Fig. 27. The dashed lines gives our best fit with $\delta(1/N_c^2) = B/N_c^2$ and the dotted line the extrapolation to infinite N_c. The resulting critical hopping parameters κ^c_{adj} are presented in Tab. 17.

b	κ_{adj}^c from $\langle\lvert\lambda_{min}\rvert\rangle$	κ_{adj}^c from m_{pcac}
0.340	0.19359(5)	0.19365(5)
0.345	0.19095(6)	0.19100(6)
0.350	0.18857(5)	0.18845(2)
0.360	0.18415(4)	0.18418(2)

Table 17: Values of the adjoint critical hopping parameter κ_{adj}^c determined from the vanishing, as a function of $1/(2\kappa_{adj})$, of $\langle\lvert\lambda_{min}\rvert\rangle$ or the m_{pcac} mass.

b	$\frac{a^X}{\sqrt{8t_1}}$	$\frac{a^X}{\sqrt{8t_0}}$	$\frac{a^X}{w_0}$	P(b)
0.34	0.1702(31)	0.1046(37)	0.2904(72)	0.5620(3)
0.345	0.1423(46)	0.0875(39)	0.2428(89)	0.57027(15)
0.35	0.1292(35)	0.0794(33)	0.2205(71)	0.57810(15)
0.36	0.1048(45)	0.0644(34)	0.1788(83)	0.5934(1)

Table 18: Lattice spacing in units of $\sqrt{8t_1}$ for the supersymmetric theory. For comparison with other authors, we also convert to $\sqrt{8t_0}$ and w_0 units using the conversion factor determined in the previous section Tab. 12. The last column displays the plaquette expectation value extrapolated to the massless gluino limit.

5.4 THE LATTICE SPACING AND THE β-FUNCTION IN THE SUSY LIMIT

After having completed the determination of the scale with good precision for our massive gluino values, we will here attempt to achieve our main goal of determining the scale for the supersymmetric theory. This will be done by extrapolating the lattice scale in units of $\sqrt{8t_1}$ to the massless-gluino limit, achieved by tuning to the limit of vanishing m_{pcac} always expressed in physical units. The resulting plot is shown in Fig. 28. In the plot, different markers were used to display the points belonging to $N_c = 289$ and $N_c = 361$. By looking at the plot, it is visible by eye that the points corresponding to different markers are compatible within errors, showing that we were able to control finite-volume effects. The points are well fitted by a straight line and no higher-order polynomial terms are necessary to perform the extrapolation, which is remarkable, taking into account the wide range of m_{pcac} values covered. The values of the scale extrapolated to the massless-gluino limit are reported in Tab. 18 for different values of the gauge coupling b. Having these values greatly simplifies future studies in both selecting the parameters in which to simulate and expressing the results in physical units.

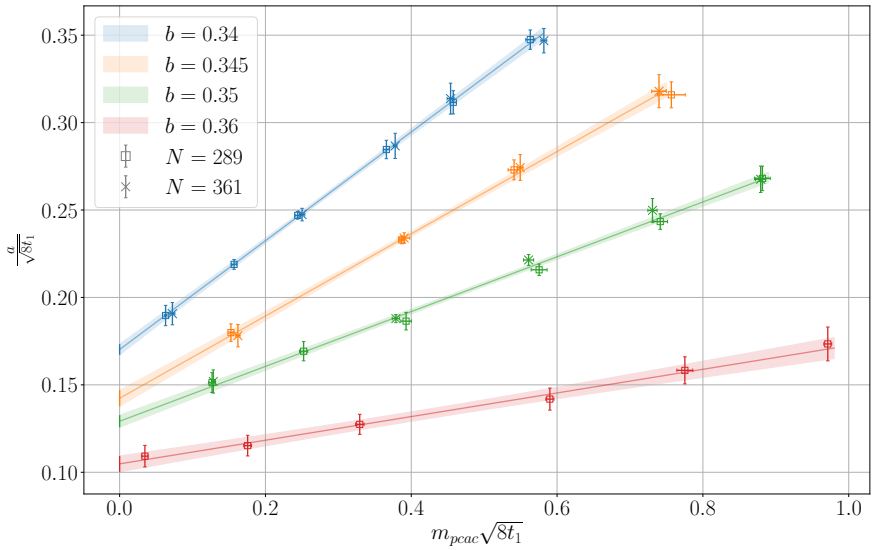

Figure 28: The lattice spacing expressed in units of the gradient flow scale $\sqrt{8t_1}$ as a function of the adjoint PCAC mass in physical units. Different markers represent a different number of colors N_c (volume). The straight lines represent the extrapolation of the lattice spacing to the massless-gluino limit, obtained through a joint fit to all the points for each b. The error bars on the y-coordinate are dominated by systematics (cfr. Tab. 13) while those on the horizontal axis take only into account the errors on the bare PCAC mass.

Our results provide the value of the lattice spacing as a function of the inverse lattice 't Hooft coupling λ, from which we can study the β-function of the theory, following the definitions we gave in Sec. 4.2 of Chapter 4.

As a reminder, perturbation theory predicts the leading behavior of the function up to next to the leading order. For Yang-Mills theory coupled to N_f flavors of adjoint Dirac fermions this gives

$$\beta(\lambda) = -b_0\lambda^2 - b_1\lambda^3 + \mathcal{O}(\lambda^4) = -\frac{d\lambda}{d\log a^2}\,, \tag{5.4.1}$$

with the coefficients b_0 and b_1 are given by Eq. (4.1.4) which we rewrite for completeness.

$$b_0 = \frac{1}{(4\pi)^2}\frac{11-4N_f}{3}, \tag{5.4.2}$$

$$b_1 = \frac{1}{(4\pi)^4}\frac{34-32N_f}{3}. \tag{5.4.3}$$

There is one particular scheme in which the β-function is known to all orders. This is the so-called Novikov-Shifman-Vainshtein-Zakharov (NSVZ) β-function [133]:

$$\beta(\lambda) = -\frac{b_0\lambda^2}{1-\frac{b_1}{b_0}\lambda}. \tag{5.4.4}$$

This functional form is particularly well-suited for performing the integration of the inverse of the β-function. One gets

$$-\log a\Lambda = \frac{1}{2b_0\lambda} + \frac{b_1}{2b_0^2}\log b_0\lambda\,, \tag{5.4.5}$$

which gives the same equation we found in Chapter 4, without the linear term in λ. Thus, although we are certainly not in the NSVZ scheme, this formula incorporates nicely the universal part of the β-function and provides a suitable parametrization that allows adding extra terms proportional to the coupling and higher powers of it. For this reason, we employ the improved coupling previously define, of which we report here the definitions.

Now let us apply these ideas to our data. As already discussed in Chapter 4, for lattice QCD the naive lattice coupling $1/b$ is not particularly well-suited for comparison with the perturbative predictions of scaling. As already mentioned one possible choice is $\lambda_I \equiv 1/(bP(b))$, where $P(b)$ represents the average value of the plaquette extrapolated to the massless-gluino limit, whose values are reported in Tab. 18. Fitting the NSVZ β-function (with $N_f = 1/2$) to our 4 data points gives a chi-square per degree of freedom $\chi^2/\text{dof} = 1.42$. If we modify the fit to include a higher order term in the β-function the fit gives a worse χ^2/dof and the additional parameter comes out compatible with zero. We conclude that our data does not have enough sensitivity to determine modifications to the NSVZ β-function. However, our data do have sensitivity to the leading coefficients of the β-function. A two-parameter fit leaving N_f and Λ free having $\chi^2/\#\text{dof} = 1.38$, gives $N_f = 0.31(20)$ ($(4\pi)^2 b_0 = 9.76(80)$) to be compared with the perturbative result $N_f = 0.5$ ($(4\pi)^2 b_0 = 11 - 4N_f = 9$).

One can repeat the procedure with another choice of the improved coupling constant, like $\lambda_E = 8(1 - P(b))$. The one-parameter fit to the NSVZ β-function gives $\chi^2/\text{dof} = 1.42$. Again a two-parameter fit leaving also N_f free gives $N_f = 0.30(22)$ ($(4\pi)^2 b_0 = 9.78(87)$), completely compatible with that obtained for the other improved coupling. In Fig. 29 we display side-by-side the logarithm of the lattice spacing as a function of both improved couplings together with the lines corresponding to the fits described before.

In summary, we emphasize that the behavior of the scale in the range explored in our study is certainly not far and even compatible with the dependence predicted by perturbation theory. The data also shows the tendency expected by the addition of an adjoint Majorana

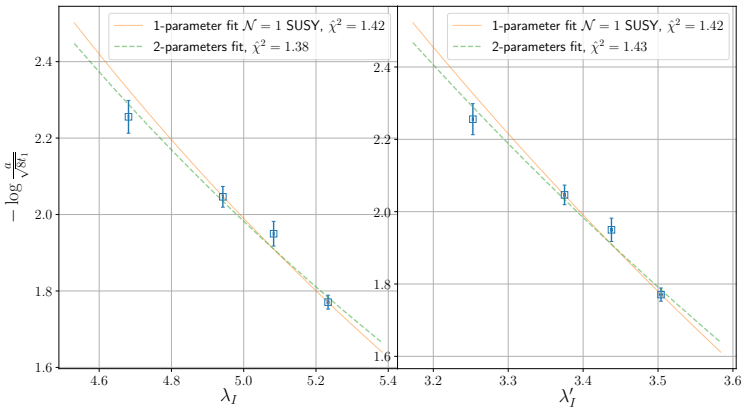

Figure 29: Dependence of the logarithm of the lattice spacing as a function of the improved coupling λ_I (left panel), and $\lambda'_I = \lambda_E$ (right panel). Points have been fitted with Eq. (5.4.5) leaving only Λ free (solid orange line), and with the same analytical form leaving also N_f as a free parameter (dashed green line).

fermion since N_f comes out larger than the value 0 corresponding to the pure gauge theory and not incompatible with the value 0.5, expected for the SUSY Yang-Mills theory at asymptotic small values of the coupling. This implies that the leading perturbative coefficient agrees within a 10% with the expected value $b_0 = 9/(4\pi)^2$.

5.5 THE CASE OF $N_f = 1, 2$

In this section, we discuss the extraction of the Wilson flow scale for the ensembles of configurations we generated in Sec. 3.2.2 corresponding to $N_f = 1$ and $N_f = 2$. After integrating the Wilson flow for each configuration in our ensembles, we apply the norm correction as in Eq. (3.4.19). The first observation is that in several ensembles the corresponding values of T_1 fall within the upper bound of the scaling window corresponding to $\gamma = 0.3$ and no extrapolation is needed. Since these ensembles correspond to the case of smaller κ_{adj}, we will refer to them as "heavy" and we directly extract the scale with a simple interpolation of the flow curve at the value $\hat{\Phi} = 0.05$. For the other ensembles (that will be referred to as "light") we employ the methodology we developed in Sec. **??**, based on the global fit on the universal curve. We treat separately each value of N_f, since the method implicitly assumes that the universal function used for the fitting can be parameterized in terms of (the integral of the inverse of) the β-function, which changes depending on the number of flavors. The results are reported in Tab. 19 and 20, where the distinction between light and heavy ensembles is spelled in the caption of the table.

κ_{adj}	$\sqrt{8T_1}$
0.100	2.2839(43)
0.110	2.3382(64)
0.120	2.4208(61)
0.130	2.5621(52)
0.140	2.7550(66)
0.150	3.0951(86)
0.155	3.306(13)
0.160	3.712(18)
0.165	4.193(27)
0.170	5.1236(28)(52)
0.172	5.7874(61)(58)
0.175	7.1691(83)(76)

κ_{adj}	$\sqrt{8T_1}$
0.100	3.255(16)
0.110	3.326(14)
0.120	3.451(27)
0.130	3.579(18)
0.140	3.925(20)
0.150	4.347(28)
0.155	4.824(28)(47)
0.160	5.345(39)(55)
0.165	6.229(61)(73)
0.170	8.240(78)(99)
0.172	9.52(13)(13)
0.175	13.63(26)(20)

Table 19: Wilson flow scales for $N_f = 1$. Those values having a single error correspond to the "heavy" ensemble and the uncertainty is the statistical error of the extrapolation evaluated with the Γ-method. For the "light" scales, the first error is the statistical (uncorrelated) error of the global fit, while the second is the systematic one calculated as explained in the text. *Left:* $b = 0.35$, *right:* $b = 0.36$.

For the light ensembles, the mean values are obtained from a universal fit to Eq. (4.1.5) with 3 parameters in addition to the universal one given by Eq. (4.1.4) with $N_f = 1$ or 2. In the tables, the scales for the light ensembles also are reported with a systematic error calculated as the dispersion of the values obtained by varying the number of parameters in the functional form, the lower and the upper limit of the scaling window.

5.5.1 *The dependence on the scale on the fermion mass*

In this subsection, we analyze for different theories the dependence of the scale on the value of the adjoint fermion mass. We focus on the case of $b = 0.350$ and 0.360 for which we have data in a large range of fermion masses at all values of N_f (cfr. Tab. 15, Tab. 20 and 20). In this section we will also use the "heavy" ensembles of $N_f = \frac{1}{2}$,i. e. the ones listed in Tab. 3, whose scale are reported in Tab. 23.

Having those at our disposal, we can attempt a quantitative study of the behavior of the corresponding theories, trying to highlight the expected substantial differences.

The critical value of the hopping parameter has been extracted by tuning the PCAC mass to zero: we obtain $\kappa_{adj}^{(c)} = 0.18418(2), 0.1777(1)$ and $0.1698(1)$, for $b = 0.360$ and $N_f = \frac{1}{2}$, 1 and 2 respectively.

κ_{adj}	$\sqrt{8T_1}$
0.100	2.3884(62)
0.105	2.4397(53)
0.110	2.5140(50)
0.115	2.6055(61)
0.120	2.7037(74)
0.125	2.8163(83)
0.130	2.9955(93)
0.135	3.217(14)
0.140	3.506(16)
0.145	3.856(24)
0.150	4.501(34)
0.155	5.35(7)(62)
0.160	6.99(7)(86)

κ_{adj}	$\sqrt{8T_1}$
0.100	3.390(16)
0.105	3.494(17)
0.110	3.522(11)
0.115	3.638(17)
0.120	3.749(27)
0.125	3.951(26)
0.130	4.146(22)
0.135	4.464(35)
0.140	4.79(1)(55)
0.145	5.42(7)(63)
0.150	6.20(7)(75)
0.155	7.67(10)(97)
0.160	10.8(1)(1.3)

Table 20: Wilson flow scales for $N_f = 2$. Those values having a single error correspond to the "heavy" ensemble and the uncertainty is the statistical error of the extrapolation evaluated with the Γ-method. For the "light" scales, the first error is the statistical (uncorrelated) error of the global fit, while the second is the systematic one calculated as explained in the text. *Left:* $b = 0.35$, *right:* $b = 0.36$.

In Fig. 30, we plot the lattice spacing in units of $\sqrt{8t_1}$ as a function of the subtracted bare quark mass, $1/2\kappa_{adj} - 1/2\kappa_{adj}^{(c)}$. The plot shows a smooth dependence of the lattice scale on the fermion mass. As expected from the decoupling of fermions in the heavy mass limit, the curves approach a unique value irrespective of the number of flavors and approximate the red band in the figure which represents the value of the scale extracted on $N_c = 841$ pure gauge configurations.

In the light fermion sector, our results approach different theories. The $N_f = \frac{1}{2}$ case has been studied in detail in Sec. 5.3 of this Chapter. In summary, $a/\sqrt{8t_1}$ shows a linear behavior in $\sqrt{8t_1}m_{pcac}$ in the light region from which we can attempt an extrapolation to the massless limit. The case of $N_f = 2$, on the other hand, is known to behave differently. The theory with 2 dynamical adjoint fermions is believed to be conformal in the chiral limit. As a direct consequence of conformality, every scale in the theory should behave like $(a\bar{m}_q)^{\frac{1}{1+\gamma^*}}$ as the fermion mass is tuned to zero. In [134], conformality was studied in the same model through the behavior of the low-modes of the Dirac operator, and a value of $\gamma^* = 0.269(2)(50)$ was found for the mass anomalous dimension. Given the lack of enough precise data in the small mass region, we can only test the compatibility of our results with the previous ones. The dependence of the scale on the subtracted bare quark

Table 21: $b = 0.35$

κ_{adj}	$\sqrt{8t_1}$	$\sqrt{8t_0}$
0.100	2.2225(43)	3.621(11)
0.110	2.2527(48)	3.670(11)
0.120	2.2993(35)	3.741(12)
0.130	2.3667(47)	3.849(11)
0.140	2.4618(62)	4.006(15)
0.150	2.5887(64)	4.189(15)
0.155	2.6848(68)	4.341(15)
0.160	2.8019(90)	4.517(22)
0.165	2.9782(76)	4.799(20)
0.175	3.493(11)	5.545(29)

Table 22: $b = 0.36$

κ_{adj}	$\sqrt{8t_1}$	$\sqrt{8t_0}$
0.100	3.204(11)	5.107(28)
0.110	3.217(10)	5.120(24)
0.120	3.265(16)	5.183(36)
0.130	3.368(11)	5.346(30)
0.140	3.496(14)	5.507(29)
0.150	3.673(18)	5.756(42)
0.155	3.815(16)	5.970(39)
0.160	3.957(19)	6.152(42)
0.165	4.256(32)	6.585(70)
0.175	5.28(20)	7.93(36)

Table 23: Wilson flow scales for "heavy gluino" configurations at $N_f = \frac{1}{2}$ for $(N_c = 289, k = 5)$.

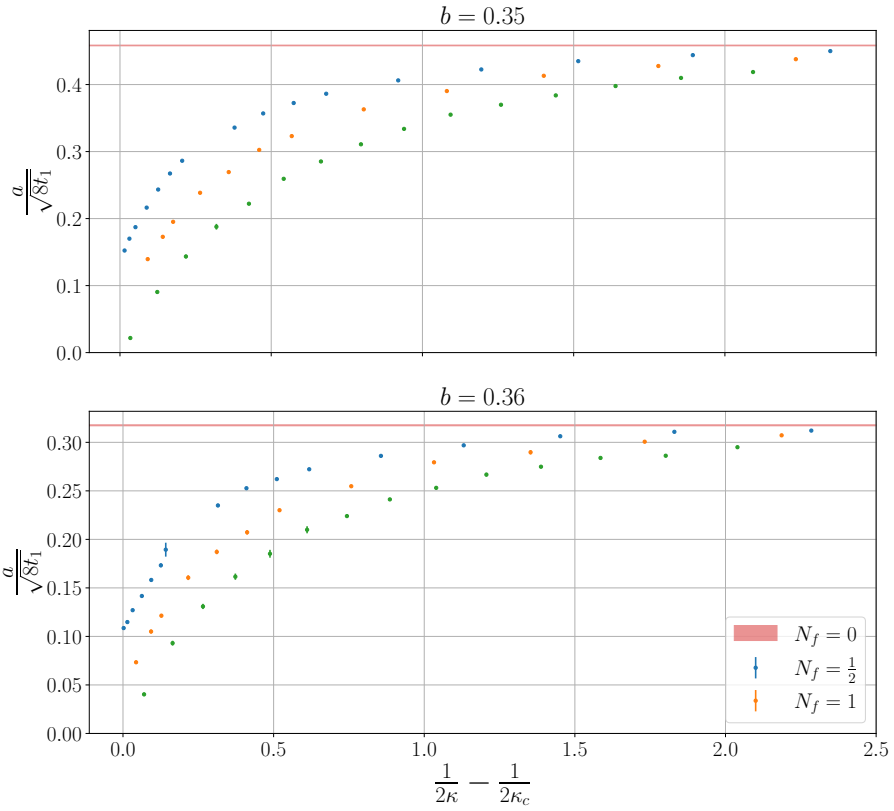

Figure 30: Lattice spacing in units of $\sqrt{8t_1}$ as a function of the bare subtracted quark mass $\frac{1}{2\kappa_a} - \frac{1}{2\kappa_c}$ for $N_f = 0, \frac{1}{2}, 1, 2$. The Yang-Mills value is represented as a red band whose width corresponds to the error.

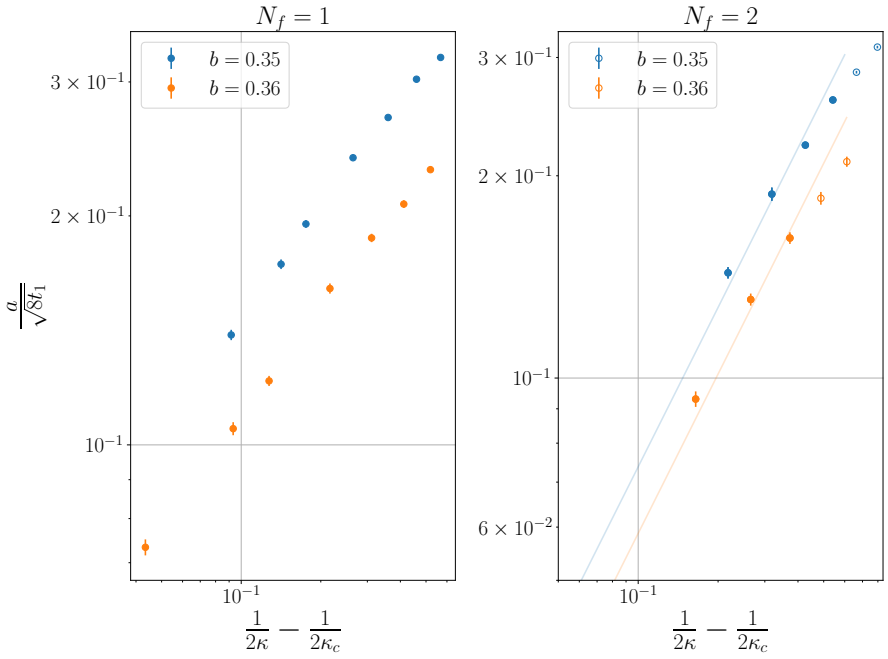

Figure 31: Light sector of the lattice scale. *Right panel:* Lattice scale for $N_f = 2$ at $b = 0.35, 0.36$. Solid points are fitted to $p_1(a\bar{m}_q)^{\frac{1}{1+0.269}}$. *Left panel:* Lattice scale for $N_f = 1$ at $b = 0.35, 0.36$.

mass has been fitted to our data fixing the anomalous dimension and leaving free the overall coefficient, showing an agreement within errors as displayed in Fig. 31 in a log-log plot. Finally, the case of $N_f = 1$ has also been argued to be conformal in a series of recent works [135]. The fermion mass dependence of the scale is also displayed in Fig. 31; as in the $N_f = 2$ case, a conclusion cannot be drawn based on our data and more precise results at lighter masses would be required to test this hypothesis.

CONCLUSIONS

In this final chapter, we draw upon the extensive research conducted throughout this doctoral thesis to provide a comprehensive conclusion to our study. Our aim in this concluding chapter is to revisit the research objectives set forth at the beginning of this journey and assess to what extent they have been achieved.

In this thesis, we focused on simulating the $SU(N_c)$ Yang-Mills theory in the limit of large N_c, along with its extensions involving N_f flavors of adjoint fermions. Our primary approach, known as the "twisted volume reduction", exploits the concept of volume independence arising in the large-N_c limit and its spelled out in Chapter 2. According to this concept, by quantizing the theory on a torus with twisted boundary conditions, the dynamical parameter representing the information of the volume is determined by a combination of the number of colors and the actual lattice size. In the limit of large-N_c, providing the center symmetry remains unbroken, we can reduce the spacetime to a single site, effectively capturing the physics of a lattice with a side length of $a\sqrt{N_c}$. This particular formulation is referred to as the TEK model. The reduction can be also applied to fermions completely or partially depending on the representation. Let us now summarize the main achievements of this work.

- In Chapter 3, we examined the primary approach utilized for generating configurations in both the pure Yang-Mills theory and the theory incorporating dynamical adjoint fermions with $N_f = \frac{1}{2}, 1, 2$. We presented the collection of ensembles that have been generated. Additionally, within the same chapter, we extensively discussed the methodology employed to set the scale of the theory. As emphasized in Sec. 3.4.1, the Wilson flow technique served as the main tool, complemented by a procedure called *norm correction*. This procedure effectively eliminates the effect of finite-N_c and lattice artifacts at the tree level in perturbation theory. Through this approach, we introduced a novel tree-level improved scale, denoted as $\sqrt{8t_1}$, enabling us to achieve high precision scale settings in our simulations. Alongside this technique, we also provided detailed information on an alternative method for scale setting, which combines Wilson flow with the utilization of Creutz ratios. We specifically applied this alternative approach to the case of $N_f = \frac{1}{2}$. Furthermore, we presented a comprehensive overview of how meson spectroscopy can be conducted within our setup.

- At the beginning of Chapter 4 we apply these methodologies to the case of pure Yang-Mills. We extensively test the applica-

bility of our scale-setting methodology to all our ensembles by comparing the results at different values of N_c and the gauge coupling b. We verify that the norm correction is effectively able to capture the systematic shift of the scale caused by lattice artifacts, and can treat finite-N_c effects. We provide a list of the scales we extracted in Tab. 7. In Sec. 4.2 we compare the determination of the scale with this method to the previous determination of the scale in the TEK model done with the string tension in [108]. We provide the values of the scale in both units in Tab. 8 and verify that the dimensionless ratio $R = \sqrt{\sigma}\sqrt{8t_1}$ is almost always compatible with a constant value, except for the case of the coarsest lattice, where it is still compatible within 2σ. This can be understood in terms of scaling violations and can be accounted for by a linear fit in a^2, leading to an extrapolated value of $R = 0.674(8)(12)$ in the continuum limit. This result is a remarkable confirmation of the validity of scaling in the range of our couplings, which extends also to a region where asymptotic scaling is expected to hold valid.

- By exploiting the analytic prediction given by perturbation theory in the region where asymptotic scaling is valid, we can calculate the value of the Λ parameter from our setup and convert it to the more familiar $\overline{\text{MS}}$ scheme. We used three different improved couplings to have a better convergence with perturbation theory and we obtain an overall value of $\sqrt{8t_1}\Lambda_{\overline{\text{MS}}} = 0.3618(47)(29)$, compatible with previous results from the TEK model [108] and also other results from standard lattice simulations in the large-N_c limit from [124, 136]. A more detailed analysis and a careful treatment of this ensemble will be issued in a future publication.

- The last section of Chapter 4 is dedicated to the computation of the chiral condensate Σ of Yang-Mills theory in the large-N_c limit. This is a crucial quantity to understand the mechanism of the spontaneous breaking of chiral symmetry. We approach the determination from two different perspectives. The first one is a fully non-perturbative proof of the GMOR relation on the lattice, which states that the chiral condensate can be read from the slope of the vanishing of the pion mass in the chiral limit. We take the relevant quantities needed from this study from [75], where the light meson spectrum in the large-N_c limit has been computed in the TEK model. Our preliminary result for the condensate in units of Z_P at the finest lattice spacings is $0.546(15)$ in units of $\sqrt{8t_0}$. The other determination comes from the study of the *mode number* of the Dirac operator following the line of [126], which leads to a value of $0.573(36)$ in units of $\sqrt{8t_0}$ for the finest lattice spacings. We found a remarkable accordance be-

tween the two results, which is a nontrivial confirmation of the solidity and consistency of our method. For the final determination of the chiral condensate, the chiral extrapolation has to be seconded to a continuum one, for which the values of the renormalization factor Z_P are needed. At the time of the writing of this Thesis, these values are not available, and thus our results have to be considered as a preliminary stage of a more complete analysis in a future publication.

- After the case of pure Yang-Mills theory, in Chapter 5 we pass to the analysis of the case of $N_f = \frac{1}{2}$ (an adjoint Majorana fermion), which in the continuum and massless limit, corresponds to $\mathcal{N} = 1$ SUSY Yang-Mills theory. The first step is to perform scale setting. To ensure the robustness of our conclusions, we employed redundancy by computing the lattice spacing using three distinct and independent observables. This analysis was performed across various simulation runs, encompassing different values of the lattice coupling and gluino mass. The results are compiled in Tab. 15. As each observable represents the lattice spacing in its respective unit, compatibility dictates that the values should be proportional to each other, with the proportionality constant determined by the ratio of units. Our findings, as indicated in the table and visually represented in Fig. 24, demonstrate that this proportionality holds for our lattice sample within the limitations of errors. It is important to note that the exact proportionality is only achieved in the continuum limit.

- The final step involved extrapolating the results to the massless gluino limit, thereby obtaining the desired value of the lattice spacing for each bare lattice coupling. First of all, we apply different methodologies to find the critical value of the hopping parameter $\kappa_{adj}^{(c)}$ at which the gluino becomes massless, obtaining perfectly consistent value, enforcing the consistency of our methods. We thus use the PCAC mass to extrapolate the lattice scale in units of $\sqrt{8t_1}$ to the limit of massless gluino, where the theory is expected to be supersymmetric. Remarkably, the resulting dependence of the β function for two commonly used improved lattice couplings closely aligns with the predictions of perturbation theory. This finding also indicates that the range of bare couplings explored in our study falls within the regime of asymptotic.

- As a last application of our method, we extract the scale also for the cases of $N_f = 1, 2$ adjoint fermion and depict our results in Fig. 30 of Section 5.5 in Chapter 5. The plot demonstrates a smooth relationship between the lattice scale and the fermion mass. In the heavy mass limit, the curves converge to a consis-

tent value independent of the number of flavors, resembling the red band representing the scale extracted from pure gauge configurations. In the light fermion sector, the results approach different theories. However, for the case of $N_f = 2$, which involves 2 dynamical adjoint fermions, the behavior is distinct. This theory is believed to exhibit conformal properties in the chiral limit as shown in [134] for our setup. Due to limited data precision in the low mass range, our results can only be compared for compatibility with the previous findings. Additionally, as suggested by recent studies, the case of $N_f = 1$ could also show signals of conformality. The fermion mass dependence of the scale does not provide a conclusive result based on our data, and more precise measurements at lighter masses would be necessary to test this hypothesis.

CONCLUSIONES

En este capítulo final, nos basamos en la amplia investigación realizada a lo largo de esta tesis doctoral para ofrecer una conclusión exhaustiva de nuestro estudio. Nuestro objetivo en este capítulo final es revisar los objetivos de investigación establecidos al principio de este viaje y evaluar hasta qué punto se han logrado.

En esta tesis, nos hemos centrado en la simulación de la teoría $SU(N_c)$ de Yang-Mills en el límite de grandes N_c, junto con sus extensiones que implican N_f sabores de fermiones adjuntos. Nuestro enfoque principal, conocido como "twisted volume reduction", explota el concepto de independencia de volumen que surge en el límite de N_c grande y se explica en Capítulo 2. Según este concepto, al cuantizar la teoría en un toro con condiciones de contorno twisted, el parámetro dinámico que representa la información del volumen viene determinado por una combinación del número de colores y el tamaño real de la red. En el límite de N_c grande, siempre que la simetría del centro permanezca intacta, podemos reducir el espaciotiempo a un único punto, capturando efectivamente la física de una red con una longitud lateral de $a\sqrt{N_c}$. Esta formulación particular se denomina modelo TEK. La reducción también puede aplicarse a fermiones total o parcialmente, dependiendo de la representación. Resumamos ahora los principales logros de este trabajo.

- En el capítulo 3, examinamos el enfoque principal utilizado para generar configuraciones tanto en la teoría pura de Yang-Mills como en la teoría que incorpora fermiones dinámicos adjuntos con $N_f = \frac{1}{2}, 1, 2$. Presentamos la colección de conjuntos que se han generado. Además, dentro del mismo capítulo, discutimos ampliamente la metodología empleada para establecer la escala de la teoría. Como se subraya en Sec. 3.4.1 la técnica del flujo de Wilson sirvió como herramienta principal, complementada por un procedimiento denominado *corrección de la norma*. Este procedimiento elimina eficazmente el efecto de finito-N_c y artefactos de reticulo al tree-level en la teoría de perturbaciones. A través de este enfoque, hemos introducido una nueva escala mejorada al tree-level, denominada $\sqrt{8t_1}$, que nos permite lograr ajustes de escala de alta precisión en nuestras simulaciones. Junto con esta técnica, también proporcionamos información detallada sobre un método alternativo para el ajuste de escalas, que combina el flujo de Wilson con la utilización de los coeficientes de Creutz. Aplicamos específicamente este enfoque alternativo al caso de $N_f = \frac{1}{2}$. Además, presentamos una visión

general de cómo se puede llevar a cabo la espectroscopia de mesones dentro de nuestra configuración.

- Al principio del capítulo 4 aplicamos estas metodologías al caso de Yang-Mills puro. Comprobamos extensamente la aplicabilidad de nuestra metodología de fijación de escala a todos nuestros conjuntos comparando los resultados a distintos valores de N_c y del acoplamiento gauge b. Verificamos que la corrección de la norma es capaz de capturar eficazmente el desplazamiento sistemático de la escala causado por artefactos de red, y puede tratar efectos finitos de N_c. Proporcionamos una lista de las escalas que extrajimos en Tab. 7. En la Sec. 4.2 comparamos la determinación de la escala con este método con la determinación previa de la escala en el modelo TEK realizada con la tensión de la cuerda en [108]. Proporcionamos los valores de la escala en ambas unidades en la Tab. 8 y comprobamos que la razón adimensional $R = \sqrt{\sigma}\sqrt{8t_1}$ es compatible casi siempre con un valor constante, excepto para el caso de la red más gruesa, donde sigue siendo compatible dentro de 2σ. Esto puede entenderse en términos de violaciones de escala y puede explicarse mediante un ajuste lineal en a^2, que conduce a un valor extrapolado de $R = 0,674(8)(12)$ en el límite del continuo. Este resultado es una notable confirmación de la validez del escalado en el rango de nuestros acoplamientos, que se extiende también a una región en la que se espera que el escalado asintótico sea válido.

- Explotando la predicción analítica dada por la teoría de perturbaciones en la región donde el escalado asintótico es válido, podemos calcular el valor del parámetro Λ a partir de nuestra configuración y convertirlo al esquema más familiar $\overline{\text{MS}}$. Utilizamos tres acoplamientos mejorados diferentes para tener una mejor convergencia con la teoría de perturbaciones y obtenemos un valor global de $\sqrt{8t_1}\Lambda_{\overline{\text{MS}}} = 0.3618(47)(29)$, compatible con resultados anteriores del modelo TEK [108] y también con otros resultados de simulaciones en el reticolo estándar en el límite N_c grande de [124, 136]. Un análisis más detallado y un tratamiento cuidadoso de este conjunto se publicarán en una futura publicación.

- La última sección del capítulo 4 está dedicada al cálculo del condensado quiral Σ de la teoría de Yang-Mills en el límite de gran N_c. Esta es una cantidad crucial para entender el mecanismo de la ruptura espontánea de la simetría quiral. Abordamos la determinación desde dos perspectivas diferentes. La primera es una prueba totalmente no-perturbativa de la relación GMOR en el enrejado, que afirma que el condensado quiral puede leerse a partir de la pendiente de la desaparición de la masa del pión en

el límite quiral. Tomamos las cantidades relevantes necesarias de este estudio de [75], donde el espectro del mesón ligero en el límite grande-N_c ha sido calculado en el modelo TEK. Nuestro resultado preliminar para el condensado en unidades de Z_P a las separaciones más finas de la red es de $0.546(15)$ en unidades de $\sqrt{8t_0}$. La otra determinación procede del estudio del *número de modo* del operador de Dirac siguiendo la línea de [126], que conduce a un valor de $0.573(36)$ en unidades de $\sqrt{8t_0}$ para los espaciamientos más finos de la red. Encontramos una notable concordancia entre ambos resultados, lo que supone una confirmación no trivial de la solidez y consistencia de nuestro método. Para la determinación final del condensado quiral, la extrapolación quiral tiene que ser secundada a una continua, para lo cual se necesitan los valores del factor de renormalización Z_P. En el momento de escribir esta Tesis, estos valores no están disponibles, por lo que nuestros resultados deben considerarse como una etapa preliminar de un análisis más completo en una futura publicación.

- Después del caso de la teoría pura de Yang-Mills, en el capítulo pasamos al análisis del caso de $N_f = \frac{1}{2}$ (un fermión de Majorana adjunto), que en el límite continuo y sin masa, corresponde a $\mathcal{N} = 1$ teoría SUSY Yang-Mills. El primer paso es realizar el ajuste de escala. Para asegurar la robustez de nuestras conclusiones, empleamos redundancia calculando el espaciado de la red utilizando tres observables distintos e independientes. Este análisis se realizó a lo largo de varias simulaciones, abarcando diferentes valores del acoplamiento del reticulo y de la masa del gluino. Los resultados se recopilan en Tab. 15. Como cada observable representa el espaciado de la red en su unidad respectiva, la compatibilidad dicta que los valores deben ser proporcionales entre sí, con la constante de proporcionalidad determinada por la relación de unidades. Nuestros resultados, como se indica en la tabla y se representa visualmente en la Fig. **??**, demuestran que esta proporcionalidad se mantiene para nuestra muestra del reticulo dentro de los errores. Es importante señalar que la proporcionalidad exacta sólo se alcanza en el límite del continuo.

- El último paso consistió en extrapolar los resultados al límite del gluino sin masa, obteniendo así el valor deseado del espaciado reticular para cada acoplamiento reticular bare. En primer lugar, aplicamos diferentes metodologías para encontrar el valor crítico del parámetro de salto $\kappa_{adj}^{(c)}$ en el que el gluino deja de tener masa, obteniendo un valor perfectamente consistente, reforzando la consistencia de nuestros métodos. Así, utilizamos la masa PCAC para extrapolar la escala del reticulo en unidades

de $\sqrt{8t_1}$ al límite de gluino masivo, donde se espera que la teoría sea supersimétrica. Sorprendentemente, la dependencia resultante de la función β para dos acoplamientos de celosía mejorados comúnmente utilizados se alinea estrechamente con las predicciones de la teoría de perturbaciones. Este hallazgo también indica que el rango de acoplamientos bare explorado en nuestro estudio cae dentro del régimen de escalamiento asintótico.

- Como última aplicación de nuestro método, extraemos la escala también para los casos de $N_f = 1, 2$ fermión adjunto y representamos nuestros resultados en la Fig. 30 de la Sección 5.5 del Capítulo 5. El gráfico muestra una relación suave entre la escala de la red y la masa del fermión. En el límite de masa pesada, las curvas convergen a un valor consistente independiente del número de sabores, asemejándose a la banda roja que representa la escala extraída de configuraciones gauge puras. En el sector de los fermiones ligeros, los resultados se aproximan a teorías diferentes. Sin embargo, para el caso de $N_f = 2$, que implica 2 fermiones dinámicos adyacentes, el comportamiento es distinto. Se cree que esta teoría exhibe propiedades conformes en el límite quiral como se muestra en [134] para nuestra configuración. Debido a la limitada precisión de los datos en el rango de masas bajas, nuestros resultados solo pueden compararse en cuanto a compatibilidad con los hallazgos anteriores. Además, como sugieren estudios recientes, el caso de $N_f = 1$ también podría mostrar señales de conformidad. La dependencia de la escala con la masa del fermión no proporciona un resultado concluyente basado en nuestros datos, y serían necesarias mediciones más precisas a masas más ligeras para probar esta hipótesis.

BIBLIOGRAPHY

[1] G. Aad et al. "Observation of a new particle in the search for the Standard Model Higgs boson with the ATLAS detector at the LHC." In: *Physics Letters B* 716.1 (Sept. 2012), pp. 1–29. DOI: 10.1016/j.physletb.2012.08.020. URL: https://doi.org/10.1016/j.physletb.2012.08.020.

[2] S. Chatrchyan et al. "Observation of a new boson at a mass of 125 GeV with the CMS experiment at the LHC." In: *Physics Letters B* 716.1 (Sept. 2012), pp. 30–61. DOI: 10.1016/j.physletb.2012.08.021. URL: https://doi.org/10.1016/j.physletb.2012.08.021.

[3] B. Abi et al. "Measurement of the Positive Muon Anomalous Magnetic Moment to 0.46 ppm." In: *Phys. Rev. Lett.* 126 (14 2021), p. 141801. DOI: 10.1103/PhysRevLett.126.141801. URL: https://link.aps.org/doi/10.1103/PhysRevLett.126.141801.

[4] T. Aoyama et al. "The anomalous magnetic moment of the muon in the Standard Model." In: *Physics Reports* 887 (Dec. 2020), pp. 1–166. DOI: 10.1016/j.physrep.2020.07.006. URL: https://doi.org/10.1016/j.physrep.2020.07.006.

[5] S. Borsanyi et al. "Leading hadronic contribution to the muon magnetic moment from lattice QCD." In: *Nature* 593.7857 (Apr. 2021), pp. 51–55. DOI: 10.1038/s41586-021-03418-1. URL: https://doi.org/10.1038/s41586-021-03418-1.

[6] David J. Gross and Frank Wilczek. "Ultraviolet Behavior of Non-Abelian Gauge Theories." In: *Phys. Rev. Lett.* 30 (26 1973), pp. 1343–1346. DOI: 10.1103/PhysRevLett.30.1343. URL: https://link.aps.org/doi/10.1103/PhysRevLett.30.1343.

[7] H. David Politzer. "Reliable Perturbative Results for Strong Interactions?" In: *Phys. Rev. Lett.* 30 (26 1973), pp. 1346–1349. DOI: 10.1103/PhysRevLett.30.1346. URL: https://link.aps.org/doi/10.1103/PhysRevLett.30.1346.

[8] Biagio Lucini and Marco Panero. "Gauge theories at large-N_c." In: *Physics Reports* 526.2 (May 2013), pp. 93–163. DOI: 10.1016/j.physrep.2013.01.001. URL: https://doi.org/10.1016/j.physrep.2013.01.001.

[9] Gerard 't Hooft. "A planar diagram theory for strong interactions." In: *Nuclear Physics B* 72.3 (Apr. 1974), pp. 461–473. DOI: 10.1016/0550-3213(74)90154-0. URL: https://doi.org/10.1016/0550-3213(74)90154-0.

[10] Kenneth G. Wilson. "Confinement of quarks." In: *Phys. Rev. D* 10 (8 1974), pp. 2445–2459. DOI: 10.1103/PhysRevD.10.2445. URL: https://link.aps.org/doi/10.1103/PhysRevD.10.2445.

[11] Hartmut Wittig. "Progress on $(g-2)_\mu$ from Lattice QCD." In: *57th Rencontres de Moriond on Electroweak Interactions and Unified Theories*. June 2023. arXiv: 2306.04165 [hep-ph].

[12] Pilar Hernández and Fernando Romero-López. "The large $$N_{c}$$ limit of QCD on the lattice." In: *The European Physical Journal A* 57.2 (Feb. 2021). DOI: 10.1140/epja/s10050-021-00374-2. URL: https://doi.org/10.1140/epja/s10050-021-00374-2.

[13] A. González-Arroyo and M. Okawa. "Twisted-Eguchi-Kawai model: A reduced model for large-N lattice gauge theory." In: *Phys. Rev. D* 27 (10 1983), pp. 2397–2411. DOI: 10.1103/PhysRevD.27.2397. URL: https://link.aps.org/doi/10.1103/PhysRevD.27.2397.

[14] A. Armoni, M. Shifman, and G. Veneziano. "From superYang-Mills theory to QCD: Planar equivalence and its implications." In: *From fields to strings: Circumnavigating theoretical physics. Ian Kogan memorial collection (3 volume set)*. Ed. by M. Shifman, A. Vainshtein, and J. Wheater. Mar. 2004, pp. 353–444. DOI: 10.1142/9789812775344_0013. arXiv: hep-th/0403071.

[15] A. Armoni, M. Shifman, and G. Veneziano. "Exact results in non-supersymmetric large N orientifold field theories." In: *Nucl. Phys. B* 667 (2003), pp. 170–182. DOI: 10.1016/S0550-3213(03)00538-8. arXiv: hep-th/0302163.

[16] Michael E. Peskin and Daniel V. Schroeder. *An Introduction to quantum field theory*. Reading, USA: Addison-Wesley, 1995. ISBN: 978-0-201-50397-5.

[17] M. Srednicki. *Quantum field theory*. Cambridge University Press, Jan. 2007. ISBN: 978-0-521-86449-7, 978-0-511-26720-8.

[18] G. Veneziano. "Some aspects of a unified approach to gauge, dual and Gribov theories." In: *Nuclear Physics B* 117.2 (Dec. 1976), pp. 519–545. DOI: 10.1016/0550-3213(76)90412-0. URL: https://doi.org/10.1016/0550-3213(76)90412-0.

[19] T. Banks and A. Casher. "Chiral symmetry breaking in confining theories." In: *Nuclear Physics B* 169.1-2 (June 1980), pp. 103–125. DOI: 10.1016/0550-3213(80)90255-2. URL: https://doi.org/10.1016/0550-3213(80)90255-2.

[20] Murray Gell-Mann, R. J. Oakes, and B. Renner. "Behavior of Current Divergences under $SU_3 \times SU_3$." In: *Phys. Rev.* 175 (5 1968), pp. 2195–2199. DOI: 10.1103/PhysRev.175.2195. URL: https://link.aps.org/doi/10.1103/PhysRev.175.2195.

[21] David B. Kaplan. "Chiral Symmetry and Lattice Fermions." In: *Les Houches Summer School: Session 93: Modern perspectives in lattice QCD: Quantum field theory and high performance computing*. Dec. 2009, pp. 223–272. arXiv: 0912.2560 [hep-lat].

[22] Kazuo Fujikawa. "A continuum limit of the chiral Jacobian in lattice gauge theory." In: *Nuclear Physics B* 546.1-2 (Apr. 1999), pp. 480–494. DOI: 10.1016/s0550-3213(99)00042-5. URL: https://doi.org/10.1016/s0550-3213(99)00042-5.

[23] M. F. Atiyah and I. M. Singer. "The Index of Elliptic Operators: V." In: *The Annals of Mathematics* 93.1 (Jan. 1971), p. 139. DOI: 10.2307/1970757. URL: https://doi.org/10.2307/1970757.

[24] S. Martin. "A SUPERSYMMETRY PRIMER." In: *Perspectives on Supersymmetry*. WORLD SCIENTIFIC, July 1998, pp. 1–98. DOI: 10.1142/9789812839657_0001. URL: https://doi.org/10.1142/9789812839657_0001.

[25] Georg Bergner and Simon Catterall. "Supersymmetry on the lattice." In: *International Journal of Modern Physics A* 31.22 (Aug. 2016), p. 1643005. DOI: 10.1142/s0217751x16430053. URL: https://doi.org/10.1142/s0217751x16430053.

[26] D. B. Kaplan. "Supersymmetry on the lattice." In: *Eur. Phys. J. ST* 152 (2007). Ed. by C. Gattringer and C. B. Lang, pp. 89–112. DOI: 10.1140/epjst/e2007-00378-1.

[27] Edward Witten. "Constraints on supersymmetry breaking." In: *Nuclear Physics B* 202.2 (July 1982), pp. 253–316. DOI: 10.1016/0550-3213(82)90071-2. URL: https://doi.org/10.1016/0550-3213(82)90071-2.

[28] N. Seiberg. "Naturalness versus supersymmetric non-renormalization theorems." In: *Physics Letters B* 318.3 (Dec. 1993), pp. 469–475. DOI: 10.1016/0370-2693(93)91541-t. URL: https://doi.org/10.1016/0370-2693(93)91541-t.

[29] G. R. Farrar, G. Gabadadze, and M. Schwetz. "Effective action of $\mathcal{N} = 1$ supersymmetric Yang-Mills theory." In: *Physical Review D* 58.1 (June 1998). DOI: 10.1103/physrevd.58.015009. URL: https://doi.org/10.1103/physrevd.58.015009.

[30] G. R. Farrar, G. Gabadadze, and M. Schwetz. "Spectrum of softly broken $\mathcal{N} = 1$ supersymmetric Yang-Mills theory." In: *Physical Review D* 60.3 (June 1999). DOI: 10.1103/physrevd.60.035002. URL: https://doi.org/10.1103/physrevd.60.035002.

[31] H.B. Nielsen and M. Ninomiya. "A no-go theorem for regularizing chiral fermions." In: *Physics Letters B* 105.2-3 (Oct. 1981), pp. 219–223. DOI: 10.1016/0370-2693(81)91026-1. URL: https://doi.org/10.1016/0370-2693(81)91026-1.

[32] H.B. Nielsen and M. Ninomiya. "Absence of neutrinos on a lattice." In: *Nuclear Physics B* 185.1 (July 1981), pp. 20–40. DOI: 10.1016/0550-3213(81)90361-8. URL: https://doi.org/10.1016/0550-3213(81)90361-8.

[33] H.B. Nielsen and M. Ninomiya. "Absence of neutrinos on a lattice." In: *Nuclear Physics B* 193.1 (Dec. 1981), pp. 173–194. DOI: 10.1016/0550-3213(81)90524-1. URL: https://doi.org/10.1016/0550-3213(81)90524-1.

[34] David B. Kaplan. "Dynamical Generation of Supersymmetry." In: *Phys. Lett. B* 136 (1984), pp. 162–164. DOI: 10.1016/0370-2693(84)91172-9.

[35] G. Curci and G. Veneziano. "Supersymmetry and the Lattice: A Reconciliation?" In: *Nucl. Phys. B* 292 (1987), pp. 555–572. DOI: 10.1016/0550-3213(87)90660-2.

[36] Sajid Ali, Georg Bergner, Henning Gerber, Istvan Montvay, Gernot Münster, Stefano Piemonte, and Philipp Scior. "Numerical results for the lightest bound states in $\mathcal{N} = 1$ supersymmetric SU(3) Yang-Mills theory." In: *Phys. Rev. Lett.* 122.22 (2019), p. 221601. DOI: 10.1103/PhysRevLett.122.221601. arXiv: 1902.11127 [hep-lat].

[37] Sajid Ali, Henning Gerber, Istvan Montvay, Gernot Münster, Stefano Piemonte, Philipp Scior, and Georg Bergner. "Analysis of Ward identities in supersymmetric Yang–Mills theory." In: *Eur. Phys. J. C* 78.5 (2018), p. 404. DOI: 10.1140/epjc/s10052-018-5887-9. arXiv: 1802.07067 [hep-lat].

[38] Sajid Ali, Georg Bergner, Henning Gerber, Pietro Giudice, Istvan Montvay, Gernot Münster, Stefano Piemonte, and Philipp Scior. "The light bound states of $\mathcal{N} = 1$ supersymmetric SU(3) Yang-Mills theory on the lattice." In: *JHEP* 03 (2018), p. 113. DOI: 10.1007/JHEP03(2018)113. arXiv: 1801.08062 [hep-lat].

[39] Gernot Münster and Hendrik Stüwe. "The mass of the adjoint pion in $\mathcal{N} = 1$ supersymmetric Yang-Mills theory." In: *JHEP* 05 (2014), p. 034. DOI: 10.1007/JHEP05(2014)034. arXiv: 1402.6616 [hep-th].

[40] Georg Bergner, Pietro Giudice, Gernot Münster, Istvan Montvay, and Stefano Piemonte. "The light bound states of supersymmetric SU(2) Yang-Mills theory." In: *JHEP* 03 (2016), p. 080. DOI: 10.1007/JHEP03(2016)080. arXiv: 1512.07014 [hep-lat].

[41] Christof Gattringer and Christian B. Lang. *Quantum Chromodynamics on the Lattice*. Springer Berlin Heidelberg, 2010. DOI: 10.1007/978-3-642-01850-3. URL: https://doi.org/10.1007/978-3-642-01850-3.

[42] Martin Lüscher. *Computational Strategies in Lattice QCD*. 2010. DOI: 10.48550/ARXIV.1002.4232. URL: https://arxiv.org/abs/1002.4232.

[43] Laurent Lellouch, R. Sommer, Anastassios Vladikas, Benjamin Svetitsky, and Leticia Cugliandolo. *Modern perspectives in lattice QCD: Quantum field theory and high performance computing. : Proceedings, International School, 93rd Session, Les Houches, France, August 3-28, 2009*. Aug. 2011.

[44] G. 't Hooft. "A property of electric and magnetic flux in non-Abelian gauge theories." In: *Nuclear Physics B* 153 (1979), pp. 141–160. ISSN: 0550-3213. DOI: https://doi.org/10.1016/0550-3213(79)90595-9. URL: https://www.sciencedirect.com/science/article/pii/0550321379905959.

[45] G. 't Hooft. "Confinement and Topology in Nonabelian Gauge Theories." In: *Acta Phys. Austriaca Suppl.* 22 (1980), pp. 531–586.

[46] Antonio González-Arroyo, J. Jurkiewicz, and C. P. Korthals-Altes. "Ground-state metamorphosis for Yang-Mills fields on a finite periodic lattice." In: Dec. 1981.

[47] M. Luscher. "Some Analytic Results Concerning the Mass Spectrum of Yang-Mills Gauge Theories on a Torus." In: *Nucl. Phys. B* 219 (1983), pp. 233–261. DOI: 10.1016/0550-3213(83)90436-4.

[48] M. Luscher and G. Munster. "Weak Coupling Expansion of the Low Lying Energy Values in the SU(2) Gauge Theory on a Torus." In: *Nucl. Phys. B* 232 (1984), p. 445. DOI: 10.1016/0550-3213(84)90038-5.

[49] Pierre van Baal and Jeffrey Koller. "QCD on a Torus and Electric Flux Energies From Tunneling." In: *Annals Phys.* 174 (1987), p. 299. DOI: 10.1016/0003-4916(87)90032-7.

[50] Jeffrey Koller and Pierre van Baal. "A Nonperturbative Analysis in Finite Volume Gauge Theory." In: *Nucl. Phys. B* 302 (1988), pp. 1–64. DOI: 10.1016/0550-3213(88)90665-7.

[51] Antonio González-Arroyo. "Yang-Mills fields on the four-dimensional torus. Part 1.: Classical theory." In: *Advanced Summer School on Nonperturbative Quantum Field Physics*. June 1997, pp. 57–91. arXiv: hep-th/9807108.

[52] Margarita García Pérez, Antonio González-Arroyo, and Masanori Okawa. "Perturbative contributions to Wilson loops in twisted lattice boxes and reduced models." In: *Journal of High Energy Physics* 2017.10 (Oct. 2017). DOI: 10.1007/jhep10(2017)150. URL: https://doi.org/10.1007/jhep10(2017)150.

[53] A. González-Arroyo and C.P. Korthals Altes. "Reduced model for large N continuum field theories." In: *Physics Letters B* 131.4-6 (Nov. 1983), pp. 396–398. DOI: 10.1016/0370-2693(83)90526-9. URL: https://doi.org/10.1016/0370-2693(83)90526-9.

[54] Tohru Eguchi and Hikaru Kawai. "Reduction of Dynamical Degrees of Freedom in the Large-N Gauge Theory." In: *Phys. Rev. Lett.* 48 (16 1982), pp. 1063–1066. DOI: 10.1103/PhysRevLett.48.1063. URL: https://link.aps.org/doi/10.1103/PhysRevLett.48.1063.

[55] Y. M. Makeenko and Alexander A. Migdal. "Exact Equation for the Loop Average in Multicolor QCD." In: *Phys. Lett. B* 88 (1979). [Erratum: Phys.Lett.B 89, 437 (1980)], p. 135. DOI: 10.1016/0370-2693(79)90131-X.

[56] Gyan Bhanot, Urs M. Heller, and Herbert Neuberger. "The quenched Eguchi-Kawai model." In: *Physics Letters B* 113.1 (1982), pp. 47–50. ISSN: 0370-2693. DOI: https://doi.org/10.1016/0370-2693(82)90106-X. URL: https://www.sciencedirect.com/science/article/pii/037026938290106X.

[57] I. Bars. "Strings from reduced large-N gauge theory via area preserving diffeomorphisms." In: *Physics Letters B* 245.1 (1990), pp. 35–42. ISSN: 0370-2693. DOI: https://doi.org/10.1016/0370-2693(90)90161-X. URL: https://www.sciencedirect.com/science/article/pii/037026939090161X.

[58] Masanori Okawa. "Monte Carlo Study of the Eguchi-Kawai Model." In: *Phys. Rev. Lett.* 49 (6 1982), pp. 353–356. DOI: 10.1103/PhysRevLett.49.353. URL: https://link.aps.org/doi/10.1103/PhysRevLett.49.353.

[59] G. Parisi. "A simple expression for planar field theories." In: *Physics Letters B* 112.6 (1982), pp. 463–464. ISSN: 0370-2693. DOI: https://doi.org/10.1016/0370-2693(82)90849-8. URL: https://www.sciencedirect.com/science/article/pii/0370269382908498.

[60] Barak Bringoltz and Stephen R. Sharpe. "Breakdown of large-N quenched reduction in SU(N) lattice gauge theories." In: *Phys. Rev. D* 78 (3 2008), p. 034507. DOI: 10.1103/PhysRevD.78.034507. URL: https://link.aps.org/doi/10.1103/PhysRevD.78.034507.

[61] Herbert Neuberger. "Quenched Eguchi-Kawai model revisited." In: *Phys. Rev. D* 102 (9 2020), p. 094503. DOI: 10.1103/PhysRevD.102.094503. URL: https://link.aps.org/doi/10.1103/PhysRevD.102.094503.

[62] A. González-Arroyo and M. Okawa. "A twisted model for large-N lattice gauge theory." In: *Physics Letters B* 120.1 (1983), pp. 174–178. ISSN: 0370-2693. DOI: https://doi.org/10.1016/0370-2693(83)90647-0. URL: https://www.sciencedirect.com/science/article/pii/0370269383906470.

[63] Antonio González-Arroyo and Masanori Okawa. "Large N reduction with the twisted Eguchi-Kawai model." In: *Journal of High Energy Physics* 2010.7 (July 2010). DOI: 10.1007/jhep07(2010)043. URL: https://doi.org/10.1007/jhep07(2010)043.

[64] Antonio González-Arroyo and Masanori Okawa. "Testing volume independence of SU(N) pure gauge theories at large N." In: *Journal of High Energy Physics* 2014.12 (Dec. 2014). DOI: 10.1007/jhep12(2014)106. URL: https://doi.org/10.1007/jhep12(2014)106.

[65] Margarita Garcia Perez, Antonio Gonzalez-Arroyo, and Masanori Okawa. "Volume independence for Yang-Mills fields on the twisted torus." In: *Int. J. Mod. Phys. A* 29.25 (2014), p. 1445001. DOI: 10.1142/S0217751X14450018. arXiv: 1406.5655 [hep-th].

[66] M. Teper and H. Vairinhos. "Symmetry breaking in twisted Eguchi–Kawai models." In: *Physics Letters B* 652.5 (2007), pp. 359–369. ISSN: 0370-2693. DOI: https://doi.org/10.1016/j.physletb.2007.06.037. URL: https://www.sciencedirect.com/science/article/pii/S0370269307007502.

[67] T. Azeyanagi, T. Hirata, M. Hanada, and T. Ishikawa. "Phase structure of twisted Eguchi-Kawai model." In: *Journal of High Energy Physics* 2008.01 (2008), p. 025. DOI: 10.1088/1126-6708/2008/01/025. URL: https://dx.doi.org/10.1088/1126-6708/2008/01/025.

[68] Wolfgang Bietenholz, Jun Nishimura, Yoshiaki Susaki, and Jan Volkholz. "A non-perturbative study of 4d U(1) non-commutative gauge theory — the fate of one-loop instability." In: *Journal of High Energy Physics* 2006.10 (Oct. 2006), pp. 042–042. DOI: 10.1088/1126-6708/2006/10/042. URL: https://doi.org/10.1088/1126-6708/2006/10/042.

[69] G. Aldazabal, N. Parga, M. Okawa, and Antonio González-Arroyo. "Large-N Reduced Models and Stochastic Quantization." In: *Phys. Lett. B* 129 (1983), pp. 90–94. DOI: 10.1016/0370-2693(83)90735-9.

[70] A. Coste, Antonio González-Arroyo, J. Jurkiewicz, and C. P. Korthals Altes. "Zero Momentum Contribution to Wilson Loops in Periodic Boxes." In: *Nucl. Phys. B* 262 (1985), pp. 67–94. DOI: 10.1016/0550-3213(85)90064-1.

[71] Margarita Garcia Perez, Antonio González-Arroyo, Liam Keegan, and Masanori Okawa. "The SU(∞) twisted gradient flow running coupling." In: *JHEP* 01 (2015), p. 038. DOI: 10.1007/JHEP01(2015)038. arXiv: 1412.0941 [hep-lat].

[72] Eduardo I. Bribian and Margarita Garcia Perez. "The twisted gradient flow coupling at one loop." In: *JHEP* 03 (2019), p. 200. DOI: 10.1007/JHEP03(2019)200. arXiv: 1903.08029 [hep-lat].

[73] Antonio González-Arroyo and Masanori Okawa. "Large N meson masses from a matrix model." In: *Phys. Lett. B* 755 (2016), pp. 132–137. DOI: 10.1016/j.physletb.2016.02.001. arXiv: 1510.05428 [hep-lat].

[74] Antonio González-Arroyo and Masanori Okawa. "Twisted spacetime reduced model of large N QCD with two adjoint Wilson fermions." In: *Phys. Rev. D* 88 (2013), p. 014514. DOI: 10.1103/PhysRevD.88.014514. arXiv: 1305.6253 [hep-lat].

[75] Margarita García Pérez, Antonio González-Arroyo, and Masanori Okawa. "Meson spectrum in the large N limit." In: *JHEP* 04 (2021), p. 230. DOI: 10.1007/JHEP04(2021)230. arXiv: 2011.13061 [hep-lat].

[76] Antonio González-Arroyo and Masanori Okawa. "Large N meson masses from a matrix model." In: *Phys. Lett. B* 755 (2016), pp. 132–137. DOI: 10.1016/j.physletb.2016.02.001. arXiv: 1510.05428 [hep-lat].

[77] Margarita García Pérez, Antonio González-Arroyo, and Masanori Okawa. "Meson spectrum in the large N limit." In: *JHEP* 04 (2021), p. 230. DOI: 10.1007/JHEP04(2021)230. arXiv: 2011.13061 [hep-lat].

[78] Pietro Butti, Margarita García Pérez, Antonio González-Arroyo, Ken-Ichi Ishikawa, and Masanori Okawa. "Scale setting for large-N_c SUSY Yang-Mills on the lattice." In: *JHEP* 07 (2022), p. 074. DOI: 10.1007/JHEP07(2022)074. arXiv: 2205.03166 [hep-lat].

[79] K. Fabricius and O. Haan. "Heat Bath Method for the Twisted Eguchi-Kawai Model." In: *Phys. Lett. B* 143 (1984), pp. 459–462. DOI: 10.1016/0370-2693(84)91502-8.

[80] Michael Creutz. "Monte Carlo study of quantized SU(2) gauge theory." In: *Phys. Rev. D* 21 (8 1980), pp. 2308–2315. DOI: 10.1103/PhysRevD.21.2308. URL: https://link.aps.org/doi/10.1103/PhysRevD.21.2308.

[81] A.D. Kennedy and B.J. Pendleton. "Improved heatbath method for Monte Carlo calculations in lattice gauge theories." In: *Physics Letters B* 156.5-6 (June 1985), pp. 393–399. DOI: 10.1016/0370-2693(85)91632-6. URL: https://doi.org/10.1016/0370-2693(85)91632-6.

[82] Michael Creutz. "Overrelaxation and Monte Carlo simulation." In: *Phys. Rev. D* 36 (2 1987), pp. 515–519. DOI: 10.1103/PhysRevD.36.515. URL: https://link.aps.org/doi/10.1103/PhysRevD.36.515.

[83] Frank R. Brown and Thomas J. Woch. "Overrelaxed heat-bath and Metropolis algorithms for accelerating pure gauge Monte Carlo calculations." In: *Phys. Rev. Lett.* 58 (23 1987), pp. 2394–2396. DOI: 10.1103/PhysRevLett.58.2394. URL: https://link.aps.org/doi/10.1103/PhysRevLett.58.2394.

[84] N. Cabibbo and E. Marinari. "A New Method for Updating SU(N) Matrices in Computer Simulations of Gauge Theories." In: *Phys. Lett. B* 119 (1982), pp. 387–390. DOI: 10.1016/0370-2693(82)90696-7.

[85] Masanori Okawa. "Monte Carlo Study of the Eguchi-Kawai Model." In: *Phys. Rev. Lett.* 49 (6 1982), pp. 353–356. DOI: 10.1103/PhysRevLett.49.353. URL: https://link.aps.org/doi/10.1103/PhysRevLett.49.353.

[86] Margarita García Pérez, Antonio González-Arroyo, Liam Keegan, Masanori Okawa, and Alberto Ramos. "A comparison of updating algorithms for large N reduced models." In: *JHEP* 06 (2015), p. 193. DOI: 10.1007/JHEP06(2015)193. arXiv: 1505.05784 [hep-lat].

[87] Simon Duane, A.D. Kennedy, Brian J. Pendleton, and Duncan Roweth. "Hybrid Monte Carlo." In: *Physics Letters B* 195.2 (Sept. 1987), pp. 216–222. DOI: 10.1016/0370-2693(87)91197-x. URL: https://doi.org/10.1016/0370-2693(87)91197-x.

[88] A. D. Kennedy, Ivan Horvath, and Stefan Sint. "A New exact method for dynamical fermion computations with nonlocal actions." In: *Nucl. Phys. B Proc. Suppl.* 73 (1999). Ed. by Thomas A. DeGrand, Carleton E. DeTar, R. Sugar, and D. Toussaint, pp. 834–836. DOI: 10.1016/S0920-5632(99)85217-7. arXiv: hep-lat/9809092.

[89] M. A. Clark and A. D. Kennedy. "The RHMC algorithm for two flavors of dynamical staggered fermions." In: *Nucl. Phys. B Proc. Suppl.* 129 (2004). Ed. by S. Aoki, S. Hashimoto, N. Ishizuka, K. Kanaya, and Y. Kuramashi, pp. 850–852. DOI: 10.1016/S0920-5632(03)02732-4. arXiv: hep-lat/0309084.

[90] M. A. Clark and A. D. Kennedy. "Accelerating Staggered Fermion Dynamics with the Rational Hybrid Monte Carlo (RHMC) Algorithm." In: *Phys. Rev. D* 75 (2007), p. 011502. DOI: 10.1103/PhysRevD.75.011502. arXiv: hep-lat/0610047.

[91] M. A. Clark. "The Rational Hybrid Monte Carlo Algorithm." In: *PoS* LAT2006 (2006). Ed. by Tom Blum, Michael Creutz, Carleton DeTar, Frithjof Karsch, Andreas Kronfeld, Colin Morningstar, David Richards, Junko Shigemitsu, and Doug Toussaint, p. 004. DOI: 10.22323/1.032.0004. arXiv: hep-lat/0610048.

[92] I. Montvay. "An algorithm for gluinos on the lattice." In: *Nuclear Physics B* 466.1 (1996), pp. 259–281. ISSN: 0550-3213. DOI: https://doi.org/10.1016/0550-3213(96)00086-7. URL: https://www.sciencedirect.com/science/article/pii/0550321396000867.

[93] J. Wuilloud. "The Wilson-Dirac operator eigenspectrum for the theories of QCD and super Yang-Mills with one flavour." PhD thesis. U. Munster, 2010.

[94] Georg Bergner, Gernot Munster, Dirk Sandbrink, Umut D. Ozugurel, and Istvan Montvay. "Supersymmetric Yang-Mills theory: a step towards the continuum." In: *29th International Symposium on Lattice Field Theory*. Nov. 2011. arXiv: 1111.3012 [hep-lat].

[95] G. Bergner and J. Wuilloud. "Acceleration of the Arnoldi method and real eigenvalues of the non-Hermitian Wilson-Dirac operator." In: *Comput. Phys. Commun.* 183 (2012), pp. 299–304. DOI: 10.1016/j.cpc.2011.10.007. arXiv: 1104.1363 [hep-lat].

[96] Richard B. Lehoucq, Danny C. Sorensen, and Chao Yang. *ARPACK users' guide - solution of large-scale eigenvalue problems with implicitly restarted Arnoldi methods.* Software, environments, tools. SIAM, 1998, pp. I–XV, 1–142. ISBN: 978-0-89871-407-4.

[97] K. Demmouche, F. Farchioni, A. Ferling, I. Montvay, G. Munster, E. E. Scholz, and J. Wuilloud. "Simulation of 4d N=1 supersymmetric Yang-Mills theory with Symanzik improved gauge action and stout smearing." In: *Eur. Phys. J. C* 69 (2010), pp. 147–157. DOI: 10.1140/epjc/s10052-010-1390-7. arXiv: 1003.2073 [hep-lat].

[98] Ulli Wolff. "Monte Carlo errors with less errors." In: *Computer Physics Communications* 156.2 (Jan. 2004), pp. 143–153. DOI: 10.1016/s0010-4655(03)00467-3. URL: https://doi.org/10.1016/s0010-4655(03)00467-3.

[99] Alberto Ramos. "Automatic differentiation for error analysis of Monte Carlo data." In: *Computer Physics Communications* 238 (May 2019), pp. 19–35. DOI: 10.1016/j.cpc.2018.12.020. URL: https://doi.org/10.1016/j.cpc.2018.12.020.

[100] Stefan Schaefer, Rainer Sommer, and Francesco Virotta. "Critical slowing down and error analysis in lattice QCD simulations." In: *Nuclear Physics B* 845.1 (Apr. 2011), pp. 93–119. DOI:

10.1016/j.nuclphysb.2010.11.020. URL: https://doi.org/10.1016/j.nuclphysb.2010.11.020.

[101] Francesco Virotta. *Critical slowing down and error analysis of lattice QCD simulations*. en. 2012. DOI: 10.18452/16502. URL: https://edoc.hu-berlin.de/handle/18452/17154.

[102] R. Sommer. "A New way to set the energy scale in lattice gauge theories and its applications to the static force and alpha-s in SU(2) Yang-Mills theory." In: *Nucl. Phys. B* 411 (1994), pp. 839–854. DOI: 10.1016/0550-3213(94)90473-1. arXiv: hep-lat/9310022.

[103] Martin Lüscher. "Properties and uses of the Wilson flow in lattice QCD." In: *JHEP* 08 (2010). [Erratum: JHEP 03, 092 (2014)], p. 071. DOI: 10.1007/JHEP08(2010)071. arXiv: 1006.4518 [hep-lat].

[104] Szabolcs Borsanyi et al. "High-precision scale setting in lattice QCD." In: *JHEP* 09 (2012), p. 010. DOI: 10.1007/JHEP09(2012)010. arXiv: 1203.4469 [hep-lat].

[105] Y. Aoki et al. "FLAG Review 2021." In: *Eur. Phys. J. C* 82.10 (2022), p. 869. DOI: 10.1140/epjc/s10052-022-10536-1. arXiv: 2111.09849 [hep-lat].

[106] Martin Luscher. "Trivializing maps, the Wilson flow and the HMC algorithm." In: *Commun. Math. Phys.* 293 (2010), pp. 899–919. DOI: 10.1007/s00220-009-0953-7. arXiv: 0907.5491 [hep-lat].

[107] Zoltan Fodor, Kieran Holland, Julius Kuti, Santanu Mondal, Daniel Nogradi, and Chik Him Wong. "The lattice gradient flow at tree-level and its improvement." In: *JHEP* 09 (2014), p. 018. DOI: 10.1007/JHEP09(2014)018. arXiv: 1406.0827 [hep-lat].

[108] Antonio Gonzalez-Arroyo and Masanori Okawa. "The string tension from smeared Wilson loops at large N." In: *Phys. Lett. B* 718 (2013), pp. 1524–1528. DOI: 10.1016/j.physletb.2012.12.027. arXiv: 1206.0049 [hep-th].

[109] S. Gusken, U. Low, K. H. Mutter, R. Sommer, A. Patel, and K. Schilling. "Nonsinglet Axial Vector Couplings of the Baryon Octet in Lattice QCD." In: *Phys. Lett. B* 227 (1989), pp. 266–269. DOI: 10.1016/S0370-2693(89)80034-6.

[110] S. Gusken. "A Study of smearing techniques for hadron correlation functions." In: *Nucl. Phys. B Proc. Suppl.* 17 (1990). Ed. by N. Cabibbo, E. Marinari, G. Parisi, Roberto Petronzio, L. Maiani, G. Martinelli, and Roberto Pettorino, pp. 361–364. DOI: 10.1016/0920-5632(90)90273-W.

[111] Gunnar S. Bali, Bernhard Lang, Bernhard U. Musch, and Andreas Schäfer. "Novel quark smearing for hadrons with high momenta in lattice QCD." In: *Phys. Rev. D* 93.9 (2016), p. 094515. DOI: 10.1103/PhysRevD.93.094515. arXiv: 1602.05525 [hep-lat].

[112] M. Albanese et al. "Glueball Masses and String Tension in Lattice QCD." In: *Phys. Lett. B* 192 (1987), pp. 163–169. DOI: 10.1016/0370-2693(87)91160-9.

[113] Mattia Dalla Brida and Alberto Ramos. "The gradient flow coupling at high-energy and the scale of SU(3) Yang–Mills theory." In: *Eur. Phys. J. C* 79.8 (2019), p. 720. DOI: 10.1140/epjc/s10052-019-7228-z. arXiv: 1905.05147 [hep-lat].

[114] O.V. Tarasov, A.A. Vladimirov, and A.Yu. Zharkov. "The gell-mann-low function of QCD in the three-loop approximation." In: *Physics Letters B* 93.4 (June 1980), pp. 429–432. DOI: 10.1016/0370-2693(80)90358-5. URL: https://doi.org/10.1016/0370-2693(80)90358-5.

[115] Martin Lüscher and Peter Weisz. "Computation of the relation between the bare lattice coupling and the coupling in SU(N) gauge theories to two loops." In: *Nuclear Physics B* 452.1-2 (Oct. 1995), pp. 234–260. DOI: 10.1016/0550-3213(95)00338-s. URL: https://doi.org/10.1016/0550-3213(95)00338-s.

[116] C. Christou, A. Feo, H. Panagopoulos, and E. Vicari. "The three-loop β-function of SU(N) lattice gauge theories with Wilson fermions." In: *Nuclear Physics B* 525.1-2 (Aug. 1998), pp. 387–400. DOI: 10.1016/s0550-3213(98)00248-x. URL: https://doi.org/10.1016/s0550-3213(98)00248-x.

[117] Eduardo I. Bribian, Jorge Luis Dasilva Golan, Margarita Garcia Perez, and Alberto Ramos. "Memory efficient finite volume schemes with twisted boundary conditions." In: *Eur. Phys. J. C* 81.10 (2021), p. 951. DOI: 10.1140/epjc/s10052-021-09718-0. arXiv: 2107.03747 [hep-lat].

[118] Chris Allton, Michael Teper, and Aurora Trivini. "On the running of the bare coupling in SU(N) lattice gauge theories." In: *JHEP* 07 (2008), p. 021. DOI: 10.1088/1126-6708/2008/07/021. arXiv: 0803.1092 [hep-lat].

[119] Anna Hasenfratz and Peter Hasenfratz. "The connection between the Λ parameters of lattice and continuum QCD." In: *Physics Letters B* 93.1-2 (June 1980), pp. 165–169. DOI: 10.1016/0370-2693(80)90118-5. URL: https://doi.org/10.1016/0370-2693(80)90118-5.

[120] G. Martinelli, G. Parisi, and R. Petronzio. "Monte Carlo Simulations for the Two-dimensional O(3) Nonlinear σ Model." In: *Phys. Lett. B* 100 (1981), pp. 485–488. DOI: 10.1016/0370-2693(81)90610-9.

[121] R. G. Edwards, Urs M. Heller, and T. R. Klassen. "Accurate scale determinations for the Wilson gauge action." In: *Nucl. Phys. B* 517 (1998), pp. 377–392. DOI: 10.1016/S0550-3213(98)80003-5. arXiv: hep-lat/9711003.

[122] Anna Hasenfratz, Curtis Taylor Peterson, Jake van Sickle, and Oliver Witzel. "Λ parameter of the SU(3) Yang-Mills theory from the continuous β function." In: (Mar. 2023). arXiv: 2303.00704 [hep-lat].

[123] Ken-Ichi Ishikawa, Issaku Kanamori, Yuko Murakami, Ayaka Nakamura, Masanori Okawa, and Ryoichiro Ueno. "Non-perturbative determination of the Λ-parameter in the pure SU(3) gauge theory from the twisted gradient flow coupling." In: *JHEP* 12 (2017), p. 067. DOI: 10.1007/JHEP12(2017)067. arXiv: 1702.06289 [hep-lat].

[124] Andreas Athenodorou and Michael Teper. "SU(N) gauge theories in 3+1 dimensions: glueball spectrum, string tensions and topology." In: *JHEP* 12 (2021), p. 082. DOI: 10.1007/JHEP12(2021)082. arXiv: 2106.00364 [hep-lat].

[125] Poul H. Damgaard and Shinsuke M. Nishigaki. "Universal spectral correlators and massive Dirac operators." In: *Nuclear Physics B* 518.1-2 (May 1998), pp. 495–512. DOI: 10.1016/s0550-3213(98)00123-0. URL: https://doi.org/10.1016/s0550-3213(98)00123-0.

[126] Leonardo Giusti and Martin Luscher. "Chiral symmetry breaking and the Banks-Casher relation in lattice QCD with Wilson quarks." In: *JHEP* 03 (2009), p. 013. DOI: 10.1088/1126-6708/2009/03/013. arXiv: 0812.3638 [hep-lat].

[127] Edoardo Di Napoli, Eric Polizzi, and Yousef Saad. "Efficient estimation of eigenvalue counts in an interval." In: *Numerical Linear Algebra with Applications* 23.4 (Mar. 2016), pp. 674–692. DOI: 10.1002/nla.2048. URL: https://doi.org/10.1002/nla.2048.

[128] G. Cossu, H. Fukaya, S. Hashimoto, T. Kaneko, and J. Noaki. "Stochastic calculation of the QCD Dirac operator spectrum with Mobius domain-wall fermion." In: *PoS* LATTICE2015 (2016), p. 067. DOI: 10.22323/1.251.0067. arXiv: 1601.00744 [hep-lat].

[129] Zoltan Fodor, Kieran Holland, Julius Kuti, Santanu Mondal, Daniel Nogradi, and Chik Him Wong. "New Approach to the Dirac Spectral Density in Lattice Gauge Theory Applications." In: *Origin of Mass and Strong Coupling Gauge Theories (SCGT15)*. WORLD SCIENTIFIC, Dec. 2017. DOI: 10.1142/9789813231467_0054. URL: https://doi.org/10.1142/9789813231467_0054.

[130] Pilar Hernández, Carlos Pena, and Fernando Romero-López. "Large N_c scaling of meson masses and decay constants." In: *Eur. Phys. J. C* 79.10 (2019), p. 865. DOI: 10.1140/epjc/s10052-019-7395-y. arXiv: 1907.11511 [hep-lat].

[131] Takashi Umeda. "A Constant contribution in meson correlators at finite temperature." In: *Phys. Rev. D* 75 (2007), p. 094502. DOI: 10.1103/PhysRevD.75.094502. arXiv: hep-lat/0701005.

[132] Margarita García Pérez, Antonio González-Arroyo, Liam Keegan, and Masanori Okawa. "Mass anomalous dimension of Adjoint QCD at large N from twisted volume reduction." In: *JHEP* 08 (2015), p. 034. DOI: 10.1007/JHEP08(2015)034. arXiv: 1506.06536 [hep-lat].

[133] V. A. Novikov, Mikhail A. Shifman, A. I. Vainshtein, and Valentin I. Zakharov. "Exact Gell-Mann-Low Function of Supersymmetric Yang-Mills Theories from Instanton Calculus." In: *Nucl. Phys. B* 229 (1983), pp. 381–393. DOI: 10.1016/0550-3213(83)90338-3.

[134] Margarita García Pérez, Antonio González-Arroyo, Liam Keegan, and Masanori Okawa. "Mass anomalous dimension of adjoint QCD at large N from twisted volume reduction." In: *Journal of High Energy Physics* 2015.8 (Aug. 2015). DOI: 10.1007/jhep08(2015)034. URL: https://doi.org/10.1007/jhep08(2015)034.

[135] Andreas Athenodorou, Ed Bennett, Georg Bergner, and Biagio Lucini. "Investigating the conformal behavior of SU(2) with one adjoint Dirac flavor." In: *Physical Review D* 104.7 (Oct. 2021). DOI: 10.1103/physrevd.104.074519. URL: https://doi.org/10.1103/physrevd.104.074519.

[136] Chris Allton, Michael Teper, and Aurora Trivini. "On the running of the bare coupling in SU(N) lattice gauge theories." In: *Journal of High Energy Physics* 2008.07 (July 2008), pp. 021–021. DOI: 10.1088/1126-6708/2008/07/021. URL: https://doi.org/10.1088/1126-6708/2008/07/021.

COLOPHON

This document was typeset using the typographical look-and-feel `classicthesis` developed by André Miede. `classicthesis` is available for both LaTeX and LyX:

https://bitbucket.org/amiede/classicthesis/

Final Version as of June 15, 2023 (`classicthesis` version 1.2).